Interaction of Rydberg hydrogen atoms with metal surfaces

Eric So

Merton College, University of Oxford

A thesis submitted for the degree of Doctor of Philosophy

Hilary Term, 2011

Interaction of Rydberg hydrogen atoms with metal surfaces

Eric So, Merton College

A thesis submitted in partial fulfilment of the requirements
for the degree of Doctor of Philosophy of the University of Oxford

Hilary Term, 2011

Abstract

This thesis presents a theoretical and experimental investigation of the interaction of electronically excited Rydberg hydrogen atoms with metal surfaces and the associated charge-transfer process. As a Rydberg atom approaches a metal surface, the energies of the Rydberg states are perturbed by the surface potential generated by the image charges of the Rydberg electron and core. At small atom-surface separations, the Rydberg atom may be ionised by resonant charge transfer of the Rydberg electron to the continuum of delocalised unoccupied metal states, with which the Rydberg electron is degenerate in energy. Typically, this 'surface ionisation' can be measured by extracting the remaining positively charged ion-cores with externally applied electric fields. By applying various levels of theory, from classical to fully time-dependent quantum calculations, this thesis explores various experimentally relevant effects on the charge-transfer process, such as the magnitude and direction of the externally applied electric field, the atom collisional velocity, the presence of local surface stray fields and electronically structured surfaces. The theoretical results give insight into the previous experimental work carried out for the xenon atom and hydrogen molecule, and point out some of the fundamental differences from the hydrogen *atom* system.

Experiments involving Rydberg hydrogen atoms incident on an atomically flat gold surface, a rough machined aluminium surface and a single crystal copper (100) surface are presented, providing for the first time the opportunity to make a quantitative comparison of theory and experiments. The ability to control the critical distance at which charge-transfer occurs is demonstrated by using Rydberg states of varying dimensions and collisional velocities. By changing the collisional angle of the incident Rydberg beam, the effect of Rydberg trajectory is also investigated. By manipulating the polarisation of the Rydberg electron with electric fields, genuine control over the orientation of the electron density distribution in the charge-transfer process is demonstrated. This property was predicted by the theory and should be unique to the hydrogen atom due to its intrinsic symmetry. By reversing the direction of the electric field with respect to the metal surface, electrons rather than positive ions are detected, with ionisation dynamics that appear to be very different, as predicted by quantum calculations. Experiments involving the single crystal Cu(100) surface also suggests possible resonance effects from image states embedded in the projected bandgap which are shown from quantum calculations to play an important role in the surface charge transfer of electronically structured metal substrates.

The experimental technique developed in this work provides some exciting future applications to study quantum confinement effects with thin films, nanoparticles and other bandgap surfaces. The ability to control the Rydberg orbital size, electronic energy, collisional velocity and orientation in the charge-transfer process will provide novel ways of probing the surface's electronic *and* physical structure, as well as being a valuable feature in offering new opportunities for controlling reactive processes at metallic surfaces.

Acknowledgements

First and foremost, I would like to thank Professor Tim Softley for his encouragement, input and advice over the past four years. I am particularly grateful to Tim for the proofreading of the drafts of this thesis and his patience in correcting my embarrassingly poor grammar. I would also like thank the whole Softley group for their friendship which has made working in the group such an enjoyable experience; in particular, Martin, Elin, James, Sashi, Will, Mark F and Mark D. Thanks also to Tertia for the many fantastic group dinners that I have attended over the years.

Many parts of the work presented in this thesis would simply have not been possible without the contributions of a few individuals. I am especially indebted to Martin, for all his ideas, help and advice with the theoretical work. Suffice to say that without Martin there would be no 'wavepackets' in this thesis. I would also like to thank Mark Ford, who not only designed the experimental setup but also taught me the experimental skills needed to complete this work. I am extremely grateful for the help of Sashikesh and Mark D in putting the experiment together and in getting the setup to work, and particularly to Mark D for working with me in the lab through many months of experimental toil. Thanks also to Rob Jacob for preparing the gold surfaces used in this work, and to the PTCL electronics and mechanical workshops for making and fixing the numerous pieces of kit required for the experiment.

I would like to thank all of my wonderful friends for making my time spent here in Oxford so enjoyable and memorable. Tim, Hugh, Catherine, Vicky, Lydia, Fran and Gill, your friendships are indispensable. I am again, particularly grateful for Martin's and Elin's friendship and support (and the weekly kicking sessions) throughout the PhD years.

Special thanks goes to Sarah, without whom the completion of my PhD and the writing of this thesis would really have not been possible. Thank you Sarah, not only for the dinners and cups of tea over the stressful months of writing up, but for all of your love and support over the years.

Lastly, I would like to thank my whole family for their continuous love and encouragement. In particular, I thank Claudia, Vera, Gerry, mum and grandmothers. I would like to dedicate this thesis to my dad, who sadly passed away in 2010. Last time I spoke to him about my research, he asked me 'What is the point of it?' and 'Can it make you rich?'. I giggled nervously and replied, 'For the sake of fundamental science' and 'Only in knowledge I'm afraid...'. Probably not the answers a businessman was looking for, but with the thesis now in its completion, I hope that he would be proud of it.

Contents

Chapter 1

Introduction

Rydberg atoms and molecules possess very large electronic orbital radii and polarisabilities, and are very susceptible to external fields, such that in the presence of a metal surface, they are strongly perturbed by the surface interactions. The interaction of Rydberg states with metal surfaces commonly leads to the charge transfer of an electron from the excited species to the metal surface. This thesis presents a theoretical and experimental investigation of the Rydberg hydrogen atom-surface interaction and the associated charge transfer process.

1.1 Motivations

Rydberg-surface interactions and charge transfer are of significance to a number of existing or potential applications in physics and chemistry. In plasma physics, it has been established that the characteristics of the plasma are strongly dependent on the interaction of metastable electronically-excited states at the surface-plasma boundary [1]. Since Rydberg species are likely to be abundant in many types of plasmas [2], the study of Rydberg-surface interaction can provide some insight to the behaviour of these media at the surface boundary. High-energy ion sputtering is known to proceed

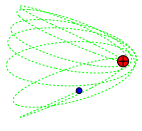

via the formation of hollow atoms with many electrons in high Rydberg orbitals [3], and the Rydberg electrons are 'stripped off' as the ion approaches the surface, in a process very similar to the Rydberg-surface charge transfer studied in this work. There is also experimental evidence for the thermal emission of Rydberg species (atoms, molecules and clusters) from impregnated metal oxide surfaces [4, 5], and the proposed mechanism for this desorption has been described as the time-reversed process of the Rydberg-surface charge transfer investigated here. Thus, studies of the kind described in this thesis may help to understand such processes by the application of microscopic reversibility.

In some applications (or potential applications), a full understanding of the close-range Rydberg-surface interaction is crucial for their successful implementation. It has been proposed that Rydberg atoms could be used for nanoscale pattern deposition on surfaces [6], especially as the spatial distribution of the Rydberg atoms could be controlled using low-intensity standing wave laser fields [6] or inhomogeneous electric fields [7, 8]. In the field of quantum computing, many recent atom-chip experiments and proposals involving trapped Rydberg states [9–12] have been motivated by the demonstration of a two-qubit quantum gate based on the excitation Rydberg blockade of trapped Rubidium atoms [13, 14]. In these experiments, the coherence properties and lifetimes of the excited Rydberg states are likely to be strongly influenced by the presence of the nearby substrates. Finally, in the area of chemical dynamics, the collisions of Rydberg states with adsorbates at surfaces could offer new opportunities for studying and controlling reactive processes at a surface.

Theoretically, Rydberg-surface interaction and its associated charge-transfer have gained much interest [15–34], especially for the case of the hydrogen atom. This is due to the simplicity (which makes it the most tractable system for quantum calculations) and intrinsic symmetry of the hydrogen atom-surface system [35, 36]. An extensive

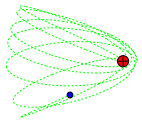

range of theoretical treatments has been applied to study atom-surface charge transfer, from classical over-the-barrier theory [15], classical trajectory and phase-space calculations [16, 17], semiclassical theory [18–20], perturbation theory [21–23], scattering theory [24], non-perturbative complex scaling calculations [25–27], etalon equation methods [28, 29], time-dependent close-coupling calculations [30], to time-dependent quantum wavepacket propagation calculations [31–34]. To date, however, only experiments involving Rydberg alkali metal atoms [37–43], xenon atoms [44–48] and hydrogen molecules [49–51] have been carried out. Although theoretical calculations for the Rydberg states of non-hydrogenic atomic systems are possible [32, 52, 53], these cannot be treated exactly, and often involve the implementation of a shielded Coulomb potential to account for the presence of the inner electrons; and the treatment of the nuclear degrees of freedom for the Rydberg *molecular* case remains a daunting and formidable task. The experimental study of the interaction of Rydberg hydrogen atoms with metal surfaces therefore provides for the first time, an opportunity for a genuine comparison of theory with experiments. Furthermore, as will be shown in the theoretical and experimental section, the fundamental differences between the hydrogen atom and non-hydrogenic species can provide new levels of control over the Rydberg-surface charge transfer process.

Unless explicitly stated or specified otherwise, atomic units are used throughout this thesis.

1.2 Rydberg states

In an atomic Rydberg state, one electron has been promoted into a diffuse, high energy orbital, with a large radius. Under field free conditions, the Rydberg electron wave function can be described by the principal quantum number n, angular momentum quantum number l, and magnetic quantum number m_l. The mean radius of the

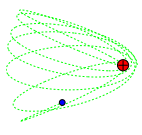

electronic orbit scales as n^2, and so the Rydberg electron binding energy is typically very small. The energy of the Rydberg state relative to the ionisation threshold to which the energy-level series converges is given by

$$E_{nlm_l} = -\frac{1}{2(n-\delta_l)^2} \tag{1.1}$$

where δ_l is the l-dependent quantum defect, which accounts for the deviation from the pure Coulombic potential for non-hydrogenic atoms which have a finite sized ion-core (δ_l is zero for the hydrogen atom). Rydberg states exhibit many attractive qualities which makes them good candidates for experimental study, and in particular the study of their interaction with metal surfaces. Due to the large orbital radius and the short time spent near the ion-core, Rydberg states have relatively long lifetimes with respect to decay process such as spontaneous emission ($\propto n^3$), blackbody decay ($\propto n^2$), or autoionisation and predissociation (for molecules) [54]. In comparison, excited valence states are generally too short-lived for beam-surface scattering experiments (with lifetimes of the order of μs), with the exception of the metastable rare gases. The large orbital radius and weak binding energy also results in a very long-range interaction with a metal surface; typically for a Rydberg principal quantum number $n = 20$ the charge transfer via resonant interaction with the unoccupied conduction band states of the metal occurs at around 100 nm. Although the Rydberg-surface interaction is relatively long-range, Rydberg states exhibits large polarisabilities ($\propto n^7$) and are highly sensitive to perturbing external fields, and thus can provide a sensitive probe of the surface characteristics. Furthermore, the spatial distribution of the Rydberg electron density can be easily manipulated by the application of external fields. Experimentally, the properties of the Rydberg orbital can be readily prepared and manipulated with a high level of control using a combination of spectroscopic selection and electromagnetic fields. In the presence of a metal surface, Rydberg states

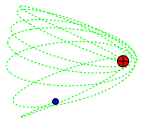

with their electron density directed either towards the surface or away from it (or with complex nodal patterns), can be spectroscopically selected with the application of an external electric field, and therefore the study of Rydberg surface collisions provides a model system for understanding charge transfer.

1.3 Stark Effect

It will be shown in Section 1.5 that in the presence of a metal surface, a Rydberg state interacts with surface fields that are generated by its image-charge. Due to the symmetry of this perturbing field, it can be compared with the effect of a homogeneous electric field (Stark effect). Furthermore, under typical experimental conditions (see Chapter 6), a homogenous electric field is applied in order to extract the charged particles formed from surface ionisation (Rydberg to the metal charge transfer).

The Schrödinger for a hydrogen atom in a homogeneous electric field, F, in the z-direction is given by

$$\begin{aligned} H\Psi &= (H^0 + H^1(F))\Psi = E\Psi \\ H^0 &= -\frac{1}{2}\nabla^2 - \frac{1}{r} \\ H^1(F) &= -\hat{F}\cdot\hat{\mu} = -F\mu_z = +Fr\cos\theta \end{aligned} \tag{1.2}$$

where $\hat{\mu}$ is the dipole moment operator and μ_z is its z-component; H^0 is the zero field Hamiltonian and $H^1(F)$ is the perturbing Stark Hamiltonian. Solving Eq. 1.2 with zero-field (H^0 only) in spherical co-ordinates leads to the hydrogenic wavefunctions $\Psi_{nlm_l}(r,\theta,\phi) = |nlm_l\rangle = R_{nl}(r)Y_{lm_l}(\theta,\phi)$ where $R_{n,l}(r)$ are radial wavefunctions for the hydrogen atom, and $Y_{l,m_l}(\theta,\phi)$ are spherical harmonics. The energies are given by Eq. 1.1 (with $\delta_l = 0$) which depends only on n, and the bound states have an electronic degeneracy of n^2. Eigenstates of the Hamiltonian $H = H^0 + H^1$ can be

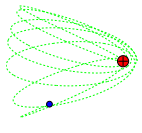

expressed as a linear combination of the hydrogen wavefunction basis $|nlm_l\rangle$. By applying the orthogonality relations of the spherical harmonics, it can be shown easily that states with $m' = m$ and $l' = l \pm 1$ are coupled by the electric field [35]. Thus, in the presence of an electric field, the orbital angular momentum number l is no longer a good quantum number, and only m_l is conserved.

The Schrödinger equation from the Hamiltonian in Eq. 1.2 is separable and may also be solved in parabolic co-ordinates [35]. The parabolic wavefunctions can be described with quantum numbers n, m_l and parabolic quantum numbers n_1 and n_2. It is generally more useful to use the difference $k = n_1 - n_2$, as a quantum number which can take $(n - m)$ integer values ranging from $-(n - |m_l| - 1)$ to $(n - |m_l| - 1)$, in steps of two. The energy levels of the H atom in an electric field are given by [55]

$$\begin{aligned} E_{nm_lk}(F) \;=\; & -\frac{1}{2n^2} + \frac{3}{2}nkF - \frac{n^4}{16}[17n^2 - 3k^2 - 9m_l^2 + 19]F^2 \\ & + \frac{3}{32}n^7k[23n^2 - k^2 + 11m_l^2 + 39]F^3 \\ & - \frac{n^{10}}{1024}[5487n^4 + 35182n^2 - 1134m_l^2k^2 + 1806n^2k^2 - 3402n^2m_l^2 \\ & - 3093k^4 - 549m_l^4 + 5754k^2 - 8622m_l^2 + 16211]F^4 \\ & + O(F^5) + \cdots . \end{aligned} \tag{1.3}$$

Thus, the n^2 degenerate energy levels at zero-field belonging to the same n-manifold split under the external electric field, and to first-order approximation the Stark splitting is linearly dependent on the strength of the electric field and the value of k. A positive k quantum number results in a blue-shifted Stark state (shifted to higher energy), whilst a negative k results in a red-shifted Stark state (shifted to lower energy). Figure 1.1 presents the hydrogen atom Stark map for $n = 10-12$. The polarisation of the electronic wavefunction may be highly asymmetric with respect to the field axis, especially for the extreme members of the Stark manifold, giving rise to a very large

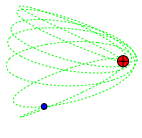

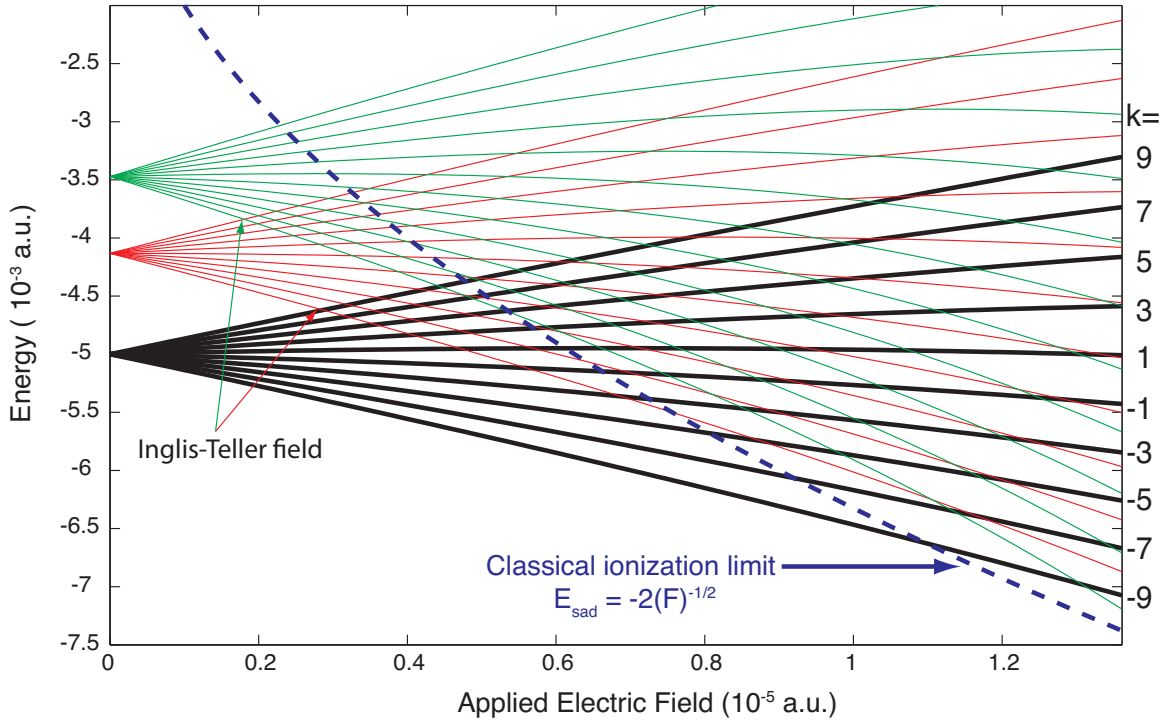

Figure 1.1: Calculated Stark map (energy *vs* applied electric field plot) for hydrogen $n = 10 - 12$, $m_l = 0$ manifolds using Eq. 1.3.

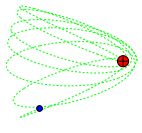

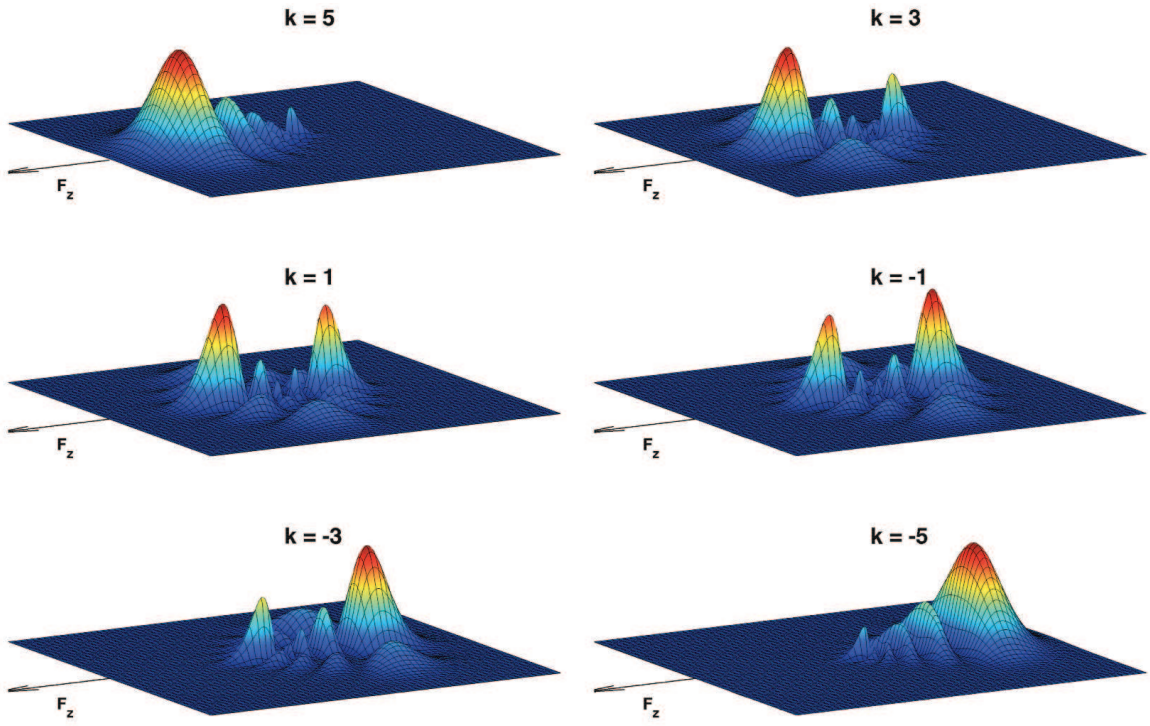

Figure 1.2: The 'parabolic' electron wavefunctions for the $n = 6$, $m_l = 0$ states of the hydrogen atom. To first order, the dipole moment of the electronic wavefunction is $1.5nk$.

effective dipole moment (the gradient of the energy versus field in the Stark map). These large dipole moments may be used to manipulate, decelerate, or trap Rydberg atoms and molecules [7, 8, 10, 56]. To first order, the dipole moment of the electronic wavefunction is $1.5nk$ (see Eq. 1.3). Figure 1.2 presents a plot of the $n = 6, m_l = 0$ hydrogen 'parabolic' eigenstates.

For hydrogenic systems, there is no coupling between different parabolic states of the same m, and so states with different n but same m may cross without interaction. The field at which the extreme blue state of the $(n-1)$-manifold crosses with the extreme red state of the n-manifold, is known as the Inglis-Teller limit ($F_{\rm IT} \approx \frac{1}{3}n^{-5}$ a.u. $= 1.7 \times 10^9 \mathrm{n}^{-5}$ Vcm^{-1}).

For the case of non-hydrogenic systems the finite sized core results in the loss of spherical symmetry near the core and the wave function is no longer fully separable in parabolic co-ordinates. This reduction in symmetry results in coupling between states with the same m and different n. As the field increases beyond the Inglis-Teller limit and adjacent manifolds begin to overlap there are now avoided crossings between the coupled red and blue states. At the avoided crossings there can be large changes to the character of the wavefunction: following an avoided crossing adiabatically, the wavefunction of the blue-shifted state will 'flip' in direction and exhibit the character of the red-shifted state with which it is coupled, and vice versa. Figure 1.3 shows the calculated Stark map for xenon atoms in the $n = 13 - 15$ energy range. Note that for non-hydrogenic atoms, low-l states, which penetrate the core most, have non-zero quantum defect δ_l (the phase shift of the radial wavefunction from the hydrogenic case due to deviations from pure Coulomb potential), and so are energetically separated from non-penetrating high-l states and only exhibit a quadratic Stark shift at low fields.

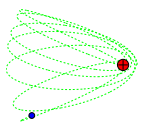

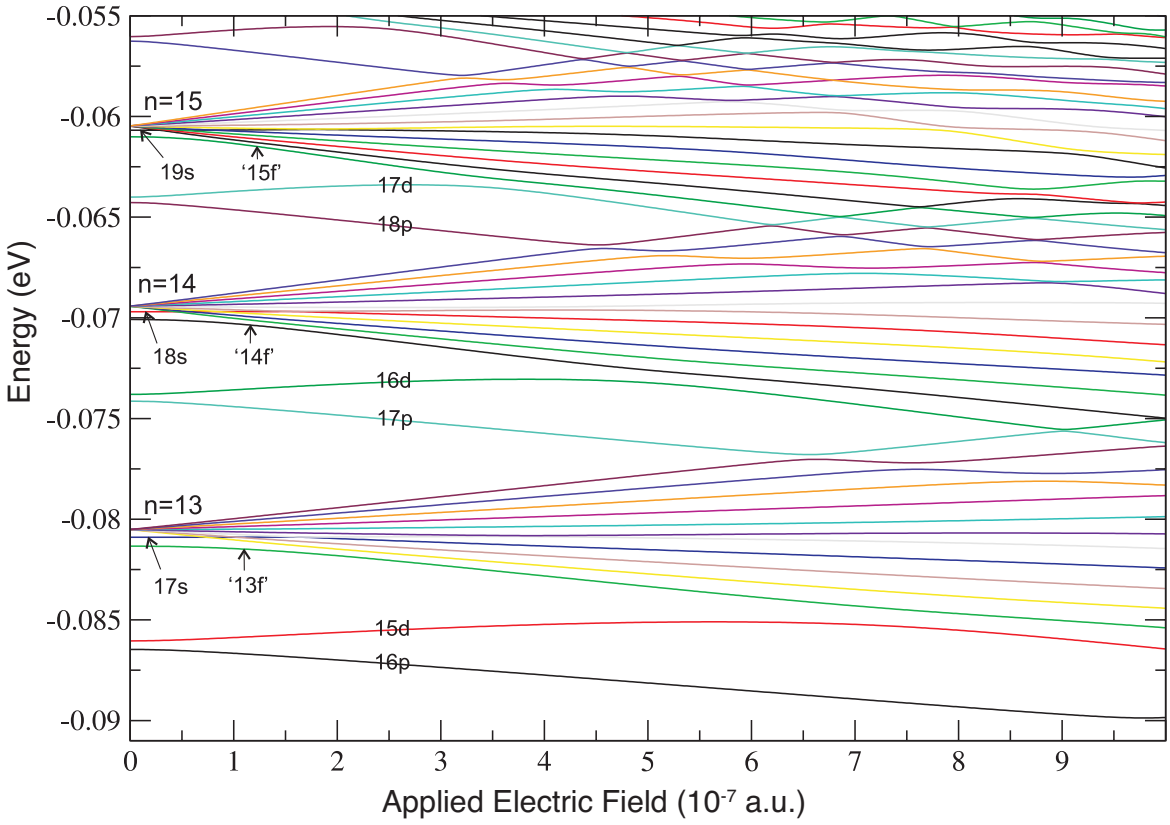

Figure 1.3: Calculated Stark map for xenon $n = 13 - 15$, $m_l = 0$ manifolds. Note the avoided crossings beyond the Inglis-Teller field unlike the hydrogen atom Stark map shown in Fig. 1.1.

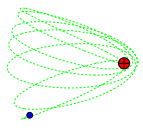

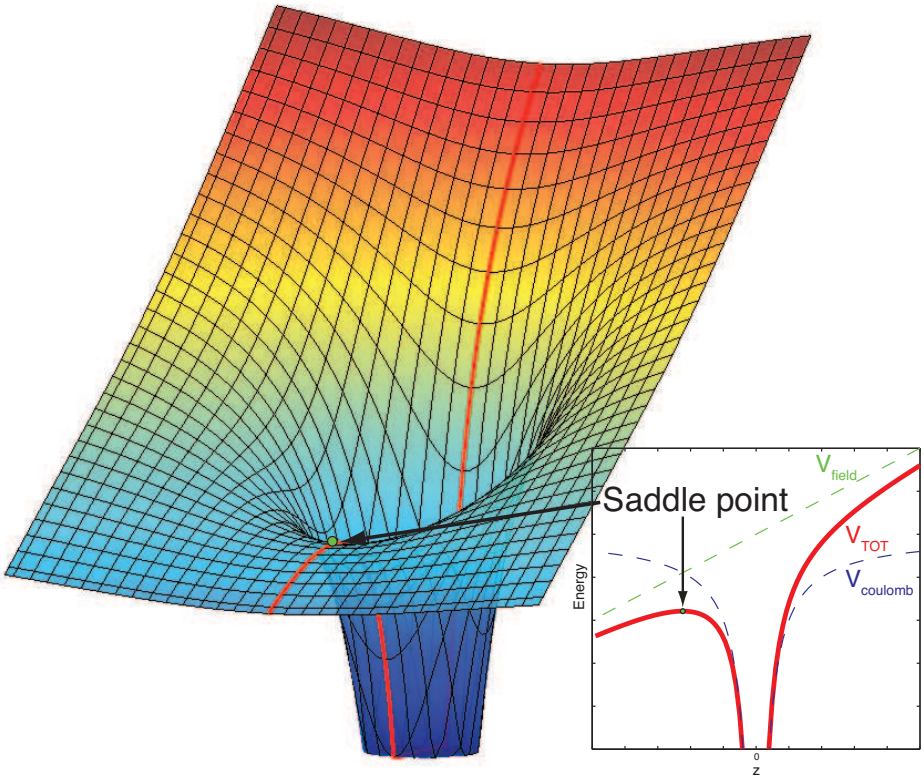

Figure 1.4: Plot of the combined Coulomb and Stark potential. Note the presence of a saddle point along the z(field)-axis.

1.4 Field Ionisation

The combined Coulomb-Stark potential when an external electric is applied along the z-axis has the form

$$V = -\frac{1}{r} + Fz. \tag{1.4}$$

Figure 1.4 shows a plot of this combined potential. At $z = -1/\sqrt{F}$ there is a saddle point with the value $V_{\text{saddle}} = -2\sqrt{F}$. As the magnitude of the electric field increases, the energy of the saddle point lowers while the potential on the opposite side of the core increases. The energy of the saddle point as a function of field is shown in Figure 1.1 as dashed line. Using Eq. 1.3, it can shown that the most extreme red-shifted $m_l = 0$ state reaches an energy above the saddle point at a field of $F \sim 1/(9n^4)$,

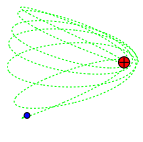

while the extreme blue states lie above the saddle point at $F \sim (11 - 4\sqrt{7})/(9n^4)$. Quantum mechanically, no electronic states are stable in the presence of electric fields as tunnelling through the potential barrier is possible. From a classical over-the-barrier perspective, all electronic states energetically above the saddle point energy will be ionised, while states energetically below the saddle point remain bound. This suggests that the higher energy blue-shifted stark states would ionise at lower fields than the red-shifted states. However, the spatial distribution of the electron density along the field axis varies strongly from red to blue states (Figure 1.2), and the electron wavefunction of blue-shifted states is in fact principally located on the opposite side of the core from the saddle point. Consequently, despite being higher in energy, the blue-shifted states are kinetically more stable than the red-shifted ones. The field ionisation rate Γ of hydrogenic Rydberg states can be approximated by [57]:

$$\Gamma = \frac{(4R)^{2n_2+m_l+1}}{n^3 n_2!(n_2+m_l)!} \exp\left[-\frac{2}{3}R - \frac{1}{4}n^3 F\left(34n_2^2 + 34n_2 m_l + 46n_2 + 7m_l^2 + 23m_l + \frac{53}{3}\right)\right] \tag{1.5}$$

where $R = (-2E_{nm_lk})^{3/2}/F$, and E_{nm_lk} is the fourth order perturbative Stark energy as given by Eq. 1.3. The filled circles in Figure 1.5 shows the electric fields at which the field ionisation of Stark states reaches the values of 10^5 s^{-1} which is the typical timescale for Rydberg-surface experiments ($\sim$ 10 μs). It can be seen from Fig. 1.5 that while the most extreme red-shifted state ionises approximately at the classically predicted field ($F = 1/(9n^4)$), about twice that field is required for the same rate of ionisation for the most extreme blue-shifted state.

1.5 Interaction with metal surfaces

The boundary conditions for a point charge above a 'perfect' metal (infinite polarisability) are for the electric potential to be zero and the electric field to have no

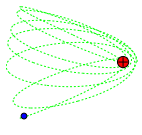

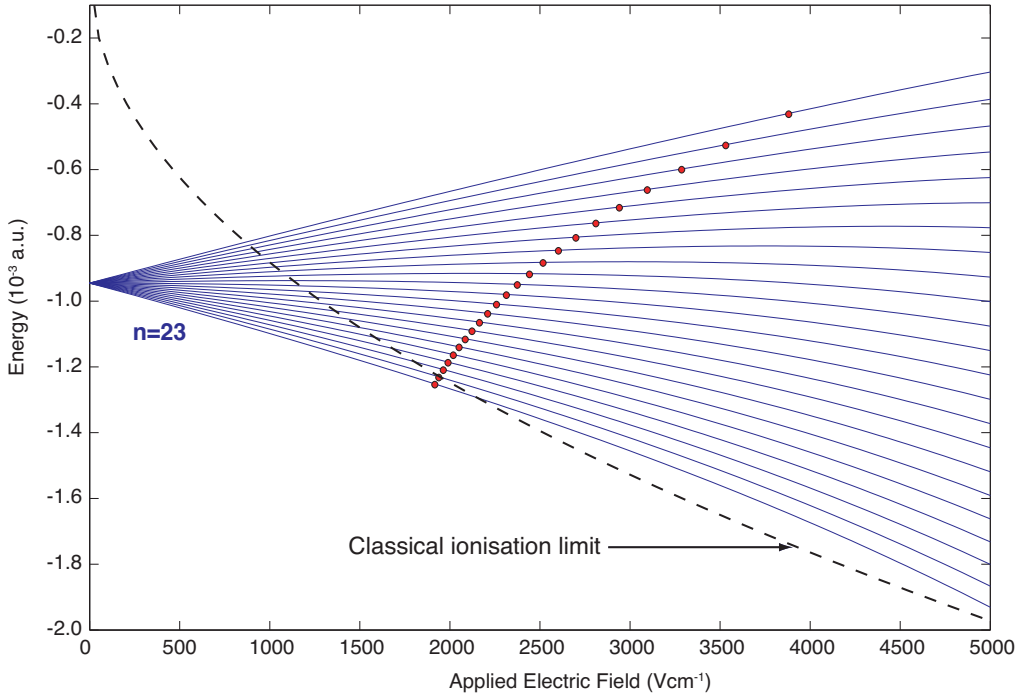

Figure 1.5: Stark map of hydrogen atom $n = 23$, $m_l = 0$ manifold. Filled circles mark the critical fields at which the field ionisation rate reaches 10^5 s^{-1}, calculated from Eq. 1.5. Note that due to the kinetic stability of blue-shifted Stark states, only the critical field for most-extreme red-shifted state approximately coincides with the classical limit.

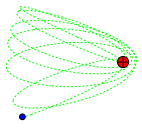

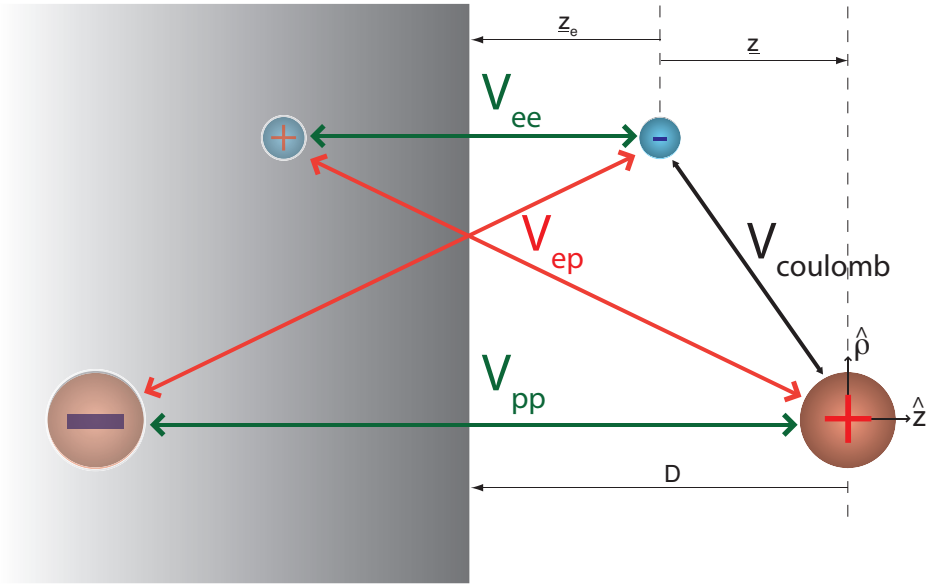

Figure 1.6: Classical image charge interaction between 'real' (right) and 'fictitious' (left) particles.

components perpendicular to the surface at the metal / vacuum interface. This leads to the representation of charge distribution induced within the metal as a fictitious image-charge which is located at the same distance below the surface as the real charge is above the surface (i.e. the surface boundary is the mirror plane). The interaction of a Rydberg state with metal surfaces at *long range* can be seen as the interaction of a point dipole with a metal surface as shown in Figure 1.6. The system is cylindrically symmetric for all electron positions about the ion-core–ion-image axis. The dipole of the Rydberg state interacts with its oppositely charged image-dipole inside the metal and the overall one-electron potential in cylindrical co-ordinates is given by:

$$\begin{aligned} V_{\text{tot}}(\mathbf{r}) &= V_{\text{coulomb}} + V_{\text{surf}} + V_{\text{field}} \\ &= -\frac{1}{r} + V_{\text{surf}} + Fz \\ &= -\frac{1}{\sqrt{(z^2+\rho^2)}} + V_{\text{surf}} + Fz \\ &= -\frac{1}{\sqrt{(z^2+\rho^2)}} + [V_{ee} + V_{pp} + V_{ep}] + Fz \end{aligned} \tag{1.6}$$

and

$$\begin{aligned}\lim_{D\to\infty} V_{\text{surf}} &= V_{ee} + V_{pp} + V_{ep} \\ &= -\frac{1}{4z_e} - \frac{1}{4D} + \frac{1}{\sqrt{(D+|z_e|)^2+\rho^2}} \\ &= -\frac{1}{4(D+z)} - \frac{1}{4D} + \frac{1}{\sqrt{(D+|D+z|)^2+\rho^2}} \end{aligned} \tag{1.7}$$

where F is an external electric applied along the z-axis, V_{ee}, V_{pp} and V_{ep} are the electron–image-electron, proton–image-proton and electron–image-proton potential respectively, D is the ion-core–surface separation, (z, ρ) are the electron co-ordinates in the ion-core frame, and $z_e = (D+z)$ is the electron-surface separation (see Figure 1.6). At the surface ($D = 0$), the repulsive electron–image-proton interaction V_{ep} cancels the coulombic interaction V_{coulomb}, and both vanish inside the metal.

For better insight into the longe-range Rydberg-surface interactions, equation 1.7 can be expanded binomially [23]:

$$\lim_{D\to\infty} V_{\text{surf}} = -\frac{1}{16D^3}(r^2+z^2) + \frac{3}{32D^4}(zr^2+z^3) + \dots \ , \tag{1.8}$$

the first non-zero term is the well known instantaneous Van der Waals interaction (or Lennard-Jones model) which scales as D^{-3}. Note that the attractive proton–image-proton interaction $V_{pp} = -1/(4D)$ is no longer present, as it has been cancelled by a repulsive electron position independent $+1/(4D)$ term from the expansion of V_{ee} and V_{pp}. It can be seen from Eq. 1.8 that as the Rydberg state approaches a metal surface, the dominant interaction is attractive. For $D^2 >> r^2$, retaining only the first term of Eq. 1.8, it can be shown that hydrogenic spherical basis functions $|nlm\rangle$ with $\Delta l = 0, \pm 2$, $\Delta m_l = 0$ are coupled by the Van der Waals perturbation. Thus, similar to the Stark effect, the n^2 degeneracy of each n-manifold is split under

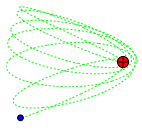

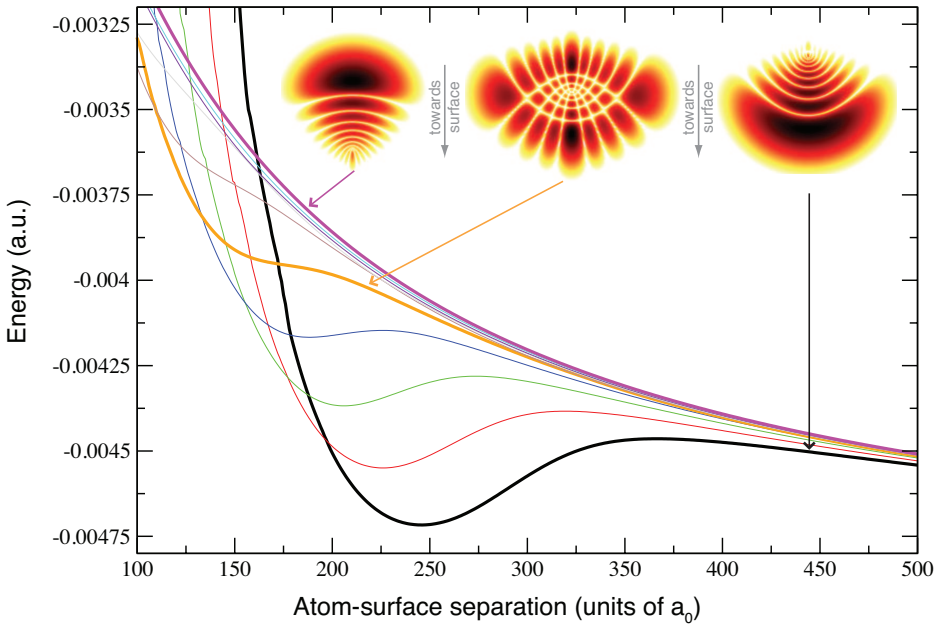

Figure 1.7: Energies of $n = 10, m_l = 0$ Rydberg states of the hydrogen atom as a function of surface separation with no externally applied fields (the attractive proton–image-proton term $V_{pp} = -1/(4D)$ is not included in the energy to show the individual Rydberg levels more clearly). The electron density of the lowest-energy surface-oriented state, highest-energy vacuum-oriented state and mid-manifold 'unpolarised' state at atom-surface separations of 600 a_0 are also shown.

the surface perturbation. Furthermore the eigenfunctions of the surface-perturbed Hamiltonian are also strongly polarised, and in this case, with respect to the surface normal. Figure 1.7 presents the energies of $n = 10, m_l = 0$ Rydberg states of hydrogen atom as a function of surface separation, calculated using complex scaling theory (see Section 2.2; note that the attractive proton–image-proton term $V_{pp} = -1/4D$ is not included in the energy to show the individual Rydberg levels more clearly); the electronic wavefunctions for the extreme surface-oriented (lowest in energy of the manifold), 'unpolarised' (middle of the manifold), and vacuum-oriented (highest in energy of the manifold) states at a surface separation of 600 a_0 are also shown (note the similarity of the surface eigenstates to Stark wavefunctions (Fig. 1.2)). Unsurprisingly, the kinetic lifetime effect responsible for the differing field ionisation rates of red- and

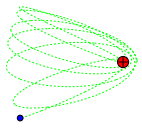

blue-shifted Stark states in a homogeneous field is also shown in the similar behaviour of the rate of surface ionisation for surface- and vacuum-oriented states, and will be discussed in more detail in Chapter 3.

1.5.1 Electron-surface interaction: Jellium model

To fully model the charge-transfer process, the electron dynamics at the metal surface/ vacuum interface and inside the metal must be described correctly. The form of the electron–image-electron V_{ee} term given by Eq. 1.7 is correct asymptotically ($D \to \infty$), but is not appropriate close to the metal interface, as it becomes singular at $z = -D$. The simple Jenning-Jones one-electron pseudopotential [58] treats the metal using the Jellium model – electrons moving in a uniform background of positive charge, and interpolates smoothly from the bulk metal potential to the asymptotic image-charge potential outside the metal:

$$V_{ee}(z, D) = \begin{cases} \frac{-1+\exp[-\beta((z+D)-z_0)]}{4((z+d)-z_0)} & \text{if } (z+D) > z_0 \\ \frac{V_0}{A\exp[B((z+D)-z_0]+1} & \text{otherwise} \end{cases} \tag{1.9}$$

$$\text{with} \qquad A = -1 - 4V_0/\beta, \quad B = -2V_0/A.$$

V_0 is the bulk metal potential, z_0 is the image-plane of the metal surface, and β is an interpolation parameter. For typical calculations carried out in this thesis, an aluminium surface with parameters: $z_0 = 0.7$, $V_0 = -0.574$ and $\beta = 1.25$ is used as a model free-electron metal. Parameters for other free-electron metals can be applied, but this has negligible effect on the results of the complex scaling and wavepacket propagation calculations carried out in Chapter 3. Figure 1.8 shows a plot of the total one-electron potential given by Eq. 1.6, and the separate contributions of V_{surf} (Eq. 1.7), with V_{ee} given by the Jellium potential (Eq. 1.9).

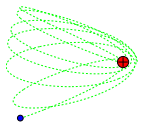

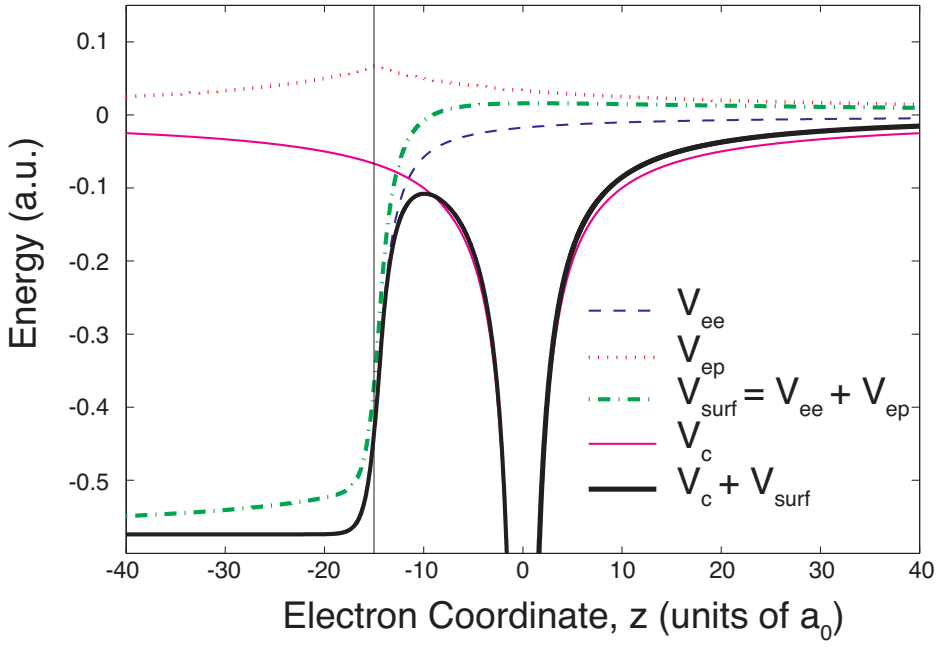

Figure 1.8: Plot of the surface interactions V_{ee} and V_{ep} (Eq. 1.9, 1.7), the total surface potential V_{surf}, the Coulomb potential V_c, and the total potential experienced by a Rydberg electron in absence of an external electric field ($V_c + V_{\text{surf}}$, Eq. 1.6). The surface is positioned at the electron co-ordinate (with respect to the ion-core position) of $z = -15$ a_0.

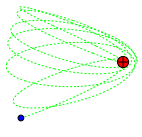

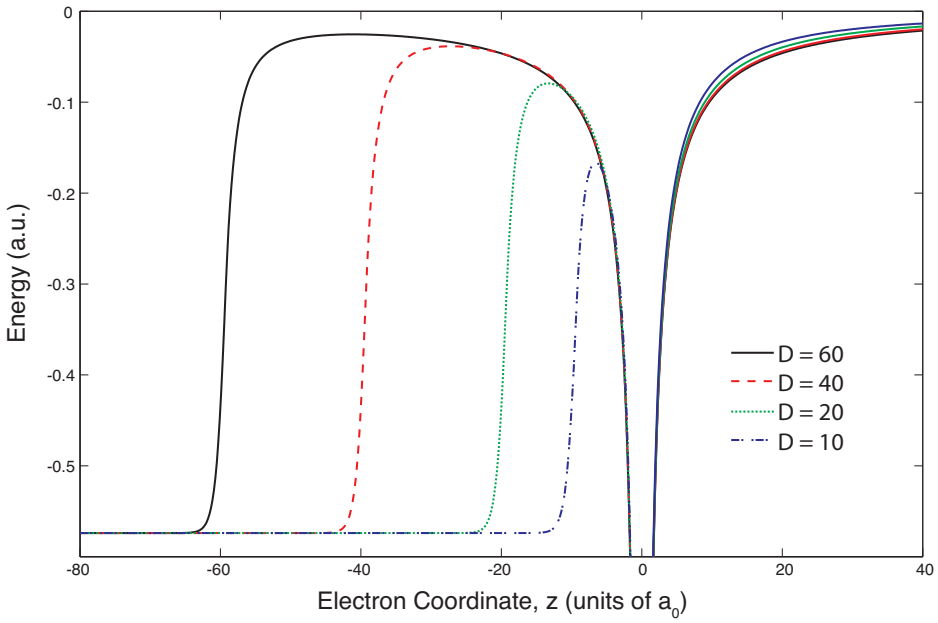

Figure 1.9: Plot of the total one electron potential $V_c + V_{\text{surf}}$ (Eq. 1.6) at atom-surface separations of $D = 60, 40, 20, 10$ a_0.

1.5.2 Classical Rydberg-surface charge-transfer

Figure 1.9 shows total one-electron potential (Eq. 1.6) at various Rydberg-surface separations. Similar to the homogenous field case, there is a saddle point located along the surface normal and at $\rho = 0$. The position of the saddle point in the ion-core frame is given by [17]:

$$z_{\text{saddle}}(D) = -\left(1 - \sqrt{\frac{4\sqrt{2}-5}{7}}\right) D \approx -0.69D, \quad \rho = 0 \tag{1.10}$$

with saddle height

$$E_{\text{saddle}} = -\frac{7\sqrt{5+4\sqrt{2}}}{4D(1+2\sqrt{2})} - \frac{1}{4D} \approx -\frac{1.7422}{D}. \tag{1.11}$$

From Fig. 1.9, Eq. 1.10 and Eq. 1.11, it can be seen that as the atom approaches the surface, the width and the height of the potential barrier decrease, thus facilitating

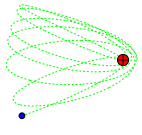

charge transfer. Comparing the saddle energy with the Rydberg electronic energy (Eq. 1.1), leads to a classical over-the-barrier (OTB) ionisation distance of $D_{\mathrm{OTB}} \approx 3.48n^2\ a_0$ in zero-field [15]. For the $n = 20$ hydrogen Rydberg state, this corresponds to an ionisation distance of ≈70 nm. Note that the $3.48n^2\ a_0$ OTB ionisation distance derived above is only valid for zero-field, which is not the case for typical Rydberg-surface experiments [44–51], and does not include the energy shifts of the perturbed Rydberg state, or the effects of the electronic wavefunction polarisation. Extension of the OTB barrier model to include the Rydberg energy shift and an external electric field is presented in Section 2.1.

1.6 Experimental studies of Rydberg-surface interactions

In general, experimentally measurable parameters for the Rydberg-surface interactions include: i) the deflection in Rydberg trajectory, such that the forces which arise from Rydberg-surface interaction can be inferred; ii) the energy shift of the Rydberg state as a results of surface perturbation, which may be measured spectroscopically; iii) the formation of charged particles (ions principally) as a consequence of Rydberg-surface charge transfer, such that the probability of ionisation as a function of surface separation can be inferred. The experimental work that is presented in this thesis is based on the last of these three, and is discussed in Chapter 6.

The following section provides a brief outline of the experimental progress to date in study of the interaction of Rydberg states with metal surfaces. Focus is placed on the ways in which detailed information on the nature of the Rydberg state as well as the metal surface can be extracted by probing the Rydberg-surface interactions.

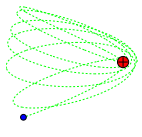

1.6.1 Studying the long-range Rydberg-surface interaction

Measuring the Van der Waals force

As explained in Section 1.5, the long-range Rydberg surface interaction for atom-surface separations (D) much greater than typical Rydberg dimensions can be approximated by the instantaneous Van der Waals interaction,

$$V_{\mathrm{VDW}} = -\frac{1}{16D^3}(r^2 + z^2) \ , \tag{1.12}$$

where r, z are the Rydberg electron co-ordinates in the ion-core frame [1]. This attractive interaction is expected to scale as the Rydberg dimension squared (n^4). Hinds and coworkers measured the long-range Van der Waals interaction by sending Cs and Na Rydberg atoms between two parallel gold-coated mirrors [37]. As Rydberg atoms pass through the 'tunnel', the long-range attractive Van der Waals force deflects the Rydberg trajectory towards the tunnel walls. Only Rydberg trajectories that pass most centrally between the plates are not deflected into the metal walls and survive at the end of the tunnel. Measuring the transmission of Rydberg atoms through the tunnel as a function of principal quantum number and plate separation, the magnitude of the deflection due to the Van der Waals force was inferred, and was found to be in good agreement with theoretical trajectory calculations. In the same experimental setup, the energy shifts and widths of the $3p - ns$ ($n = 10 - 13$) transitions of Na Rydberg atoms were measured as a function of plate separation (500-2000 nm) [38, 39]. The measured energy-shifts were in good agreement with first order perturbative energy-shifts predicted using Eq. 1.12 (see Section 2.1). For both sets of experiments however, small deviations from the theoretical predictions were observed. These deviations were

[1] Note that the 'Van der Waals' interaction between the (instantaneous) atomic dipole and the 'induced' image-dipole described by Eq. 1.12 scales with D^{-3}, in common with the well known dipole-dipole interaction, but in contrast to the familiar dispersion interaction between two neutral atoms which scales with D^{-6}.

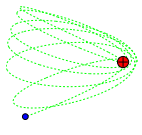

attributed to the presence of patch field effects due to the polycrystalline structure of the evaporated gold surfaces, and were found to scale as D^{-2} [38, 39], typical for stray patch fields [59–61]. Thus, by comparing the experimental results with theory, it was demonstrated that it is possible to extract information on the nature of the metal surface from the study of relatively longe-range Rydberg-surface interactions.

Spectroscopic measurement of the Rydberg energy shift at atom chips

As mentioned in the introduction, recent developments in using ultracold, strongly interacting Rydberg atoms as quantum devices has developed much interest for studying Rydberg-surface interactions. For the application of any quantum device, control over the quantum states energies, populations and coherence lifetimes is essential. Using excited-state electromagnetically induced transparency (EIT), Tauschinsky *et al.* [11] recently measured the energy shifts and linewidths of the $5p-nd_{\frac{5}{2},\frac{3}{2}}$ and $5p-ns_{\frac{1}{2}}$ levels ($n = 22 - 36$) of ultracold Rb Rydberg atoms which have been trapped on a atom chip as a function of atom-surface separation ($10 - 200\mu$m). Although no significant broadening of the Rydberg levels was observed, thus not inhibiting the coherence of the Rydberg states, significant energy-shifts were measured. The corresponding local electric field strengths required to bring about the energy shifts did not follow the expected D^{-3} scaling from Van der Waals interaction (Eq. 1.12), but a much slower decay power-law $\propto D^{-0.7}$. The slow decaying local electric fields were accounted for by assuming a gaussian distribution of Rb adsorbates deposited on the chip surface (from the trapped cloud), and treating each adsorbate as an electric dipole oriented perpendicular to the surface [62]. Again, experiments such as this illustrate how Rydberg states may be used as a sensitive, spatially resolved probe of close-range electric fields.

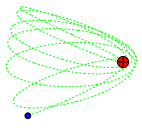

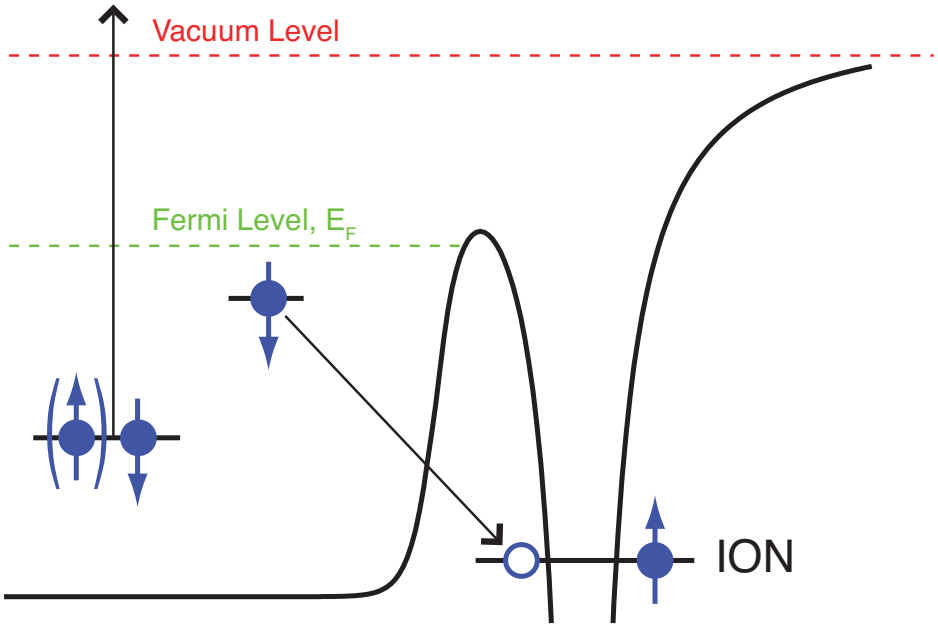

Figure 1.10: Schematic illustration of the Auger neutralisation process at a metal surface, modified from Ref. [63]. At close range, an electron is transferred from the conduction band of the metal to the ground state of the ion. To conserve energy, a secondary Auger electron is emitted from the metal to the vacuum.

1.6.2 Studying Rydberg-surface charge-transfer

The experimental studies discussed so far involve very long range Rydberg surface interaction with relatively low n (< 40), and D on the order of μm. At *close* range ($D \approx n^2$), Rydberg-surface interactions can result in the charge-transfer of the Rydberg-electron to the metal conduction band (surface ionisation). After ionisation, the positively charged ion-core is accelerated toward the surface by its own image-charge, and unless the ion-core is extracted before hitting the surface, it will be neutralised at the surface (via Auger neutralisation [63], see Figure 1.10). The close-range interaction and surface ionisation of Rydberg atoms at metallic surfaces can therefore be studied by either monitoring the fraction of Rydberg atoms that are not surface ionised (survival probability), or detecting directly the residual positively charged ion-cores which result from surface ionisation. The possibility of extracting

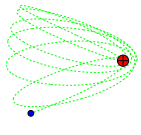

electrons produced by the charge-transfer process is discussed in Chapter 3.

Rydberg atom transmission through a metallic mesh

One of the first experiments to investigate the details of ionisation of Rydberg atoms at a metallic surface was performed by Fabre *et al.* [40], who passed a beam of Na(nd) Rydberg atoms through a thin ($\sim 3\mu$m) gold foil with micron sized slits. Similar to the work of Hinds *et al.* (see previous section), the transmission of the Rydberg atoms through the slits was measured as a function of the Rydberg atom principal quantum number, n. In this case, the Van der Waals deflection has a very minor effect as the foil is very thin, and therefore the observed transmission provides a direct measure of the fraction of Rydberg states that do not undergo surface ionisation by impact at the surface on passing close to the slit edge. Treating the Rydberg states as hard-spheres, and the slits as a 'sieve' of Rydberg dimensions, an 'effective' scaling radius (or surface ionisation distance) of $\sim 4.5n^2a_0$ was inferred from the experimental results, larger than the $\sim 3.5n^2a_0$ predicted from the hydrogenic over-the-barrier model (Section 1.5.2).

Kocher *et al.* extended these experiments to look at the effects of adlayer formation on the surface [41]. The transmission of a beam of Li Rydberg atoms through a baked gold metal mesh was found to exhibit strong variations as a function of time. These changes were attributed to the changes in the overall local surface electric field due the formation of a monolayer of adsorbed water and Li on both sides of the gold mesh that is capable of ionising the Rydberg Li atoms, i.e. adsorbates can be 'seen' growing on the gold mesh as the time progresses. Comparing with theoretical adsorption rates, a sensitivity to changes of $\approx 1 \times 10^{-4}$ of a monolayer of adsorbate on the gold mesh was deduced [42]. It is this sensitivity towards external fields which makes Rydberg states such an attractive system for probing surface characteristics.

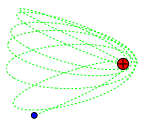

Ionisation of grazing incidence Rydberg beams

The experimental work presented in this thesis is based on the pioneering experiment of Gray *et al.* [43], who recorded the ion production due to the ionisation of a grazing-incidence beam of K(nd) Rydberg atoms at a flat gold mirror metallic surface. To prevent neutralisation of the positive ions at the surface, which have initial velocity towards the surface and are also attracted by their image-charges, a large electric field perpendicular to the surface was applied. For a sufficiently large electric field, the initial momenta of the ions and the attractive image-charge force on them can be overcome, allowing the ions to be collected, and detected by a charged-particle detector.

Using the classical image-charge model, the perpendicular component of energy of a point charge in the presence of a homogeneous electric field F, and at distance of D from the surface, is given by

$$U_\perp = T_\perp - \frac{1}{4D} - Z_c F D \tag{1.13}$$

where $T_\perp$ is the kinetic energy component normal to the surface, and Z_c is the charge of the particle (for the proton $Z_c = +1$). Applying the law of conservation of energy, the minimum field $\vec{F}_{\rm min}$ required to extract a charged-particle formed at distance D_i from surface with kinetic energy $T_\perp$ is given by

$$\vec{F}_{min}\left(D_i, T_\perp\right) = Z_c \left[\frac{1}{2D_i} + \sqrt{\frac{T_\perp}{D_i}}\right]^2 . \tag{1.14}$$

Alternatively, Eq. 1.14 can be rearranged to give the minimum ionisation distance

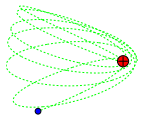

from the surface, $D_{\min}$, that can be extracted for a given applied field $\vec{F}$,

$$D_{\min}(\vec{F}, T_\perp) = \frac{T_\perp + \sqrt{(\vec{F}/Z_c)} + \sqrt{T_\perp^2 + 2T_\perp\sqrt{(\vec{F}/Z_c)}}}{2(\vec{F}/Z_c)}. \tag{1.15}$$

Eq. 1.14 and Eq. 1.15 show how the external field required to detect the ions is related to the ionisation distance from the metallic surface: the closer to the surface the ion is formed, the greater is the extraction field required to pull the ion away; by measuring the ion signal as a function of the external applied field, the ionisation distance can be inferred. In the asymptotic limit of $T_\perp \to 0$, and assuming that $D_i \propto n^2$ (from over-the-barrier model, Section 2.1), it can be shown from Eq. 1.14 that

$$\lim_{T_\perp \to 0} \vec{F}_{min}(D_i, T_\perp) = \frac{Z_c}{4D_i^2} \sim\propto n^{-4}. \tag{1.16}$$

By varying the principal quantum number of the K(nd) Rydberg atoms, and therefore the Rydberg orbital dimensions, Gray *et al.* [43] observed a rise in the ion signal within the $(4-5)n^2$ a_0 range as determined by Fabre *et al.* [40] previously. However, the observed ion signal which scaled with n^2 was a secondary rise, and the actual threshold fields for ion extraction were very low, and independent of principal quantum number of the Rydberg state. It was believed that these experiments using alkali atoms suffered from problems of alkali atom deposition on the metallic surfaces, causing inhomogeneous fields which were able to ionise the Rydberg atoms at large surface separations (*c.f.* the experiments of Kocher [41] and Tauschinsky [11] described above).

Ionisation of grazing Rydberg Xenon atoms

The problem of atom adsorption at the metal surface can be removed by using rare-gas Rydberg atoms, which do not adhere to the surface. Dunning and co-workers studied

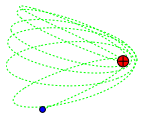

the charge transfer of $n = 13 - 30$ grazing incident Rydberg xenon atoms with a flat evaporation-deposited Au(111) surface [44, 47, 48]. In their work, the most red- and blue-shifted Xe Rydberg states of a given principal quantum number n were populated in the presence of a weak homogeneous electric field. For the most extreme red-shifted states ($k = -(n-1), m_l = 0$), which are oriented *towards* the metal surface, the ionisation distances inferred from the threshold field for ion-extraction were found to vary as $D_i = (4.5 \pm 0.9)n^2$ a_0, in agreement with the earlier measurements [40, 43]. For the most extreme blue-shifted states ($k = +(n-1), m_l = 0$), which are oriented *away* from the surface, a similar threshold field for ion detection to the red-shifted states was found [45, 53] (see Figure 1.11). This lack of polarisation dependence was very surprising, and cannot be accounted for by hydrogenic calculations [25–27, 34]. The loss of Stark polarisation was attributed to avoided crossings between red- and blue-shifted states in adjacent n-manifolds on approach toward the surface. When the Xe Rydberg atom approaches a surface, the perturbing surface potential can bring about similar state crossings as those induced by an applied electric field, as explained in Section 1.3. Given that red-shifted surface-oriented Stark states ionise at much greater distances from the surface than blue-shifted vacuum-oriented states, surface ionisation tends to occur as soon as the Rydberg state can 'flip' to surface-oriented character. Thus, the control over the initial orientation of the Rydberg Stark states is effectively lost, allowing the initially populated blue-shifted (vacuum-oriented) states to exhibit similar surface ionisation behaviour to red-shifted (surface-oriented) states.

Dunning and co-workers fitted their experimental results to rate equations [47], and found that although the ionisation rate increases exponentially with decreasing distance from the surface as expected, the exponential decrease was much slower than expected from lifetime calculations for equivalent H atom levels [26, 27] (see Chapter 3). Further theoretical and experimental work involving different incidence angles

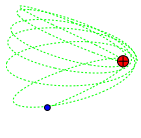

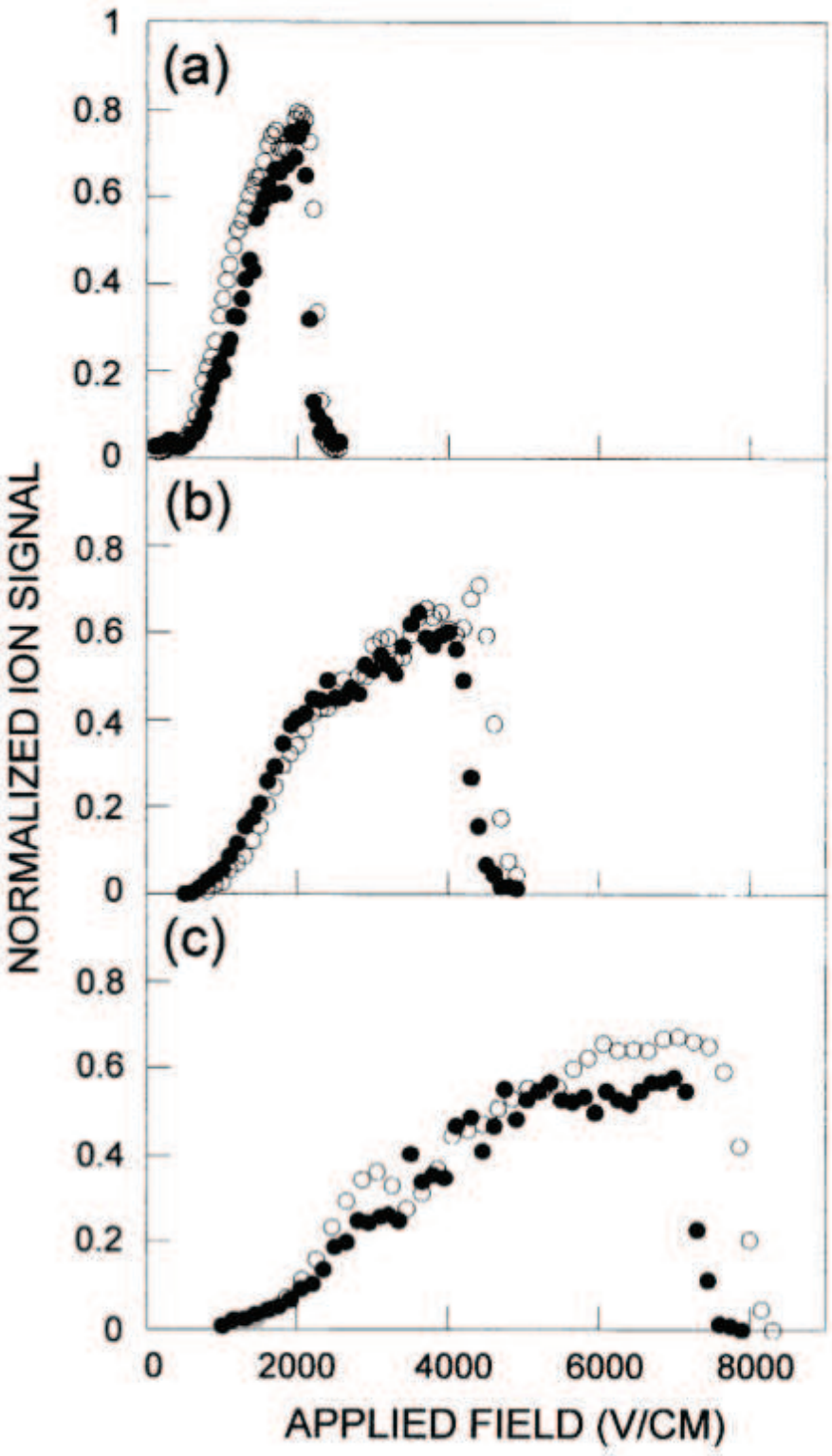

Figure 1.11: Experimental results of Dunning and co-workers, showing the surface ionisation signal as a function of electric field (surface ionisation profiles) of the initially prepared most red- (open circles) and blue- (filled circles) shifted Stark states of the (a) $n = 20$, (b) $n = 17$, (c) $n = 15$, $m_l = 0$ Xe manifolds, copied from Ref. [53]. Note the nearly identical ionisation profiles of the red and blue states.

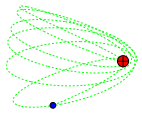

at the Au(111) surface [47] suggested that this discrepancy could be attributed to local fields from surface inhomogeneities (*c.f.* experiments of Hinds *et al.* above). Indeed, the characteristic surface features and potential variations for the experimental Au(111) surface have been recently measured by atomic force microscopy (AFM) and Kelvin probe microscopy [48]. It was found that even for gold surfaces where AFM measurements showed to be close to atomically flat, variations in surface potential of up to $\sim \pm 60 - 70$ mV were observed across features on length scales of $\sim$ 50-250 nm. The potential variations were suggested to be caused by changes in the surface work function caused by adsorbates on the surface [48]. Using a classical over-the-barrier model with the incorporation of the measured stray field potentials in Monte Carlo trajectory simulations, Dunning and co-workers were able to produce good quantitative fits of the experimental profiles, accounting for the large decay lengths of the corresponding rates of surface ionisation. The effects of the stray fields observed by Dunning and co-workers [48] might be expected to be typical for deposited surfaces formed by evaporation [61] – a technique that is used to prepare the gold surface used in the experimental work presented in this thesis (see Section 6.3). The application of the stray field calculation of Dunning and co-workers to the hydrogen Rydberg atom system is presented in Section 5.2, and is used as one of the approaches to fit the experimental results presented in Section 7.1.

Dunning and co-workers also studied the ionisation of Rydberg Xe atoms at rough and dielectric target surfaces. Results from a rough surfaced copper mirror (variations in height of 40 nm compared to the atomically flat Au(111) surface) [44] showed that the effect of local fields from surface defects can be exaggerated to give even greater ionisation probability and ion detection efficiency at lower extraction fields. Studies of surface ionisation at dielectric n- and p-type Si(100) surfaces [46] led to the conclusion that although the ionisation profiles do not differ greatly between the

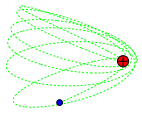

two types of semiconductors, a much earlier onset of ion signal at lower fields can be observed compared with the Au(111) surface. This was attributed to localised stray patch fields at the semiconductor surface and the reduced image-charge attraction of the ion to the dielectric surface. Overall, the experimental studies of Dunning and co-workers provided the first detailed investigations of the charge transfer dynamics of Xe Rydberg atoms at metallic and semiconductor surfaces, and demonstrated that the technique of ionisation of grazing incidence Rydberg beam can probe both the details of the Rydberg state and of the target surface.

Ionisation of grazing Rydberg hydrogen molecules

Softley and co-workers studied the ionisation of Rydberg hydrogen *molecules* at metallic surfaces [49–51]. The interaction of Rydberg molecules with metallic surfaces adds a new degree of complexity to the process of surface ionisation. The core has vibrational and rotational degrees of freedom that might affect the charge transfer dynamics. Indeed, the surface ionisation dynamics of rotationally excited $N^+ = 2$ Rydberg H_2 molecules was found to be dominated by the coupling to the $N^+ = 0$ channel with no core rotation (rotation to electronic energy transfer). The inferred ionisation distance scaled with the square of the larger effective principal quantum number (v_0) with respect to the $N^+ = 0$ channel instead of the principal quantum number of the initially excited $N^+ = 2$ state, and gave a scaling of $D_i \sim (3-5)v_0^2$ a_0, in accord with the measurements with alkali [40–43] and Xe [44–48] atoms. The surface ionisation profiles (plot of the ion signal *vs* extraction field) were found to exhibit strong resonances at specific values of the externally applied field (see Figure 1.12). The resonances were found to coincide with the electric fields at which the $N^+ = 2$ state encounters a crossing with $N^+ = 0$ states on the Stark map. Although strictly, the two channels are not coupled by a homogeneous electric field, any field inhomogeneity and the addition of the perturbing image-charge fields from the surface will facilitate

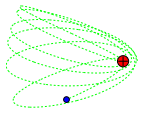

the rotational-coupling and population transfer. These experiments demonstrated the ability to probe details of Rydberg dynamics as well as surface characteristics from studying the Rydberg-surface charge transfer. Recently, the detection of electrons from the Rydberg H_2 surface ionisation process has been achieved by reversing the direction of the electric field [64], but the origin of the detected electrons is unclear. A theoretical investigation of the reversed-field ionisation dynamics is presented in Section 3.4 and 4.3.

The experimental work presented in this thesis has been carried out with a newly built UHV setup and laser system (details are given in Section 6.1). As a test system, the experiments involving Rydberg hydrogen *molecules* were repeated for a rough machined aluminium surface (see Section 6.3), and the obtained surface ionisation profiles for $n = 16-19$, $N^+ = 2$, $M_J = 0$ states (populated in zero-field) are presented in Figure 1.12. The reproducibility of the surface ionisation profiles compared to the older experimental apparatus is clear, particularly the field positions of the '$N^+ = 2$ / $N^+ = 0$ resonances'. The apparent lower resolution of the resonances can be attributed to the lower field resolution from a rough surface, and the similar signal intensity despite a steeper incidence angle (see figure caption) can be attributed the increase of detection probability from the rough target surface (see Section 5.2).

1.7 Aims and outline

The past experimental techniques and findings reviewed above demonstrate that by studying Rydberg-surface charge transfer of alkali atoms, Xe atoms, and H_2 molecules, information on the surface characteristics *and* Rydberg properties may be inferred when compared with appropriate theory. The work presented in this thesis aims to provide a detailed understanding of the charge transfer of Rydberg hydrogen atoms at metal surfaces, with the aid of theory and experiment. Because of the simplicity of the

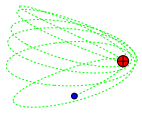

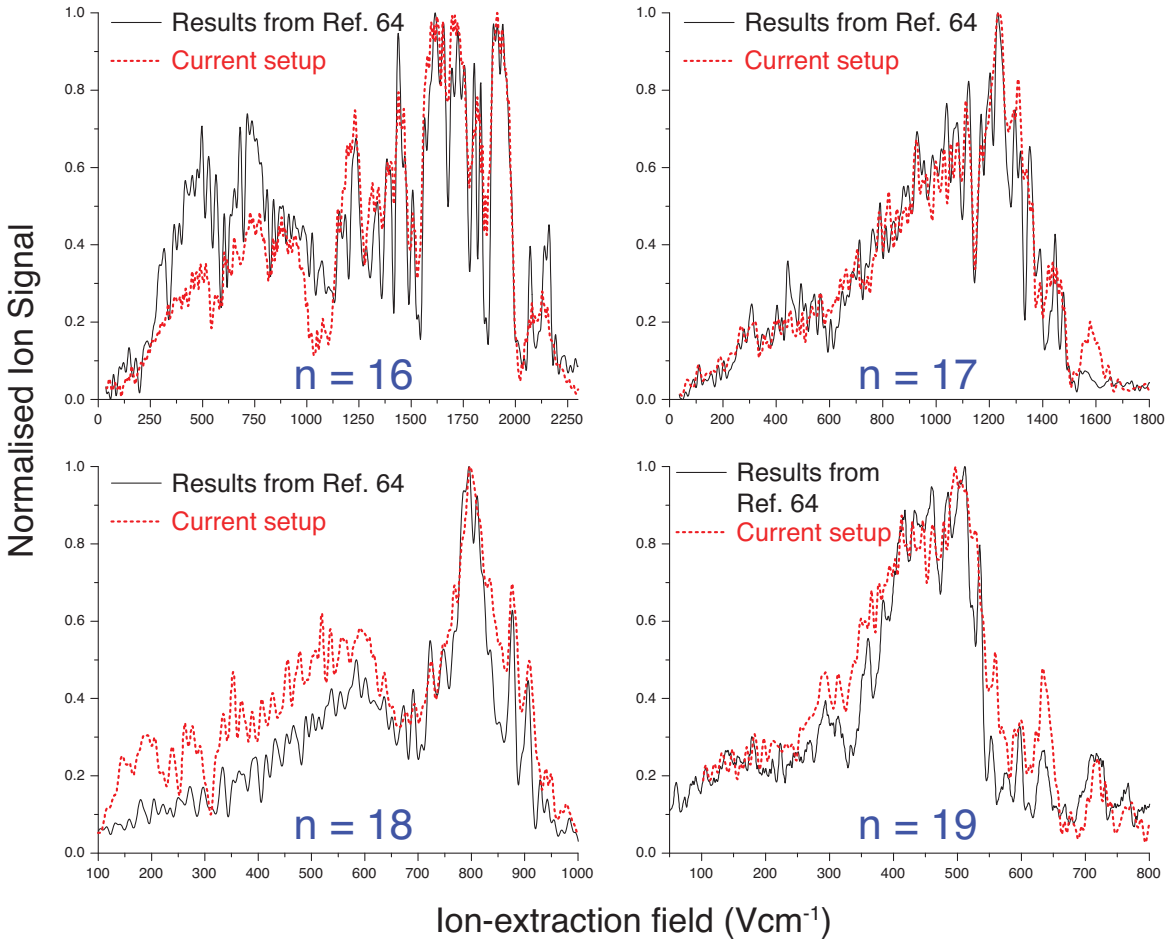

Figure 1.12: Surface ionisation profiles for the $n = 16 - 19$, $N^+ = 2$, $M_J = 0$, H_2 Rydberg states obtained from the current experimental rig with a rough machined aluminium surface (see Section 6.3) at 15° incidence from the molecular beam [dotted lines]; compared with the previous results of McCormack [64] carried out with a evaporated gold surface (see Section 6.3) at 7° incidence from the molecular beam [full lines].

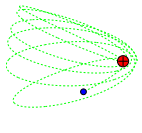

hydrogen atom, theoretical treatments from classical to full time-dependent quantum calculations can be carried out, allowing for a more quantitative comparison with the experiments. This work also aims to point out some of the fundamental differences between the H atom system and the non-hydrogenic systems studied previously, and in particular, the greater degree of control over the surface ionisation process that can be achieved for the hydrogenic case (see Section 7.2).

Chapter 2 outlines the theoretical techniques used in thesis. Chapters 3 and 4 present the theory of Rydberg-surface charge transfer for hydrogen atoms and xenon atoms respectively, with the aim of developing a better theoretical understanding of the previous Xe and H_2 experimental results as well as for the experimental studies of Rydberg H atoms in this work. In particular, the surface ionisation dynamics for the case of electron-extraction fields as opposed to the typical ion-extraction fields are studied theoretically. Due to computational demands, the quantum calculations are limited to principal quantum numbers of $n \leq 10$. Chapter 5 investigates how the ionisation behaviour scales with principal quantum number, and develops model calculations to include the effects of local surface fields and surface roughness.

Chapter 6 presents the implementation details of the experimental work carried out. Chapter 7 presents the results of the experimental investigation on the ionisation dynamics of Rydberg H atoms at metal surfaces, and focuses on the effects of Rydberg orbital size, Stark polarisation, collisional velocity, incident collisional angle, surface roughness and surface electronic structure for ion- *and* electron-extraction fields. The theory developed in Chapters 3−5 is compared with, and helps to explain, the experimental observations. Chapter 8 summarises the main findings of this thesis, and discusses some of the future applications and opportunities for further study that arise as a direct consequence of this work.

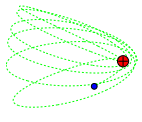

Chapter 2

Theoretical techniques

Several theoretical techniques are utilised in this thesis to model the interaction of Rydberg states with metal surfaces. In order of increasing accuracy and complexity, these include the classical over-the-barrier approach [15], time-independent complex scaling approach [25–27] and time-dependent wavepacket propagation approach [31–34]. In this chapter, details of the theoretical techniques and of their implementation are presented. The individual advantages and deficiencies of these techniques are discussed.

2.1 Classical over-the-barrier (OTB) approach

The atom-surface separation at which charge-transfer occurs can be calculated classically using an over-the-barrier (OTB) model, *i.e.*, ionisation takes place when the energy of the Rydberg electron is greater than the maximum of the potential barrier between the core and the metal surface. For a Rydberg hydrogen atom in zero-field, and with the surface potential given by the image-charge model (Eqn. 1.7), it is shown in Section 1.5.2 that the OTB approach gives an ionisation distance of $\approx 3.5n^2\ a_0$. However, when the Rydberg state approaches the metal surface, the Rydberg energy

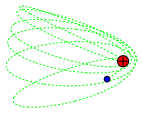

is perturbed by the image-charge interaction. Furthermore, under typical experimental conditions, the Rydberg state interacts with the metal surface in the presence of a homogeneous electric field. Thus, incorporation of the Rydberg energy shift from the surface-interaction and the electric field will provide a much better estimation of the classical ionisation distance. At the same time, it is important to note that the classical over-the-barrier approach does not include any kinetic effect, e.g. the differing field ionisation rates of red- and blue-shifted Stark states (Section 1.4). It is shown in Chapter 3 that the same kinetic effect plays an important role in the surface ionisation dynamics of Stark states, such that the classical OTB approach is only appropriate for the most extreme surface-oriented state of a given n-manifold.

2.1.1 The Rydberg energy

The energy shift of the Rydberg state due to the surface potential can be estimated using first-order perturbation theory. At long-range, the surface potential can be approximated by the Van der Waals interaction (Eq. 1.12). Given the common cylindrical symmetry of a homogeneous electric field and the surface potential (Eq. 1.7), and the fact that under typical experimental conditions, the Rydberg state interacts with the metal surface in the presence of a homogeneous electric field, it is intuitive to work in the parabolic hydrogen basis $|nm_lk\rangle$. The first order perturbation energy shift is given by [65]:

$$\Delta^1 E^{\text{surf}}_{nm_lk} = -\frac{1}{16D^3}\left\langle nm_lk\right|\left(\rho^2+2z^2\right)\left|nm_lk\right\rangle = -\frac{n^2}{64D^3}(8n^2+8-4m_l^2+12k^2). \quad (2.1)$$

It can be seen from Eq. 2.1 that the first-order effect of the Van der Waals potential is a lowering of the total Rydberg energy. The Rydberg energy of a Stark state $|nm_lk\rangle$ in the presence of an electric field F, at a distance D from the metal surface can therefore

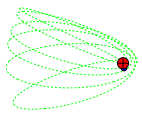

be expressed approximately as:

$$E_{nm_lk}(F,D) \approx E^{\text{Stark}}_{nm_lk}(F) - \frac{n^2}{64D^3}(8n^2 + 8 - 4m_l^2 + 12k^2), \tag{2.2}$$

where $E^{\text{Stark}}_{nm_lk}(F)$ is the Rydberg Stark energy given by Eq. 1.3. Although the first order energy shift from the Van der Waals potential used in Eq. 2.2 is not strictly valid at very small atom-surface separations – such as those at which surface charge transfer occurs (see Section 5.1)– it nonetheless provides a simple analytical form of the approximate Rydberg energy. The Rydberg energy at the charge-transfer range of distances can be calculated accurately using techniques such as complex scaling, as presented in Section 2.2.

2.1.2 Saddle point energy

The overall one-electron potential of a hydrogen atom in the presence of a surface and an electric field given by Eq. 1.6 and Eq. 1.7 can be expressed in scaled co-ordinates

$$\mathbf{z'} = \mathbf{z}/D, \quad \boldsymbol{\rho'} = \boldsymbol{\rho}/D. \tag{2.3}$$

Multiplying through by the atom-surface separation D, the scaled effective one-electron potential becomes

$$\begin{aligned}
\widetilde{V}_{\text{tot}} = V_{\text{tot}}D &= (V_{\text{coulomb}} + V_{\text{surf}} + V_{\text{field}})D \\
&= (V_{\text{coulomb}} + V_{ee} + V_{pp} + V_{ep} + V_{\text{field}})D \\
&= -\frac{1}{\sqrt{\rho'^2 + z'^2}} - \frac{1}{4(1+z')} - \frac{1}{4} + \frac{1}{\sqrt{(2+z')^2 + \rho'^2}} + FD^2z' \\
&= -\frac{1}{\sqrt{\rho'^2 + z'^2}} - \frac{1}{4(1+z')} - \frac{1}{4} + \frac{1}{\sqrt{(2+z')^2 + \rho'^2}} + \tilde{F}z'
\end{aligned} \tag{2.4}$$

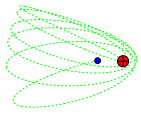

where $\tilde{F} = FD^2$ is the scaled electric field. As shown in Figure 1.9, the one-electron potential has a saddle point (z_{saddle}) along the z-axis (ρ=0) between the core and the surface. The position of this unique critical point along the z-axis can be determined by finding the common root of partial derivatives of Eq. 2.4 with respect to z' and ρ', and with the substitution of $\rho' = 0$. Following this, the scaled saddle point $z'_{\text{saddle}} = z_{\text{saddle}}/D$ is then given by the solution of the following polynomial equation in the interval (-1,0) [17]:

$$4\tilde{F}z'^6 + 24\tilde{F}z'^5 + (52\tilde{F} - 7)z'^4 + (48\tilde{F} - 28)z'^3 + (16\tilde{F} - 52)z'^2 - 48z' - 16 = 0. \quad (2.5)$$

For $\tilde{F} = 0$, the polynomial is fourth order, and can be solved analytically to give $z_{\text{saddle}} \approx -0.69D$ (Eq. 1.10). For $\tilde{F} \neq 0$, solutions to Eq. 2.5 can be found numerically, using techniques such as the Newton-Raphson method [66]. Asymptotically ($\tilde{F} \to 0$), z'_{saddle} can be expressed as [17]

$$z'_{\text{saddle}}(\tilde{F}) = -0.693673 + 0.044466\tilde{F} + 0.006259\tilde{F}^2 + 0.000220\tilde{F}^3 + O(\tilde{F}^4). \quad (2.6)$$

Substituting z_{saddle} and $\rho = 0$ back into Eq. 1.6 gives the saddle energy E_{saddle}. In the zero-field limit, $E_{\text{saddle}} \approx -1.7422/D$ (Eq. 1.11). At low fields, retaining only the field independent term in Eq. 2.6, the saddle energy varies approximately linearly with the electric field

$$\lim_{FD^2 \to 0} E_{\text{saddle}} \approx -1.7422/D - 0.693673FD. \quad (2.7)$$

Equation 2.6 and Eq. 2.7 shows that as the electric field increases, the saddle point shifts towards the core, and the saddle height of the overall potential barrier decreases. Figure. 2.1 shows the variation of the potential barrier and the saddle point position and energy with ion-extraction electric field at a given atom-surface separation D. Thus, at a given atom-surface separation, the application of an electric field

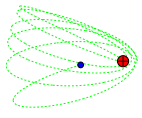

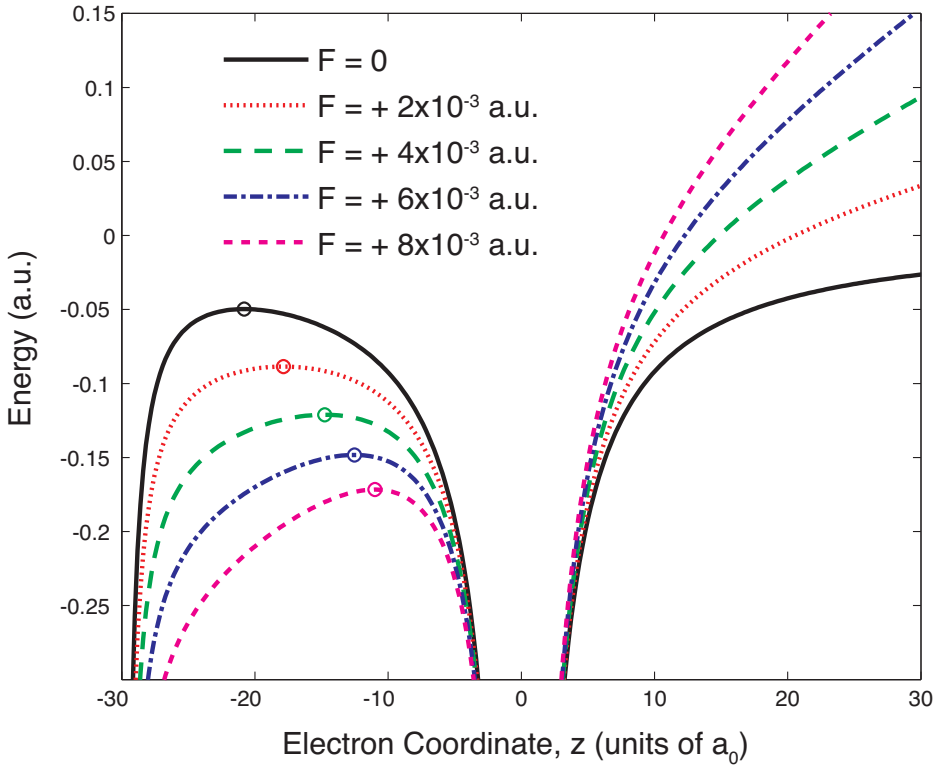

Figure 2.1: Plot of the total one electron potential $V_c + V_{\text{surf}} + V_{\text{field}}$ (Eq. 1.6) at atom-surface separation of $D = 30$, with an applied extraction field (in the ion-extraction direction) of $\vec{F} = 0, +2 \times 10^{-3}, +4 \times 10^{-3}, +6 \times 10^{-3}$, and $+8 \times 10^{-3}$ a.u.. The saddle point positions and energies calculated by solving Eq. 2.5 are shown as open circles.

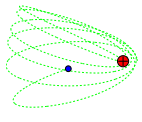

in the positive z-direction facilitates Rydberg-surface charge transfer, both classically in terms of the over-the-barrier mechanism, as well as quantum mechanically, in terms of tunnelling through the barrier.

2.1.3 Classical ionisation distance

The critical classical ionisation distance for a given externally applied electric field is determined by the atom-surface separation at which the saddle energy of the total one-electron potential is equal to the energy of the Rydberg state (in zero-field $D_{\mathrm{OTB}} \approx 3.48n^2a_0$). Thus, the cumulative ionisation probability $\Upsilon(D, F)$ at atom-surface separation D and electric field F is given by

$$\Upsilon(D, F) = h(D_{\mathrm{OTB}}(F) - D), \tag{2.8}$$

where $h(D_{\mathrm{OTB}}(F) - D)$ is a heaviside step function centred at $D_{\mathrm{OTB}}(F)$. The corresponding ionisation probability distribution (or ionisation rate) is a delta function $P(D, F) = \delta(D_{\mathrm{OTB}}(F) - D)$.

Figure 2.2 shows the change in classical ionisation distance $D_{\mathrm{OTB}}(F)$ (determined by solving Eq. 2.5 for the saddle point, and comparing potential at the saddle point with the Rydberg energy given by Eq. 2.2) as a function of ion-extraction electric field for the most extreme red-shifted state in the $n = 20$ Stark manifold. At low electric field strengths, the ionisation distance scales approximately linearly with field, but increases dramatically near the field ionisation threshold. As explained in the previous section, as the electric field increases, the saddle point energy decreases (Eq. 2.7), and so the Rydberg-surface charge transfer takes place at larger distances. The variation of the classical ionisation distance $D_{\mathrm{OTB}}(F)$ with ion-extraction field as a function of principal quantum is discussed in Section 5.1.

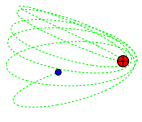

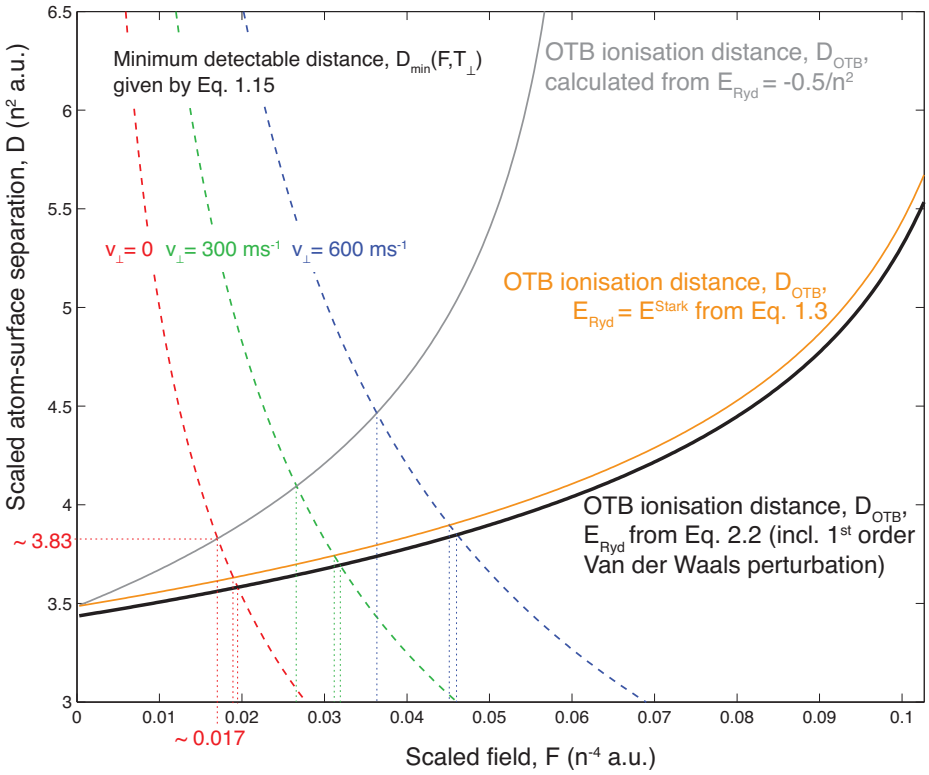

Figure 2.2: Variation of the over-the-barrier ionisation distance $D_{\mathrm{OTB}}(F)$ as a function of electric field for the most extreme red-shifted $k = -19$, $m_l = 0$, $n = 20$ Rydberg H state. The field axis is scaled by n^{-4} and the atom-surface separation is scaled by n^2. Black full line: OTB ionisation distance calculated using the Rydberg energy given by Eq. 2.2, which includes the Stark shift and the first order perturbation energy shift from the Van der Waals potential (Eq. 1.12). Orange full line: OTB ionisation distance calculated using the Rydberg energy given by Eq. 1.3, which includes up to the 4^{th} order Stark shift. Grey full line: OTB ionisation distance calculated using the unperturbed -0.5/n^2 Rydberg energy. Dashed lines: the minimum detectable distance $D_{\mathrm{min}}(F, T_\perp)$ as given by Eq. 1.15, for a hydrogen atom with collisional velocities of $v_\perp = 0, 300, 600$ ms^{-1}. Note the crossing of $D_{\mathrm{OTB}}(F)$ and $D_{\mathrm{min}}(F, T_\perp)$ marks the position of the critical ion-detection field $F_{\mathrm{crit}}(T_\perp)$.

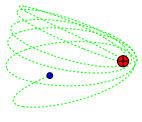

2.1.4 Ion-detection probability

Experimentally, the surface-ionisation process is typically observed by detecting positive ions extracted by the externally applied field. For an ion formed by ionisation at distance D from the surface, the minimum extraction field $F_{min}\,(D, T_\perp)$ required is given by Eq. 1.14. Thus, we can define a critical ion-detection field $F^{\sigma}_{\rm crit}(T_\perp)$, corresponding to the minimum field required to detect ions formed from the surface ionisation of an initial state σ. This is illustrated in Figure 2.2 as the crossing point between the minimum detectable ionisation distance $D_{\rm min}(F, T_\perp)$ for a given electric field F (Eq. 1.15), and the actual ionisation distance curve $D_{\rm OTB}(F)$. At the critical ion-detection field, the OTB approach assumes that the ion-detection signal will step from zero to unity, $S_\sigma(F, v_\perp) = h(F - F^{\sigma}_{\rm crit}(v_\perp))$. For the experimental Rydberg beam with velocity distribution $f(v_\perp)$, the OTB model therefore predicts an overall total ion-detection signal of

$$S_\sigma(F) = \int_0^\infty h(F - F^{\sigma}_{\rm crit}(v_\perp))dv_\perp. \tag{2.9}$$

The lower limit of the critical detection ion-extraction field ($F^{\rm lim}_{\rm crit}$) and the corresponding ionisation distance ($D_{\rm crit}$) can be estimated by taking the low kinetic energy ion-detection limit $F_{min} = 1/4D_i^2$ (Eq. 1.16), such that Eq. 2.7 is approximately valid. Combining the two equation gives

$$F^{\rm lim}_{\rm crit} = \frac{(E_{\rm saddle})^2}{(1.7422 \times 2 + 0.693673/2)^2} = \frac{(E_{\rm Ryd})^2}{14.6784}. \tag{2.10}$$

As noted in Ref. [32], if the Rydberg energy shift due to the electric field and the surface is not included (*i.e.*, assuming $E_{\rm Ryd} = -0.5n^{-2}$), the lower critical ion-detection field limit is simply given by $F^{\rm lim}_{\rm crit} = 0.017n^{-4}$ (see Fig. 2.2), corresponding to an ionisation distance of $3.83n^2$ a_0. This n^{-4} scaling of ionisation distance has been previously

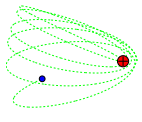

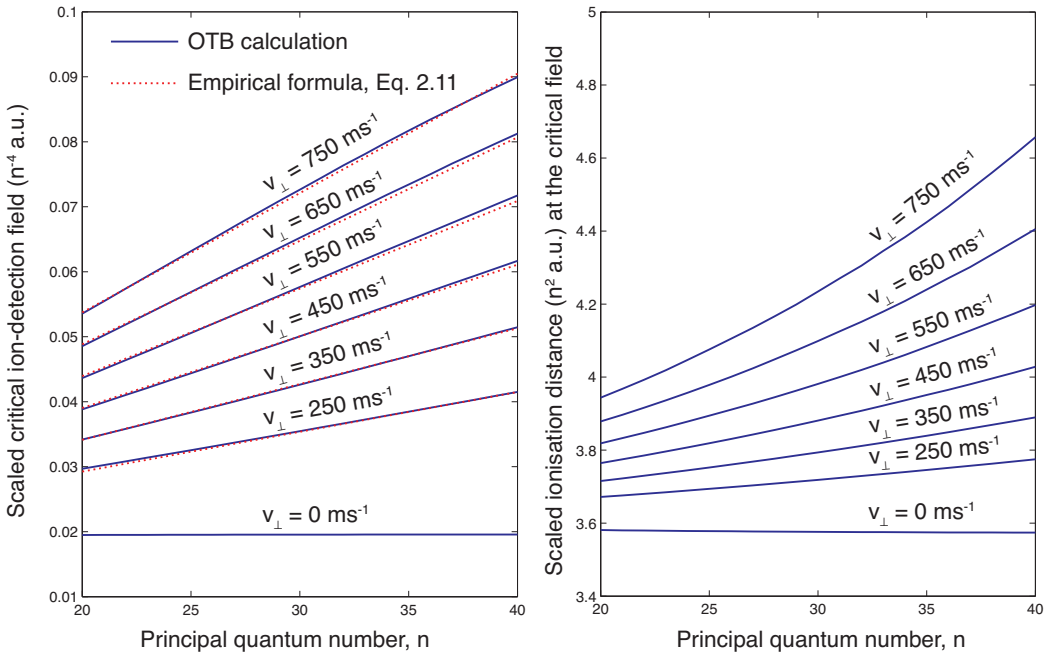

Figure 2.3: Left panel: plot of the critical ion-detection field $F_{\rm crit}(n, T_\perp)$ calculated from the OTB approach as a function of principal quantum number for various collisional velocities (note the experimental range studied in this thesis is $v_\perp \sim 300 - 600$ ms^{-1}). The empirical formula given by Eq. 2.11 (found from least-squares fit) is shown as dotted lines. Right panel: the ionisation distances corresponding to the critical ion-detection fields shown on the left panel. Note that at the low kinetic energy limit ($v_\perp \sim 0$), the ionisation distance is proportional to n^2, and the critical ion-detection field is proportional to n^{-4}.

applied to model the surface ionisation of xenon atoms [45, 47]. However, under typical experimental conditions, the kinetic energy of the ion is non-negligible, and Eq. 2.10 is generally not valid. When the Rydberg energy shift (Eq. 2.2) and the kinetic energy of the ion (typically $\sim 8 \times 10^5$ a.u. in the experiments) are included, the critical ion-detection field does not strictly follow the n^{-4} scaling derived above, and the corresponding ionisation distance does not scale simply as n^2. Figure 2.3 shows the variation of critical ion-detection field and the corresponding ionisation distance with principal quantum number n, for the most extreme red-shifted state with these factors included. It can be seen that for $v_\perp \neq 0$, the scaled critical ion-detection field is no longer independent of principal quantum number, but increases approximately linearly,

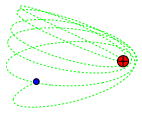

and the corresponding ionisation distances vary non-linearly from $(3.9 - 4.5)n^2$ a_0.

For typical principal quantum numbers ($n \sim 20 - 40$) and incident kinetic energies ($v_\perp \sim 300 - 600\,\mathrm{ms}^{-1}$) studied experimentally in this thesis, the variation of the critical ion-extraction field with principal quantum number can be fitted approximately by introducing a n^{-3} term, in addition to the asymptotic $\approx 0.017n^{-4}$ term. Using a least-squares fit procedure, the critical ion-extraction field for the most extreme red-shifted Stark state of a given n-manifold can be expressed empirically as

$$F_{\mathrm{crit}}(n, T_\perp) \approx \frac{0.017}{n^4} + \frac{\sqrt{T_\perp}}{(3.174)^{\frac{3}{2}} n^3}. \tag{2.11}$$

The dotted lines in Fig. 2.3 show the fit of this empirical formula. More discussion on the scaling of ionisation distances with principal quantum number n is given in Section 5.1.

2.2 Time-independent complex scaling approach

The charge-transfer process occurs at atom-surface separations at which there are non-negligible overlap between the Rydberg and metal electronic wavefunction, *i.e.*, the Rydberg electron's wave function is no longer fully localised on the ion core. Therefore, the system is no longer a bound- or stationary-state problem, and cannot be solved using standard bound-state techniques, which involve finding the *real* eigenvalues of a Hermitian Hamiltonian matrix. Instead, these 'resonance states' (because the Rydberg state is in resonance with continuum metal states) and their associated lifetimes can be found by using a time-independent complex scaling approach, as previously utilised by Nordlander and co-workers [25–27, 52, 53]. A detailed review of this technique is given in Ref. [67], and only a brief summary and details specific to this current application are provided below.

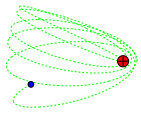

2.2.1 Complex-rotation

A simplistic description of the electron wavefunction of a resonance state is

$$\Psi(t) = e^{-iEt}\Psi(t=0) \ , \tag{2.12}$$

where

$$E = E_R - i\frac{\Gamma}{2}. \tag{2.13}$$

E_R and $\Gamma/2$ are the real energy E, and the half width of the resonance state respectively in atomic units (*i.e.* the wavefunction $\Psi(t)$ decays in time with lifetime Γ^{-1}). The electronic wave function of the resonance state satisfies the Siegert boundary condition [67],

$$\Psi(r \to \infty) = \frac{A}{r}e^{ikr} = \frac{A}{r}e^{i|k|e^{-i\alpha}r} \tag{2.14}$$

The central idea behind the complex scaling method which allows one to calculate the energies and lifetimes of resonance states, is the rotation of the electron co-ordinate, $\mathbf{r}$, into the complex plane by a complex scaling angle, $0 \leq \theta \leq \pi/2$, such that

$$\mathbf{r} \to \mathbf{r}e^{i\theta}, \qquad 0 < \theta < \frac{\pi}{2}. \tag{2.15}$$

The rotated Hamiltonian, $\hat{H}(\theta)$, is now a non-Hermitian operator, given by

$$\hat{H}(\theta) = e^{-2i\theta}\hat{T} + \hat{V}(\mathbf{r}e^{i\theta}). \tag{2.16}$$

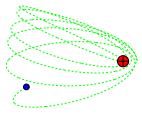

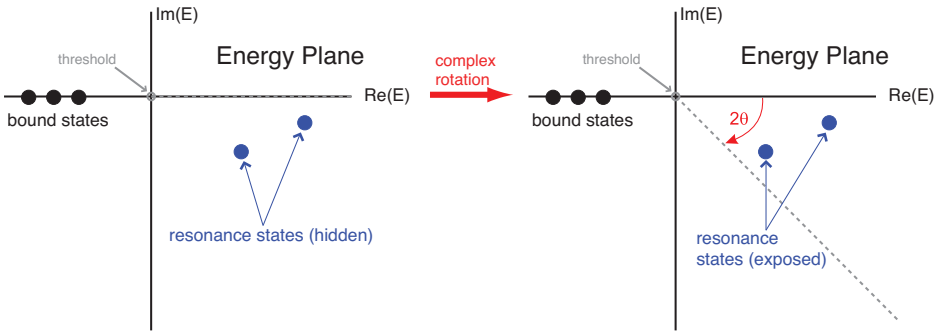

Figure 2.4: Spectrum of the unrotated (left) and the rotated Hamiltonian (right), modified from Ref. [67]. Note that the bound states and the threshold are invariant, while the complex resonance eigenvalues may be exposed for a large enough complex-rotation angle θ.

The resonance boundary condition (Eq. 2.14) now becomes

$$\begin{aligned}\Psi(r \to \infty) &\to \frac{A}{re^{i\theta}} \exp[i|k|e^{-i\alpha} re^{i\theta}] \\ &= \frac{A}{re^{i\theta}} \exp[i|k|r(\cos[\theta-\alpha] + i\sin[\theta-\alpha])] \\ &= \frac{A}{re^{i\theta}} \exp[i|k|r\cos(\theta-\alpha)] \exp[-|k|r\sin(\theta-\alpha)]. \end{aligned} \tag{2.17}$$

Thus, for $\theta > \alpha$, Eq. 2.17 is transformed into a bound state boundary condition, and the eigenfunctions are square-integrable and vanish asymptotically, and can be solved by diagonalisation of the non-Hermitian Hamiltonian matrix (Eq. 2.16). The real and imaginary parts of these eigenvalues correspond to the energies (E_R) and half widths ($\Gamma/2$) of the resonance states.

The effect of the complex variable substitution (Eq. 2.15), can be viewed as a distortion of the Hamiltonian spectrum (Fig. 2.4). While the bound state energies are invariant with respect to the complex transformation, the continuous spectrum associated with each energetic threshold is rotated downwards in the energy plane by 2θ, 'revealing' the discrete resonance eigenvalues.

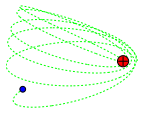

2.2.2 Scaled parabolic co-ordinates

As explained in Section 2.1, parabolic co-ordinates (ξ, η, ϕ) are particularly suited to the cylindrical symmetry (z, ρ, ϕ) of the Rydberg-surface system.

$$\begin{aligned} \eta &= r - z = (\rho^2 + z^2)^{\frac{1}{2}} - z \\ \xi &= r + z = (\rho^2 + z^2)^{\frac{1}{2}} + z \\ \phi &= \tan^{-1}\left(\frac{y}{x}\right) \end{aligned} \tag{2.18}$$

The invariance of the surface interaction in ϕ renders the system two-dimensional. For a finite basis, the Rydberg electronic wavefunction, which can vary significantly in size, can be described more efficiently in scaled parabolic co-ordinates (u, v)

$$\begin{aligned} u = \eta/\lambda, \quad v = \xi/\lambda \\ \rho \mathrm{d}\rho \mathrm{d}z = \frac{\lambda^3}{4}(u+v)\mathrm{d}v\mathrm{d}u \end{aligned} \tag{2.19}$$

where λ is an arbitrary scaling parameter. The complex-rotated Hamiltonian (Eq. 2.16) in parabolic co-ordinates has the form

$$\hat{H}(\theta) = e^{-2i\theta}\hat{T} + \hat{V}(ue^{i\theta}, ve^{i\theta}) \tag{2.20}$$

with

$$\hat{T} = \frac{2}{\lambda^2(u+v)}\left[-\frac{\partial}{\partial u}u\frac{\partial}{\partial u} - \frac{\partial}{\partial v}v\frac{\partial}{\partial v} + \frac{m^2}{4}\left(\frac{1}{u} + \frac{1}{v}\right)\right]. \tag{2.21}$$

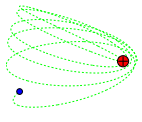

The one-electron pseudopotential given by Eq. 1.6 can be recast in the scaled and complex-rotated parabolic co-ordinates,

$$\begin{aligned}\hat{V}(ue^{i\theta}, ve^{i\theta}) &= \hat{V}_{\text{coulomb}} + \hat{V}_{\text{surf}} + \hat{V}_{\text{field}} \\ &= -\frac{2}{\lambda(u+v)e^{i\theta}} + \hat{V}_{surf}(ue^{i\theta}, ve^{i\theta}) + \frac{\lambda(u-v)e^{i\theta}}{2}F. \end{aligned} \quad (2.22)$$

2.2.3 Lagrange-Laguerre DVR basis functions

For an efficient representation of the electronic wavefunction, Lagrange-Laguerre basis functions [68] are employed,

$$f_i(x) = (-1)^i x_i^{\frac{1}{2}} \frac{L_N(x)}{x - x_i} e^{-\frac{x}{2}}, \quad i = 1, ..., N \quad (2.23)$$

where N is the number of basis functions or discrete variable representation (DVR) grid points, x_i is the ith (unscaled) DVR grid point corresponding to the position of the ith root of the Laguerre polynomial of order N, *i.e.*, $L_N(x_i) = 0$.[1] The roots of orthogonal polynomials of order N can be evaluated from the diagonalisation of a symmetric tridiagonal matrix with matrix elements given by the three-term recurrence relation [70]

$$\mathbf{Q} = \mathbf{U}\mathbf{X}\mathbf{U}^{\dagger} = \begin{bmatrix} a_1 & b_1 & & & & \\ b_1 & a_2 & b_2 & & & \\ & b_2 & a_3 & b_3 & & \\ & & \ddots & \ddots & \ddots & \\ & & & b_{N-2} & a_{N-1} & b_{N-1} \\ & & & & b_{N-1} & a_N \end{bmatrix}. \quad (2.24)$$

[1] A full review of the DVR approach is given in Ref. [69].

For Laguerre polynomials $L_N(x)$, $a_j = 2j - 1$ and $b_j = -j$. The roots or (unscaled) DVR grid points $\{x_1, x_2, ..., x_N\}$ are given by the eigenvalues of matrix $\mathbf{X}$ [1].

2.2.4 Implementation

The dimensions spanned by the scaled parabolic u- and v-co-ordinates are described by N_u and N_v grid points respectively. The DVR grid points (u_α, v_β) are the scaled roots of $L_{N_u}(x)$ and $L_{N_v}(x)$ ($\{x_1, x_2, ..., x_N\}$ multiplied by factor of λ) found from the diagonalisation described above (Eq. 2.24). Taking a direct product of the one-dimensional basis functions forms the overall two-dimensional basis, and the complex-rotated Hamiltonian matrix in this grid representation is given by [71]

$$H(\theta)_{\alpha\beta,\alpha'\beta'} = e^{-2i\theta} T_{\alpha\beta,\alpha'\beta'} + V(u_\alpha e^{i\theta}, v_\alpha e^{i\theta}) \delta_{\alpha\beta}\delta_{\alpha'\beta'} \tag{2.25}$$

where

$$T_{\alpha\beta,\alpha'\beta'} = \frac{2(t^u_{\alpha\alpha'}\delta_{\beta\beta'} + t^v_{\beta\beta'}\delta_{\alpha\alpha'})}{\lambda^2 (u_\alpha + v_\beta)^{\frac{1}{2}} (u_{\alpha'} + v_{\beta'})^{\frac{1}{2}}} \ , \tag{2.26}$$

and

$$t^u_{\alpha\alpha'} = \begin{cases} \frac{1}{3}\left(N_u - \frac{u_\alpha}{4} - \frac{m^2-1}{2u_\alpha} + \frac{|m|+1}{2}\right) & \alpha = \alpha' \\ \frac{2(-1)^{\alpha-\alpha'}(u_\alpha u_{\alpha'})^{\frac{1}{2}}}{(u_\alpha - u_{\alpha'})^{\frac{1}{2}}} & \alpha \neq \alpha'. \end{cases} \tag{2.27}$$

The potential energy matrix $\mathbf{V^{DVR}}$ is diagonal, with matrix elements given by the values at the grid points.

Eigenvalues from the diagonalisation of the Hamiltonian matrix (Eq. 2.26) gives directly the energies E_R and half widths $\Gamma/2$ of the 'resonance' Rydberg states. The complex scaling angle, θ, can be taken as a convergence parameter, such that the

[1] The tridiagonal matrix $\mathbf{Q}$ is the position matrix in the finite-basis representation (FBR), $\mathbf{X}$ is the position matrix in the discrete variable representation (DVR), and $\mathbf{U}$ is the FBR-DVR transformation matrix.

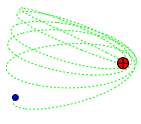

eigenvalues do not vary with small changes in the rotation angle. The scaling factor λ is adjusted to optimise the basis so that it reflects the size of the Rydberg orbital for the principal quantum number n of interest. For typical calculations carried out in this work, the parameters used are: $\lambda \approx n/2$ [72], $N_u, N_v = 50$, and $\theta = 0.4$.

The complex scaling results presented in thesis are typically in the form of energy and/or half-width versus atom-surface separation plots. In order to show more clearly the variation of the Rydberg energy of a given n-manifold with atom-surface separation, the energy plots presented in this thesis omit the electron-position independent proton–image-proton attractive contribution $V_{pp} = -0.25/D$ (see Eq. 1.7). Figure 3.2 illustrates some of the energies and half-widths of the hydrogen atom Rydberg states as a function of atom-surface separation obtained from the complex scaling calculations.

2.2.5 Cumulative ionisation probability and ionisation rate

For a state σ, at a distance D from a metal surface and in the presence of an electric field F, the instantaneous population (or Rydberg survival probability) n_σ, is related to its width Γ_σ (inverse of the lifetime) via the rate equation

$$\frac{dn_\sigma(t)}{dt} = -\Gamma_\sigma(D, F)n_\sigma(t). \tag{2.28}$$

After a change of variable and integration with respect to atom-surface separation D, for a given perpendicular collisional velocity $v_\perp(D)$ at distance D, Eq. 2.28 becomes,

$$n_\sigma(D, v_\perp, F) = \exp\left(-\int_\infty^D \frac{\Gamma_\sigma(D', F)}{v_\perp(D')} dD'\right). \tag{2.29}$$

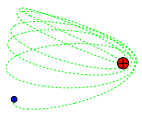

Assuming a constant collisional velocity throughout the Rydberg trajectory, the cumulative ionisation probability $\Upsilon_\sigma(D, v_\perp, F)$ is given by

$$\Upsilon_\sigma(D, v_\perp, F) = 1 - n_\sigma(D, v_\perp, F) = 1 - \exp\left(-\frac{1}{v_\perp}\int_\infty^D \Gamma_\sigma(D', F)dD'\right). \quad (2.30)$$

The probability $P_\sigma(D, v_\perp, F)$ that the ionisation occurs at a distance D can be expressed as

$$\begin{aligned} P_\sigma(D, v_\perp, F) &= -\frac{d\Upsilon_\sigma(D, v_\perp, F)}{dD} \\ &= \frac{\Gamma_\sigma(D, F)}{v_\perp}\exp\left(\frac{1}{v_\perp}\int_\infty^D -\Gamma_\sigma(D', F)dD'\right) \\ &= \frac{\Gamma_\sigma(D, F)}{v_\perp} n_\sigma(D, v_\perp, F). \end{aligned} \quad (2.31)$$

Examples of ionisation probability curves calculated using this approach are given later in Chapter 3.

2.2.6 Ion-detection probability

In the complex scaling calculations, the width $\Gamma_\sigma(D, F)$ for specified initial quantum state σ, in the presence of electric field F, is evaluated as function of atom-surface separation D through a series of matrix diagonalisations. For ion-extraction fields (F positive in Eq. 2.22), the cumulative ionisation probability $\Upsilon_\sigma(D, v_\perp, F)$ given by Eq. 2.30 can be related to experimental ionisation profiles (detected ion signal $S_\sigma(F)$ *vs* field F):

$$\begin{aligned} S_\sigma(F) &= \int_0^\infty f(v_\perp)\Upsilon_\sigma(D_{\min}, v_\perp, F)dv_\perp \\ &= 1 - \int_0^\infty f(v_\perp)\exp\left(-\int_\infty^{D_{\min}(F,v_\perp)} \frac{\Gamma_\sigma(D', F)}{|v_\perp|}dD'\right)dv_\perp, \end{aligned} \quad (2.32)$$

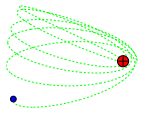

where $f(v_\perp)$ is the velocity distribution of the incoming Rydberg beam, and $D_{\min}(F, v_\perp)$ is the minimum ionisation distance for which the applied field F can pull the bare ion of initial velocity $v_\perp$ away from the surface, as given by Eq. 1.15.

2.3 Time-dependent wavepacket propagation approach

High principal quantum number Rydberg states have many electronic states closely spaced in energy, and it will be shown in the following section that as the Rydberg state approaches a metal surface, it can strongly couple with neighbouring Rydberg states and exhibit numerous energy-level crossings. The extent of non-adiabaticity at these energy crossings is determined by the strength of the coupling and the rate of the traversal (for a two state system, the avoided crossing can be described by the Landau-Zener model [73]). Sjakste *et al.* have carried out wavepacket propagation calculations to study the ionisation of Rydberg xenon atoms at metal surfaces [32], and have shown that non-adiabatic effects can play an important role, especially for spatially polarised Rydberg states. The advantages in using such a time-dependent approach is that all the non-adiabatic transitions that may occur between the Rydberg states during the collisional process can be taken into account naturally, and the corresponding evolution of the electronic wavefunction can be visualised in 'real time'. In calculations where ionisation probabilities are determined from time-independent techniques such as complex scaling (outlined in the previous section), it is generally assumed that crossings are traversed adiabatically. The disadvantage of the wavepacket propagation approach is the difficulty in performing calculations at the principal quantum numbers and velocities appropriate to experiments. This arises from the n^2 scaling of the size of the Rydberg orbital and the distance for the onset of surface ionisation (see Section 2.1).

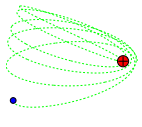

As a result, on moving to higher quantum numbers the calculations rapidly become more computationally demanding, since the size of grid upon which the wavepacket is propagated, the number of grid points required to adequately describe the ionisation process, and the number of time steps required to propagate the wavefunction before the Rydberg atom is surface ionised increases rapidly. Consequently, to date, it has not been possible to carry out time-dependent wavepacket calculations at the experimental range of principal quantum numbers ($n > 15$) and collisional velocities ($v_\perp \sim 10^{-4}$ a.u. $\sim 10^2$ ms^{-1}).

In the wavepacket calculations of Sjakste *et al.* [32] a change of variable in the cylindrical co-ordinates is performed to concentrate more grid points near the origin, in order to treat the Coulomb potential efficiently. Even with this co-ordinate mapping, an extremely large number of grid points were required for the calculations (2000×425 in the $z - \rho$ co-ordinates). In this work, the Coulomb-Wave Discrete Variable Representation (CWDVR) and the Legendre DVR are used to describe the radial and angular co-ordinates in the wavepacket calculations. It is shown below that this grid array treats the Coulomb potential very efficiently and allows for studies involving both higher principal quantum numbers and/or lower velocities to be carried out.

2.3.1 Atomic frame and nuclear trajectory

To study the charge-transfer process of the Rydberg electron to a metal surface, we treat the center-of-mass motion of the ion-core of the Rydberg atom classically and monitor the time evolution of the electronic wavefunction under the influence of the time-dependent potential due to the metal surface. The initial quantum-state-selected electronic wavefunction is discretised on a spatial grid (see Fig. 2.5). To minimise the area covered by the numerical grid, and thus the total number of grid points, we have chosen to define the electronic co-ordinates with respect to the moving atomic

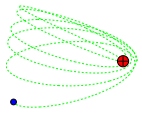

frame. In the atomic frame, the ion-core is taken to be stationary and is located at the origin, whilst the metal surface is incoming from the negative z-axis at a constant collisional velocity. The classical straight-line trajectory (perpendicular to the surface) is described by

$$D(t) = D_0 - v_\perp t, \tag{2.33}$$

where $D(t)$ is the atom-surface separation at time t, D_0 is the initial atom-surface separation at $t = 0$ and $v_\perp$ is the velocity of the Rydberg atom perpendicular to the surface. This constant velocity assumption has been applied in previous studies [25–27, 31, 32], and is used as a first approximation. However, this approximation does not fully describe the coupling between the nuclear and electron dynamics, and at the experimental range of collisional energies ($v_\perp \sim 10^{-4}$ a.u. $\sim 10^2$ ms^{-1}), this approximation cannot be fully justified: the errors associated with this assumption are discussed in Section 3.7.

2.3.2 Electronic Hamiltonian

The electronic wavefunctions are the solutions to the time-dependent Schrödinger equation:

$$i\frac{\partial}{\partial t}\Psi(\mathbf{r};t) = \hat{H}\Psi(\mathbf{r};t) \tag{2.34}$$

with

$$\hat{H}(\mathbf{r};t) = \hat{T}(r) + \hat{V}_{\text{atom}}(\mathbf{r}) + \hat{V}'(\mathbf{r};t). \tag{2.35}$$

In this equation, $\hat{T}(r)$ is the radial kinetic energy operator, $\hat{V}_{\text{atom}}(\mathbf{r})$ is the 'atomic' potential energy operator that includes the Coulomb potential and the centrifugal potential (expanded over a spherical basis),

$$\hat{V}_{\text{atom}}(\mathbf{r}) = \sum_{l,m} \frac{l(l+1)}{2\mu r^2} |lm\rangle \langle lm| + \hat{V}_c(r). \tag{2.36}$$

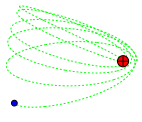

$\hat{V}'(\mathbf{r};t)$ in Eq. 2.35 is the 'perturbing' potential energy operator composed of the applied electric field potential $\hat{V}_{\text{field}}(z)$ and the cylindrically symmetric surface potential $\hat{V}_{\text{surf}}(z,\rho;t)$ (given by Eq. 1.7 and Eq. 1.9),

$$\hat{V}'(\mathbf{r};t) = \hat{V}_{\text{field}}(z) + \hat{V}_{\text{surf}}(z,\rho;t) = Fz + \hat{V}_{\text{surf}}(z,\rho;t). \tag{2.37}$$

Note that due to the cylindrical symmetry of the overall potential, the magnetic quantum number, m_l, is conserved. In the work presented in this thesis, only $m_l = 0$ states are considered.

2.3.3 Initial Rydberg wavefunction

The initial wavefunction $\Psi(\mathbf{r};t=0)$ is found by diagonalizing the Hamiltonian given by Eq. 2.35 at time $t = 0$ and distance $D = D_0$. The initial atom-surface separation D_0 is chosen to be large enough that negligible surface-ionisation takes place before the atom reaches this separation, and that the surface potential is not yet large enough to bring about any level crossings. For the calculations carried out here, D_0 is typically set to values $\sim 8n^2\mathrm{a}_0$, where n is the principal quantum number of the state of interest.

In the initial diagonalisation step, the angular co-ordinate is described by N_θ Legendre polynomials in the Finite Basis Representation (FBR) [69], since $\hat{V}_{\text{atom}}(\mathbf{r})$ (which includes the centrifugal potential, Eq. 2.36) is diagonal in this basis. The corresponding N_θ angular grid points in the DVR basis, and the $(N_\theta \times N_\theta)$ FBR/DVR transformation matrix $\mathbf{U}$, are given by the eigenvalues and the eigenvector matrix of the tridiagonal matrix given by Eq. 2.24, with $a_j = 0$ and $b_j = j/\sqrt{(4j^2-1)}$. The 'perturbing' potential energy matrix $\mathbf{V}'$ (Eq. 2.37), is diagonal in the angular DVR (with matrix elements given by the potential at the grid points), and is transformed to the angular

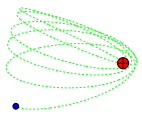

FBR for the initial diagonalisation

$$\mathbf{V'^{FBR}} = \mathbf{U}\mathbf{V'^{DVR}}\mathbf{U}^{\dagger}. \tag{2.38}$$

For the radial coordinate, although it is possible to carry out the diagonalisation directly in the CWDVR basis $\{f_\nu(r) \equiv |\nu\rangle\}_{\nu=1}^{N_r}$ that is used in the propagation, at such large separations from the surface where the surface-ionisation is negligible and the radial extension of the wavefunction into the metal surface is small, it is unnecessary to include such a large number of grid points at large radii (see the properties of the CWDVR detailed below). The initial diagonalisation step is therefore carried out in the regularised Lagrange-Laguerre DVR basis $\{\tilde{f}_j(r)\}_{j=1}^{N_k}$ [68] for the radial co-ordinate, which has grid points closely spaced near the core with progressively larger spacing at larger radius.

The regularised Lagrange-Laguerre DVR basis is closely related to the Lagrange-Laguerre basis (Eq. 2.23),

$$\tilde{f}_i(x) = \frac{x}{x_i} f_i(x) = (-1)^i x_i^{-\frac{1}{2}} \frac{x L_N(x)}{x - x_i} e^{-\frac{x}{2}}. \tag{2.39}$$

It is regularised such that the singular r^{-1} Coulomb potential *and* r^{-2} centrifugal potential can be treated exactly at the Gauss quadrature approximation [68]. In this DVR basis, the kinetic energy matrix $\mathbf{T}$ is given by

$$T_{ii} = \frac{1}{24x_i^2}[4 + (4N+2)x_i - x_i^2] \tag{2.40}$$

$$T_{ij} = \frac{(-1)^{(i-j)}}{2(x_i x_j)^{-\frac{1}{2}}} \frac{x_i + x_j}{(x_i - x_j)^2}. \tag{2.41}$$

After diagonalisation, the appropriate initial wavefunction, $\Psi(r; t=0) = \sum_j \tilde{c}_j \tilde{f}_j(r)$, is projected onto the CWDVR basis for time propagation. Taking advantage of the

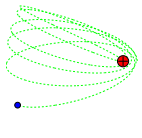

collocation property of DVRs ($\langle f_\nu \,|\, \Psi(r)\rangle = w_\nu^{\frac{1}{2}} \Psi(r_\nu)$) [69]:

$$\sum_{\nu}^{N_r} \langle \nu | \Psi(t=0)\rangle = \sum_{\nu}^{N_r} \langle \nu | \Psi \rangle = \sum_{\nu}^{N_r} w_\nu^{\frac{1}{2}} \Psi(r_\nu) = \sum_{\nu,j}^{N_r,N_k} w_\nu^{\frac{1}{2}} \tilde{c}_j \tilde{f}_j(r_\nu), \tag{2.42}$$

where $\{r_\nu\}_{\nu=1}^{N_r}$ are the CWDVR grid points, and $\{w_\nu\}_{\nu=1}^{N_r}$ are the CWDVR quadrature weights associated with the grid points (see below).

2.3.4 Coulomb-Wave Discrete Variable Representation

The Coulomb-Wave Discrete Variable Representation (CWDVR) proposed by Dunseath *et al.* [74] is used to describe the electron wavefunction in the radial co-ordinate. The CWDVR consists of grid points defined as the positive roots of a positive-energy Coulomb reference function $v(r)$, which is the solution to the Coulomb differential equation for the case of $L = 0$:

$$\begin{aligned} \left[\frac{d^2}{dr^2} - \frac{L(L+1)}{r^2} + \frac{2Z}{r} + \kappa^2\right] v(r) &= 0 \\ \left[\frac{d^2}{dr^2} + \frac{2Z}{r} + \kappa^2\right] v(r) &= 0. \end{aligned} \tag{2.43}$$

The Coulomb wave functions can be expressed in terms of confluent hypergeometric functions [75]

$$v(r) = \frac{1}{\sqrt{\kappa}} F_0(-Z/\kappa, \kappa r). \tag{2.44}$$

The grid points (roots of the Coulomb wave) are non-uniformly distributed, with a high concentration of points near the Coulomb singularity, and an almost regular spacing at large distances (see Fig. 2.5). The particular advantage of using this DVR is that the Coulomb singularity is treated naturally and so no regularisation of the potential near the origin is required. The distribution of grid points can be controlled by adjusting two grid parameters, κ and Z. The grid parameter Z corresponds to the

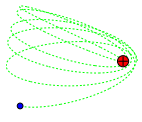

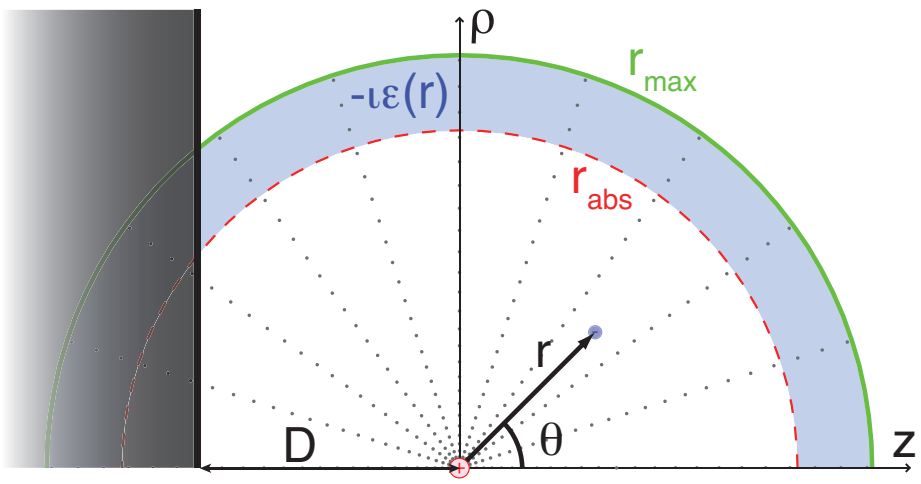

Figure 2.5: A schematic illustration of the CWDVR grid, as used in the wavepacket calculations, in the reference frame of the ion-core. Note the higher concentration of grid points near the origin and the regularly spaced points at large radius. The distance of the ion-core from the metal surface is labeled D, $r_{\rm abs}$ is the lower bound of the absorbing potential and the position of the radial flux plane, and $r_{\rm max}$ is the maximum radius of the numerical grid and the upper bound of the absorbing potential.

effective charge of the ion-core of the Coulomb wave, and varies the concentration of points near the Coulomb singularity, while κ is related to the energy of the Coulomb wave, and is a linear scaling factor that varies the separation between grid points at large distances. Thus, the CWDVR is particularly suited to the surface-ionisation problem, which involves wavefunctions that are bound by the Coulomb potential at small distances, but become free waves when the electron is transferred into the metal.

In the CWDVR, the kinetic-energy matrix is given by a simple analytical expression [74], and the potential-energy matrix in the radial co-ordinate is diagonal, with matrix elements given by the value of the potential at the grid points:

$$T_{ij}^{DVR} = -\delta_{ij}\frac{W(r_i)}{6} + (1-\delta_{ij})\frac{(-1)^{i+j}}{(r_i - r_j)^2} \quad (2.45)$$

$$V_{ij}^{DVR} = \delta_{ij}V(r_i), \quad (2.46)$$

where $W(r_i) = (\kappa^2 + 2Z/r_i)$. The quadrature weights associated with the CWDVR

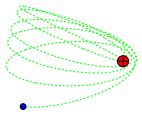

grid points are given by

$$w_\nu \approx \frac{\pi}{\kappa}[F_0'(-Z/\kappa, \kappa r_\nu)]^{-2} = \frac{\pi}{a_\nu^2} \tag{2.47}$$

where a_ν is the first derivative of the reference Coulomb function $v(r)$ at $r = r_\nu$. The positive-energy Coulomb wavefunction and its derivative are computed using the COUFLG subroutine of Barnett [76], and the roots, which are the positions of the radial grid points, are found using the Newton-Raphson Method [66].

2.3.5 Absorbing Potential

To remove the spurious reflections of the wavefunction at the edge of the numerical grid and to maintain the correct outgoing-wave boundary condition for the electron wavefunction, the Manolopoulos transmission-free absorbing potential [77],$-i\epsilon(r)$, is added to the Hamiltonian.

$$\tilde{\mathbf{H}} = \mathbf{H} - \mathbf{V}_{abs}(r) = \mathbf{H} - i\boldsymbol{\epsilon}(r) \tag{2.48}$$

where $\mathbf{V}_{abs} = -i\boldsymbol{\epsilon}$ is a diagonal matrix with elements

$$-i\epsilon(r) \times h(r - r_{\text{abs}}). \tag{2.49}$$

r is the electron radial co-ordinate, r_{abs} is the radial lower bound of the absorbing region, and $h(f(r))$ is the Heaviside step function. The negative complex potential, $-i\epsilon(r)$, has the form:

$$-i\epsilon(r) = -i\frac{y(x)}{2}\left(\frac{2\pi}{\Delta r}\right)^2 \tag{2.50}$$

where

$$x = \frac{c(r - r_{\text{abs}})}{\Delta r} \tag{2.51}$$

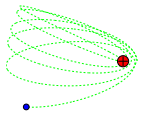

and the approximate form of $y(x)$ is

$$y(x) = \frac{4}{(c-x)^2} + \frac{4}{(c+x)^2} - \frac{8}{c^2}. \tag{2.52}$$

Here $\Delta r = r_{\max} - r_{\text{abs}}$ is the width of the absorbing region, $r_{\max}$ is the maximum radius for the numerical grid, and the numerical value of $c \approx 2.62206$ [77]. The width of the absorbing region, Δr, depends on the momentum of the outgoing wave. For the calculations carried out in this work, it has been found that a width of 30 a_0 is sufficient to remove the outgoing wavefunction at the edge of the grid. A schematic illustration of the CWDVR grid, the absorbing boundary and the co-ordinates used in the wavepacket calculations is shown in Fig. 2.5.

2.3.6 Time Propagation

The formal solution of the time-dependent Schrödinger equation (Eq. 2.34) is

$$\Psi(t + \Delta t) = e^{-i\hat{\hat{H}}\Delta t}\Psi(t). \tag{2.53}$$

Starting from an initial wavefunction, $\Psi(t)$, the wavefunctions of the system at a later time, $\Psi(t + \Delta t)$, may be computed through the action of the propagator, $e^{-i\hat{\hat{H}}\Delta t}$. For small timesteps, the propagator may be approximated by the symmetric split operator [78]

$$e^{-i(\mathbf{H}-i\boldsymbol{\epsilon})\Delta t} = e^{-i\frac{\mathbf{V}'}{2}\Delta t} e^{-i(\mathbf{T}+\mathbf{V}_{\text{atom}}-\mathbf{i}\boldsymbol{\epsilon})\Delta t} e^{-i\frac{\mathbf{V}'}{2}\Delta t} + O(\Delta t^3), \tag{2.54}$$

where $\mathbf{T}$, $\mathbf{V}_{\text{atom}}$ and $\mathbf{V}'$ are the matrix representations of the operators defined in Eq. 2.35, and $-i\boldsymbol{\epsilon}(r)$ is the absorbing potential. The error associated with the split operator expression decreases as the size of the time steps decreases, and, for typical calculations carried out in this work, a time step of $\Delta t = 1$ a.u. is found to be sufficient. From Eq. 2.54, the advantage of using a radial DVR and an angular FBR/DVR [69] is

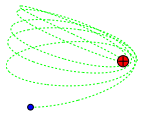

now clear. The kinetic energy matrix $\mathbf{T}$ in the CWDVR is given by simple analytical expressions (Eq. 2.45), the absorbing potential $-i\boldsymbol{\epsilon}(r)$ is diagonal in the radial DVR, and the *time-independent* potential energy matrix $\mathbf{V}_{\text{atom}}$ is diagonal in the radial DVR and the angular FBR, and is given by the value of the potential at the radial grid points for a given angular-momentum quantum number, l. Since the middle term in Eq. 2.54 is time-independent, it can be precomputed before the propagation of the wavefunction.

The exponential $e^{-i(\mathbf{T}+\mathbf{V}_{\text{atom}}-\mathbf{i}\boldsymbol{\epsilon})\Delta t}$ term in Eq. 2.54 can be evaluated via the diagonalisation of the complex matrix: $-i(\mathbf{T}+\mathbf{V}_{\text{atom}}-\mathbf{i}\boldsymbol{\epsilon})\Delta t = \mathbf{X}\mathbf{D}\mathbf{X}^{-\mathbf{1}}$. The exponential matrix is then simply given by

$$e^{-i(\mathbf{T}+\mathbf{V}_{\mathbf{H}}-i\boldsymbol{\epsilon})\Delta t} = \mathbf{X}\mathbf{D}^{\mathbf{e}}\mathbf{X}^{-\mathbf{1}} \tag{2.55}$$

where $\mathbf{D}^{\mathbf{e}}$ is a diagonal matrix with elements given by exponential of the eigenvalues in matrix $\mathbf{D}$.

The *time-dependent* potential term $\mathbf{V}'$ which depends on both the radial and angular co-ordinates is diagonal in both the radial DVR and angular DVR. The operation of $e^{-i\frac{\mathbf{V}'}{2}\Delta t}$ on the wavefunction can be evaluated by simply transforming the wavefunction between the angular FBR and DVR and multiplying by a diagonal matrix $\mathbf{D}^{\mathbf{e}}_{\mathbf{V}'}$,

$$e^{-i\frac{\mathbf{V}'}{2}\Delta t} = \mathbf{U}\mathbf{D}^{\mathbf{e}}_{\mathbf{V}'}\mathbf{U}^{\dagger} \tag{2.56}$$

where the matrix elements of $\mathbf{D}^{\mathbf{e}}_{\mathbf{V}'}$ are given by the exponential of the value of the potential at the given radial and angular points, *i.e.*, $D^{e}_{V'ii} = e^{V'^{DVR}_{ii}}$, and $\mathbf{U}$ is the angular FBR/DVR transformation matrix (Eq. 2.24).

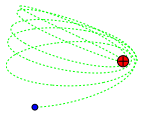

2.3.7 Ionisation probability

To study the ionisation of the Rydberg electron, the total electron density lying within the region enclosed by the lower bound of the absorbing region ($r_{\rm abs}$) and the metal surface is monitored as a function of the atom-surface distance. The derivative of the electron population inside this 'bound' region with respect to the atom-surface separation may be interpreted as the ionisation probability per unit length of the Rydberg atom ionising at that distance, $P(D, v_\perp, F)$ (c.f. Section 2.2). This is equivalent to having a stationary circular flux plane with radius $r_{\rm abs}$ that is truncated by a moving (z-)flux plane which represents the approach of the metal surface. It is important to include the 'vacuum'-boundary as well as the metal flux plane because not all of the electron density escapes into the metal; under certain field conditions, some density escapes through the vacuum side away from the metal. It is also important to have a sufficiently large radius $r_{\rm abs}$ such that the Rydberg electron may be considered as ionised beyond this radial limit. For the calculations carried out in this thesis, $r_{\rm abs}$ is typically set to values of $\geq 6n^2 {\rm a}_0$.

The fractions of the outgoing electron density in the 'forward' ($\theta > 90°$, towards the surface) and 'backward' ($\theta < 90°$, away from the surface) directions are monitored by radial 'flux planes' placed at the absorbing boundary. Since the motion of ion-core is much slower than that of the tunnelling electron, the ionisation probability at atom-surface separation D, can be expressed as:

$$\begin{aligned} P(D, v_\perp, F) = -\frac{1}{v_\perp}\frac{d}{dt}\langle\Psi(t)|\Psi(t)\rangle &= v_\perp^{-1}[-i\,\langle\hat{\tilde{H}}\Psi(t)|\Psi(t)\rangle + i\,\langle\Psi(t)|\hat{\tilde{H}}\Psi(t)\rangle] \\ &= v_\perp^{-1}[-i\,\langle\hat{V}_{abs}\Psi(t)|\Psi(t)\rangle + i\,\langle\Psi(t)|\hat{V}_{abs}\Psi(t)\rangle] \\ &= v_\perp^{-1}[2i\,\langle\Psi(t)|\hat{V}_{abs}|\Psi(t)\rangle]. \end{aligned} \tag{2.57}$$

where $\hat{\tilde{H}}$ is the modified Hamiltonian given by Eq. 2.48, and $\hat{V}_{abs} = -i\epsilon(r)$ is the radial

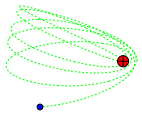

heaviside absorbing boundary potential given by Eq. 2.50. The radial 'flux' operator is therefore a diagonal matrix, with matrix elements given by

$$F_{i,j}^{DVR} = 2v_{\perp}^{-1}[\epsilon(r_i) \times h(r_i - r_{abs})]\delta_{i,j}. \tag{2.58}$$

Integration over the 'forward' and 'backward' angles subsequently provides the angular resolved outgoing electron flux.

2.3.8 Ion-detection probability

In the wavepacket calculations, the ionisation probability (or ionisation rate) $P_\sigma(D, v_\perp, F)$ for specified initial quantum state σ, field F and collisional velocity $v_\perp$, is evaluated as function of atom-surface separation D. For the cases where the direction of the field is set for ion-extraction (F positive in Eq. 2.37), these ionisation curves can be related to experimental ionisation profiles (detected ion signal $S_\sigma(F)$ *vs* field F) by the integration:

$$S_\sigma(F) = \int_0^\infty f(v_\perp) \int_\infty^{D_{\min}(F)} P_\sigma(D', v_\perp, F)\, dD'\, dv_\perp, \tag{2.59}$$

where $f(v_\perp)$ is the velocity distribution of the Rydberg atoms and $D_{\min}(F)$ is the minimum ionisation distance for which the applied field F can pull the bare ion away from the surface, as given by Eq. 1.15.

2.4 Merits and deficiencies of the theoretical techniques

The theoretical techniques used in this thesis have been presented above. In this section, the advantages and deficiencies of these approaches are discussed and compared.

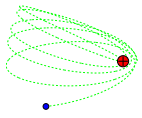

The classical-over-the barrier approach assumes that surface ionisation occurs as soon as the energy of the Rydberg electron is greater than the saddle point of the potential barrier between the ion-core and the metal surface at some critical distance D_{OTB}. There are three main problems with this technique: i) an accurate knowledge of the Rydberg electronic energy at the surface ionisation range is required; ii) only energetics are considered, kinetic lifetime effects are not considered; iii) quantum effects such as sub-barrier tunnelling and quantum reflection are not included. Consequently, the over-the-barrier model can only provide a rough qualitative estimate of the ionisation distance for surface-oriented states (such that the electron wavefunction is localised near the saddle point, and kinetic effects are unimportant). As will be shown in Section 5.1, quantitatively, the OTB approach predicts different ionisation distances compared with the wavepacket (and complex scaling) results. However, the advantage of using this classical approach is that the ionisation distance can be determined numerically very efficiently, and it is straightforward to extend the calculations to incorporate additional perturbing potentials, such as localised fields from surface defects or adsorbates (see Section 5.2 and Ref. [48]).

The complex scaling approach can provide the energy and lifetime of the Rydberg state at the charge-transfer distance range, thus eliminating the problems associated with the classical OTB approach. Under the adiabatic regime, such that the Rydberg state follows all crossings adiabatically, the complex-scaling method produces the same results as wavepacket calculations (see Chapter 3). However, such a time-independent technique implicitly requires an adiabatic assumption, which is not necessarily valid for the case of Rydberg-surface collisions where the Rydberg level can encounter numerous crossings with other close-in-energy states with non-negligible velocity. Furthermore, the calculations are computationally demanding; a $N \times N$ complex non-Hermitian matrix is diagonalised at every atom-surface separation (the number of operations per

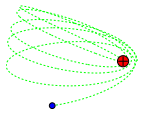

diagaonlisation scales as N^3), and the number of basis functions also increases rapidly with the principal quantum number of interest.

The time-dependent wavepacket approach naturally includes any non-adiabatic effects which may occur as the Rydberg state approaches the metal surface. Furthermore, only a single matrix diagonalisation is required before time propagation which involves only matrix multiplications that scale as N^2. However, as explained in Section 2.3, carrying out the full time-dependent calculation at the experimental range of principal quantum numbers ($n > 15$) and collisional velocities ($v_\perp \sim 10^{-4}$ a.u. or 10^2 ms^{-1}) remains a formidable task, even with a carefully chosen basis such as the CWDVR. In the work of Sjakste *et al.*, the wavepacket calculations carried out for the xenon Rydberg atoms at a metal surface have been limited to $n = 7 - 8$ and at collisional velocities as low as $v_\perp = 2 \times 10^{-3}$ a.u. (approximately an order of magnitude greater than the experimental range), and provided a qualitative comparison with the experimental results of Dunning and co-workers [44]. In the work presented in this thesis, using a CWDVR grid, calculations have been extended to principal quantum number of $n = 10$, and at the experimentally relevant range of velocities ($v_\perp \sim 10^{-4}$ a.u.).

Another disadvantage of the time-dependent wavepacket approach is that each propagation is specific to the initial state, the applied electric field *and* the collisional velocity, while the complex-scaling calculation provides the collisional velocity independent lifetimes of 'all' states for a given electric field from each diagonalisation.

In Chapter 3 and 4, the complex scaling and wavepacket propagation approach are used as complementary techniques to study theoretically the ionisation dynamics of low principal quantum number ($n \leq 10$) H atom and Xe atom Rydberg states at metal surfaces under various experimentally relevant effects - such as varying the size of the Rydberg atom, the electric field strength, the direction of the electric field, the collisional velocity of the Rydberg atoms and the nature of the metal surface. While

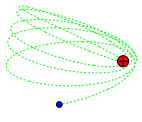

the wavepacket calculations give the accurate ionisation dynamics, insight into the extent of non-adiabatic contribution and the details of Rydberg level interactions can be obtained by comparing with the complex scaling results.

In Chapter 5 the simple classical over-the-barrier calculations are compared with the wavepacket results, as the OTB approach can be most feasibly carried out at the experimental range of principal quantum numbers. Although there is still a significant gap between the principal quantum numbers studied theoretically using the complex scaling and wavepacket approach and the experimental range studied in this thesis ($20 \leq n \leq 40$), by applying appropriate scaling relationships, it is possible to model at the experimental range of principal quantum numbers.

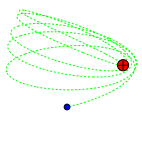

Chapter 3

Theory of the interactions of H atoms with metal surfaces

In this chapter, the interaction of hydrogen Rydberg atoms with metal surfaces is investigated by applying a combination of the theoretical approaches outlined in the previous chapter. Focus is placed on studying the effects of: the magnitude and direction of the applied electric field (electron-extraction as well as the conventional ion-extraction field), the velocity of the Rydberg atom (possible non-adiabatic transitions), the mean-field perturbed Rydberg trajectory (Rydberg acceleration), and the electronic structure of the metal target (resonance ionisation to discrete band-gap embedded states) on the overall charge transfer dynamics. In the following sections, with the exceptions of Section 3.6, the results presented are for the interaction of Rydberg hydrogen atoms with the Jellium model potential outlined in Section 1.5.1.

3.1 Rydberg dimension and polarisation

Before considering the ionisation dynamics of Rydberg states under the influence of externally applied electric fields, a better understanding of the effects of the perturb-

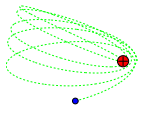

ing surface potential (Eq. 1.7 and Eq. 1.9) can be gained by studying the zero-field case. Figure 3.1 presents the zero-field ionisation probabilities for the Rydberg states of the $n = 2 - 8$ manifolds, at a typical experimental velocity of 3×10^{-4} a.u. ($\equiv 656$ ms^{-1}), calculated using the wavepacket propagation approach (positive axis). Figure 3.2 presents the electronic energy and widths calculated from the complex scaling approach, and the inferred ionisation probabilities (or rates) calculated according to Eq. 2.31 are plotted on the negative axis of Fig. 3.1. In accord with the OTB model, the most probable ionisation distance of the most surface-oriented state (see below) indeed scales approximately with the Rydberg dimension, n^2 (more discussion on scaling properties is given in Section 5.1).

As mentioned in Section 1.5 and illustrated by energy levels obtained from the complex scaling calculations, the surface potential splits the degeneracy of the n-manifold (c.f. the Stark effect). The lowest energy state, which exhibits the shortest lifetime (largest width), is ionised at greatest distance in the wavepacket calculations, and is polarised toward the surface; while progressively higher energy states, which have longer lifetimes (smaller widths), are ionised progressively closer to the surface, and exhibit polarisations that are oriented progressively more toward the vacuum (see Fig. 1.7). For $n = 2$, the surface- and vacuum-oriented states are effectively the two sp_z hybrids directed towards and away from the surface [25].

The different shifts in energies shown in Fig. 3.2 (which excludes the state-independent attractive proton–image-proton V_{pp} contribution [see Section 2.2]) for the various states of the n-manifolds can be explained with reference to the form of the surface-potential (Fig. 1.8). For a vacuum-oriented state, mainly the long-range surface potential, which is dominated by the repulsive electron–image-proton interaction, V_{ep}, is probed. The repulsive electron–image-proton interaction depends on both the electron z-co-ordinate *and* the atom-surface separation (Eq. 1.7), and it increases as the atom-surface separa-

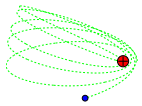

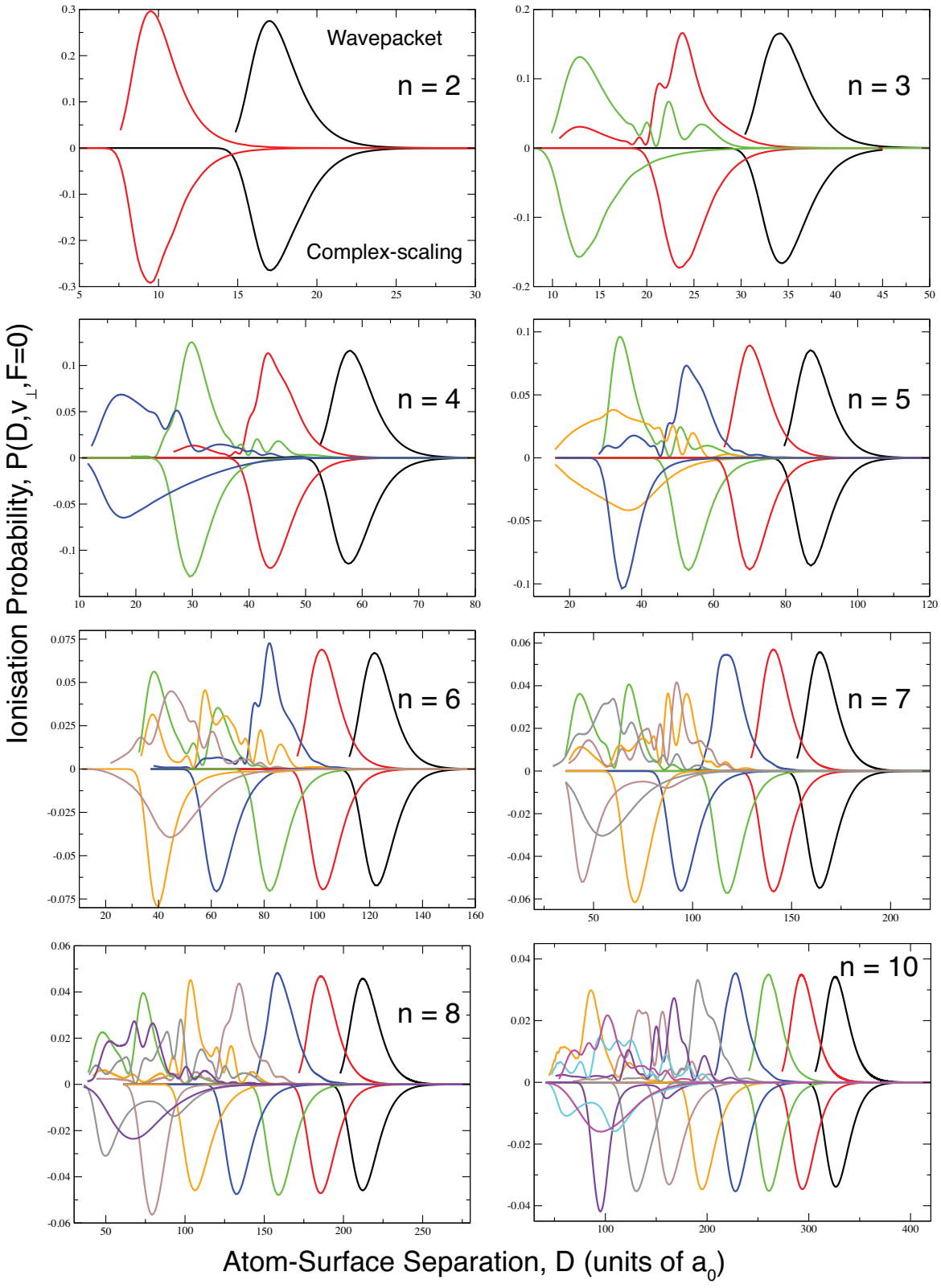

Figure 3.1: Ionisation probabilities $P(v_\perp, D, F = 0)$ as a function of atom-surface separation, calculated using wavepacket propagation (positive axis) from Eq. 2.57, and complex scaling approach (negative axis) from Eq. 2.31, for the $n = 2 - 10$, $m_l = 0$ Rydberg states approaching a Jellium metal surface at a typical experimental collisional velocity of $v_\perp = 3 \times 10^{-4}$ a.u. ($\equiv 656$ ms^{-1}).

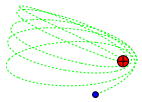

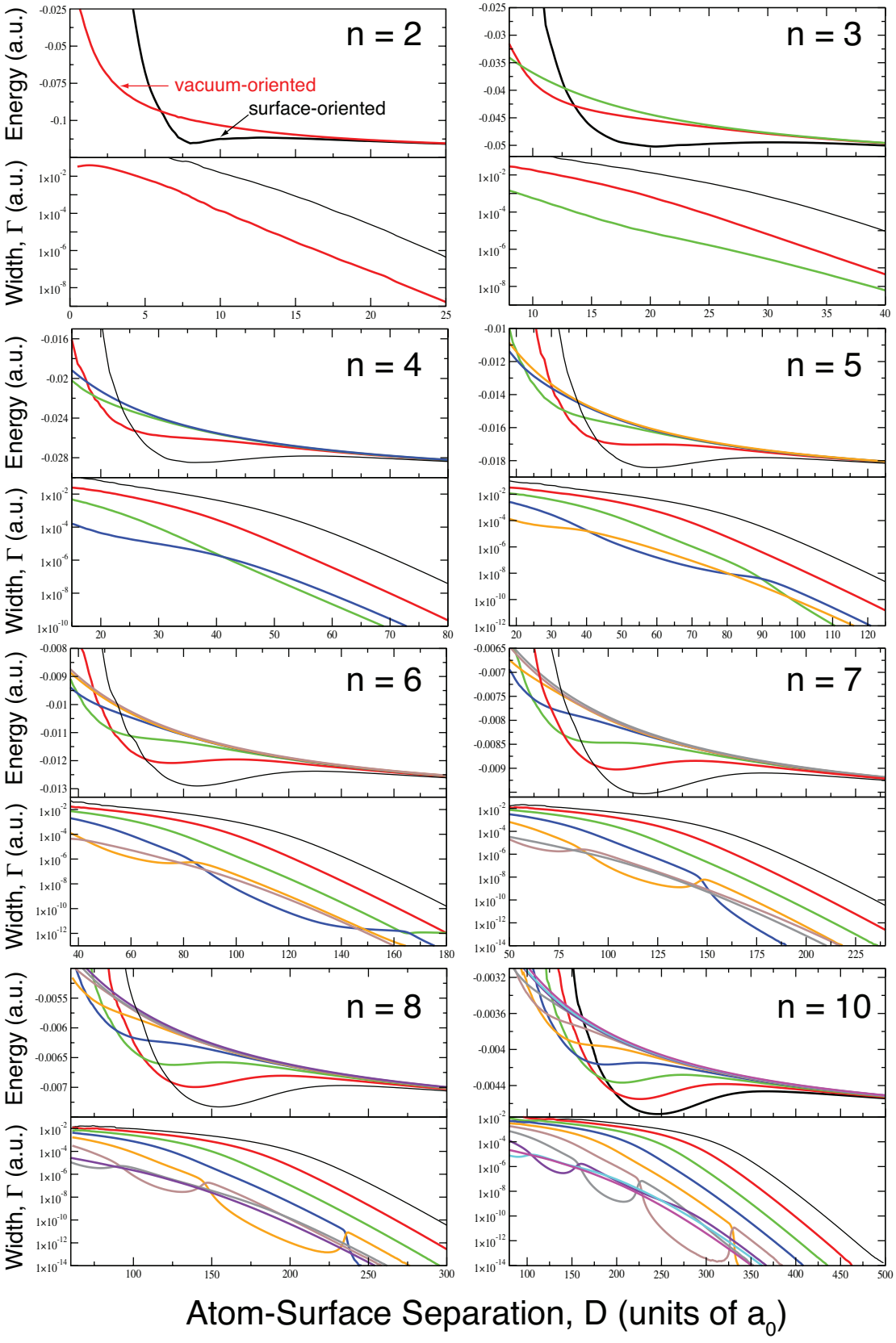

Figure 3.2: Energies and widths as a function of atom-surface separation, calculated using complex scaling theory, for the $n = 2 - 10$, $m_l = 0$ Rydberg states.

tion decreases. Thus, the energies of the vacuum-oriented Rydberg states increase with decreasing atom-surface separation. From Eq. 1.8 (taking away the V_{pp} term), this upward energy shift is $\sim 1/(4D)$. In contrast, for a surface-oriented state, the attractive part of the surface potential may be probed provided that the atom-surface separation is sufficiently small. This attractive surface potential is dominated by the electron–image-electron potential, V_{ee}, which lowers the energies of the Rydberg states. Thus, as the surface-oriented state approaches the surface, its energy initially increases just as the vacuum-oriented state, and then decreases as it begins to probe the attractive V_{ee} potential. As the atom-surface separation decreases further, the electron–image-proton interaction, V_{ep}, becomes highly repulsive and once again dominates and the energies of the Rydberg states increase again.

3.2 Collisional velocity and non-adiabatic effects

The energy crossings and discontinuities of the level widths in Fig. 3.2 show that unlike the case of the hydrogen atom in a homogeneous electric field, *avoided* crossings can occur in the presence of the image charge field. This is because although the cylindrical symmetry is preserved (see Section 1.5), the surface potential breaks the z-parity symmetry of the system, allowing interactions between the levels with the same value of m_l. At zero (or low) extraction field, the Rydberg energy levels of a given n-manifold are close together, and given the differing energetic shifts of surface- and vacuum-oriented states (see previous section), the vacuum-oriented states which stay close together in energy and ionise closer to the surface are more likely to encounter level crossings before ionisation. Figure 3.2 also shows that the number of crossings increases with principal quantum n, as the number of states per manifold and the energy density of states increases.

At the avoided crossings, the polarisation of the wavefunctions (vacuum or surface-

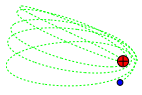

oriented) may be exchanged or become mixed, the extent of which depends on the adiabaticity of the avoided crossing traversal. The resulting variation of ionisation probabilities with atom-surface separation can therefore be complex.

Figure 3.1 show that while the ionisation probabilities for the surface-oriented states obtained from complex scaling are in good agreement with the wavepacket calculations, the results for the other states of the n-manifolds are generally not the same. For some states, the wavepacket ionisation probabilities even appear to correspond to another state within the manifold when compared with the complex scaling results (*e.g.* the green curves in Fig. 3.1). As discussed in Section 2.4, the complex scaling calculations assume that all crossings are followed adiabatically, while the wavepacket propagation approach includes all non-adiabatic dynamics. In the Landau-Zener avoided-crossing model, the extent to which crossings are traversed adiabatically is dependent on the off-diagonal coupling matrix elements in the adiabatic basis (which is reflected by the size of the gap of the avoided crossing), and the rate of the traversal of the crossing (*i.e.* the collisional velocity of the Rydberg atom) [73]. Therefore, at the collisional velocity of 3×10^{-4} a.u. (a typical experimental velocity) *and* in the presence of a small or negligible electric field, where the Rydberg energy levels for a given n-manifold are very close together in energy, the surface ionisation dynamics does not fall in the adiabatic regime and a time-dependent description is required to describe the non-adiabatic dynamics.

Figure 3.3(a) shows that a better match of the complex scaling results and the wavepacket calculations at zero field can be achieved for all states of the $n = 6$ manifold at a lower collisional velocity of $v_\perp = 3 \times 10^{-5}$ a.u.. Although the underlying profile appears the same, the wavepacket ionisation probabilities exhibit some high frequency oscillation amongst some of the Rydberg states, in particular Fig. 3.3(b) shows oscillations for the $k = +5$ (orange curve) and $k = -1$ (blue curve) states that are approximately π

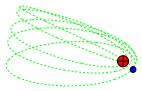

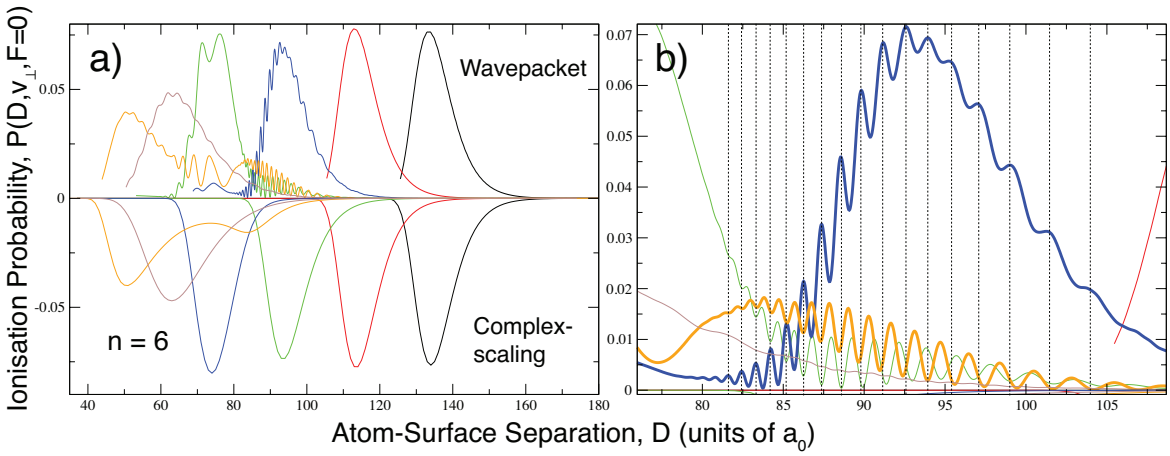

Figure 3.3: (a) Ionisation probabilities $P(D, v_\perp, F = 0)$ as a function of atom-surface separation, calculated using wavepacket propagation (positive axis) from Eq. 2.57, and complex scaling approach (negative axis) from Eq. 2.31, for the $n = 6$, $m_l = 0$ Rydberg states approaching a Jellium metal surface at a collisional velocity of $v_\perp = 3 \times 10^{-5}$ a.u. ($\equiv 65.6$ ms^{-1}). (b) The wavepacket results in the strongly oscillating region: the $k = +5$ (orange curve) and $k = -1$ (blue curve) states are approximately π out of phase with each other.

out of phase. This can be explained in terms of a non-stationary state formed from a superposition of the close-in-energy Rydberg states, resulting in interference beats as time evolves. Thus, the dynamics *at zero-field* is still not fully adiabatic at $v_\perp \sim 10^{-5}$ a.u.. It will be shown below that the extent of non-adiabatic interaction also depends on the magnitude and direction of the electric field.

3.3 Magnitude of the applied electric field

The introduction of an externally applied ion-extraction electric field (*i.e.*, oriented so as to repel positive ions from the surface) is now considered. Figure 3.4 presents the complex scaling results for the $m_l = 0$, $n = 10$ states of the hydrogen atom at various electric fields (the Stark states are labeled by the parabolic quantum number k). For an ion-extraction field, the lower energy red-shifted Stark states are surface-oriented, and therefore have a larger level width at a given atom-surface separation, compared

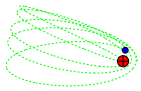

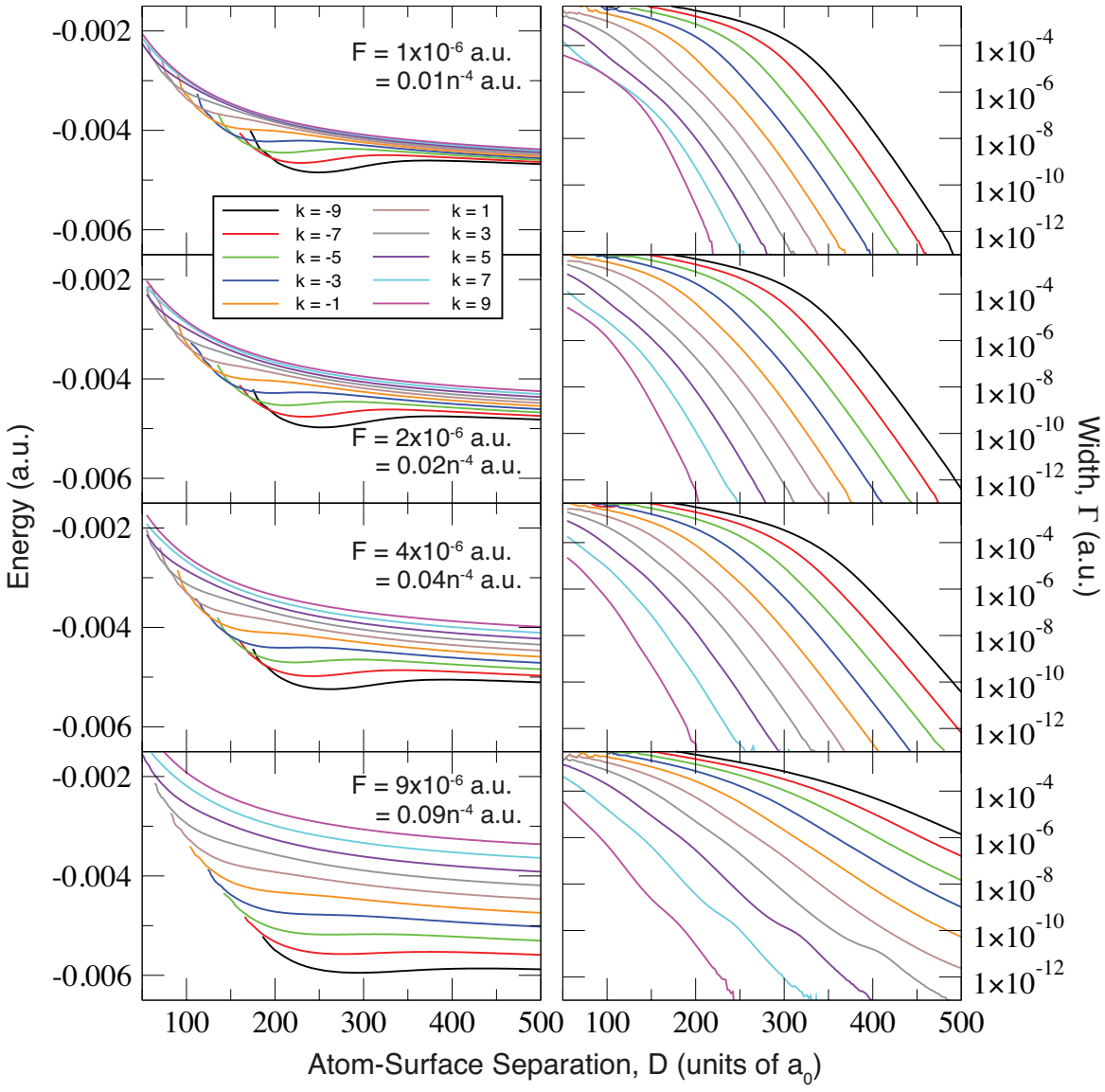

Figure 3.4: Energies (left panel) and widths (right panel) of the $n = 10$, $m_l = 0$ hydrogen Rydberg states under ion-extraction fields of $F = +(1-9) \times 10^{-6}$ a.u..

with the higher energy blue-shifted Stark states which are vacuum-oriented.

At zero or low fields, the blue-shifted states exhibit numerous avoided level crossings (see bottom right plot in Fig. 3.2), but as the field increases, the number of level crossings decreases rapidly. This is due to large Stark splittings of individual energy levels at high fields, which effectively spreads the manifold further apart. Thus, as the field increases, the extent of level interaction decreases, and the dynamics of the charge transfer should exhibit less contribution from non-adiabatic effects. To illustrate this, Fig. 3.5 presents the wavepacket and complex scaling ionisation probabilities for the $n = 10$, $m_l = 0$ states of the hydrogen atom approaching a metal surface with the collisional velocity of 3×10^{-4} a.u. ($\equiv 656$ ms^{-1}) and in the presence of ion-extraction fields of $F = +(1-9)\times 10^{-6}$ a.u. $= +(0.01-0.09)n^{-4}$. A field of magnitude 1×10^{-6} a.u. is relatively weak for the principal quantum number $n = 10$, *i.e.*, well below the Inglis-Teller field ($F_{\rm IT} = 3.3 \times 10^{-6}$ a.u.), while a field of 9×10^{-6} a.u. is close to the field ionisation limit of the most extreme red-shifted state. For comparison, the OTB approach (Section 2.1) predicts a critical threshold ion-extraction field in the range of $\approx (0.02 - 0.08)n^{-4}$ for the most extreme red-shifted state (see Fig. 2.3). It can be seen from Fig. 3.5 that even for a 'weak' field of $F = +1 \times 10^{-6}$, there is very good agreement between the wavepacket and complex scaling results (except for the two most vacuum-oriented states), and the results are nearly identical for the higher fields. Thus, at the experimental range of ion-extraction fields, an adiabatic picture of the ionisation dynamics is likely to be sufficient (at least for $n = 10$), and the individual Stark levels are sufficiently far apart that they are expected to exhibit a single gaussian-like ionisation probability (rather than multiple-peaks spanning a large range of distances) as shown in Fig. 3.5. This feature is important when considering scaling the results obtained for lower principal quantum numbers ($n \leq 10$) to the experimental range ($20 < n < 40$) in Section 5.1.

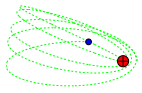

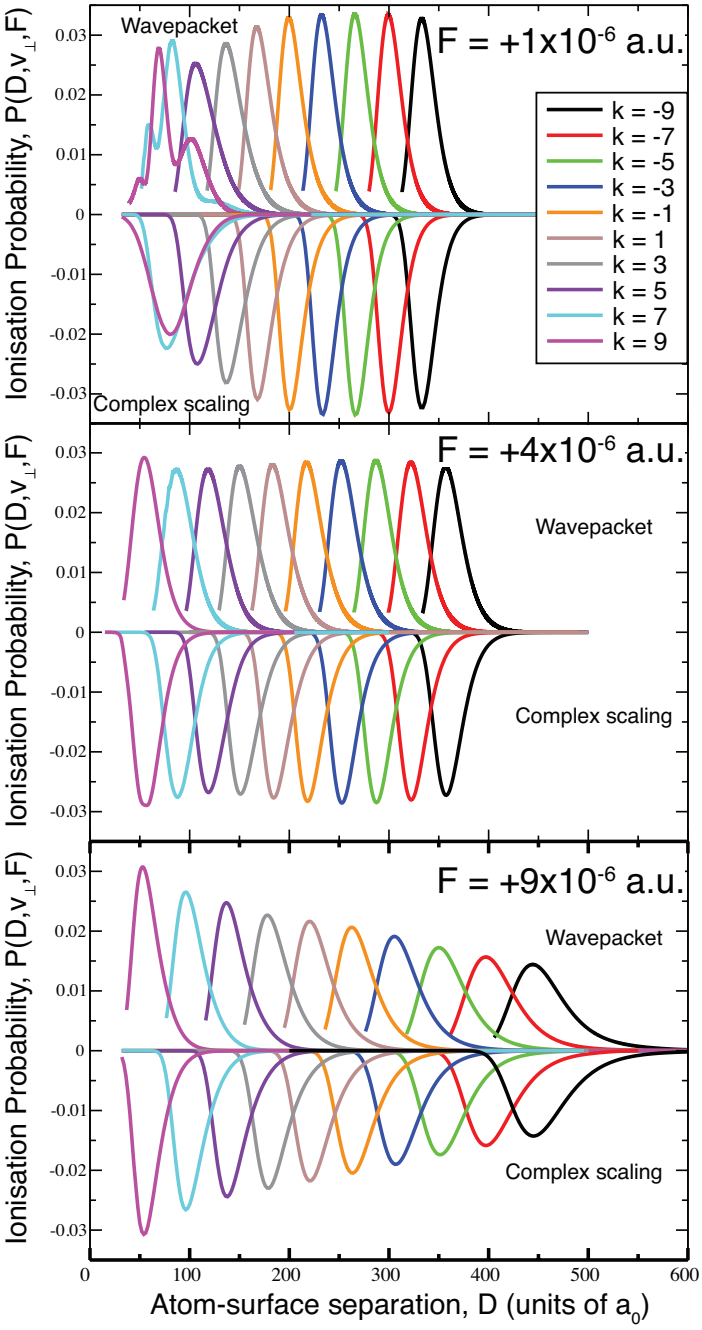

Figure 3.5: Wavepacket propagation (positive axis) and complex scaling (negative axis) ionisation probabilities for the $n = 10$, $m_l = 0$ states of the hydrogen atom approaching a metal surface with the collisional velocity of 3×10^{-4} a.u. and in the presence of ion-extraction fields of $F = +1 \times 10^{-6}$ a.u., $+4 \times 10^{-6}$ a.u., and $+9 \times 10^{-6}$ a.u..

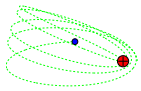

As explained in Section 2.1, for an ion-extraction field, as the field increases, the potential barrier between the surface and the ion-core decreases (Fig. 2.1), facilitating surface ionisation. This is shown in Fig. 3.5, where the lower-energy surface-oriented states (which have electron density close to potential barrier) are ionised further away from the surface with increasing extraction field.

3.4 Ion- *vs* electron-extraction field

In this section, particular attention is given to the effects of the direction of the electric field on the ionisation dynamics of the Rydberg atom. The 'reversed' field case (positive ions pulled toward the surface, and electrons repelled towards the detector) has been neglected in previous theoretical work, presumably because of the lack of related experimental data. Recently, McCormack [64] has detected an electron signal from the surface ionisation of Rydberg H_2 molecules, by reversing the direction of the extraction electric field. The source of the electron signal is however, uncertain, as the typical picture of the charge transfer process is described by the tunnelling of the Rydberg electron into the metal conduction band. The electrons are not from secondary processes due the neutralisation of positive ions close to the surface, since in the experiments of Ref. [64] the 'late' electron signal (at the surface signal time gate) is only detected below the field ionisation threshold. Thus, a theoretical study of the ionisation dynamics in the 'reversed' electron-extraction may elucidate the experimental observations. The experimental results presented in Chapter 7 also show an electron signal for the surface ionisation of hydrogen *atoms*.

Figure 3.6 compares the wavepacket propagation and complex scaling ionisation probabilities as a function of atom-surface separation for the $n = 10$, $m_l = 0$ states of the hydrogen atom under an ion- and electron-extraction field of $\pm 1 \times 10^{-6}$ a.u., and with a collisional velocity of 3×10^{-4} a.u.. Figure 3.7 shows the corresponding calculated en-

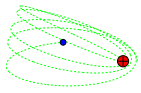

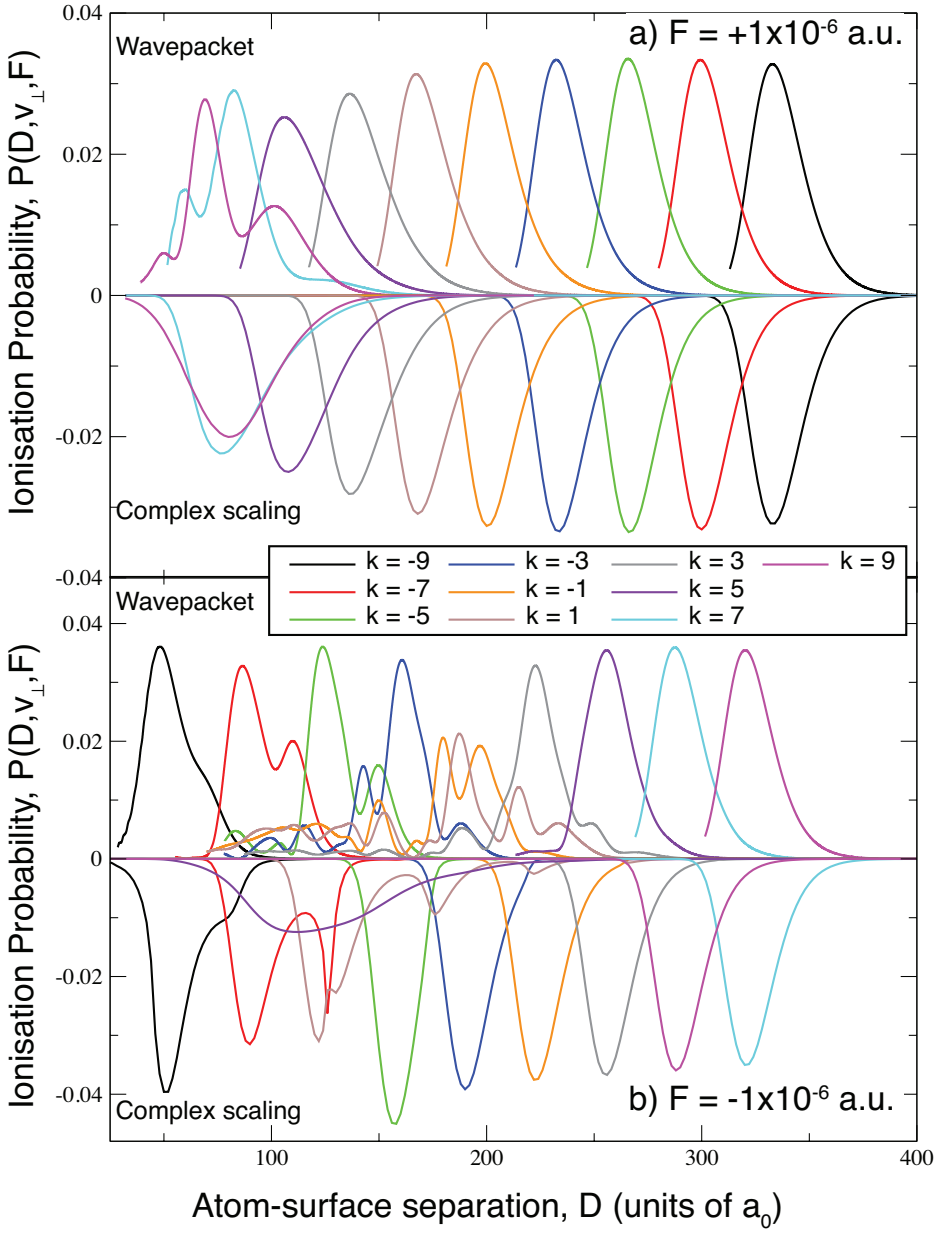

Figure 3.6: Wavepacket propagation (positive axis) and complex scaling (negative axis) ionisation probabilities for the $n = 10$, $m_l = 0$ states of the hydrogen atom approaching a metal surface under an externally applied field of (a) $+1 \times 10^{-6}$ a.u. (ion-extraction) and (b) -1×10^{-6} a.u. (electron-extraction). The collisional velocity of the Rydberg atom is $v_\perp = 3 \times 10^{-4}$ a.u. $\equiv 656$ ms^{-1}.

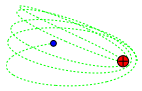

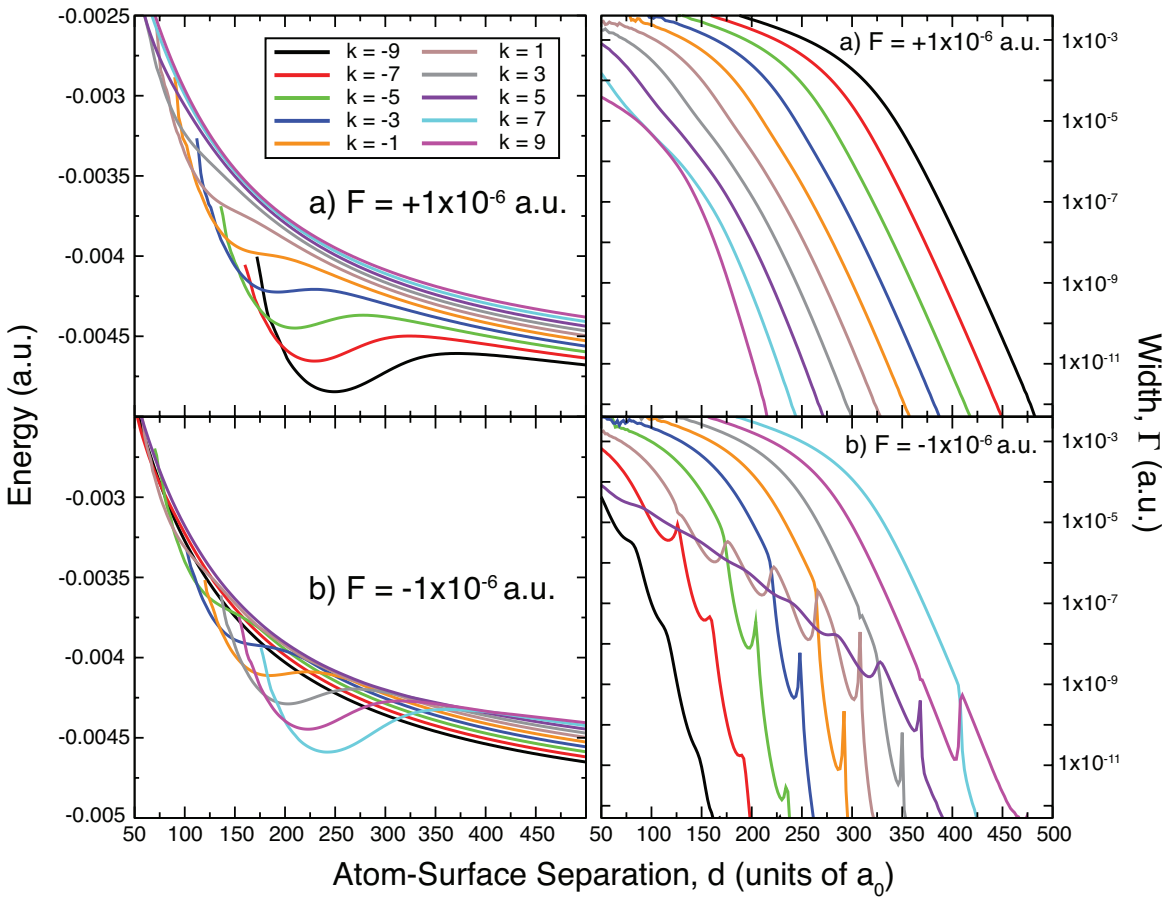

Figure 3.7: Comparison of the energies (left panel) and widths (right panel) of the $n = 10$, $m_l = 0$ hydrogen atom Rydberg states under ion- and electron-extraction fields of (a) $F = +1 \times 10^{-6}$ a.u. and (b) $F = -1 \times 10^{-6}$ a.u. calculated using complex scaling theory.

ergies and lifetimes obtained from the complex scaling calculations. For the 'reversed' electron-extraction field, the polarisations of the Stark wavefunctions with respect to the field axis (which is also the surface normal) are also reversed. Thus, the electron densities of the blue-shifted positive-k states are oriented towards the surface, while the red-shifted negative-k states' are oriented towards the vacuum. This is illustrated by Figure 3.6(b) and Fig. 3.7(b), where the blue-shifted states are now ionised at the greatest distance from the surface and exhibit the largest widths, while the red-shifted states ionise at much shorter distances with significantly smaller level widths.

As explained in Section 3.1, neglecting the state-independent proton–image-proton interaction V_{pp}, surface-oriented states tend to drop in energy when approaching the surface before rising again at close-range, while vacuum-oriented states tend to continuously rise in energy. For the positive ion-extraction field (Fig. 3.7(a)), the higher energy states are initially vacuum-oriented and there is therefore a spreading of the energy levels as the surface is approached, until short distances are reached where all states move up in energy. For the negative-field electron-extraction scheme (Fig. 3.7(b)), the higher-energy states are initially surface-oriented, while the lower-energy states are vacuum-orientated. Thus there is a tendency for the levels to converge and cross as the surface is approached in the electron-extraction scheme. The larger number of possible avoided level crossings that occur in the electron-extraction scheme is illustrated in Fig. 3.7(b), and is the origin of the greater tendency for oscillations in the wavepacket ionisation probability plots for the electron-extraction case compared to the ion-extraction case (see Fig. 3.6).

The higher probability of encountering avoided level crossings as the Rydberg state approaches the surface also leads to more likely non-adiabatic contributions to the ionisation dynamics. Comparing the ionisation probabilities obtained from the wavepacket calculations and the complex scaling calculations in Fig. 3.6 for both directions of the

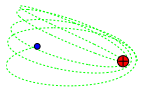

field, show that, while the results of the two approaches are quite similar for the ion-extraction field, there are significant differences in the electron-extraction field, especially for the Rydberg states in the middle of the n-manifold which encounter the largest number of crossings.

Figure 3.8 shows that similar to the ion-extraction fields, the level interactions can be 'suppressed' by increasing the magnitude of the applied electron-extraction field (*c.f.* Fig. 3.4). As the magnitude of the electron-extraction field increases from $F = -1 \times 10^{-6}$ a.u. to -9×10^{-6} a.u., the number of avoided crossings decreases, although some 'kinks' still remain in the level width. The effect of smaller level interaction and decreased number of crossings with increasing field is reflected in the wavepacket propagation results shown in Fig. 3.9, where the ionisation probabilities resemble more of a single-peaked profile as the field increases, and the agreement between the wavepacket and complex scaling results improves.

Figure 3.6 also shows that, for the electron-extraction case, the ionisation curves are collectively shifted to lower atom-surface separations compared to the ion-extraction case. As illustrated by Fig. 2.1, for an increasing ion-extraction field (F positive), the potential barrier on the surface-side of the ion-core becomes lower and thinner, thus enhancing the surface-ionisation process. Figure 3.10 shows that for the electron-extraction scheme (F negative), however, the potential barrier on the surface-side of the core is raised and widened, thus hindering the surface-ionisation process. The effect of this, is also illustrated in Fig. 3.9, where the ionisation probabilities of the surface-oriented states shift to lower atom-surface separations as the magnitude of the electron-extraction field increases. It can be seen from Fig. 3.10 that for the electron-extraction field, the potential barrier on the vacuum-side of the core is lowered. Thus, there is a non-zero probability of surface-induced ionisation involving a 'back-scattered' flux of electrons (with respect to the nuclear trajectory) to occur. The opening of

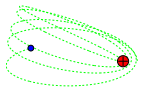

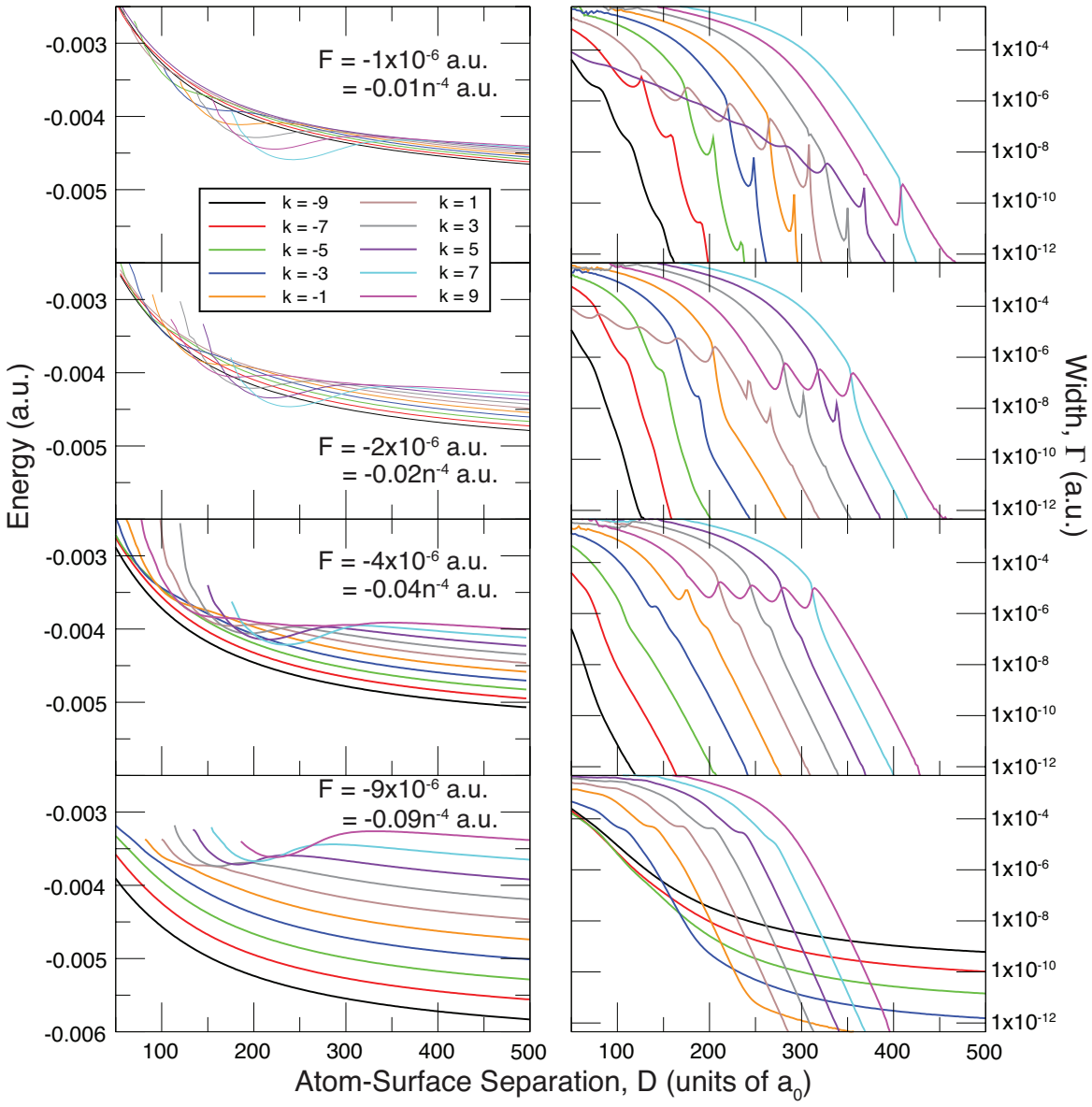

Figure 3.8: Energies (left panel) and widths (right panel) of the $n = 10$, $m_l = 0$ hydrogen Rydberg states under electron-extraction fields of $F = -(1-9) \times 10^{-6}$ a.u. (*c.f.* Fig. 3.4 for the ion-extraction case).

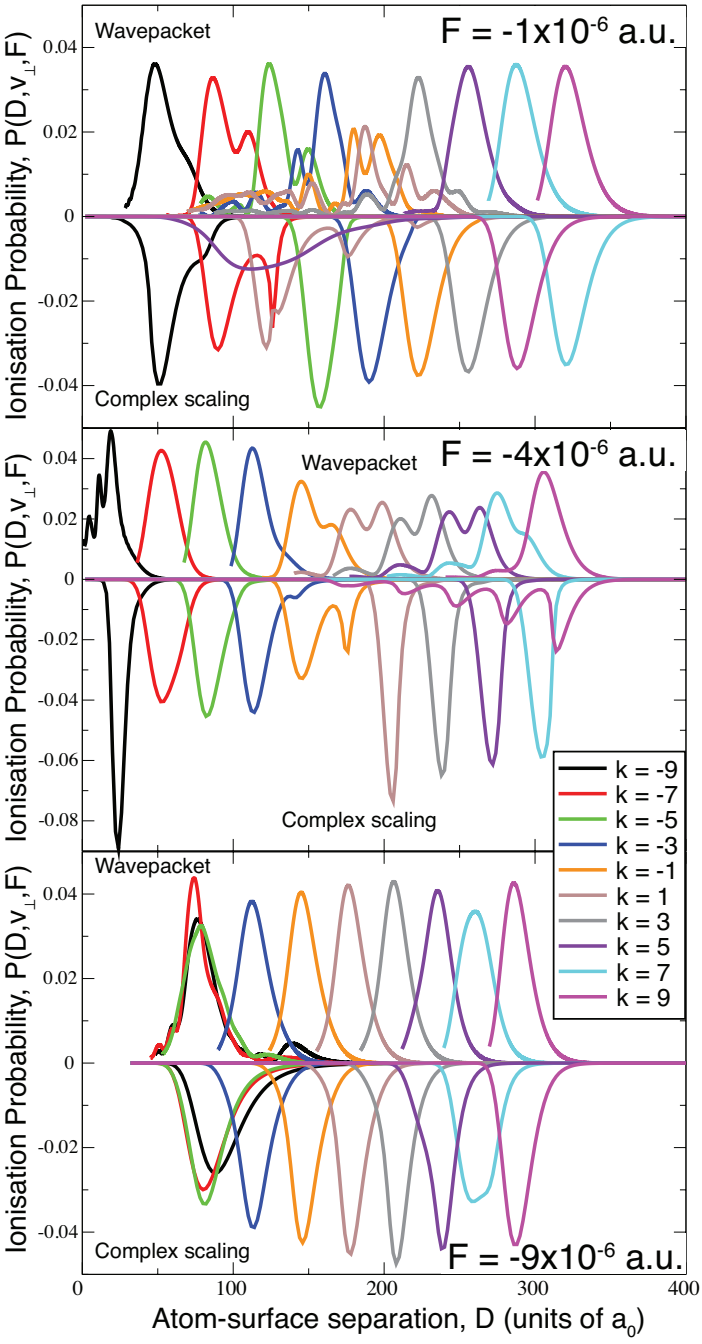

Figure 3.9: Wavepacket propagation (positive axis) and complex scaling (negative axis) ionisation probabilities for the $n = 10$, $m_l = 0$ states of the hydrogen atom approaching a metal surface with the collisional velocity of 3×10^{-4} a.u. and in the presence of electron-extraction fields of $F = -(1-9) \times 10^{-6}$ a.u. (*c.f.* Fig. 3.5 for the ion-extraction case).

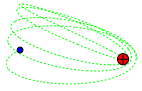

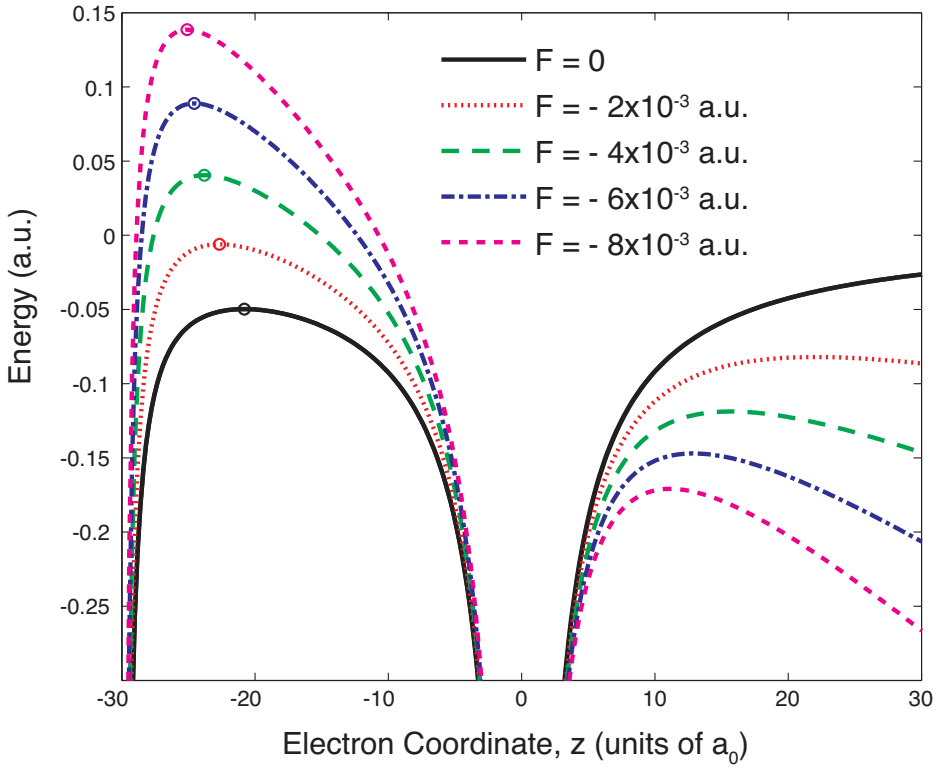

Figure 3.10: Plot of the total one electron potential $V_c + V_{\text{surf}} + V_{\text{field}}$ (Eq. 1.6) at atom-surface separation of $D = 30$ a$_0$, with an electron-extraction field of $\vec{F} = 0, -2 \times 10^{-3}, -4 \times 10^{-3}, -6 \times 10^{-3}$, and -8×10^{-3} a.u.. The saddle point positions and energies calculated by solving Eq. 2.5 are shown as open circles. *c.f.* Fig. 2.1 for the ion-extraction case.

this additional ionisation channel at larger fields explains the earlier ionisation of the most-vacuum oriented states at greater distance for the highest field of -9×10^{-6} a.u. compared with the intermediate field of -4×10^{-6} a.u. in Fig. 3.9.

3.5 Backscattered ionisation under electron-extraction fields

The wavepacket propagation results presented so far, are for the *total* flux of electrons 'escaping' the ion core (into the metal surface or the vacuum), detected by radial flux planes positioned near the edge of the numerical grid. The separate fractions of forward (towards the metal) and backward (towards the vacuum) electron flux can be obtained by integrating over a set of forward ($90° \leq \theta \leq 180°$) and backward ($0° \leq \theta < 90°$) angles (using Eq. 2.57 and Eq. 2.58). The results for a field of $F = -9 \times 10^{-6}$ a.u. are shown in Fig. 3.11 (the backward flux has been plotted on the negative axis). As expected, only the most vacuum-oriented states with electron density near the lowered barrier on the vacuum-side of the core (Fig. 3.10) have a significant fraction of electron density escaping towards the vacuum side.

Figure 3.12 shows the fraction of forward and backward electron flux for the three most-vacuum oriented states of the $n = 10$ manifold ($k = -9, -7, -5$) at various magnitudes of electron-extraction fields. It can be seen that, as the strength of the applied field increases, the fraction of back-scattered electron flux, and the average ionisation distance, increases due to the further lowering of the vacuum-side potential barrier with the increasing field. The lowest field required for which there is a significant contribution of the back-scattered mechanism to the ionisation process increases for progressively less vacuum-oriented states. For the $k = -9, -7, -5$ Stark states, the threshold field for back-scattered electron loss is approximately $-0.04n^4$ a.u., $-0.06n^4$

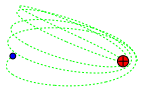

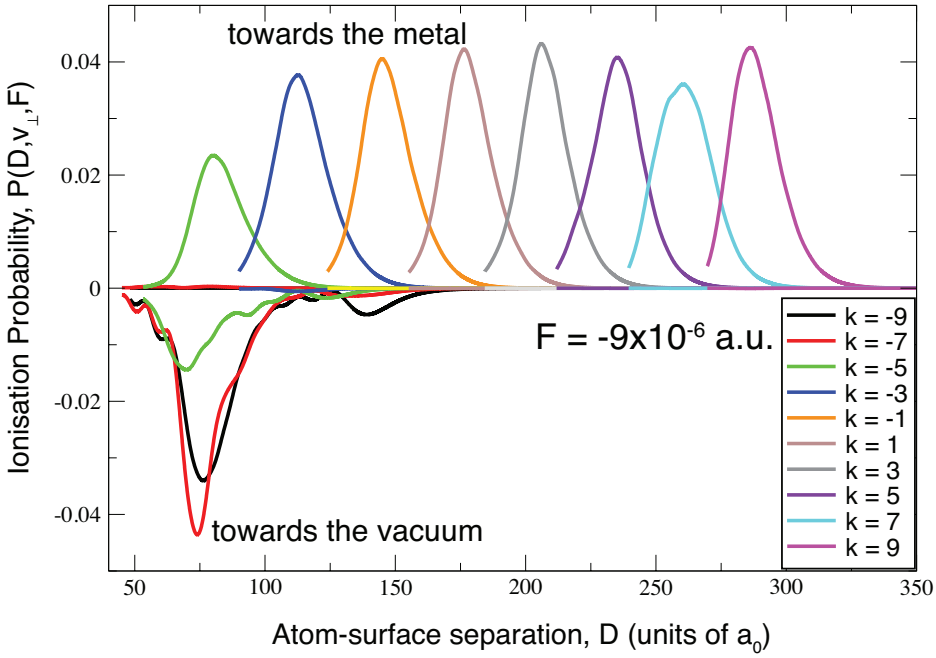

Figure 3.11: The forward- ($\theta > 90°$) and backward- ($\theta < 90°$) electron flux as a function of atom-surface separation for the $n = 10$, $m_l = 0$ hydrogen states colliding with the surface with the collisional velocity of 3×10^{-4} a.u. and in the presence of an electron-extraction field of $F = -9 \times 10^{-6}$ a.u.. The flux measured by the backward flux plane is plotted on the negative axis.

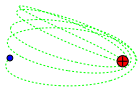

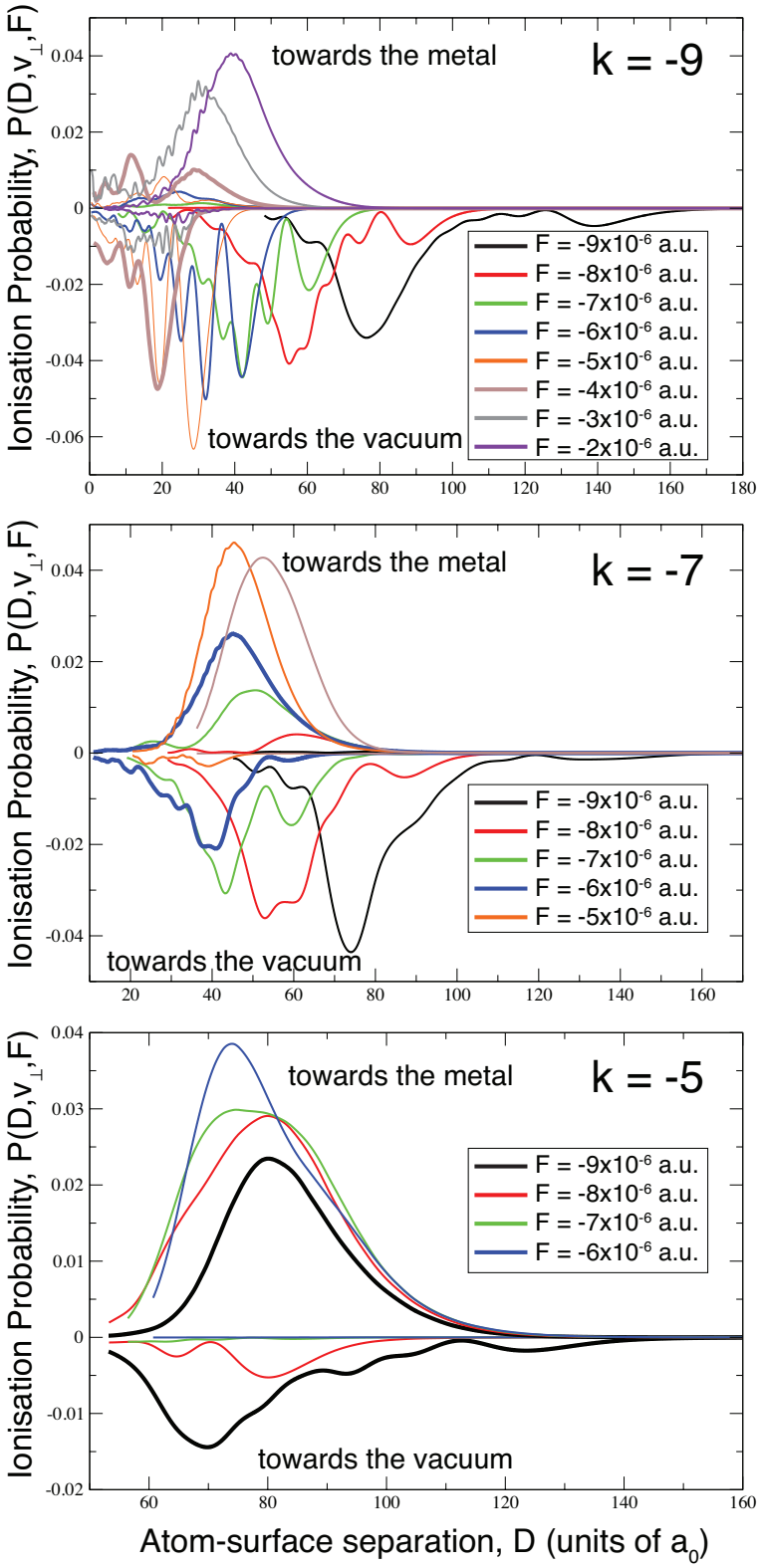

Figure 3.12: The forward- ($\theta > 90°$) and backward- ($\theta < 90°$) electron flux as a function of atom-surface separation for the $k = -9, -7, -5$, $n = 10$, $m_l = 0$ vacuum-oriented H Stark states colliding with the surface with the collisional velocity of 3×10^{-4} a.u. and in the presence of an electron-extraction field of $F = -(2 - 9) \times 10^{-6}$ a.u.. The flux measured by the backward flux plane is plotted on the negative axis.

a.u., and $-0.09n^{-4}$ a.u. respectively.

It is important to note that this back-scattered flux of electrons is a surface process, rather than gas-phase field ionisation. For the field range shown in Fig. 3.12, the system has not undergone the transition from the surface-ionisation regime to the field-ionisation regime. The back-scattering electron flux from the surface is induced by the surface potential, where the repulsive electron–image-proton potential V_{ep} (see Fig. 1.8), essentially 'pushes' the electron over the potential barrier on the vacuum-side of the ion-core.

This additional ionisation channel whereby the electron is lost towards the vacuum, could account for the electron signal that has been detected experimentally for hydrogen *molecules* colliding with a metal surface [64]. But the electron signal was observed for a range of differently polarised Stark states, and also spanned a range of detection fields as large as observed for the positive-ion signal [64]. Considering that experimentally, the ion-signal is observed at a field range of $(0.02 - 005)n^{-4}$ [49, 50]), and the calculations above show that the back-scattered ionisation channel opens at around $0.04n^{-4}$ a.u. for the most extreme red-shifted state, it is feasible that the electrons could come from the backscattered mechanism. Furthermore, as noted at the end of Section 1.6.2, for the hydrogen molecule, surface ionisation occur via transitions (by the perturbing surface field) to degenerate levels belonging to different core rotational states, and as such, the initially prepared orientation of the Rydberg state may not be preserved through its trajectory toward the surface. This 'scrambling' of Rydberg polarisation could allow non-vacuum-oriented states to ionise via the backscattered mechanism, as well as broadening the range of fields at which it can occur. It will be shown in the experimental Section 7.5 that an electron signal can be obtained from the surface ionisation of hydrogen *atoms*. Further discussion on the origin of the electron signal is presented there.

3.6 Electronically structured surfaces: Cu(111) *vs* Cu(100)

So far only a free-electron metal surface (the Jellium mode potential) has been considered, to focus on the effects the Rydberg states and their dynamics. However, an equally important aspect of the charge transfer process is the nature of the surface. The target surface can be physically structured (e.g. a rough surface, a stepped or vicinal surface, a surface with adsorbates) or electronically structured (e.g. band-gap structure, or thin films or adlayers with embedded quantised states). The effects of surface roughness and local surface fields are considered in Section 5.2.

Quantisation effects of a thin metallic film on the charge transfer dynamics of H^- ions (from the negative ion to the metal surface) have been studied previously [79]. A thin metal film can be compared with a quantised 1D well in the dimension perpendicular to the surface, and free (un-quantised) in the dimensions parallel to the surface (thus forming a 2D band), as opposed to a Jellium surface which is free in all dimensions. It was found that when the electronic energy is close to that of a 1D quantised well state, the rate of charge transfer is enhanced by a resonant effect, and the resultant ionisation probability as a function of distance was found to exhibit multiple peaks due to the many quantised thin film states that the atomic energy level passes when approaching the thin film [79]. The observation of a resonance effect close to the 1D quantised level can be explained by the preferential direction of charge transfer, which is along the saddle point z-axis; and so the charge transfer is most efficient when there is minimum transfer of momentum in the direction parallel to the surface (when the Rydberg energy is close to the 1D quantised state). Recent studies of this quantised state resonance effect for the charge transfer of Rydberg H atom at a thin Jellium metal film [80], have shown that, although theoretically this resonance effect is observable,

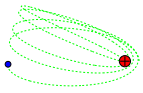

it would be limited to very low principal quantum numbers ($n \sim 2$), and very thin films ($\sim$10 a_0), and would require sub-monolayer control of the film thickness (order of $\sim$0.5 a_0), which is clearly unrealistic experimentally.

A similar quantised state resonance effect has been studied for the charge transfer of H^- ions at a Cu(111) metal surface, but in the context of surface and image states embedded in the projected band-gap [31], rather than quantised 1D well states for the case of thin films. Cu(100) also exhibits surface and image states within the projected metal band-gap, which extend up to the vacuum level (see Fig. 3.13), and it will be of interest to see if such resonance effects can be observed for the charge-transfer of Rydberg H atoms. In this section the effects of electronically structured surfaces are considered for the Rydberg hydrogen atom system, specifically effects of the presence of a projected band-gap, and the resonance effects of embedded surface and image states for the Cu(111) and Cu(100) surfaces.

3.6.1 Surface states and image states

Surface states and image states are closely related, having energies within an energy gap of the band structure in the direction of the surface normal ($\vec{z}$). Their electronic wavefunctions tend to zero towards the bulk metal as well as towards the vacuum ($\Psi \rightarrow 0, z_e \rightarrow \pm\infty$), and they are therefore mainly confined at the metal-vacuum interface.

Intrinsic surface states arise from the cleavage of the bulk metal (translational symmetry perpendicular to the surface is lost), and are localised mainly at the surface atomic layer [81, 82], with wavefunction that decays exponentially towards the vacuum. Image states arise from the Coulomb-like attractive image potential for an electron outside the metal surface ($-\frac{1}{4}(z_e - z_{\rm im})^{-1}$) and the surface barrier created by a gap of available bulk electronic states in the metal. Image states are localised mainly in the vacuum

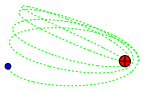

region of the interface (or more precisely, beyond the image plane position z_{im}) [83]. The energies of the image states form a hydrogen-like Rydberg series (setting the usual nuclear charge term Z as 1/4):

$$E_n^{\mathrm{IS}} = -\frac{1}{16} \cdot \frac{1}{2(n+a)^2} \ , \tag{3.1}$$

where n is the image-state index and a is the quantum defect parameter for a given surface (for the Cu(111) and Cu(100) surfaces studied below, a is approximately 0.02 and 0.24 respectively [84, 85]). The corresponding 1D wavefunctions have the form [85]

$$\Psi_n^{\mathrm{IS}}(z_e) = z_e R_{n,l=0}(z_e/4), \tag{3.2}$$

where $R_{n,l=0}(z_e/4)$ is the normalised hydrogenic (s-wave) radial wavefunction. Thus, image states can extend far into the vacuum ($\langle z_e \rangle_n^{\mathrm{IS}} = 6(n+a)^2 \mathrm{a}_0$), and in the context of Rydberg-surface interaction there can be significant overlap with the Rydberg electronic wavefunction. Thus, the resonance effects from image states are expected to be significant, especially when compared with surface states which reside inside the surface.

For an uncorrugated surface, the electron moves quasi-freely parallel to the surface ($\vec{\rho}$), such that each surface state and image state forms a 2D continuum of states with energy

$$E_n^{\mathrm{IS,SS}}(k_\parallel) = E_n^{\mathrm{IS,SS}} + \frac{\boldsymbol{k}_\parallel^2}{2\mu} \ , \tag{3.3}$$

where the second term is the dispersion energy, with electron momentum parallel to the surface $\boldsymbol{k}_\parallel$, and an electron of effective mass $\mu \simeq 1$ [86]. Figure 3.13 shows the projected bulk band structure and the energies of the surface and image states of the Cu(111) and Cu(100) surfaces. Note that the full 3D bulk states are shaded in grey, and the projected band-gap is unshaded. Surface and image states that lie outside the

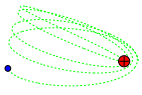

	a_s (a.u.)	A_{10} (eV)	A_1 (eV)	A_2 (eV)	β (a_0^{-1})
Cu(111)	3.94	-11.895	5.14	4.3279	2.9416
Cu(100)	3.415	-11.480	6.10	3.7820	2.5390

Table 3.1: Values of the parameters used in the one-electron pseudo-potential given by Eq. 3.4 for the Cu(111) and Cu(100) surface [84].

energy gap, and are degenerate with the 3D bulk continuum, are commonly referred to as surface and image resonances (rather than 'states').

3.6.2 One-electron pseudo-potential

Following the work of references [31, 85, 86, 88], the one-electron pseudo-potential of Chulkov *et al.* [84] is used to model the Cu(111) and Cu(100) surfaces in the direction normal to the surface ($\vec{z}$), while the electron is allowed to move freely in the direction parallel to the surface ($\vec{\rho}$). The potential has the analytical form:

$$\begin{aligned}
V_{ee}(z_e) &= V_1(z_e) + V_2(z_e) + V_3(z_e) + V_4(z_e) \\
V_1(z_e) &= A_{10} + A_1 \cos\left(\tfrac{2\pi}{a_s} z_e\right) && z_e < 0 \\
V_2(z_e) &= -A_{20} + A_2 \cos[\beta(z_e)] && 0 < z_e < z_1 \\
V_3(z_e) &= A_3 \exp[-\alpha(z_e - z_1)] && z_1 < z_e < z_{\mathrm{im}} \\
V_4(z_e) &= \tfrac{\exp[-\lambda(z_e - z_{\mathrm{im}})] - 1}{4(z_e - z_{\mathrm{im}})} && z_{\mathrm{im}} < z_e \ ,
\end{aligned} \tag{3.4}$$

where a_s is the bulk interlayer spacing, A_{10}, A_1, A_2 and β are the independent model potential parameters, and the values for the Cu(111) and Cu(100) surfaces are given in Table 3.1. The remaining parameters in Eq. 3.4 are determined by requiring the potential and its first derivative to be continuous:

$$\begin{aligned}
A_{20} &= A_2 - A_{10} - A_1 & \qquad A_3 &= -A_{20} - \tfrac{A_2}{\sqrt{2}} \\
z_1 &= \tfrac{5\pi}{4\beta} & \qquad \alpha &= \tfrac{A_2 \beta}{A_3} \sin(z_1 \beta) \\
\lambda &= 2\alpha & \qquad z_{\mathrm{im}} &= z_1 - \tfrac{1}{\alpha} \ln\left(\tfrac{-\alpha}{2A_3}\right) .
\end{aligned} \tag{3.5}$$

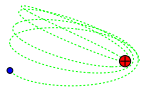

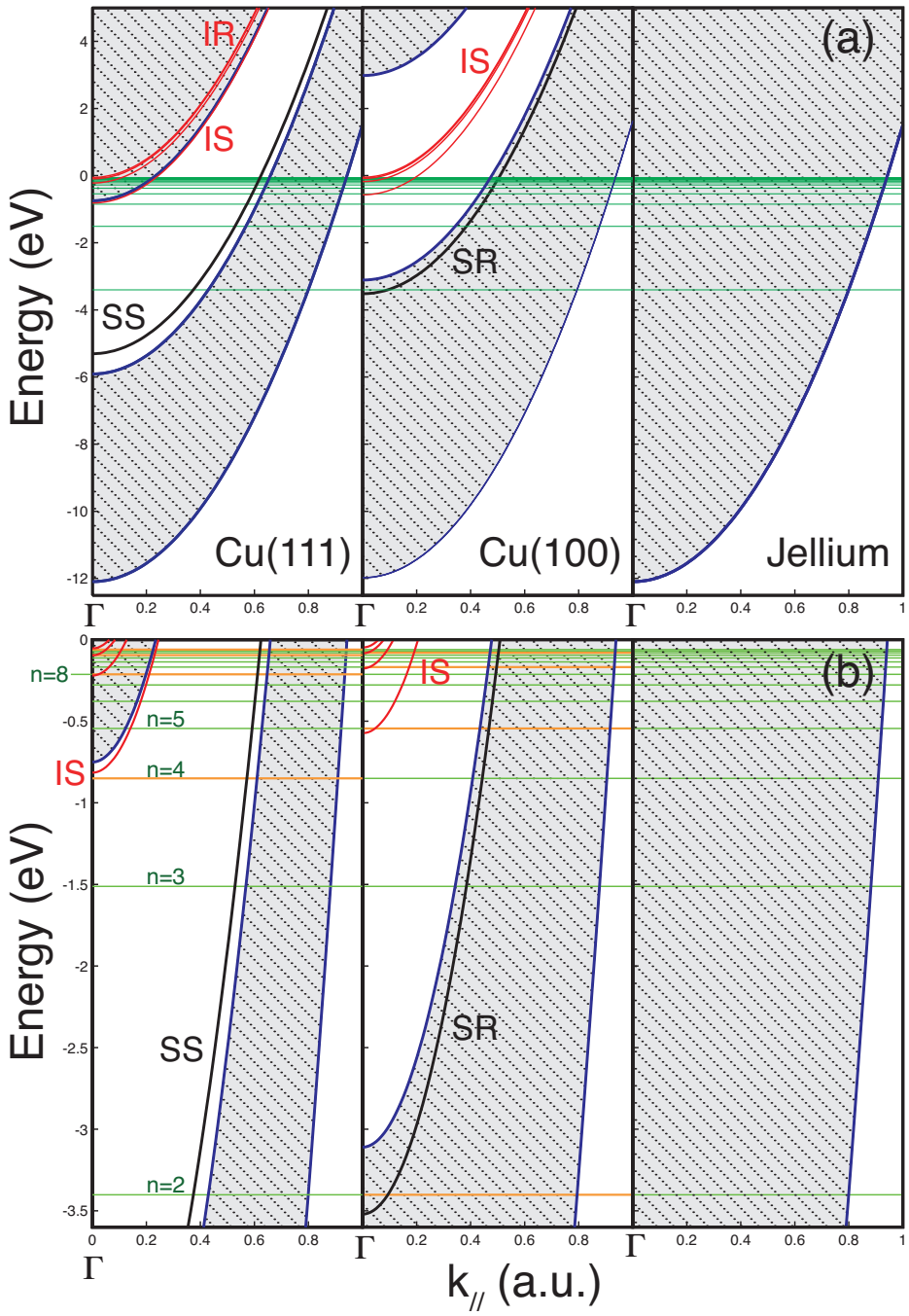

Figure 3.13: (a) Energy of the electronic states in the model Cu(111), Cu(100) and free electron Jellium surface, as a function of electron momentum parallel to the surface, $k_{\|}$. The 3D bulk states are hatched and shaded in grey, the surface state (SS) and surface resonance (SR) are plotted as full black lines, image states (IS) and image resonance (IR) are plotted as full red lines, and the H atom Rydberg energies ($0.5/n^2$ a.u.) are shown as green horizontal lines. (b) is the same as (a) but expanded in the Rydberg energy range. Rydberg levels close to a surface- or image-state or resonance are coloured orange. The gamma point $\bar{\Gamma}$ at $k_{\|} = 0$ is also marked. The diagrams are based on those from Ref. [87].

The bulk potential and the width and position of the energy gap is described by V_1 in Eq. 3.4, while the metal-vacuum interpolation potential and the energies of the surface and image states are described by V_2 and V_3, with the V_4 term describing the long range image-potential. The form of the Cu(111) and Cu(100) pseudo-potential, and the energies and wavefunctions of the surface state and image states calculated from diagonalisation of the 1D potential are shown in Fig. 3.14.

3.6.3 Resonant charge transfer to surface states and image states

It should be noted that the computation of the wavepacket propagation for the electronically structured Cu(111) and Cu(100) surfaces is much more demanding than the Jellium surface. This is due to the periodic nature of the pseudo-potential inside the metal, which requires a large number of radial grid points, and the large components of the electron momentum parallel to the surface (see below), which requires a large angular momentum basis. Typically for the calculations carried out below, the numerical grid consists of $\sim 1000 \times 200$ (radial $\times$ angular) grid points. Even so, for the charge transfers that are restricted by the band-gap and un-aided by the resonance effects of surface or image states (see below), it is found that high frequency oscillations are superimposed on the ionisation probability profiles, and an increase of radial and angular points would alter the *form* of the profiles. However, it was found that for the results presented below, the calculations are 'sufficiently' converged that the average ionisation distance, and the range of atom-surface separations spanned by the ionisation probability profiles, do not change significantly with a larger radial or angular basis, and so are acceptable for the qualitative comparison carried out below. Furthermore, it is shown below that resonance charge transfer to band-gap embedded surface and image states can be observed directly from 'snapshots' of the

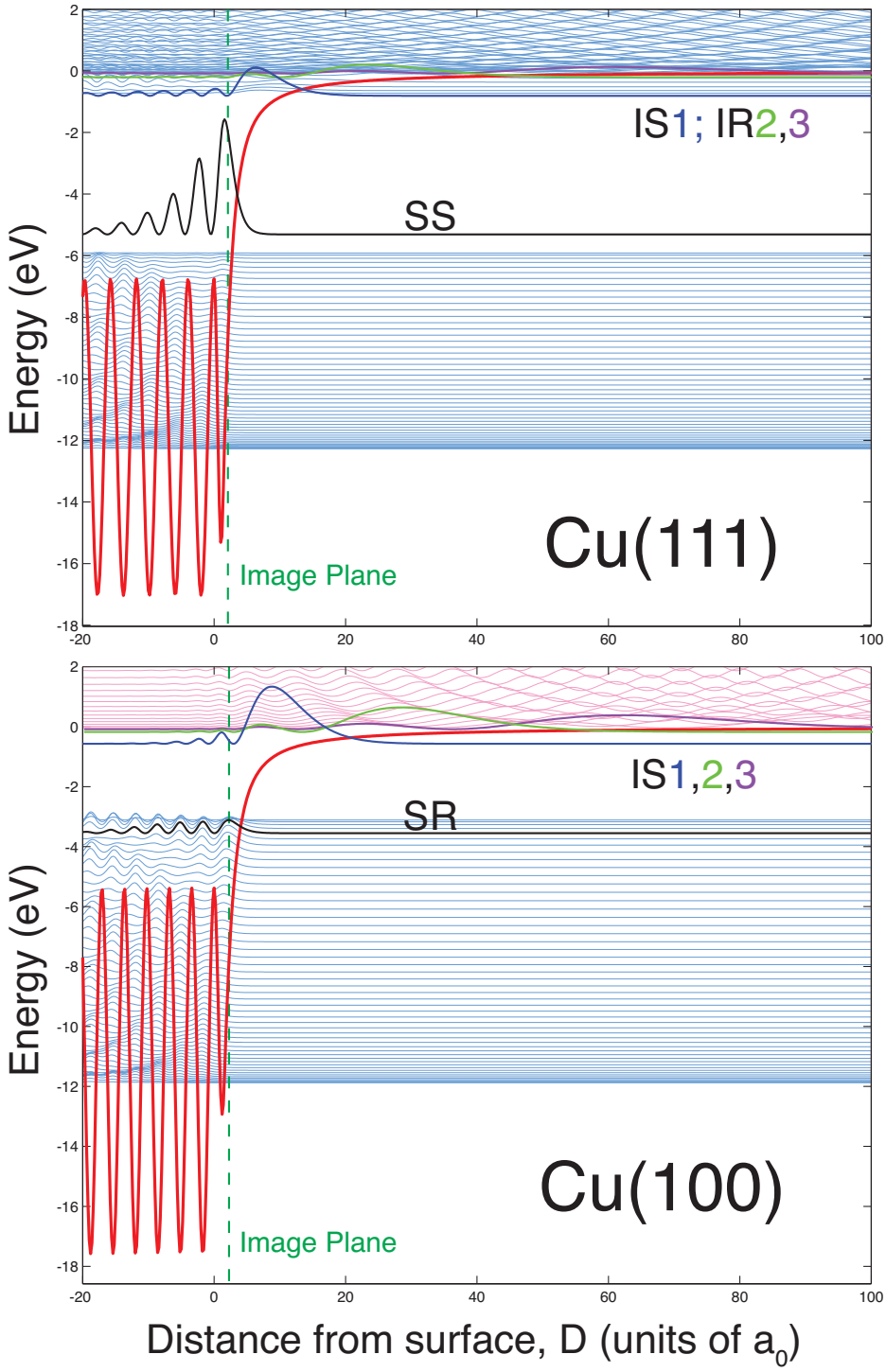

Figure 3.14: Energies and wavefunctions of the bulk, surface and image states for the Cu(111) and Cu(100) surface, calculated from the diagonalisation of the 1D pseudopotential given by Eq. 3.4 with a Sinc DVR basis [69]. The energies and wavefunctions are the eigenvalues and eigenvectors respectively obtained from the matrix diagonalisation. SS, SR, IS, IR labels the surface state, surface resonance, image state and image resonance respectively.

wavepacket propagation, confirming that the different onset of ionisation distances is not an artefact of the un-converged calculations.

To focus on the resonance effects of the band-gap embedded surface states and image states only the zero-field case and the most surface-oriented state of the n-manifold (largest overlap with the surface) is considered below. The energies of the unperturbed H atom states are shown in Fig. 3.13 as horizontal lines to compare with the energies of Jellium, Cu(111) and Cu(100) electronic states. The values of the energies are tabulated in Figure 3.15 to provide a more quantitative comparison. Figure 3.16 shows a comparison of the $m_l = 0$, $n = 2-8$ wavepacket propagation ionisation probabilities calculated for a Jellium, Cu(111) and Cu(100) model potential.

Figure 3.16 shows that for $n = 2$, the charge transfer occurs in the order of distance from the surface (with the greatest distance first): Cu(100), Jellium and Cu(111). Figure 3.17(a) shows a 'snapshot' of the wavepacket calculation for the three different surfaces. The Rydberg energy level is nearly degenerate with the surface resonance of the Cu(100) surface at $\boldsymbol{k}_{\parallel} = 0$ ($\bar{\Gamma}$ point, see Fig. 3.13 and Fig. 3.15), and so efficient charge transfer to the 3D bulk states can occur via the surface resonance with little momentum transfer parallel to the surface (the effect is so large that the charge transfer is even more efficient than for the Jellium surface). For the Cu(111) surface, the $n = 2$ Rydberg energy is in the energy gap at $\boldsymbol{k}_{\parallel} = 0$, and so charge transfer to the surface state or the 3D bulk states can only occur with large $\boldsymbol{k}_{\parallel}$ component, which is inefficient since the dominant and preferential charge transfer axis is along $\vec{z}$ where the saddle point lies.

Figure 3.16 shows that for $n = 3$, the charge transfer occurs much closer to the metal surface for the copper surfaces compared with the Jellium. This is because the Rydberg energy level is in the energy gap of both Cu(111) and Cu(100) surfaces at the $\bar{\Gamma}$ point

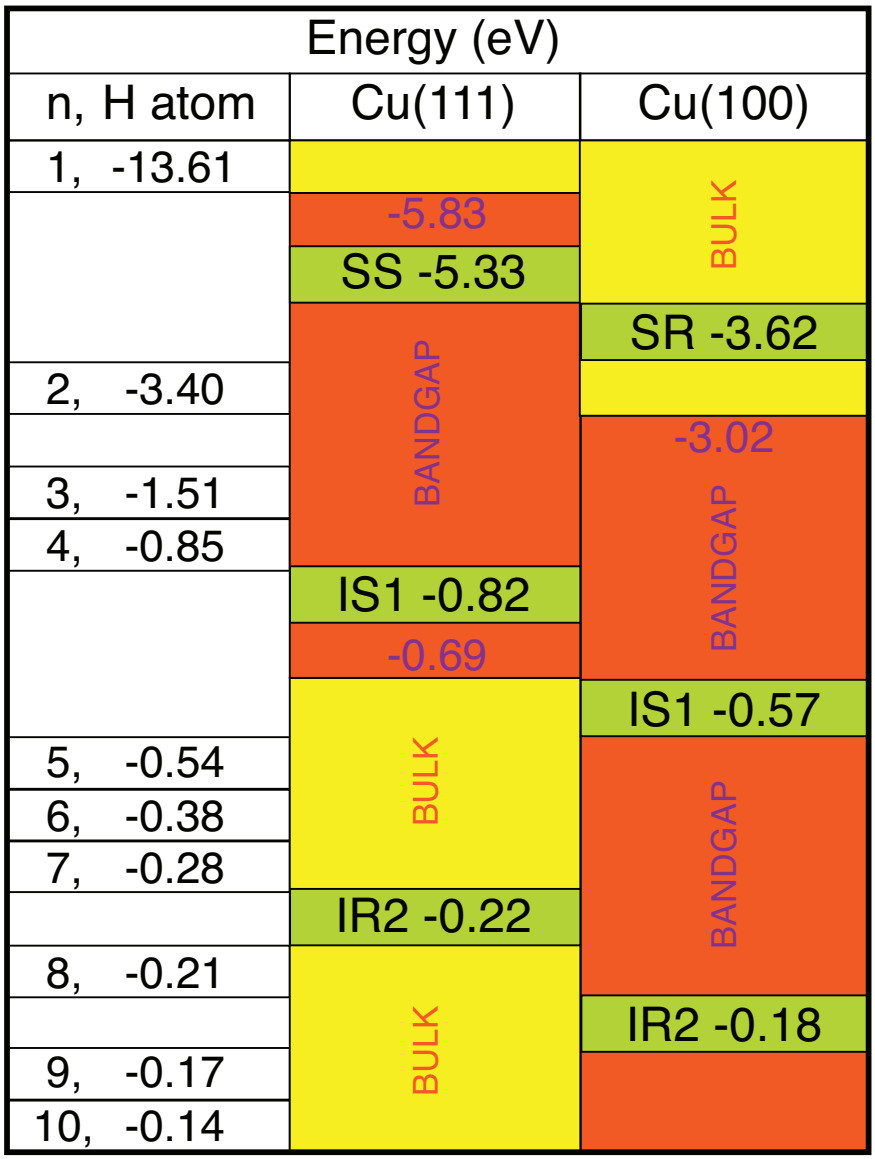

Figure 3.15: Table of energies of the energy gap, surface and image states or resonances for the Cu(111) and Cu(100) surface at the gamma point $\bar{\Gamma}$ ($k_{\|} = 0$), compared with those of the Rydberg states of the hydrogen atom.

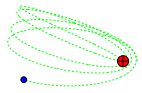

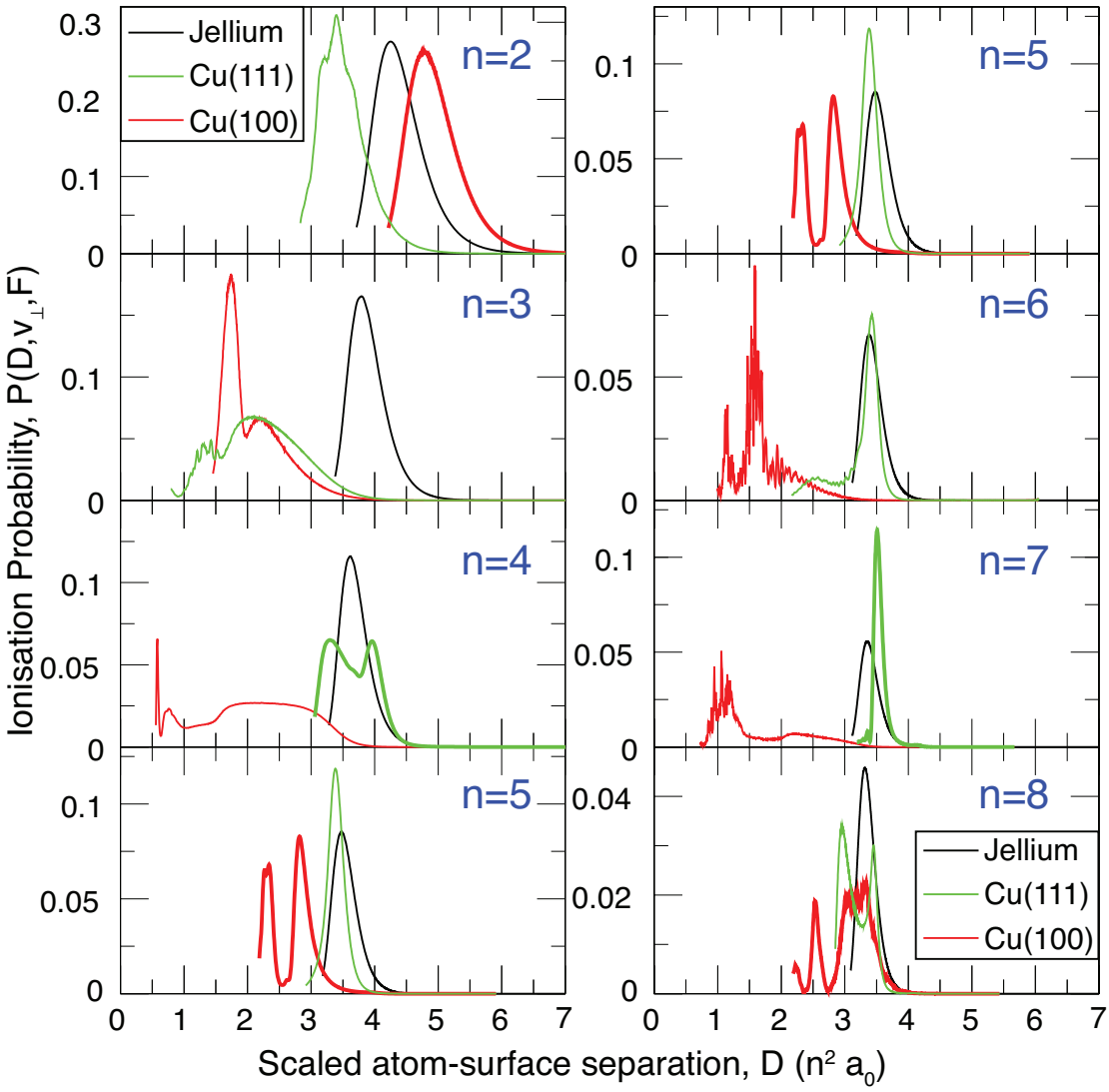

Figure 3.16: Ionisation probabilities as a function of *scaled* atom-surface separation for the $n = 2-8$ most surface-oriented Rydberg states calculated from the wavepacket propagation approach for a Jellium, Cu(111) and Cu(100) model potential. Note that the $n = 5$ ionisation probabilities are plotted twice to aid the comparison of the scaled ionisation distances for each column. Rydberg states that are close to resonance with the surface or image states of Cu(111) and Cu(100) surfaces are shown in bold.

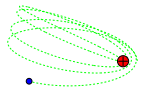

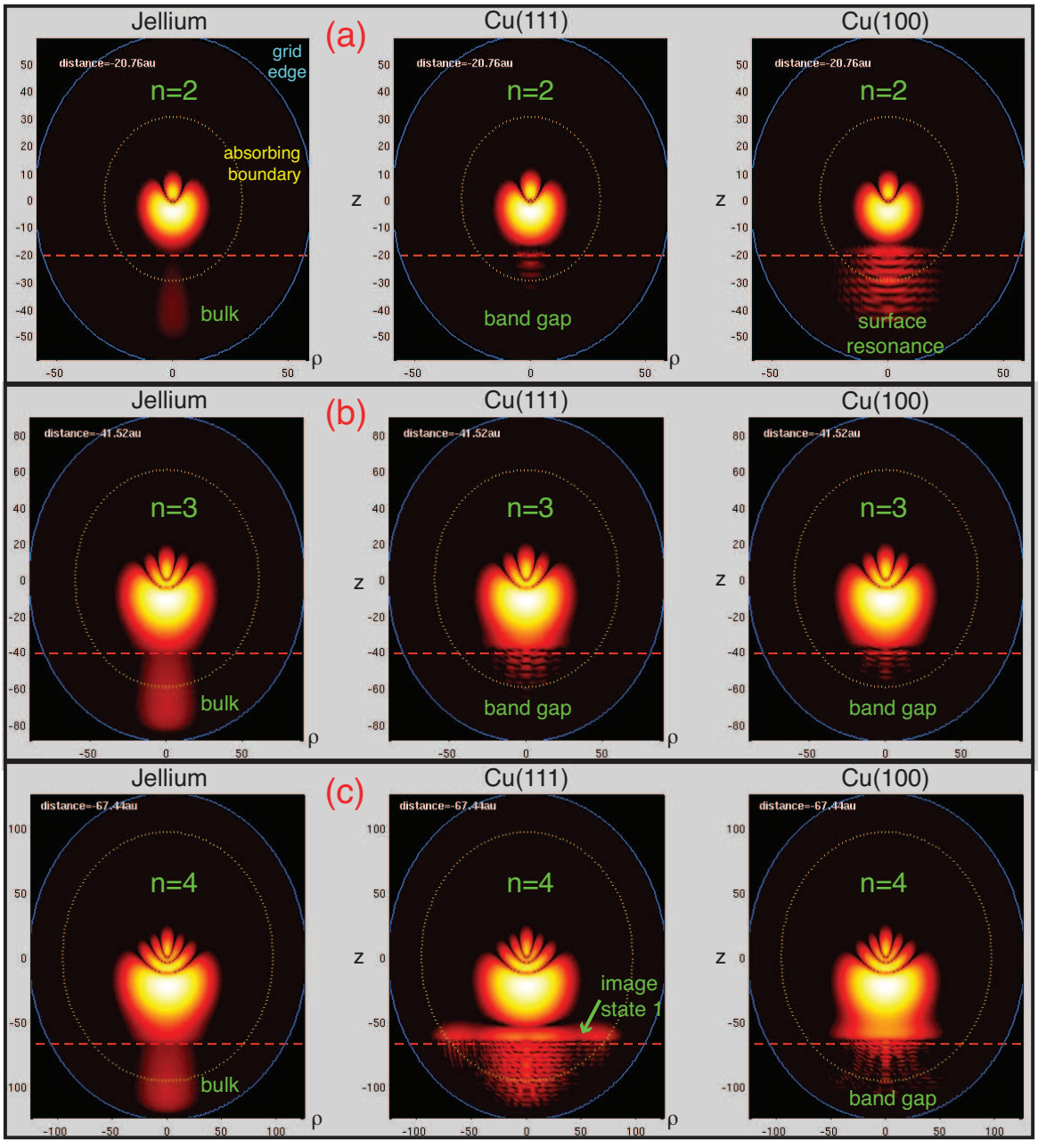

Figure 3.17: Snapshot of the electronic wavefunction, $|\Psi(\mathbf{r};t)|^2$, during the wavepacket propagation calculation for the Jellium potential (left panels), Cu(111) potential (middle panels) and Cu(100) potential (right panels) for the (a) $n = 2$, (b) $n = 3$ and (c) $n = 4$ Rydberg states.

(see Fig. 3.13 and Fig. 3.15), and so charge transfer occurs relatively inefficiently with non-negligible $\boldsymbol{k}_{\parallel}$ components.

Figure 3.16 shows that for $n = 4$, the charge transfer distances for the Cu(111) and Jellium surfaces are similar, while it is much smaller for Cu(100) surfaces. Figure 3.17(c) shows a 'snapshot' of the wavepacket calculation for the three different surfaces. The Rydberg energy level is nearly degenerate with the image state of the Cu(111) surface, and so charge transfer can occur via the population of the image state, which can be clearly seen from the 'snapshot' in Fig. 3.17(c). For the Cu(100) surface, the Rydberg energy is within the band-gap and so charge transfer is inefficient.

Above $n = 4$ the Rydberg energies are above the upper edge of the projected band-gap of the Cu(111) surface, and are degenerate with the 3D bulk states (see Fig. 3.13 and Fig. 3.15), and so the ionisation distance is similar to the Jellium model (although resonant transfer to image resonances can still be observed by studying the evolution of the electronic wavefunction, see below).

For $n = 5$, the Rydberg energy is nearly degenerate with the first image state of the Cu(100) surface (see Fig. 3.13 and Fig. 3.15), and the population of this image state in the charge transfer process can be clearly seen in the 'snapshot' of the wavepacket propagation shown in Fig. 3.18(a). The resonance charge transfer to the image state results in a similar ionisation distance to the Cu(111) and Jellium model surface. This resonance effect to the first image state of Cu(100) is 'lost' for $n = 6$ and 7, which involves a large $\boldsymbol{k}_{\parallel}$ transfer, and so the ionisation distance becomes progressively smaller than the Cu(111) and Jellium surface.

For the Cu(111) surface, ionisation of the $n = 7$ Rydberg state via the close-in-energy image state resonance (see Fig. 3.13 and Fig. 3.15) can be observed in Fig. 3.18(b). In fact, the effect of the image state resonance is so large that the charge transfer is at

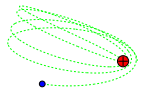

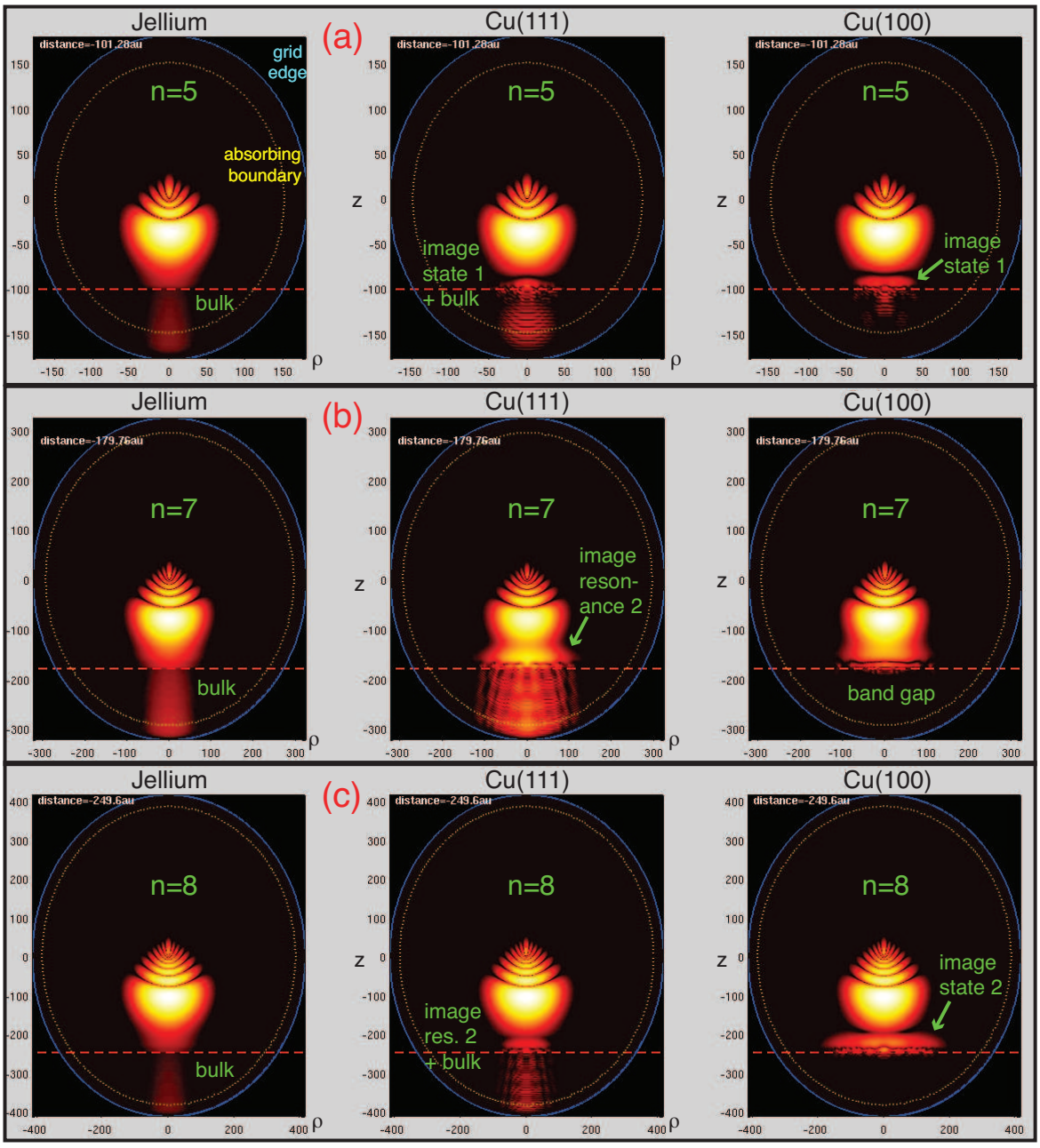

Figure 3.18: Snapshot of the electronic wavefunction, $|\Psi(\mathbf{r};t)|^2$, during wavepacket propagation calculation for the Jellium potential (left panels), Cu(111) potential (middle panels) and Cu(100) potential (right panels) for the (a) $n = 5$, (b) $n = 7$ and (c) $n = 8$ Rydberg states.

slightly larger distances than the Jellium surface (Fig. 3.16).

For the Cu(100) surface, the $n = 8$ Rydberg energy is close in energy with the second image state embedded in the projected band-gap (see Fig. 3.13 and Fig. 3.15). The population of the second image states is illustrated in Fig. 3.18(c), and the resonance effect is reflected in the ionisation probability shown in Fig. 3.16 (the ionisation distance is similar to the Cu(111) and Jellium model surface).

It is shown from the results above, that the resonance charge transfer of the Rydberg electron to surface and image states embedded in the projected energy gap has a strong effect on the ionisation dynamics and the atom-surface separations at which the ionisation occurs. For the Cu(100) surface, the projected band-gap extends to above the vacuum level (upper edge is at +2.98 eV), and exhibits a Rydberg series of image states that can be described by Eq. 3.1 with a quantum defect of $a = 0.24$ (and a pre-factor of 1/15.93 instead of 1/16) [85]. Thus, resonance effects are expected to play an important role in the charge transfer dynamics even for the experimental range of principal quantum numbers of $n = 20 - 40$ (see Section 7.7).

3.7 Mean-field effects on nuclear trajectory

The wavepacket propagation results presented so far have been calculated under the assumption that the ion-core is moving at a constant velocity (the initial collisional velocity). This constant velocity assumption is applied as a first approximation to examine the qualitative effects of various experimental variables on the Rydberg hydrogen ionisation dynamics. However, the constant-velocity approximation may not be strictly valid for very light atoms (such as the hydrogen atom), and at very low velocities (such as those of the typical Rydberg-surface grazing collision experiments, $v_\perp \approx 10^{-4}$ a.u.$\simeq 10^2$ ms^{-2}), where the trajectory of ion-core is susceptible to the forces

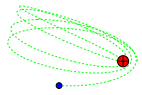

from the Rydberg electron and its image charge, the image charge of the ion-core, and the externally applied electric field.

For a full description of the dynamics of the Rydberg electron *and* the ion-core, the coupling between the two systems needs to be correctly included. The validity of the constant velocity approximation can be evaluated by carrying out mean-field calculations [89]. The expectation value of the electronic Hamiltonian (*i.e.* the mean-field potential) is calculated 'on the fly', such that the force on the ion core is given by

$$\begin{aligned} M\ddot{D} &= -\left\langle \Psi_{el}(\mathbf{r};t) \left| \frac{d\hat{H}_{el}(\mathbf{r};t)}{dD} \right| \Psi_{el}(\mathbf{r};t) \right\rangle - \frac{1}{4D^2} + F \\ &= -\left\langle \Psi_{el}(\mathbf{r};t) \left| \frac{d[\hat{V}_{\rm surf}(z,\rho;t) + FD]}{dD} \right| \Psi_{el}(\mathbf{r};t) \right\rangle - \frac{1}{4D^2} + F \\ &= -\left\langle \Psi_{el}(\mathbf{r};t) \left| \frac{d\hat{V}_{\rm surf}(z,\rho;t)}{dD} + F \right| \Psi_{el}(\mathbf{r};t) \right\rangle - \frac{1}{4D^2} + F, \end{aligned} \tag{3.6}$$

where M is the proton mass, $\hat{H}_{el}(\mathbf{r};t)$ is the electronic Hamiltonian as given by Eq. 2.35, but with the electron independent terms taken out explicitly; *i.e.*, the proton–image-proton term $V_{pp} = -1/(4D)$, and the proton's field potential $V^p_{\rm field} = -FD$. The time- (or distance-) dependent surface potential $\hat{V}_{\rm surf}(z,\rho;D)$ is given by Eq. 1.7 and Eq. 1.9. $\Psi_{el}(\mathbf{r};t)$ is the time- (or distance-) dependent electronic wavefunction in the moving atom-core frame, and is given by

$$\Psi_{el}(\mathbf{r};t+\Delta t) = e^{-i([\dot{D}(t+\Delta t)-\dot{D}(t)]z)} e^{-i\hat{\tilde{H}}_{el}(\mathbf{r};t)\Delta t} \Psi_{el}(\mathbf{r};t). \tag{3.7}$$

The additional phase term (the first term on the left hand side of Eq. 3.7) is the consequence of the Galilean transformation in an accelerating atomic frame [90]. On carrying out the calculations it was found that the introduction of this electronic phase term has negligible effect.

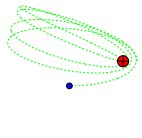

The electronic dynamics are treated quantum mechanically as before. The motion of the ion core under the mean-field given by Eq. 3.6 is treated classically, and is propagated using a velocity Verlet algorithm

$$\begin{aligned} D(t+\Delta t) &= D(t) + \dot{D}(t)\Delta t + \frac{1}{2}\ddot{D}(t)\Delta t^2 \\ \dot{D}(t+\Delta t/2) &= \dot{D}(t) + \frac{1}{2}\ddot{D}(t)\Delta t \\ \ddot{D}(t+\Delta t) &= [\text{ Eq. 3.6 }]/M \\ \dot{D}(t+\Delta t) &= \dot{D}(t+\Delta t/2) + \frac{1}{2}\ddot{D}(t+\Delta t)\Delta t \ . \end{aligned} \tag{3.8}$$

with initial conditions $\ddot{D}(t=0) = 0, \dot{D}(t=0) = v'_\perp(D_0)$ and $D = D_0$ (see Section 2.3). The velocity $v'_\perp(D_0)$ at the initial propagation distance D_0 from the surface is corrected from the velocity at infinite distance $v_\perp$, by the Rydberg energy shift at distance D_0 from the surface:

$$v'_\perp(D_0) = -\sqrt{v_\perp^2 - \frac{2}{1836}\cdot\left(E^{\text{Ryd}}_{nm_lk}(D_0,F) - E^{\text{Stark}}_{nm_lk}(F)\right)} \ , \tag{3.9}$$

where $E^{\text{Ryd}}_{nm_lk}(D_0,F)$ is the energy of the Stark state at a distance D_0 from the metal surface, calculated from the initial diagonalisation step (see Section 2.3), and $E^{\text{Stark}}_{nm_lk}(F)$ is the Stark energy given by Eq. 1.3. This takes into account the acceleration (or deceleration) of the Stark states as the potential energy changes with the distance from the surface.

Figure 3.19 presents a comparison of the results of the mean-field calculation with the constant-velocity calculations for various $n = 10$ hydrogen atom Rydberg states at a typical threshold ion-extraction field of $F = +4 \times 10^{-6}$ a.u. (see Section 2.1), and with an *initial* collisional velocity (at infinite distance) of $v_\perp = -3 \times 10^{-4}$ a.u.. Figure 3.20 shows the calculated velocity of the Rydberg atom as a function of distance from the metal surface. It can be seen that the inclusion of mean-field effects results

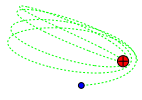

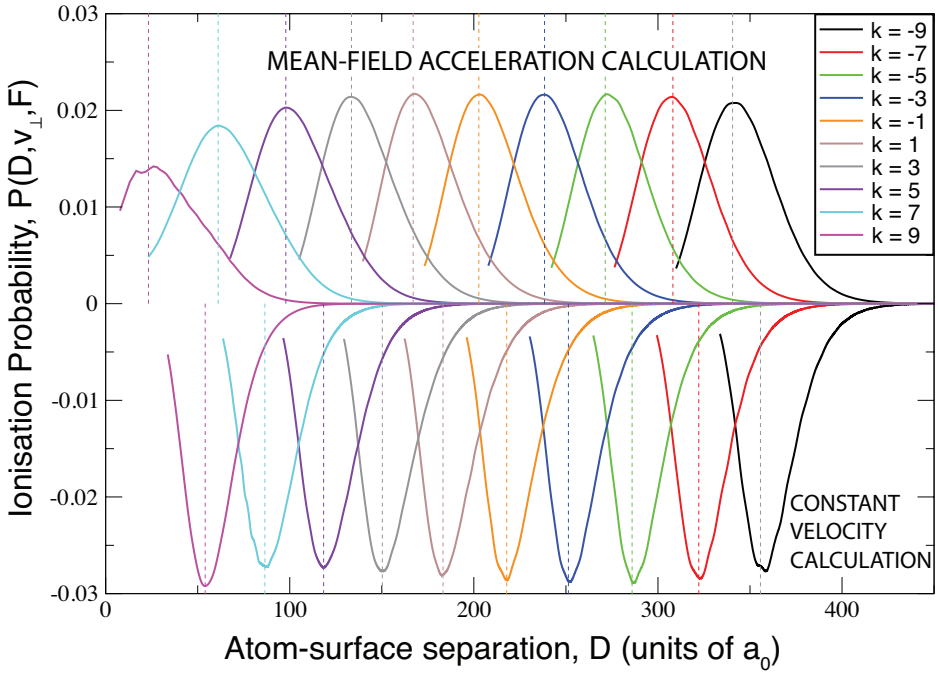

Figure 3.19: Comparison of the wavepacket results for various $n = 10$ hydrogen atom Rydberg states obtained using the constant velocity approximation (negative axis) with results obtained with the ion-core moving under the mean-field of the Rydberg electron and its image charge (positive axis). The magnitude of the extraction field is $F = +4 \times 10^{-6}$ a.u., and the *initial* collisional velocities are $v_\perp = -3 \times 10^{-4}$ a.u. (see Fig. 3.20).

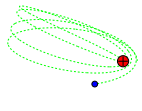

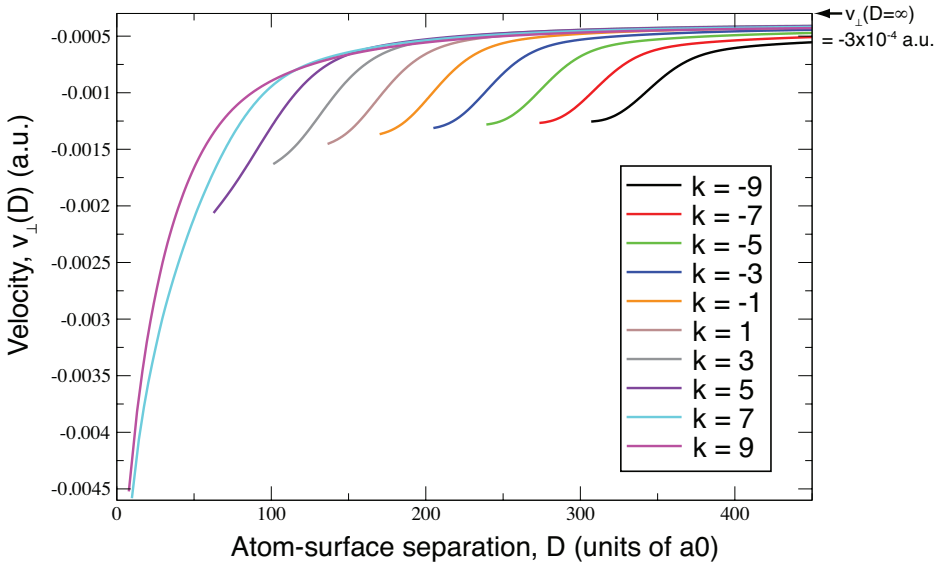

Figure 3.20: The velocity of the various $n = 10$ Rydberg states calculated from the mean-field wavepacket calculation presented in Fig. 3.19. Note that the initial velocity at infinite distance is $v_\perp = 3 \times 10^{-4}$ a.u..

in the acceleration of the ion-core as the surface is approached. At long range, this acceleration follows the Van der Waals attractive interaction of the neutral Rydberg atom (see Section 2.1) , but increases rapidly as the Rydberg electron is lost to the metal surface. The form the of acceleration generally follows the ionisation probability: the larger the change in population per unit distance, the larger the change in the ion-core velocity. This is because the *electronic* energy of the Rydberg levels generally increases ($\simeq +1/(4D) - 5n^4/(16D^3)$, see Eq. 2.2) with decreasing atom-surface separations (as shown by the complex-scaling results in Section 3.1), which nearly cancels the proton–image-proton attraction ($-1/(4D)$). But as the overall electron population of the Rydberg state decreases, the proton effectively becomes less shielded from its image-charge, and it accelerates towards the surface. A further contribution to the acceleration comes from the attraction of the ion-core to the departing electron density, which effectively draws the ion towards the metal surface. As a result of the ion-core acceleration, all the ionisation probability curves shown in Fig. 3.19 are shifted and

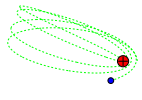

broadened towards lower atom-surface separations with respect to the constant velocity result (*i.e.*, surface ionisation occurs closer to the surface, and with a broader range of distances). As expected, the Rydberg states which ionise closest to the surface have the largest final velocity toward to the surface (Fig. 3.20), since they interact with the accelerating mean-fields for longer, and with a stronger image-charge field at closer range. For the most surface-oriented state which ionises furthest from the surface, the ionisation probabilities are shifted by $\sim 0.2n^2$ a_0 closer to the surface, and the final ion velocities are approximately four times the initial collisional velocity. For the most vacuum-oriented state, the ionisation probabilities are shifted by $\sim 0.4n^2$ a_0 closer to the surface, and the final ion velocity is approximately an order of magnitude greater than the initial velocity. This increase in the ion collisional velocity will have a strong effect on the ion-detection probability and is discussed in more detail in Section 5.1.

Although the ionisation distances obtained from the mean-field wavepacket calculation differ from the constant velocity approximation results, the *qualitative* findings on the effects of the Rydberg dimension and polarisation, the Rydberg collisional velocity, the magnitude and direction of the applied field, and the electronic structure of the metal substrate presented in the sections above are general and remain valid for both accelerating and constant-velocity frames. However, it appears that in order to *quantitatively* compare the calculations with the experimental results, inclusion of ion-acceleration effects is required.

3.8 Conclusions

For a Rydberg hydrogen atom approaching a metal surface with a typical collisional velocity of $v_\perp \sim 10^{-4}$ a.u. or $\sim 10^2$ ms^{-1}, the classical over-the-barrier approach predicts a surface ionisation distance which scales with the size of the Rydberg orbital: $(3.5-5)n^2$ a_0 (including the effects of the Rydberg energy shift as it approaches the

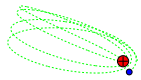

metal surface, and of its incident kinetic energy), with a corresponding threshold ion-detection field of $\approx (0.02 - 0.08)n^{-4}$.

By carrying out time-independent complex scaling calculations and time-dependent wavepacket propagation calculations, it is found that distance at which charge transfer occurs does not solely depend on the Rydberg dimensions, but it also varies strongly with the polarisation of the electronic wavefunction, the collisional velocity, the direction and magnitude of the electric field and the nature of the metal surface (both physical (see Chapter 5) and electronic characteristics).

When no external electric field is applied, the degeneracy of the hydrogen atom n-manifold is split under the surface perturbation, similar to the Stark effect for the case of a homogeneous electric field. The eigenstates of the surface potential each exhibit a different polarisation with respect to the surface. The lowest-energy, most surface-oriented state is found to ionise at much larger atom-surface separations compared with the higher-energy vacuum-oriented states. However, as the surface is approached, the Rydberg levels can encounter numerous avoided crossings, particularly for the vacuum-oriented states. Thus, while the ionisation probabilities (as a function of atom-surface separation) of the surface-oriented states resemble a single-peak gaussian profile, those of the vacuum-oriented states exhibit multiple peaks, and are strongly dependent on the collisional velocity of the Rydberg atom (which determines the adiabaticity of avoided crossings). It is found that, at zero-field and at the experimental range of collisional velocities, the non-adiabatic contributions to the ionisation dynamics are significant, and a full time-dependent approach is required for its proper description.

When a homogeneous ion-extraction electric field is applied, the Rydberg manifold is split apart by the Stark effect. The red-shifted Stark states are oriented towards the surface, and are ionised further from the surface than the blue-shifted states, which are oriented towards the vacuum. The wider spreading of the Rydberg levels and the

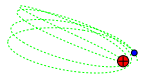

extra symmetry imposed by the electric field (z-parity) suppresses the level interactions of the Rydberg manifold, and the ionisation dynamics are mostly adiabatic at the experimental range of collisional velocities. For all the Stark states of a given n-manifold, the ionisation probabilities (as a function of atom-surface separation) resemble a single-peak gaussian profile. It is found that the ionisation distance can be increased by increasing the magnitude of the ion-extraction field, which reduces both the height and the width of potential barrier in between the ion-core and the metal surface.

When a homogeneous electron-extraction electric field is applied, the polarisation of the red- and blue-shifted Stark states with respect to the surface is now reversed compared to the ion-extraction fields. The blue-shifted Stark states are now surface-oriented, and are ionised further from the surface than the vacuum-oriented red-shifted Stark states. Due to the different energy shifts of surface- and vacuum-oriented states, the Rydberg manifold tends to converge in energy when approaching the metal surface under an electron-extraction field. Consequently, the Rydberg levels in the centre of the Stark manifold are found to encounter numerous avoided crossings as the surface is approached. Although increasing the magnitude of the applied field suppresses the extent of level interactions (similar to the ion-extraction field case), the ionisation dynamics at the experimental range of collisional velocities are found to exhibit some contributions from non-adiabatic transitions.

In the presence of an electron extraction field, the ionisation distance of the surface-oriented states can be decreased by increasing the magnitude of the field, which increases both the height and the width of potential barrier in between the ion-core and the metal surface. But increasing the magnitude of the electron-extraction field also reduces the height and the width of the potential barrier in between the ion-core and the vacuum. Thus, for a sufficiently large field, the Rydberg electron can escape

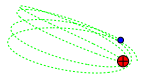

into the vacuum via a back-scattered mechanism, whereby the surface potential drives the electron over the barrier on the vacuum-side of the core. This novel ionisation channel is observed in the calculations for the vacuum-oriented states of the $n = 10$ Rydberg manifold. For the most extreme red-shifted state, the threshold field for the back-scattered electron loss is $\approx 0.04n^{-4}$. It is possible that the recently observed electron signal from the surface ionisation of Rydberg H_2 molecules [64] comes from this back-scattered electron loss.

The surface ionisation dynamics at an electronically structured surface is found to be very different compared to a free-electron metal surface. Cu(111) and Cu(100) have surface and image states embedded in a projected band-gap along the surface normal, forming a series of 2D bands. The electron motion inside the metal is restricted (based on the energetically available electronic states) in the direction normal to the surface, and is free in the direction parallel to the surface. Since the charge transfer of the Rydberg electron to the metal occurs preferentially along the surface normal (where the saddle point lies), with a minimum component of momentum parallel to the surface, the ionisation distance is larger when the Rydberg electron is nearly degenerate in energy with the surface and image states. The resonant charge transfer to the surface and image states can be seen directly from the electronic wavefunctions during the wavepacket propagation. For the Cu(100) surface, the projected band-gap extends beyond the vacuum level, and the Rydberg-series of image-states exhibits spacings that are approximately four times that of the hydrogen atom. Thus, the resonance effects from image states should be observable even at the experimental range of principal quantum numbers. The experimental study of the surface ionisation of $20 \leq n \leq 38$ Rydberg H states at a Cu(100) surface is presented in Section 7.7.

To analyse the validity of the constant velocity approximation used in the wavepacket calculations, mean-field calculations are carried out, where the ion-core moves classi-

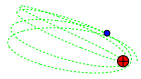

cally under the mean-field potential of the electronic wavefunction, the electric field and the image-charge fields. It is found that as the Rydberg atom approaches the metal surface and begins to ionise, the attraction of the ion-core to the departing electron density and the reduced shielding of the ion-core from its image-charge results in a rapid acceleration of the ion-core towards the surface. At longe-range, there is also a smaller acceleration due to the Van der Waals force on the Rydberg state. At the experimental range of initial collisional velocity, the ionisation distance of the most surface-oriented state (which ionises furthest from the surface) is shifted to smaller separations by $\sim 0.2n^2$ a_0 compared with the constant-velocity calculation, and exhibits a final ion-velocity (when there is no Rydberg electron population left outside the metal) approximately four times the initial collisional velocity. For the most vacuum-oriented state (which ionise closest to the surface), the ionisation distance is shifted to smaller separations by $\sim 0.4n^2$ a_0, and the final ion-velocity is approximately an order of magnitude greater than the initial collisional velocity. The increase in the ion collisional energy will have a strong effect on the resultant ion-detection probability. Thus, although the conclusions based on the studies with the constant velocity approximation are qualitatively valid, for a quantitative comparison with experiments, mean-field calculations are required.

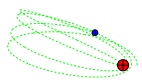

Chapter 4

Interaction of non-hydrogenic atoms with metal surfaces

It is of interest to compare the hydrogenic calculations presented in Chapter 3 with a study of the same effects in a non-hydrogenic system, which could give some insight into some of the experimental results of xenon [44–48] and molecular hydrogen [49–51] Rydberg states. In the work presented in this chapter, the xenon atom is chosen as the model system. As explained in Section 1.6, the previous experimental studies [44] using xenon atoms have shown that the ionisation dynamics of the xenon Rydberg atom under an *ion*-extraction field are very different from the hydrogenic predictions. Specifically, the distance at which there is an onset of ionisation for the most vacuum-oriented state in the manifold is very similar to that of the most surface-oriented state, and this has been explained by the exchange of ionisation behaviours of the Rydberg states *near* an avoided crossing between states of different n on the Stark map [32]. It will be of interest to examine how the ionisation dynamics are affected by application of an electron-extraction field. The wavepacket propagation approach has also been carried out by Sjakste *et al.* [32] previously for the xenon Rydberg atom, where a non-linear grid transformation (or change of variables) is used to minimise

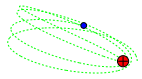

	$l=0$	$l=1$	$l=2$	$l=3$	$l>3$
A_l	-1.17984	-0.89700	-0.49906	-0.00823	0

Table 4.1: The coefficients A_l used in this work for the pseudo-potential of the xenon atom [32, 53]

the total number of grid points. Therefore the choice of xenon allows a comparison of the CWDVR wavepacket propagation approach presented in this thesis directly with the implementation by Sjakste *et al.*. Note that for the qualitative study presented below, the wavepacket calculations do not include effects of mean-fields on the nuclear trajectory.

4.1 Modelling xenon Rydberg atoms

To model the complex many-body interaction of the Rydberg electron with the xenon core ion and inner electrons, the Coulomb potential, V_c, in the Hamiltonian given by Eq. 2.35 is replaced by a simple l-dependent Bardsley pseudo-potential [91],

$$V^{PS}(r) = -\frac{1}{r} + \sum_l V_l(r) \left|l\right\rangle \left\langle l\right| \tag{4.1}$$

with

$$V_l(r) = A_l e^{-Br^2} - \frac{\alpha_d}{2(r^2+d^2)^2} - \frac{\alpha_q}{2(r^2+d^2)^3}, \tag{4.2}$$

where $\alpha_d = 4.044$ a.u., $\alpha_q = 14.235$ a.u., $B = 0.01$ and d is set to 1.0 a_0 [53]. The coefficients A_l are chosen such that the calculated atomic energies of the Rydberg states using the pseudo-potential matches the experimentally determined quantum defects [92, 93], whilst maintaining the correct number of radial nodes. For the $n = 7$ states (studied below), the values of the coefficients A_l are given in Table 4.1.

The calculated Stark map for the $\nu \approx 7$ states of the xenon atom is shown in Fig. 4.1. Note that the large quantum defects of the low-l states shift states with $n = 10$ and

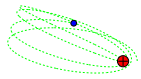

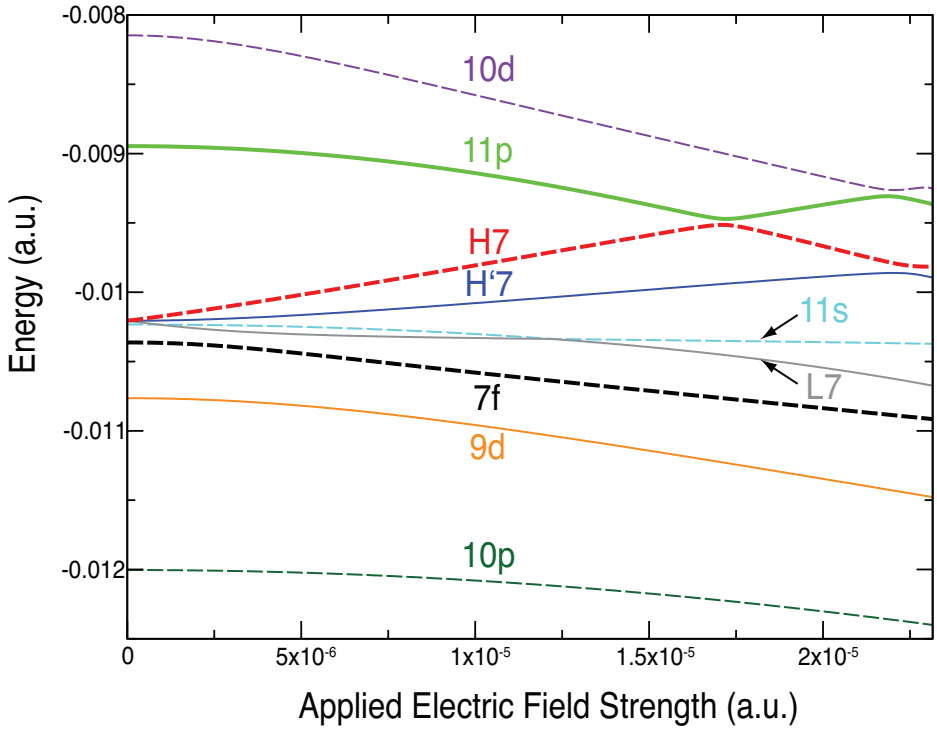

Figure 4.1: Stark map of the Rydberg xenon $\nu \approx 7$ states calculated using the Lagrange-Laguerre mesh method [68]. $\nu = (n - \delta_l)$ is the effective principal quantum number.

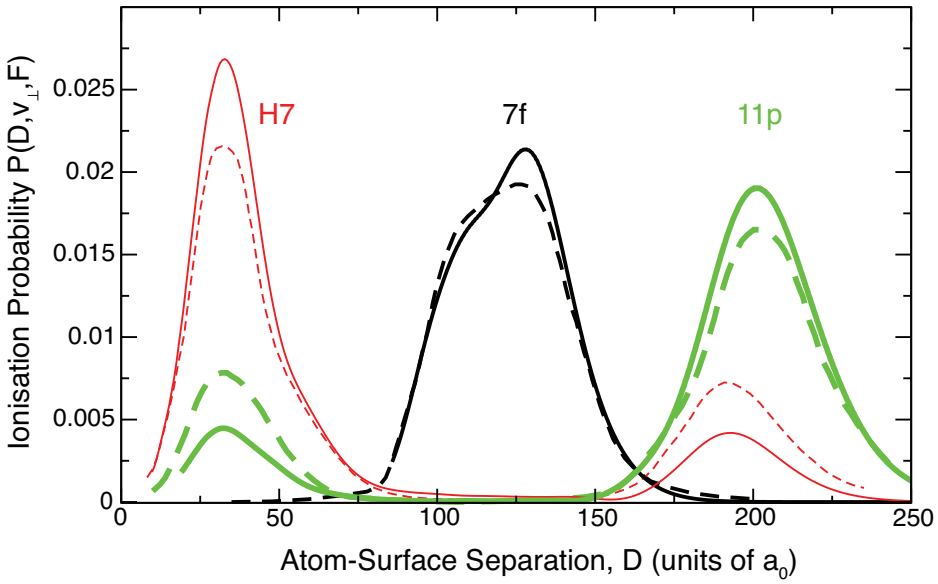

Figure 4.2: Wavepacket results for the $7f$, $H7$ and the $11p$ states of xenon in an ion-extraction field of $F = 1.6 \times 10^{-5}$ a.u. and a collisional velocity of 5×10^{-3} a.u.. Solid lines are results obtained using the CWDVR described in this work, and dashed lines are the results of Sjakste *et al.* [32].

11 into the $\nu = 7$ region. At zero-field, states with $l < 4$ have non-zero quantum defects and are separated from the rest of the manifold; these states have been labeled with their associated l quantum number at zero-field. States with $l \geq 4$, which remain degenerate in energy at zero-field, have been labeled $H7$ for the highest-energy state within the manifold at non-zero-field, $H'7$ for the second highest-energy state and $L7$ for the lowest-energy state.

4.2 Ion-extraction field dynamics

4.2.1 Comparison with previous study

Figure 4.2 shows the results from the wavepacket approach using a CWDVR (outlined in Section 2.3) for the $7f$, $H7$ and the $11p$ states of xenon (solid lines) compared with the results obtained in the study by Sjakste *et al.* using a 'change of variables' [32]

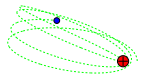

(dashed lines) for a collisional velocity of 5×10^{-3} a.u. and an ion-extraction field of $F = 1.6 \times 10^{-5}$ a.u. ($\equiv 8.23 \times 10^{6}$ Vm^{-1}) (this field value is close to the avoided crossing of the H7 and 11p states in Fig. 4.1, which is also the onset of the ion detection signal [32]). Minor differences are observed in the relative magnitudes of the peaks of the two sets of results which may be explained by the slightly different values of the parameters used in the pseudo-potential: although the parameters used in the work of Sjakste *et al.* [32] produces the correct energy, they do not produce the correct number of radial nodes in the wavefunction.

The calculations by Sjakste *et al.* using the 'change of variables' method typically required 2000×425 grid points [32], whilst the calculations using the CWDVR require only 474×70 (radial $\times$ angular) points to produce the data presented in Fig. 4.2. This significant decrease in the number of grid points shows that the CWDVR can be better suited to ionisation problems involving the Coulomb potential (such as the surface-ionisation problem studied here) than a grid obtained from the co-ordinate transformations of uniformly distributed grids. Naturally, as it is demonstrated in the previous sections, the reduction of the number of grid points leads to a decrease in the number of operations per time step, and therefore allows for calculations involving lower collisional velocities and/or Rydberg states of higher principal quantum numbers to be carried out.

4.2.2 Level interactions and non-adiabatic effects

The interactions between the Rydberg states are much stronger for the non-hydrogenic system compared with the hydrogen atom. In the case of hydrogen, level interactions only occur as a result of the perturbing surface potential. In contrast, for a non-hydrogenic atom, level interactions occur as a consequence of the externally applied electric field as well as the surface potential. The overall dynamics are thus expected

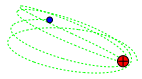

to be complex. The energy gap at the avoided crossings will generally be larger for Xe, making it likely that each crossing is traversed more adiabatically. There are now more crossings however, and there is also an increased probability of level transition through non-adiabatic interactions between curves that are well separated, and which would be regarded as non-crossing.

The strong level interactions between Rydberg states are illustrated by the form of the ionisation probabilities shown in Fig. 4.2. As explained in Ref. [32], the double peaks in the ionisation probabilities for the $H7$ and the $11p$ states are attributed to the mixing of the 'initially' surface-oriented $11p$ state with the 'initially' vacuum-oriented $H7$ state as the xenon atom passes through an avoided crossing between the $H7$ and $11p$ states at a distance of ≈ 250 a_0 from the surface [1]. This is shown in Figure 4.3 which presents the energies and widths of the Rydberg states as a function of atom-surface separation (obtained from complex scaling calculation). Note that for the xenon atom the energy gap at the avoided crossings are larger, and the changes in the widths are more dramatic when compared with the hydrogen atom (Fig. 3.2), reflecting the stronger nature of the level interactions. A shoulder is also observed for the surface-oriented $7f$ state curve in Fig. 4.2 at low atom-surface separation, even though this state appears far in energy from other Rydberg states in the Stark map (Fig. 4.1). This is due to an avoided crossing with the $L7$ state at ≈ 130 a_0 from the surface (see Figure 4.3).

Figure 4.4 compares the ionisation probabilities of the $S7$, $H7$ and $11p$ states obtained from wavepacket propagation (positive axis) with those obtained from the adiabatic model complex scaling calculations (negative axis) at various velocities. It can be seen that at the higher velocity of $v_\perp = 5 \times 10^{-3}$ a.u. $\equiv 1094$ ms^{-1}, the wavepacket

[1] The similar onset of surface ionisation signal for red and blue Xe Stark states observed experimentally [44] is attributed to the $Hn/(n+3)p$ level crossing (for a given n-manifold), where the oppositely polarised Stark states can mix [32].

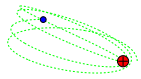

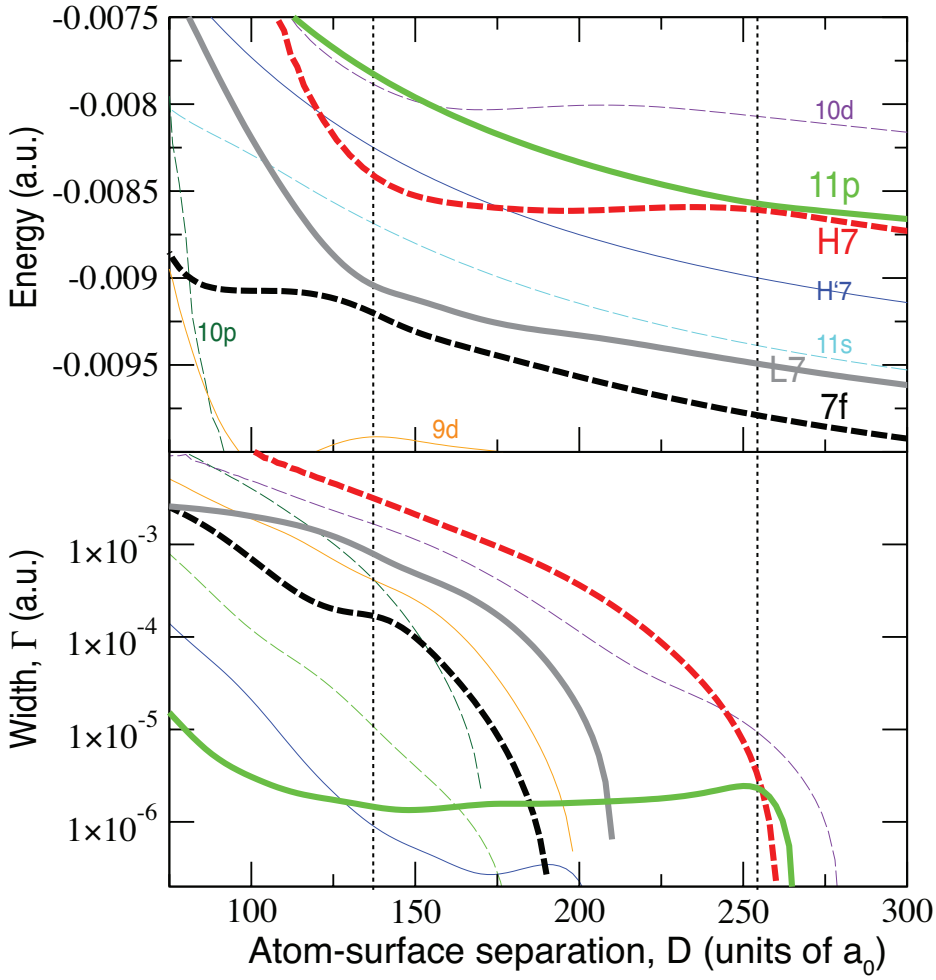

Figure 4.3: The energies and widths of the Rydberg xenon $\nu \approx 7$ states as a function of atom-surface separation, in the presence of an ion-extraction field of $F = 1.6 \times 10^{-5}$ a.u.. Vertical dashed lines mark the avoided crossing between the $11p$ and $H7$ states at D$\approx$ 250 a_0, and between the $7f$ and $L7$ states at D$\approx$ 130 a_0. Note the sharper changes in both the energies and widths for the xenon atom compared with the hydrogen atom (Fig. 3.2).

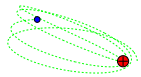

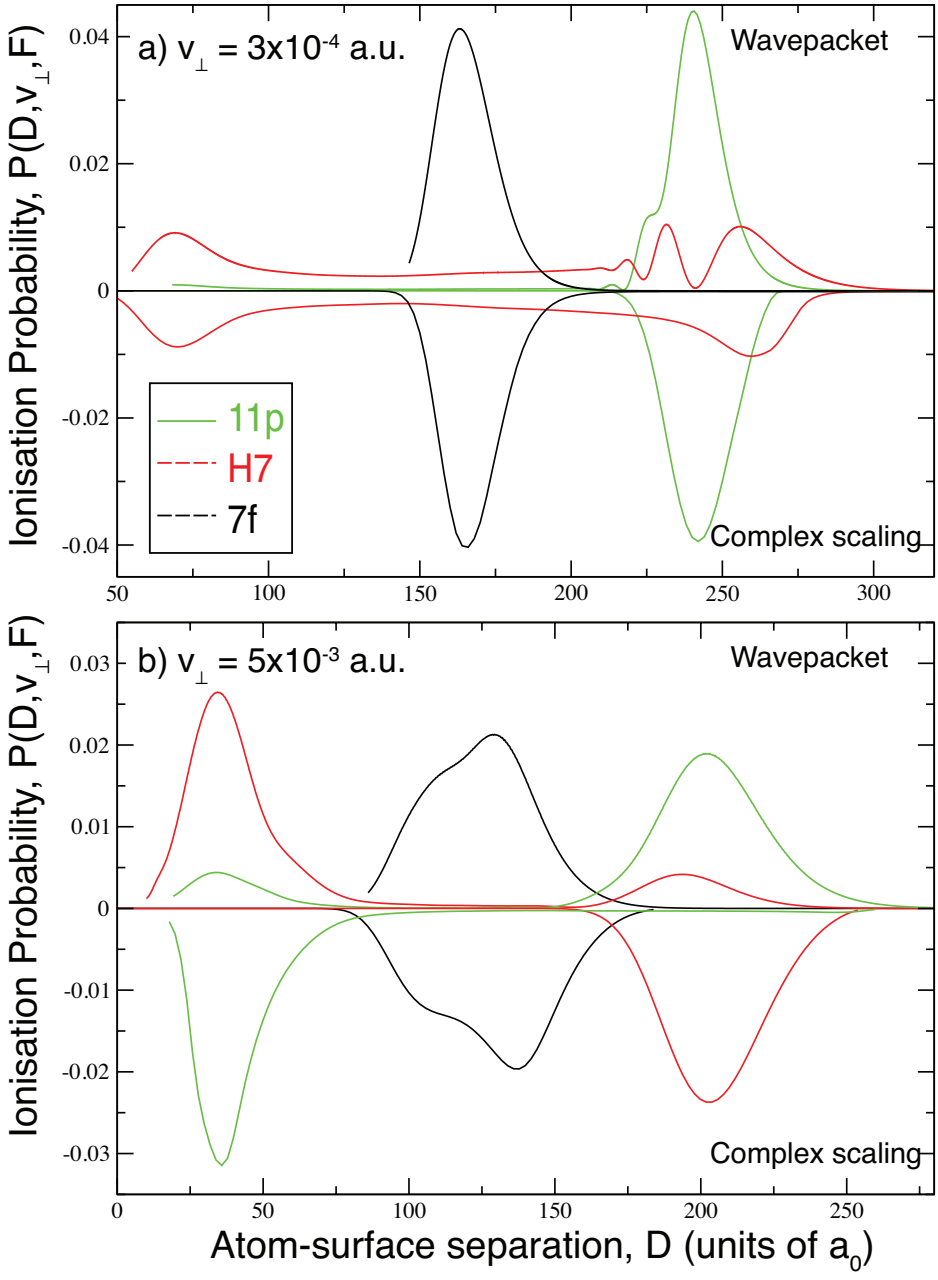

Figure 4.4: Wavepacket propagation results for the ionisation of the $\nu \approx 7$ xenon Rydberg states approaching a metal surface in the presence of an ion-extraction field of $F = +1.6 \times 10^{-5}$ a.u. and with the collisional velocity of (a) 3×10^{-4} a.u. and (b) 5×10^{-3} a.u.. Note the different scale of the x-axis on the two plots.

results show that the ionisation dynamics is mostly *diabatic*: there is only a partial exchange of ionisation behaviour between the $H7$ and $11p$ state (the double peaks), while the complex scaling calculation predicts a complete exchange ($H7$ state behaves as surface-oriented, and $11p$ vacuum-oriented). At the lower collisional velocity of $v_\perp = 3 \times 10^{-4}$ a.u. $\equiv 656$ ms^{-1} (which is within the experimental range [44, 49]), the complex scaling result is in better agreement with the wavepacket calculation, but there are still some discrepancies arising from the non-adiabatic transitions between the $11p$ and $H7$ state. Thus for the non-hydrogenic system, the ionisation dynamics under ion-extraction fields at the experimental range of collisional velocities ($\sim 10^{-4}$ a.u. or 10^2 ms^{-1}) are susceptible to non-adiabatic effects, particularly when the Rydberg levels are brought close together in energy on the Stark map.

The results presented above also illustrate some fundamental differences between the surface charge transfer of non-hydrogenic and hydrogenic systems. The ionisation probability curves shown in Fig. 4.4 are unlike the typical ionisation probability curves observed for the hydrogen atom (*e.g.* Fig. 3.1). For the hydrogen atom, although the ionisation probabilities may exhibit multiple peaks due to avoided crossings, the crossings tend to only occur between states of similar polarisation and so the ionisation distances are confined to a single small range. For the xenon atom however, crossings can occur between states with very different polarisation with respect to the surface (at the appropriate electric field), and so can exhibit ionisation probabilities that span a much larger range of distances, making it difficult to define a single 'average' ionisation distance. Consequently, the corresponding ionisation profiles (detected ion signal as a function of extraction field), which reflects the ionisation distance as a function of electric field, can be strongly varying, and can exhibit 'resonance' effects such as those seen for the H_2 Rydberg states [49–51]. Although the features are quite small, some peaks and dips can also be seen in the Xe ionisation profiles shown in Fig. 1.11 [53].

4.3 Electron-extraction field dynamics

Figure 4.5 shows the wavepacket (positive axis) and complex scaling (negative axis) ionisation probabilities of xenon Rydberg atom $\nu = 7$ Rydberg states in the presence of an electron-extraction field of $F = -1.4 \times 10^{-5}$ a.u. ($\equiv 3.06 \times 10^3$ ms^{-1}) for collisional velocities of 1.4×10^{-4} a.u. and 1.4×10^{-3} a.u.. Figure 4.6 shows the energies and widths of the Rydberg states as they approach the metal surface at this field. At large distances all the Stark states in the $\nu = 7$ energy range (except for the $11s$ and $L7$ states) are well spread apart in energy (see the Stark map, Fig. 4.1). Despite this, Fig. 4.6 shows that as the atom approaches the surface, the manifold tends to converge in energy, and beyond atom-surface separations of $D \sim 140$ a$_0$ (shown as dotted line), the $7f$ to $H7$ Rydberg states encounter numerous avoided crossings as they approach the metal surface. This is illustrated by the multiple peaks seen for the wavepacket ionisation probabilities at the higher collision velocity (which are mainly distributed at $D < 140$ a$_0$), and the discrepancies with the complex-scaling calculations (which are due to non-adiabatic transitions). At the lower collisional velocity (top plot in Fig. 4.6), the dynamics is adiabatic, since ionisation occur before any level crossings. Thus, as in the case of the H atom (and for the same reason), it can be seen that there is an increased number of avoided crossings in the reversed electron-extraction field compared with the ion-extraction field (Section 3.4). Although this could imply an increase in susceptibility towards non-adiabatic effects, as illustrated above, the susceptibility also depends on the positions of the level crossings relative to the mean ionisation distance.

Interestingly, the ionisation of all the $\nu \approx 7$ states shown in Fig. 4.5 occurs principally at quite a similar distance (for both collisional velocities), and does not appear to exhibit the drastic effects of different polarisations as has been observed for the ion-extraction fields (see Fig. 4.4). Under the electron-extraction field of $F = -1.4 \times$

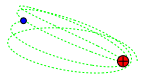

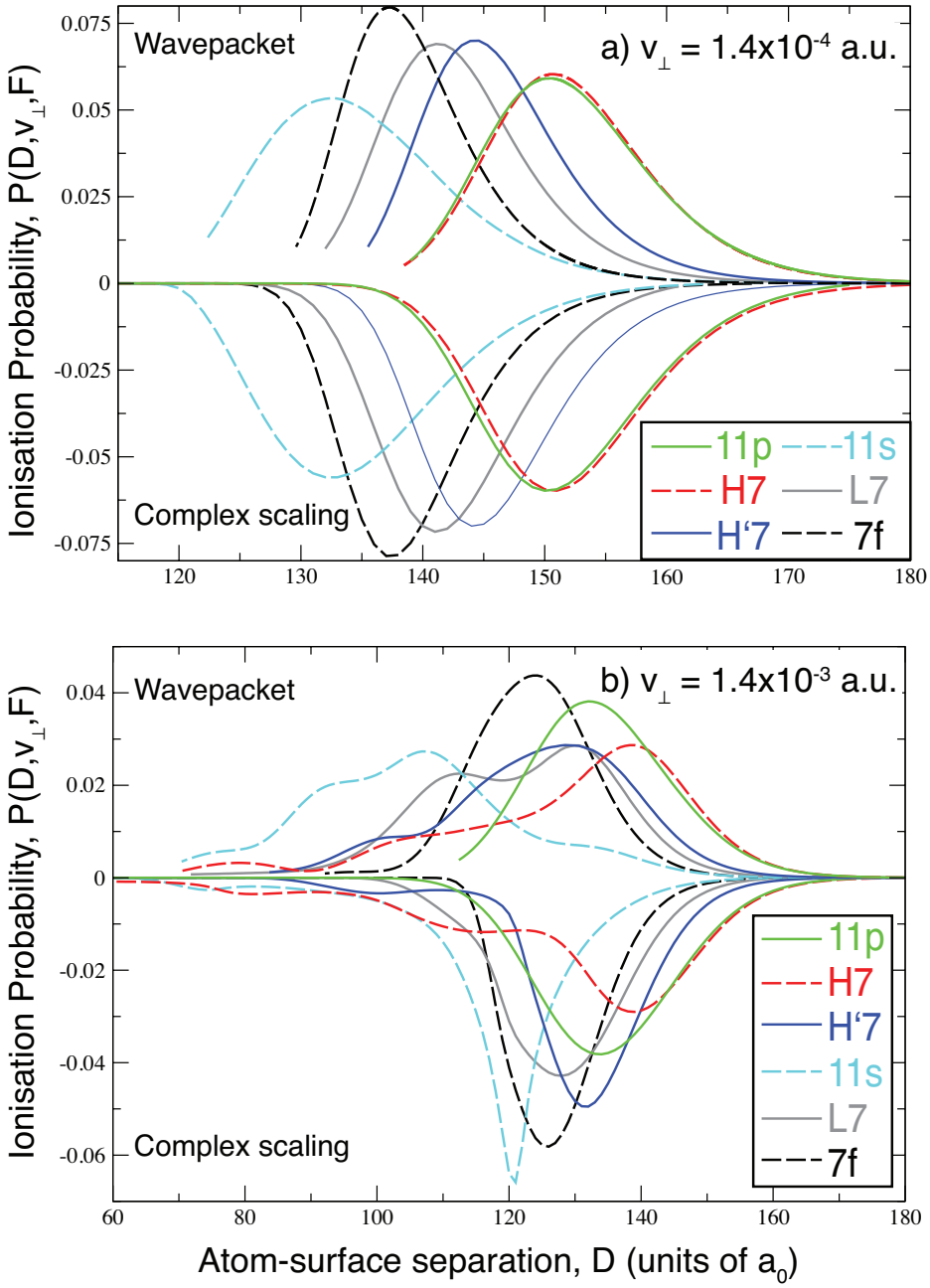

Figure 4.5: Wavepacket propagation results for the ionisation of the $\nu \approx 7$ xenon Rydberg states approaching a metal surface in the presence of an electron-extraction field of $F = -1.4 \times 10^{-5}$ a.u. and with the collisional velocity of (a) 1.4×10^{-4} a.u. and (b) 1.4×10^{-3} a.u.. Note the different scale of the x-axis on the two plots.

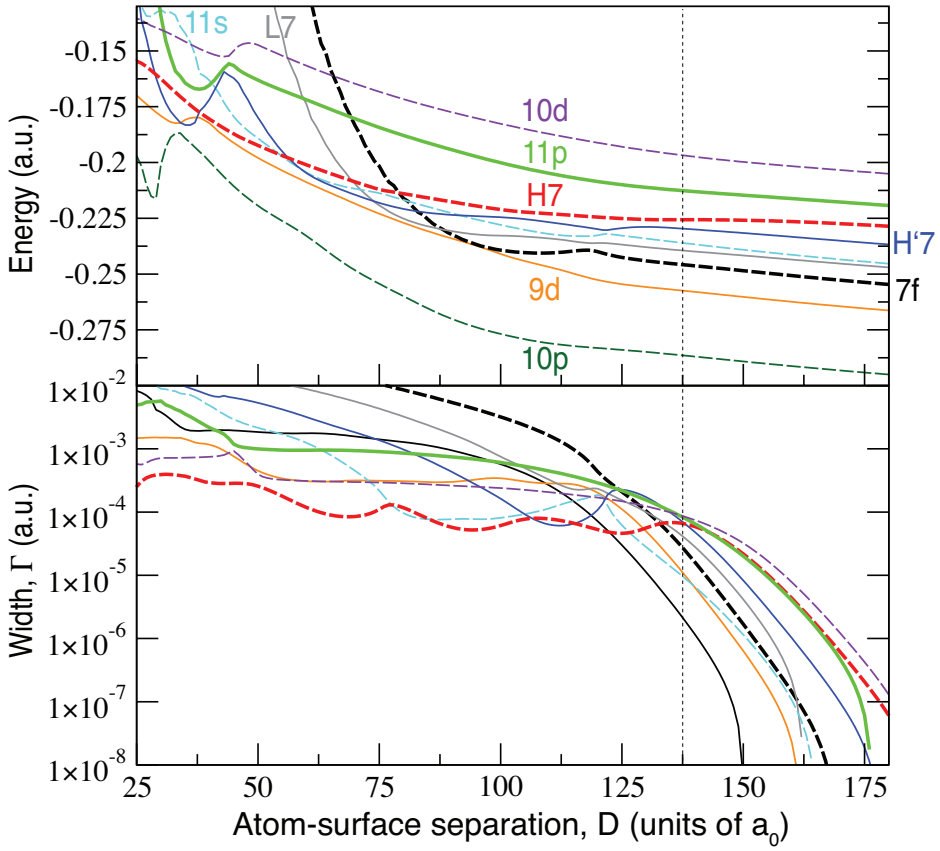

Figure 4.6: The energies and widths of the xenon $\nu \approx 7$ manifold in the presence of an electron-extraction field of -1.4×10^{-5} a.u. as a function of atom-surface separation. Note the way the manifold converges in energy (particularly for $D < 140$ a_0) and the small spread in ionisation width compared with the ion-extraction case shown in Fig. 4.3.

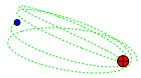

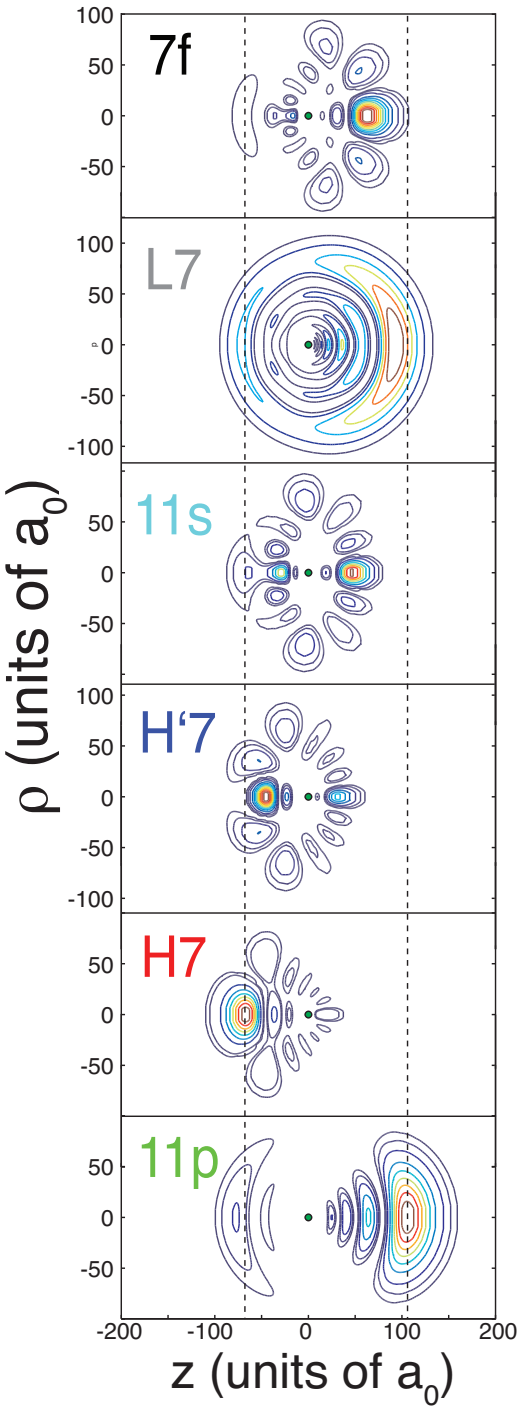

Figure 4.7: Contour plot of the electronic wavefunction of the xenon $\nu = 7$ Rydberg states in the presence of an electron-extraction field of $F = -1.4 \times 10^{-5}$ a.u.. For the case of electron-extraction the metal surface would be on the left of the plot (negative z), and for ion-extraction fields the right (positive z). Note that the states are labelled according to the Stark map shown in Fig. 4.1. The $L7$ state resembles an s state at this field due to an $L7/11s$ avoided crossing at a lower field.

10^{-5} a.u., and following the Stark map Fig. 4.1 adiabatically, the $7f$, $L7$, $11s$ and $11p$ states are vacuum-oriented, and $H'7$, $H7$ states are surface-oriented. However, Fig. 4.5 shows that the oppositely polarised, most extreme red- and blue-shifted, $H7$ and $11p$ state ionising at nearly the same atom-surface separation. This ionisation behaviour is due admixture of the wavefunctions of the non-zero quantum defect $l = s, p, d, f$ states into the red-shifted Stark states of a given manifold, as a result of the electric field. This can be seen from the Stark map shown in Fig. 4.1. In the presence of the field, the higher principal quantum number low-l states mixes with the high-l group of the lower principal quantum number manifold, and consequently, the s, p, d, f states are red-shifted. Figure 4.7 shows a contour plot of the electronic wavefunctions of the $\nu = 7$ states under an applied field of $F = -1.4 \times 10^{-5}$ a.u.. The surface potential is removed, but for electron-extraction fields the metal surface would be located on the left of the plot (negative z in Fig. 4.7), and for ion-extraction fields the right (positive z in Fig. 4.7). It can be seen that, for the electric field in the direction of electron-extraction (surface located on the left), the z-extension of the wavefunctions are very similar, due to contributions from low-l states to red-shifted states. While for the electric field in the direction of ion-extraction (surface located on the right), the z-extension of the wavefunctions are much more varied, particularly the $H7$ state, which has very little extension towards positive-z in Fig. 4.7. This leads to the much larger range ionisation distances observed in Fig. 4.4 (ion-extraction fields) compared with Fig. 4.5 (electron-extraction fields).

The mixing of higher principal quantum number low-l states into the lower principal number Stark manifold occurs for the full range of principal quantum numbers, this is illustrated by the xenon Stark map in the $\nu = 13 - 15$ energy range shown in Fig. 4.8 (the experimental range of principal quantum numbers is $\nu > 15$ [44–48]). Thus, a similar onset of ionisation for the whole Stark manifold is expected to be

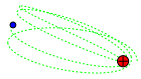

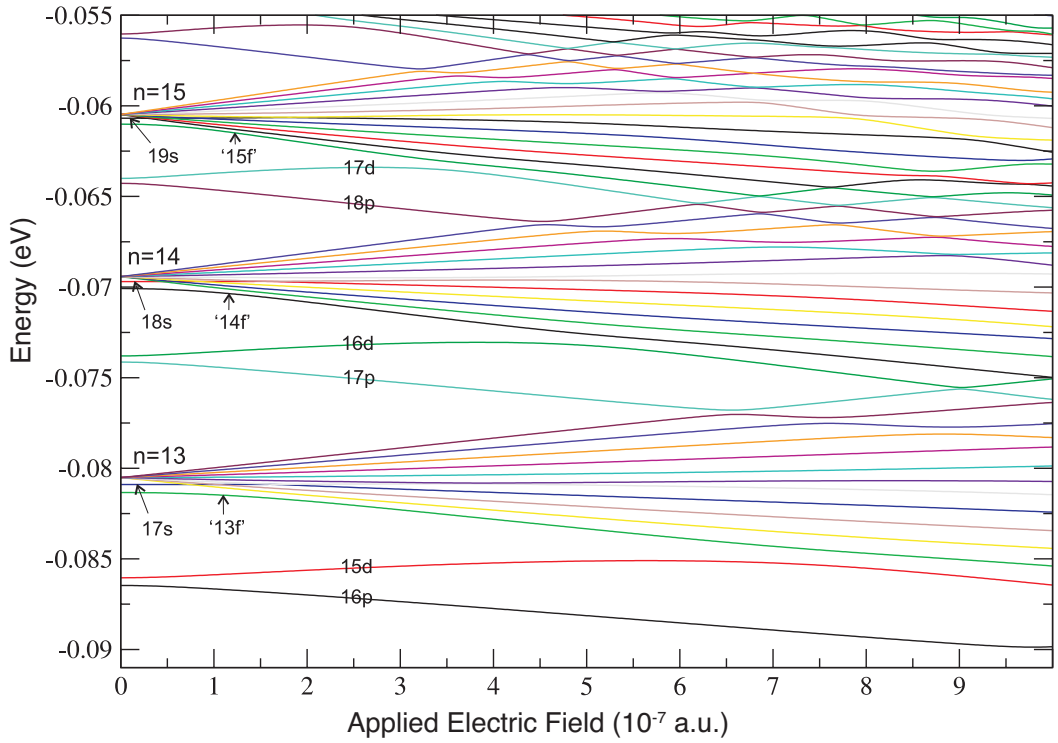

Figure 4.8: Calculated Stark map for xenon $n = 13 - 15$, $m_l = 0$ manifolds. (Shown previously as Fig. 1.3.)

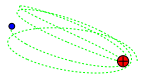

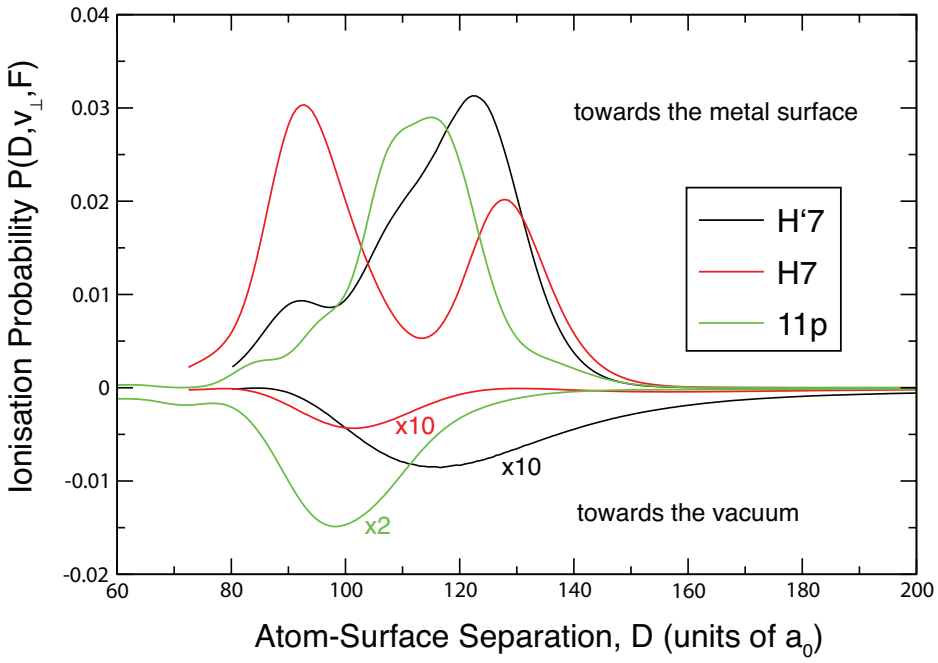

Figure 4.9: The electron flux measured by the forward ($\theta > 90°$) and backward ($\theta < 90°$) radial flux planes, plotted as a function of atom-surface separation for the $H'7$, $H7$ and $11p$ xenon Rydberg states colliding with the surface with the collisional velocity of 1.4×10^{-3} a.u. and in the presence of an electron-extraction field of $F = -2.3 \times 10^{-5}$ a.u.. The flux measured by the backward flux plane is plotted on negative axis.

observed experimentally for electron-extraction fields, similar to the observation in ion-extraction field [53] (but not for the same reason).

4.4 Back-scattering of the electron flux

For the hydrogenic case, it was shown that when the electron-extraction field is just below that required for field ionisation, the most vacuum-oriented states are ‘surface’-ionised by losing the electron toward the vacuum-side of the ion-core. For the xenon atom however, the back-scattering of the Rydberg electron could occur for any state that mixes with a vacuum-oriented state as it approaches the surface. Figure 4.9 shows the fraction of forward-scattered electron flux and back-scattered electron flux for the various higher-energy states of the $\nu = 7$ xenon Rydberg manifold at an electron-

extraction field of $F = -2.3 \times 10^{-5}$ a.u.. In the presence of this externally applied field, and provided the Stark map is followed adiabatically, the $11p$ and $H'7$ states are vacuum-oriented, and the $H7$ state is surface-oriented at large distances from the surface. Although it is predominately the vacuum-oriented states that exhibit a back-scattered electron flux, the mixing amongst the three states as they approach the surface (shown by the shared ionisation peaks) results in the $H7$ state gaining some vacuum-oriented characteristics on its trajectory towards the surface, and consequently some of the electron density is back-scattered.

4.5 Conclusions

Complex scaling and wavepacket calculations are carried out for the $\nu = 7$ Rydberg states of the xenon atom. Due to the stronger level interactions for non-hydrogenic systems compared to the hydrogen atom, a greater number of avoided energy crossings are encountered when approaching the surface, and the changes in the level widths at the crossings can be more drastic. Consequently, the ionisation probabilities can span a very large range of atom-surface separations, and cannot be assigned a single 'average' ionisation distance. The level interactions also lead to some non-adiabatic effects in the ionisation dynamics at the experimental range of collisional velocities.

In electron-extraction fields, the energy levels of the xenon Rydberg manifold converge in energy when approaching the surface, just as for the hydrogen atom case, and encounter numerous avoided crossings. Thus, the ionisation dynamics are expected to be more complex than for ion-extraction fields. However, the ionisation probabilities show that all the states of the $\nu = 7$ manifold ionise at a similar atom-surface separation. This is due to the mixing of higher principal quantum number states with low angular momentum ($l = 0 - 3$), to the lower principal quantum Rydberg manifold ($l > 3$) by the electric field, resulting in red-shifted Stark states that are less polarised

with respect to the field (and surface normal) axis than the corresponding hydrogenic parabolic states. Consequently, while the extension of the electronic wavefunction towards the surface is varied for the Stark manifold for ion-extraction fields, they are very similar in electron-extraction fields, leading to the similar surface ionisation distances that are observed.

For the xenon atom, it is shown that back-scattered electron loss is not limited to Stark states that are initially vacuum-oriented, but can occur for any states that can gain vacuum-oriented characteristics (via an avoided crossing or non-adiabatic transistion) as they approach the surface. This 'scrambling' of polarisation with respect to the surface can account for the electron signals detected for the Stark states of the H_2 molecule [64].

Chapter 5

Bridging from theory to experiment

In this chapter, the scaling of the results of quantum wavepacket propagation calculations to the experimental range of principal quantum numbers ($20 \leq n \leq 40$) is investigated. Model calculations including the effects of local surface fields and surface roughness on the ionisation dynamics and ion-extraction probabilities of Rydberg states at the experimental range of principal quantum numbers are also developed.

5.1 Scaling to higher principal quantum numbers

The quantum calculations for the hydrogen atom presented in Chapter 3 have been limited to the principal quantum numbers of $n \leq 10$, due to computational demands. Although it has been possible to gain qualitative insight into the Rydberg ionisation dynamics under various experimentally relevant effects from the studies at low n, in order to compare more directly with the experimental results in Chapter 7, scaling properties which allow for extrapolations to high principal quantum numbers are required. These are investigated below.

5.1.1 Extreme red-shifted Stark state

First, the scaling properties with principal quantum number of the most extreme red-shifted, surface-oriented Stark states under ion-extraction fields are considered. In Chapter 3, it is shown that inclusion of mean-field effects is required for an accurate calculation of the ionisation distance; the ionisation distances are found to be broadened and $\sim 0.2n^2$ a_0 smaller for the mean-field calculations. But more importantly, there is a significant acceleration of the ion-core during surface ionisation, such that the ion velocity at the end of ionisation is approximately four times the initial velocity for the most red shifted Stark state. This will strongly modify the extraction probability of the ions (see Eq. 1.14), and consequently, the surface ionisation profile (the fraction of detected ions as a function of extraction field). For a better understanding of the different effects introduced by the mean-field calculation, and how they scale with principal quantum number, the wavepacket results obtained with the constant velocity approximation are also examined.

Figure 5.1 presents the wavepacket-propagation calculated ionisation probabilities (with and without the inclusion of mean-field) for the most surface-oriented, red-shifted state in the presence of various ion-extraction fields for principal quantum numbers of $n = 2 - 10$, and a typical *initial* velocity of 3×10^{-4} a.u. ($= 656$ ms^{-1}). The ionisation probabilities are presented as a density plot in order to illustrate the variation of ionisation distance with electric field. The critical ionisation distances calculated from the over-the-barrier model outlined in Section 2.1 are shown as dashed green lines. As explained in Section 3.3, as the ion-extraction electric field increases, both the height and the width of the potential barrier between the core and the metal surface decreases, making surface ionisation more facile, which is clearly shown by the increasing ionisation distance with electric field in Fig. 5.1.

Figure 5.1 shows that the ionisation distances calculated from the OTB approach

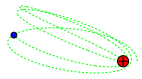

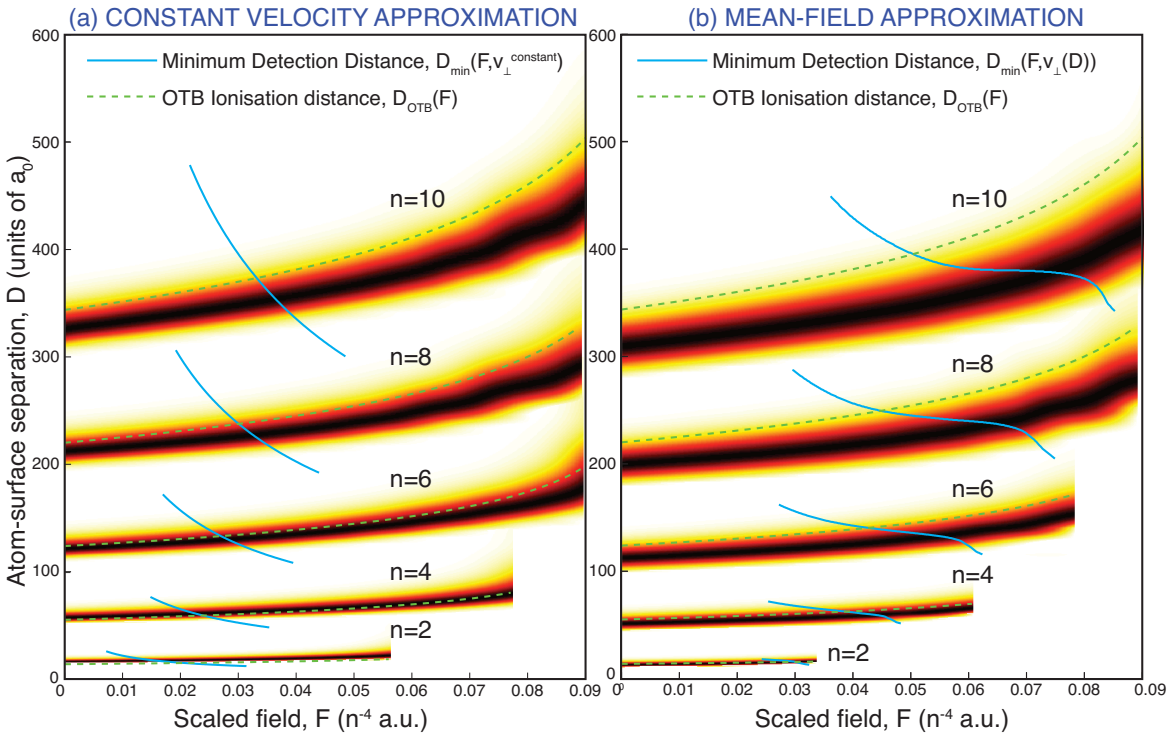

Figure 5.1: Density plot of the ionisation probability of the most surface-oriented, red-shifted state of $n = 2 - 10$ manifold as a function of scaled ion-extraction field (by a factor of n^{-4}), calculated from the wavepacket propagation approach using the constant velocity approximation (left), and using the mean-field approximation (right). The *initial* collisional velocity of the atom is 3×10^{-4} a.u.. For clarity, the maximum ionisation probability calculated for each electric field is normalised to unity (such that on the colourmap, black represents the maximum ionisation probability for the given electric field). Green dashed lines are the ionisation distances calculated from the over-the-barrier model. The minimum detectable ionisation distances corresponding to the given ion-extraction field and velocity (as given by Eq. 1.15) are shown as full cyan lines.

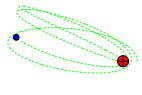

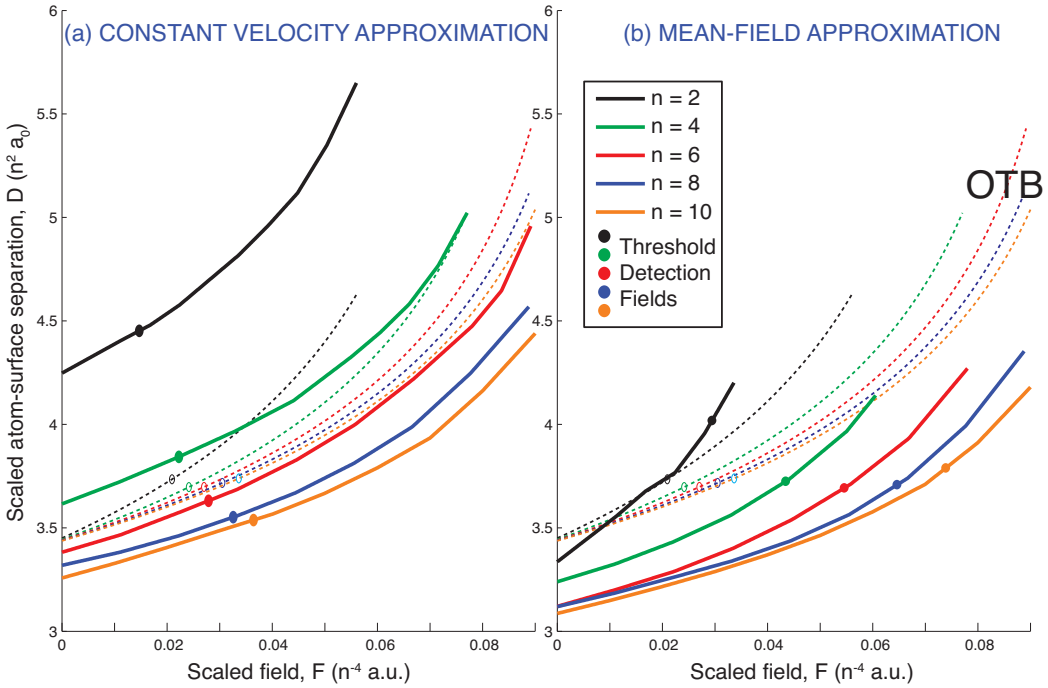

Figure 5.2: Plot of the position of maximum ionisation probability of the most surface-oriented, red-shifted state of $n = 2-10$ manifold as a function of scaled ion-extraction field (by a factor of n^{-4}), calculated from the wavepacket propagation approach using the constant velocity approximation (left), and using the mean-field approximation (right). The *initial* collisional velocity of the atom is 3×10^{-4} a.u.. The atom-surface separation axis is scaled by a factor of n^2. Dashed lines are the ionisation distances calculated from the over-the-barrier model. Circles mark the critical threshold field at which the resulting positive ion from the charge transfer process can be pulled away from the surface.

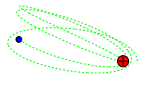

follow qualitatively the form of the wavepacket propagation ionisation probabilities, but the results are quantitatively different. For a clearer comparison of the ionisation distances predicted by wavepacket propagation and by the OTB calculation, and to find out how they scale with principal quantum number, Figure 5.2 plots the line of ionisation probability maximum for the wavepacket propagation results, with the atom-surface separation axis scaled by a factor of n^2. It can be seen that for the constant velocity wavepacket calculations, the OTB approach underestimates the atom-surface separation at which charge transfer occurs for $n < 6$, which may be due to the lack of the inclusion of quantum tunnelling effects which are significant at close range (when the width of potential barrier is small). As the principal quantum number increases, the OTB results appear to increasingly overestimate the ionisation distance. Due to the acceleration of the ion-core, the corresponding ionisation distances obtained from mean-field wavepacket calculations are noticeably lower than both the constant velocity calculation and OTB predictions.

Figure 5.2 shows that, the difference between adjacent sets of wavepacket-calculated *scaled* ionisation distances (with and without mean-field effects) decreases with increasing principal quantum number. Thus, the results for $n = 10$ should provide an *upper* bound for the ionisation distances occurring for higher principal quantum numbers. Although there is still a small (but visible) difference between the $n = 8$ and $n = 10$ results, it is reasonable approximation to use the scaled ionisation distances (as a function of scaled field) calculated for $n = 10$ as a model for higher principal quantum numbers (as is done in Chapter 7).

Figure 5.1 shows that due to the acceleration of the ion-core by the mean-field potential as the surface is approached, the calculated minimum detection distances (from Eq. 1.15) are drastically modified, and the curve 'cuts across' the ionisation density map at a shallower angle than the constant velocity case. This results in much larger

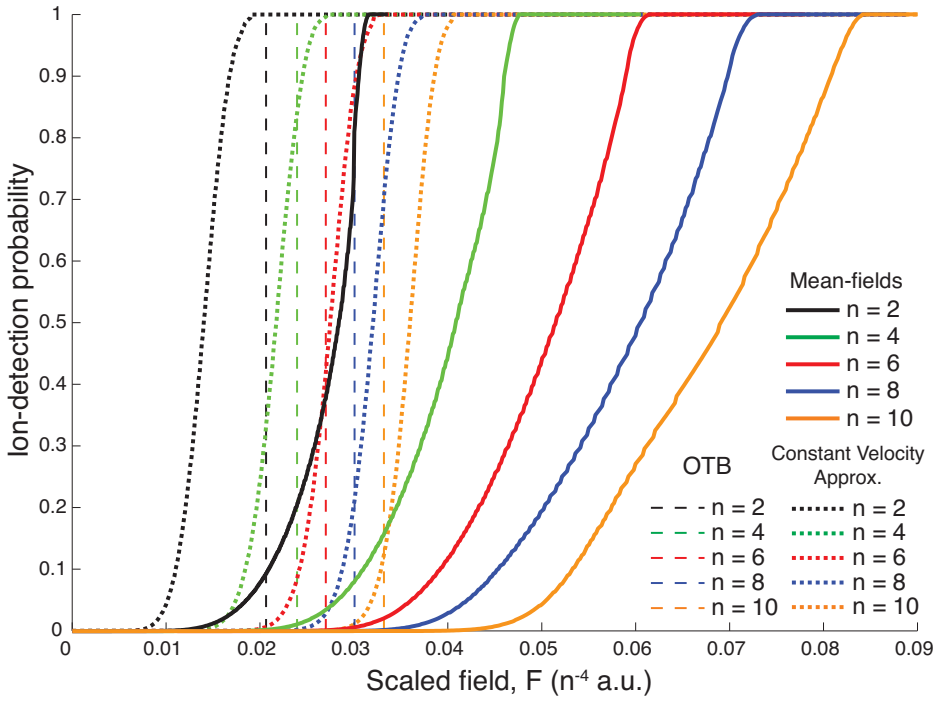

Figure 5.3: Ion-detection probability of the most surface-oriented, red-shifted state of $n = 2 - 10$ manifold as a function of scaled ion-extraction field, calculated from the wavepacket propagation approach using the constant velocity approximation (dotted lines), and using the mean-field approximation (full lines). The over-the-barrier ion-detection probability is shown as thin dashed lines. The *initial* collisional velocity of the atom is 3×10^{-4} a.u.. Note that the threshold ion-detection field for OTB and constant velocity wavepacket calculations are much lower than the mean-field result. The overall profiles for the mean-field wavepacket calculations are also much broader.

(average) threshold ion-detection fields compared to the constant velocity calculation and the OTB calculation (which are quite similar), as shown by Fig. 5.2.

For a given field, the ion-detection probability is calculated by integrating the ionisation probabilities from the minimum detection distance to infinity, corresponding to the areas of the density map shown in Fig. 5.1 that are above the cyan lines. The ion-detection probabilities for the most extreme red-shifted Stark state of the $n = 2 - 10$ manifold, calculated from the mean-field and constant velocity wavepacket, and the OTB approach, are shown in Fig. 5.3. It can be seen that the ion-detection profile for the mean-field wavepacket calculations are shifted to significantly higher fields and are much broader compared to the other two approaches.

Typically in experiments, a surface ionisation profile (the detected ion signal as a function of extraction field) is recorded for any given Rydberg state, which corresponds to the ion-detection probabilities shown in Fig. 5.3. It has been suggested above, that the ionisation distances for $n > 10$ can be approximated by scaling the ionisation distances calculated for the $k = -9$, $n = 10$ state from the mean-field wavepacket approach. Although the ionisation distances intrinsically depend on the collisional velocity of the Rydberg atom, it is shown above that the minimum distances at which ions can be pulled away from the surface are much more strongly affected by the increase in collisional velocity (see Fig. 5.1). Thus, it is also important to consider how the mean-field acceleration of the ion-core scales with principal quantum number.

Figure 5.4(a) shows the collisional velocity of the most surface-oriented, red-shifted state of $n = 4-10$ manifold as a function of scaled atom-surface separation at zero-field (the results at other fields are typically the same). It can be seen that as the principal quantum number increases, the change in collisional velocity from the *initial* velocity at infinite distance decreases (in this case $\vec{v}_{\perp}(D \to \infty) = -3\times10^{-4}$ a.u.). Although the change in the collisional velocity profile between adjacent principal quantum numbers

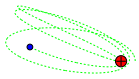

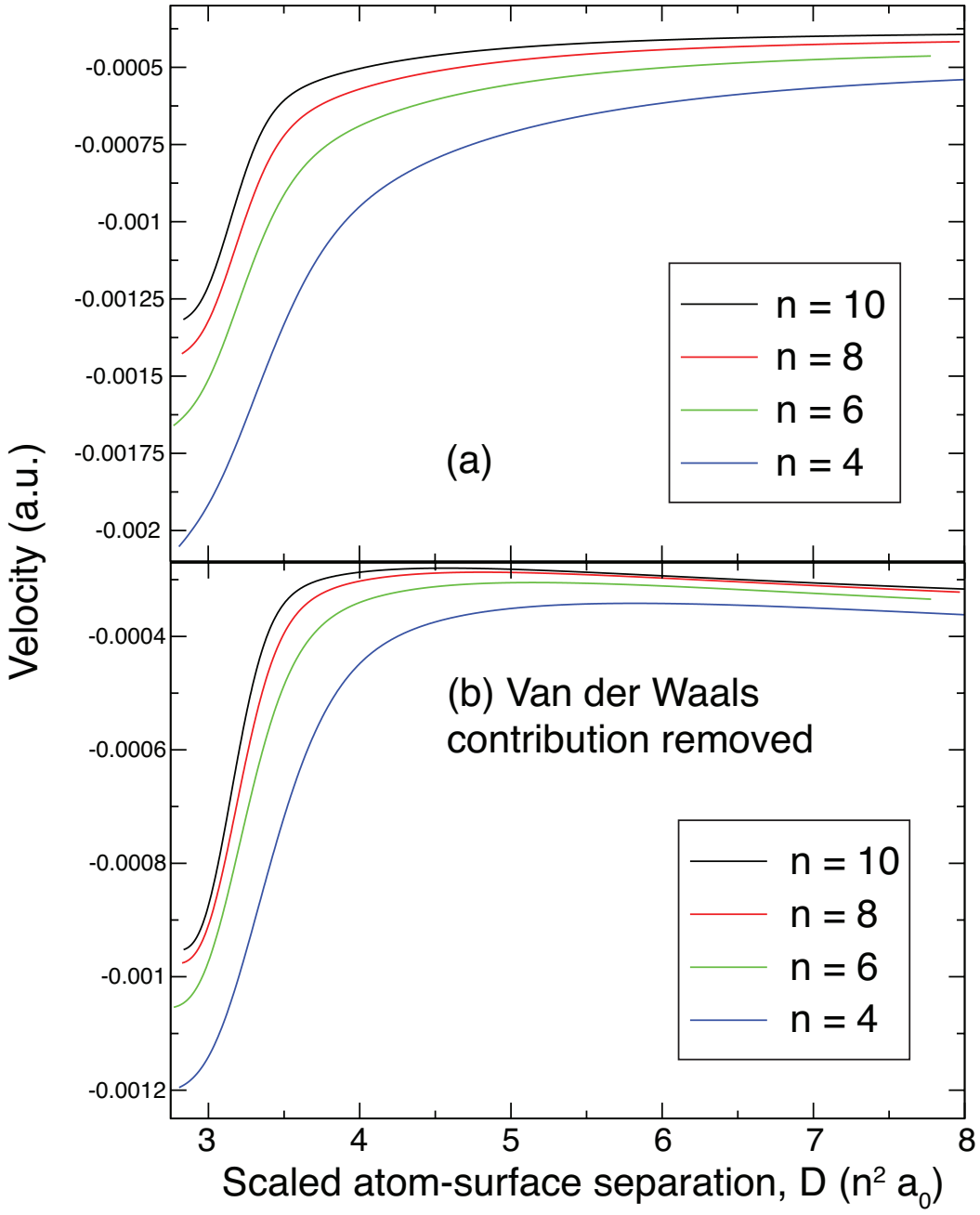

Figure 5.4: (a) Collisional velocity of the most surface-oriented, red-shifted state of $n = 4 - 10$ manifold as a function of scaled atom-surface separation at zero-field. The *initial* collisional velocity of atom is -3×10^{-4} a.u.. (b) Same as for (a) but with the Van der Waals component of the acceleration removed (see text). Note that with the Van der Waals contribution removed, the difference between the $n = 8$ and $n = 10$ results is much smaller.

also decreases with n, the difference is still significant between the results for $n = 8$ and $n = 10$. As explained in Section 3.7, there are two contributions to the acceleration of the ion-core; at long-range the acceleration is mainly dominated by the Van der Waals attraction ($\propto n^4/D^3$, see Eq. 1.12), and its variation with distance *does not* scale with n^2. While at the surface ionisation range of distances, which *does* scale with n^2 (see above), a much sharper acceleration occurs due to the un-shielding of the proton to its image-charge. The Van der Waals acceleration can be calculated from the Rydberg energy shift given by Eq. 2.1, and by applying the law of energy conservation: the change in kinetic energy of the ion core is equal to the change in the Rydberg electronic energy. Figure 5.4(b) shows the same collisional velocities curves as Fig. 5.4(a), but with the Van der Waals contribution removed. Although there is still a visible difference between the $n = 8$ and $n = 10$ curves, the difference is now much smaller. Without carrying out further calculations at higher principal quantum numbers, the most appropriate approximation for the collisional velocities of higher principal quantum numbers is from the $n = 10$ mean-field calculation with the Van der Waals contribution to the acceleration corrected for the n of interest (using Eq. 2.1).

Figure 5.5 shows the calculated ion-detection probabilities as a function of ion-extraction field for the $n = 20-36$ most red-shifted Stark state with an *initial* collisional velocity of 3×10^{-4} a.u., using the scaled ionisation distances and *corrected* collisional velocities (as a function of scaled extraction field) from the $n = 10$ mean-field wavepacket calculations. The OTB results are also shown for comparison (dashed lines). It can be seen that the wavepacket ion-detection probability profiles are broad (as for $n \leq 10$ (Fig. 5.3), and for the same reasons), and appear similar to the broad surface ionisation profiles observed experimentally [44, 47, 48, 50, 51]. These profiles are compared directly with the experimental results in Section 7.1.

A range of collisional velocities (380-650 ms^{-1} $\equiv$ (1.7-3)$\times 10^{-4}$ a.u.) is studied in the

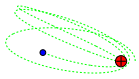

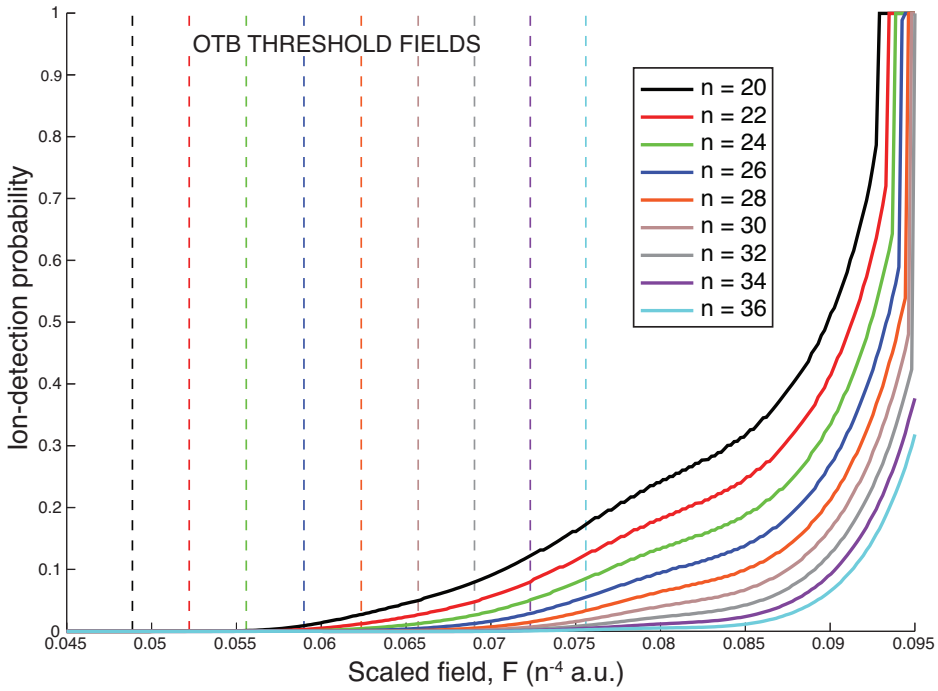

Figure 5.5: Ion-detection probabilities as a function of ion-extraction field, calculated for the $n = 20 - 36$ most red-shifted Stark state with an *initial* collisional velocity of 3×10^{-4} a.u., using the scaled results from the $n = 10$ mean-field wavepacket calculations. The OTB threshold fields are shown as dashed lines (the OTB ionisation probability is a step function at the threshold field). Note the broad width and the late onset of ion-signal for the mean-field results.

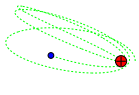

experimental work presented in Chapter 7. In principle, complete sets of mean-field wavepacket calculation should be carried out for the modelling of any given velocity, but this has not been carried out in this work. The shift in ionisation distance is less sensitive to the change in collisional velocity than the ion-detection probability (Eq. 1.15). Since a relatively small range of collisional velocities is considered experimentally, for the modelling of the experimental surface ionisation profiles in Chapter 7 with collisional velocities other than $\sim 3 \times 10^{-4}$ a.u. $\equiv 656$ ms^{-1}, the ionisation distances are assumed to be unshifted, while the *corrected* collisional velocities (see above) used to calculate the minimum detection distances for a given extraction field are simply shifted by the difference from the value of 3×10^{-4} a.u..

5.1.2 Extreme blue-shifted state

It is explained in Section 2.4 that the over the barrier approach, which can be carried out at the experimental range of principal quantum numbers, is only valid for the most surface oriented Rydberg states, which are localised near the potential barrier. However, by studying theoretically the wavepacket ionisation probabilities as a function of field for Stark states of other polarisations at lower quantum numbers, it may be possible to derive a similar scaling model as has been done above for the most red-shifted state.

Figure 5.6 presents the mean-field wavepacket propagation calculated ionisation probabilities for the most vacuum-oriented, blue-shifted state in the presence of various ion-extraction fields for principal quantum numbers of $n = 6 - 10$, at a typical *initial* velocity of 3×10^{-4} a.u. ($= 656$ ms^{-1}). The extraction field and atom-surface separation axes are scaled for clarity. The minimum detection distances for the corresponding ion-core velocities and the extraction fields are shown as cyan lines. It can be seen that ionisation typically occurs at separations $< 1.5n^2$ a$_0$, and the scaled dis-

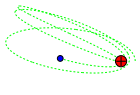

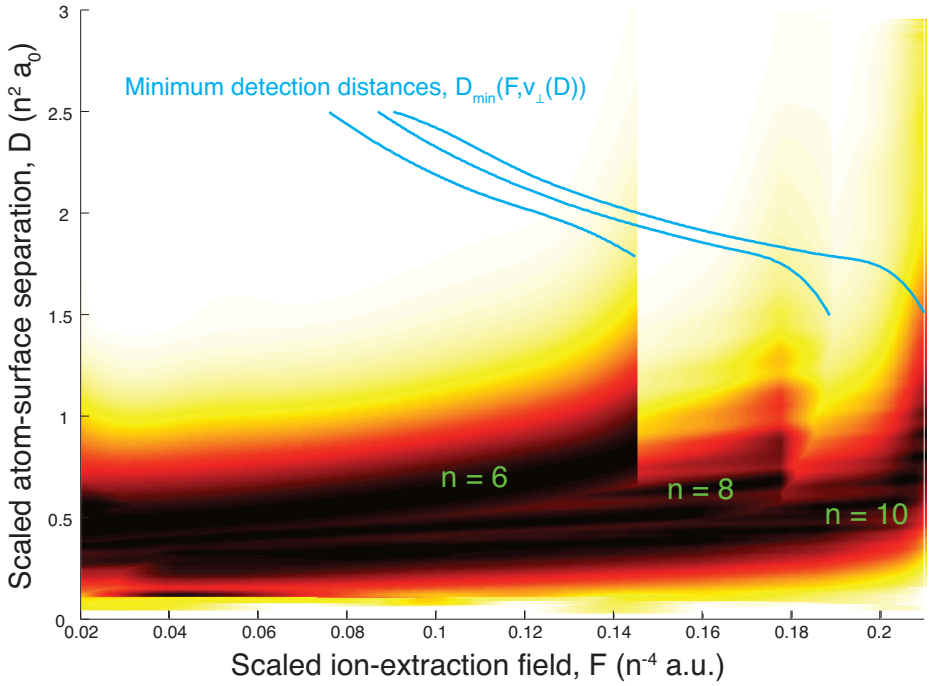

Figure 5.6: Density plot of the ionisation probability of the most vacuum-oriented, blue-shifted state of $n = 6 - 10$ manifold as a function of scaled ion-extraction field (by a factor of n^{-4}), calculated from the mean-field wavepacket propagation approach. The *initial* collisional velocity of the atom is 3×10^{-4} a.u.. The minimum detectable ionisation distances corresponding to the given ion-extraction field and velocity (as given by Eq. 1.15) are shown as full cyan lines.

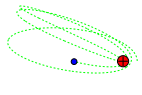

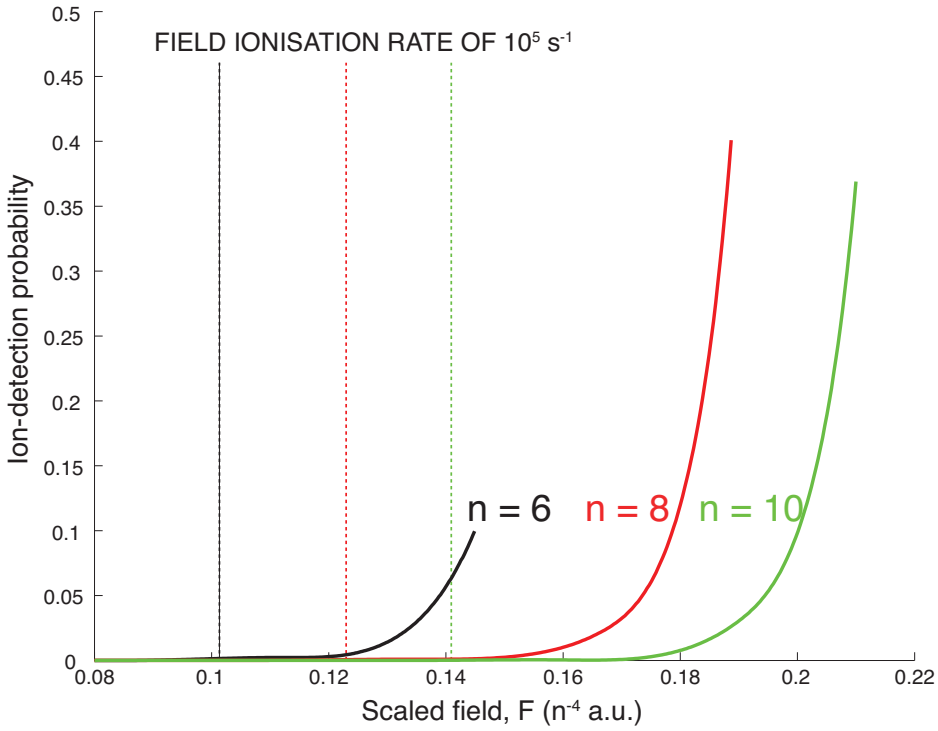

Figure 5.7: Ion-detection probability of the most vacuum-oriented, blue-shifted state of $n = 2 - 10$ manifold as a function of scaled ion-extraction field, calculated from the mean-field wavepacket propagation approach. The *initial* collisional velocity of the atom is 3×10^{-4} a.u.. The field values at which the field ionisation rate reached 10^5 s^{-1} calculated from Eq. 1.5 is shown as dotted lines.

tance decreases as n increases. However, similar to the red-shifted state, the ionisation probability shifts to larger distances (up to $3n^2$ a_0) for fields near the field ionisation limit for the given n. Figure 5.7 shows the corresponding ion-detection probabilities as a function of field for the $n = 6 - 10$ most blue-shifted Rydberg states.

It is important to note that the time-dependent wavepacket calculations only describe the Rydberg dynamics over a timescale of $\sim$ 10 ps before surface ionisation, while in the experiments, the time between Rydberg excitation and surface ionisation can be as large as 10 μs. Thus, under the experimental timescale, for a given magnitude of ion-extraction field, if the rate of field ionisation is $\sim\geq 10^5$ s^{-1} for the state of interest, then the Rydberg state is likely to be field ionised in the gas phase before getting

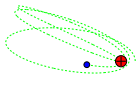

the chance to reach the surface. Figure 5.7 shows (by the vertical dotted lines) the critical field values for the most blue-shifted Stark states of the $n = 6 - 10$ manifolds at which the field ionisation rate reaches a value of 10^5 s^{-1} (calculated from Eq. 1.5). It can be seen that the minimum fields required for the onset of ion signal from the surface ionisation process are greater than the critical field values for a field ionisation rate of 10^5 s^{-1}. Thus, for H atoms with *initial* collisional velocity of 3×10^{-4} a.u., ions formed by surface ionisation are not expected to be observed for any given field (under the experimental timescale) for the most blue-shifted states of the $n = 6 - 10$ manifolds. Whether it is possible to observe an ion signal from the surface ionisation process for the most blue-shifted Stark states at the experimental range of principal quantum numbers depends on the scaling of the field ionisation limit and the ionisation distances with principal quantum number. But, as mentioned above (and shown by Fig. 5.6 and 5.7), the field at which there is a sharp rise in the ionisation distance appears to scale directly with the field ionisation threshold. Thus, an experimental surface ionisation signal is generally not expected for the most blue-shifted states of a given n-manifold.

5.2 Local surface fields and surface roughness

As discussed in the Section 1.6, past experimental works of Hinds and coworkers [37–39], Tauschinsky *et al.* [11], Kocher *et al.* [41, 42], Gray *et al.* [43] and Dunning and co-workers [46–48] have all found that the interactions and the ionisation dynamics of Rydberg atoms at metal surfaces are highly sensitive to the presence of local surface fields, which may be from the presence of adsorbates, surface defects or the polycrystalline nature of the surface [60, 61, 94]. These localised fields can extend far into the vacuum, and patch fields for typical evaporated surfaces (such as the gold surface studied in Chapter 7) have been shown to vary as D^{-2} [48, 60] (see Fig. 5.8), exhibiting the

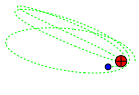

same scaling as the image-charge fields. For Rydberg states with principal quantum numbers $n = 20 - 40$ (studied in this thesis), the charge transfer process typically occurs in the range of ∼60-400 nm, and so is likely to be susceptible to local surface fields. Additionally, the detection of the charged particles (protons or electrons) will also be strongly affected (see Eq. 1.14).

In Chapter 7, an experimental study of the surface ionisation of Rydberg H atoms at a rough machined aluminium surface (roughness is of the order of μm) is studied to compare with the results of the nearly atomically flat gold surface. Although theoretically it is possible to include the effects of stray fields and / or surface structure in the wavepacket propagation calculations, it would require a full three-dimensional calculation (currently the cylindrical symmetry of the surface potential reduces the system to two-dimensions), thus significantly increasing the computational load. Instead, to gain some qualitative insight on the effects of local surface fields and surface roughness on the ionisation dynamics and ion-detection, Monte Carlo trajectory simulations with the incorporation of the classical over-the-barrier approach are carried out in this section, following the work of Dunning and co-workers [46–48]. The trajectory calculation developed in this section, is used as a qualitative comparison with some of the experimental results in Chapter 7.

5.2.1 Stray field potential

Dunning and co-workers have recently measured the surface potential variations at a nearly atomically flat evaporated Au(111) surface [48] (Fig. 5.8), and have shown that the incorporation of the resulting local fields in the trajectory simulations produces results that are in good agreement with the experimentally observed ionisation profiles for the xenon atom (detected ion signal as a function of extraction field). The surface potentials of the evaporated gold surface used in the experimental studies of this thesis

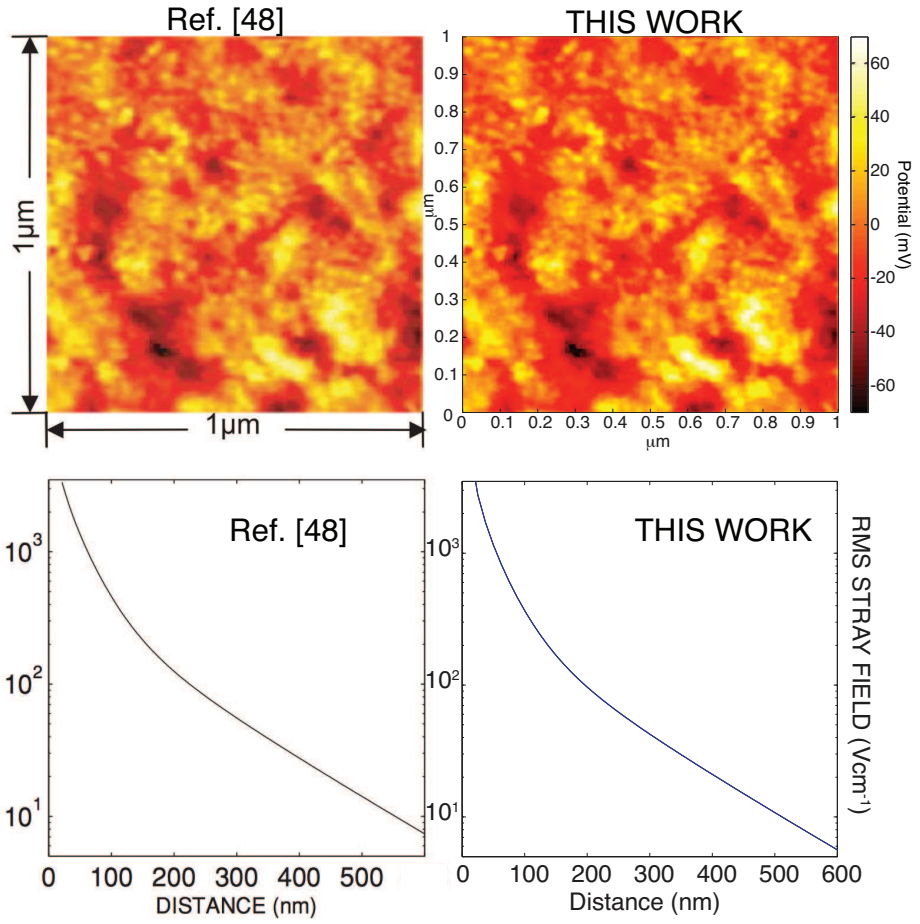

Figure 5.8: Top left: The surface potential of a deposited gold surface measured in Ref. [48] using Kelvin probe force microscopy [94]. Top right: The surface potential used in this study extracted from Ref. [48]. Bottom left: the calculated root-mean-squared (RMS) stray field in Ref. [48]. Bottom right: the calculated RMS stray field in this work.

have not be measured, but the characteristics are likely to be similar to surface used by Dunning and co-workers [60, 61]. As such, the surface potential data from Ref. [48] is used as a model system in this work.

Figure 5.8 presents the measured the surface potentials from Ref. [48] and the 'extracted' surface potentials used in this study [1]. It can be seen that the two images are nearly identical, and there appears to be negligible loss in resolution of the data.

[1]The raw data from Dunning and co-workers are not available, instead a 245 × 245 pixels image of the measured surface potential is copied from Ref. [48].

However, the image in Ref. [48] is generated from a $N \times N \equiv 512 \times 512$ matrix spanning an area of 1 μm^2, while the resolution of the 'extracted' image used in the present study is $N \times N \equiv 245 \times 245$ pixels spanning the same area. The consequence of this lower resolution will be shown below.

To compute the local surface fields, it can be noted that a surface potential provides a boundary condition for Laplace's equation

$$\frac{\partial^2 \phi}{\partial x^2} + \frac{\partial^2 \phi}{\partial y^2} + \frac{\partial^2 \phi}{\partial z^2} = 0, \tag{5.1}$$

which for $z > 0$ (requiring that $\phi(z \to \infty) = 0$) is satisfied by linear combinations of periodic functions of the form [48]

$$\begin{aligned} \phi(x,y,z) &= \sum_i \sum_j [A_{i,j} \cos(k_{xi}x + k_{yk}y) + B_{i,j} \sin(k_{xi}x + k_{yj}y)] \exp[-k_z(i,j)z] \\ &= \sum_i \sum_j \mathrm{Re}\{(A_{i,j} + \mathrm{i}B_{i,j}) \exp[-\mathrm{i}(k_{xi}x + k_{yj}y)]\} \exp[-k_z(i,j)z] \\ &= \sum_i \sum_j \mathrm{Re}\{C_{i,j} \exp[-\mathrm{i}(k_{xi}x + k_{yj}y)]\} \exp[-k_z(i,j)z] \end{aligned} \tag{5.2}$$

where $k_z(i,j) = \sqrt{k_{xi}^2 + k_{yj}^2}$. Discrete values of $\phi(x,y,0)$ are taken from the 'extracted' image (top right plot of Fig. 5.8), and the complex coefficients $C_{i,j}$ in Eq. 5.2 can be determined straightforwardly from discrete 2D Fourier transform

$$C_{i,j} = \frac{1}{N^2} \sum_{n=0}^{N-1} \sum_{m_l=0}^{N-1} \phi\left(\frac{nL}{N}, \frac{nL}{N}, 0\right) \exp\left[2\pi\mathrm{i}\left(\frac{ni+mj}{N}\right)\right], \quad i,j = 0,1,...,(N-1). \tag{5.3}$$

The potential at any point (x,y,z) above the surface can then be calculated from the real component of the inverse 2D Fourier transform

$$\phi(x,y,z) = \mathrm{Re}\left\{\sum_{i=0}^{N-1} \sum_{j=0}^{N-1} C_{i,j} \exp\left[-2\pi\mathrm{i}\left(\frac{ix+jy}{L}\right)\right] \exp[-k_z(i,j)z]\right\} \tag{5.4}$$

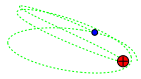

where $k_z(i,j) = \frac{2\pi N}{L}\sqrt{i'^{\,2} + j'^{\,2}}$, with $i' = \mathrm{mod}(0.5 + \mathrm{i/N}, 1)$ and $j' = \mathrm{mod}(0.5 + \mathrm{i/N}, 1)$ (where mod(a, b) is the modulus after division), since the maximum frequency component is half of the sample frequency [66].

Figure 5.8 compares the root-mean-squared (RMS) stray field calculated in the present study with those of Ref. [48]. The effect of a lower resolution of data points from the 'extracted' image can now be seen: the RMS stray field calculated in this work is slightly lower than of Ref. [48], and at a distance of 600 nm the difference is $\sim$2 Vcm^{-1}. But since the general form and magnitude of the fields are very similar, it does not pose a problem for the current qualitative study.

5.2.2 Over-the-barrier ionisation

For the calculations presented below, only the most red-shifted Stark state of a given n-manifold, for which the classical over-the-barrier (OTB) approach is approximately valid (see Section 2.4), is considered.

Dunning and co-workers have found that the main effect of the stray fields that brought good agreement between the experiments and theory, was the introduction of a range of detection and ionisation distances (which are also larger under the influence of stray fields). This can be compared with Figure 2.2 which shows only a single OTB ionisation distance and minimum detectable distance (for which a proton at a given velocity can be extracted) at any given ion-extraction field. This broadening of ionisation and detectable distances results in a range of critical detection fields, and so the ionisation profiles (ion detection signal *vs* extraction field plots) are no longer step functions, as given by Eq. 2.9. These findings are discussed in more detail below.

For the trajectory simulations, although it is possible to calculate the ionisation distance for each individual trajectory 'on-the-fly', for a large number of trajectories, it

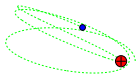

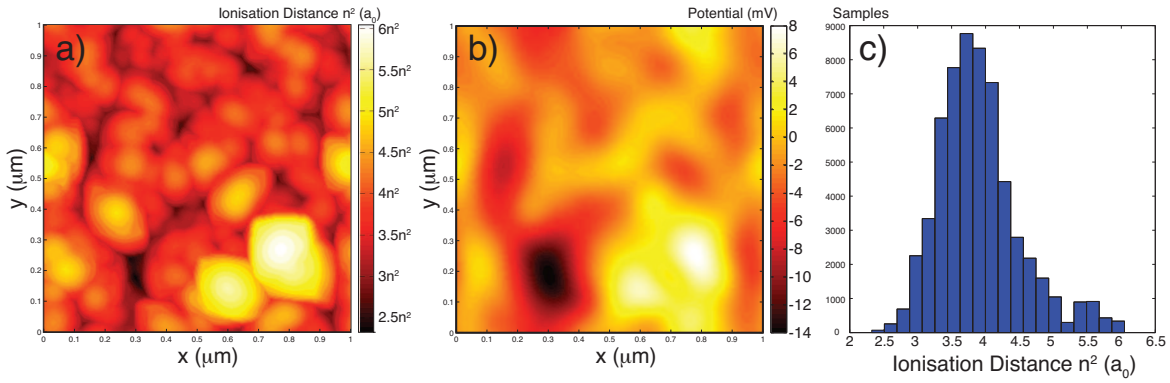

Figure 5.9: (a) The over-the-barrier 'ionisation surface' for the $n = 20$ H Rydberg state under the influence of the surface potential given in Fig. 5.8. No externally applied extraction field is present. (b) The surface potential calculated from Eq. 5.4 at distance of $1600 \equiv 4 \times 20^2$ a_0. (c) Histogram of the ionisation distances from the 'ionisation surface' shown in (a). Note that the OTB ionisation distance without the influence of stray fields is $3.48n^2$ a_0.

is more efficient to pre-compute the ionisation distances at any (x, y) position above the surface. For a given principal quantum number n and electric field F, an 'ionisation surface' is calculated, which gives the maximum height above the surface (at the particular (x, y) coordinate) at which the energy of the most-extreme red-shifted Stark state is greater than the saddle point energy. Since the potential energy surface is inhomogeneous due to the presence of the stray field, the saddle point does not necessarily lie along the z-axis, and its position and energy is found numerically from a search procedure. Figure 5.9(a) and 5.9(c) shows the 'ionisation surface' and the corresponding histogram of the ionisation distances for the $n = 20$ Rydberg state under zero externally applied electric field. Note that the ionisation distances vary greatly from the zero-field OTB ionisation distance of 3.48 n^2 (Section 2.1). Unsurprisingly, the 'ionisation surface' maps onto the $\phi(x, y, z = 0)$ surface potential shown in Fig. 5.8, where negative (positive) surface potential regions induces ionisation closer to (further from) the surface. The resolution of this 'mapping' is dependent on the size of the Rydberg atom. Firstly, it can be seen from Eq. 5.4 that the z-component of

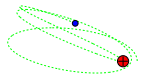

the surface potential decays more slowly for lower frequency components, and so for larger Rydberg states which ionise further from the surface, the variation in surface potential that the Rydberg state 'sees' is more 'washed out'. This is illustrated by Fig. 5.9(b) which shows the surface potential at $4n^2 \equiv 1600$ a_0. There is a second effect, which is based on the fact that the direction of passage over the saddle point does not have to lie along the z-axis, and so each data point of the 'ionisation surface' actually represents the effect of the nearest and most positive area of surface potential that can lead to the earliest ionisation. This uneven sampling of the surface potential explains why the histogram in Fig. 5.9(c) does not spread evenly about the 3.48 n^2 a_0 OTB ionisation distance calculated for the absence of stray fields.

5.2.3 Rydberg and ion trajectories

Monte Carlo trajectory calculations are carried out to model the effects of the stray fields on the ionisation distances sampled and the ion extraction probabilities. In the implementation, a random set of initial x_0, y_0 positions are chosen, and the initial height z_0 is set at $30n^2$ a_0. The direction of the parallel velocity vector on the xy-plane is also randomly chosen. When comparing with the experimental results in Chapter 7, the Rydberg normal incidence angle θ and the parallel and perpendicular velocity components are chosen randomly from a model angular and velocity distribution (pre-determined from Monte Carlo simulation, see Section 6.1.4). Here, the normal incidence angle θ and magnitudes of the parallel and perpendicular velocity components are fixed in order to focus on purely the effects of the local surface fields. As a first approximation, and following Ref. [48], the Rydberg atom is assumed to follow a straight-line trajectory towards the surface at the constant initial velocity. However, this cannot be justified for polarised Stark states under the influence of the local surface and image-charge fields (of the order of $10^2 - 10^3$ Vcm^{-1}) which can

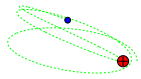

strongly perturb the Rydberg trajectory and accelerate or decelerate the atom towards the surface [95–97]. The inclusion of field perturbations on the Rydberg trajectories is discussed further in Section 7.1.

The Rydberg atoms are assumed to ionise when the trajectories intersect the pre-computed 'ionisation surface' of the given field. These points of intersection provide the starting conditions of the ion trajectory calculations, which are carried out using Matlab's^{TM} ODE45 differential equation solver (which is based on the Runge-Kutta method [66]). The trajectories of the positive ions are affected by their image charge attraction towards the surface ($-1/(4D)$), the applied ion-extraction field, *and* the local surface fields. The trajectory calculation is terminated either when the ion crashes into the surface ($z = 1$ to avoid the image-charge singularity), or when the ion's velocity *away from* the surface is greater than 1000 ms^{-1}, when it is assumed that the ion escapes the surface and is detected.

Figure 5.10(a) shows a log density plot of all the ionisation distances of the $k = -19, n = 20$ Stark state sampled by trajectories at a normal incidence angle of $\theta = 15°$ as a function of electric field. It can be seen that, although the overall variation with field follows the case with no local surface fields (full blue line), there is now a large spread of ionisation distances ($\sigma \sim n^2$ a$_0$), and the mean ionisation distance is $\sim 0.5n^2$ a$_0$ larger than before. The effect of the local surface fields on the ion detection probability can be seen by comparing Fig. 5.10(a) with Fig. 5.10(b), which shows only the trajectories in which the ion with initial perpendicular velocity of $v_\perp = 3\times10^{-4}$ a.u. $\equiv 656$ ms^{-1} (typical for the experiments) escapes the surface and is detected (the total velocity $v = 2535$ ms^{-1}, and $v_\perp = v\sin\theta$). The minimum detectable distance cutoff is broadened by the local surface fields when compared with the value of $D_{\min}(F, v_\perp)$ given by Eq. 1.15 (green dotted line in Fig. 5.10): some trajectories below the line are detected, while not all trajectories above the line are detected.

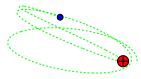

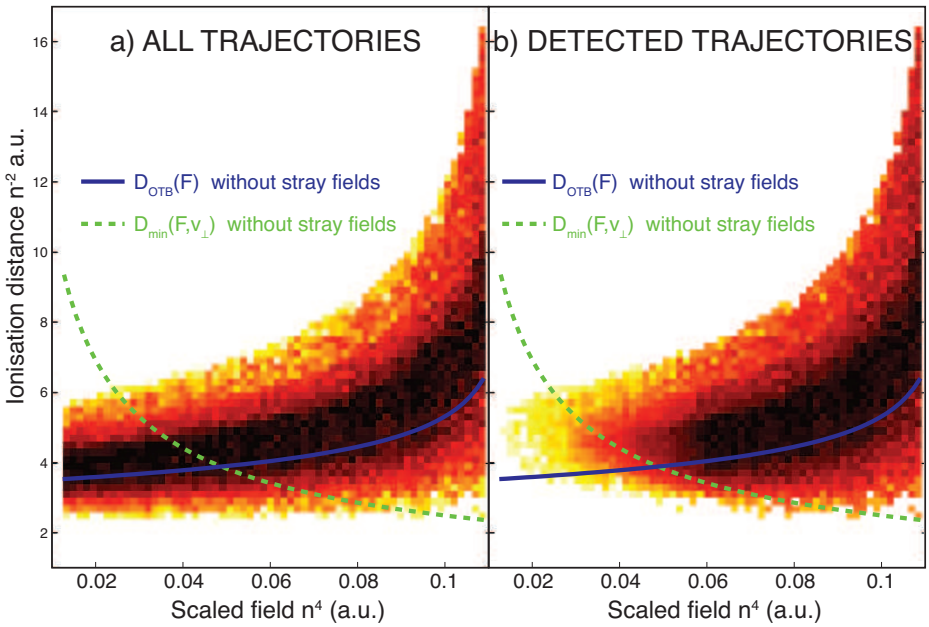

Figure 5.10: (a) Log density plot of all the ionisation distances of the $k = -19, n = 20$ Stark state sampled by trajectories at a normal incidence angle of 15° as a function of electric field, calculated using the OTB approach with the inclusion of the local surface fields from Ref. [48]. The calculation at each field consists of 1000 trajectories. The OTB distance calculated with no stray fields is shown as full blue line. The minimum detectable distance with no stray fields ($D_{\min}(F, v_\perp)$, given by Eq. 1.15) for a perpendicular velocity of $v_\perp = 3 \times 10^{-4}$ a.u. $\equiv 656$ ms^{-1}, is shown as dashed green line. (b) Same as (a), but only for trajectories in which the ion is detected (the ion escapes the surface).

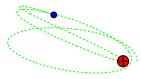

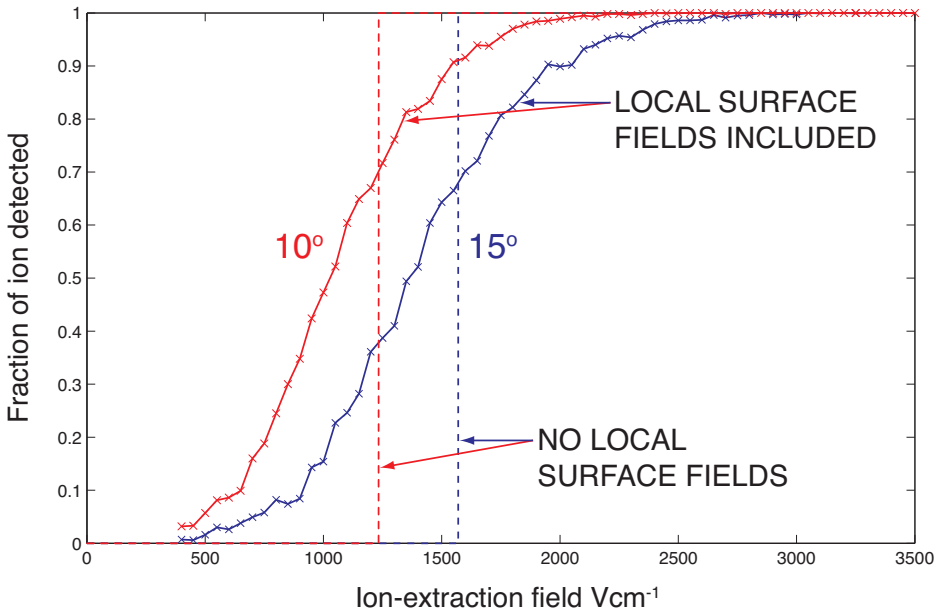

Figure 5.11: Fraction of ions detected as a function of extraction field, calculated for the $k = -19, n = 20$ Stark state, with a *total* velocity of $v = 2535$ ms^{-1} ($v_\perp = v \sin\theta$). Red and Blue full lines: results of the OTB calculations with the inclusion of local surface fields (Eq. 5.4) for trajectories at normal incidence angles of $\theta = 10°$ and $15°$ respectively. Red and Blue dotted lines: the corresponding results with the presence of no surface fields.

5.2.4 Simulating the experimental ion signal

The density plot of the detected ions shown in Fig. 5.10(b) can be summed along the 'ionisation distance' dimension to give a 2D line plot of the fraction of detected ions as a function of field (corresponding to the experimental 'surface ionisation profile'). Figure 5.11 shows the calculated surface ionisation profile for the $k = -19, n = 20$ Stark state at a normal incidence angle of $\theta = 10°$ (red full line) and $15°$ (blue full line) with a *total* velocity of $v = 2535$ ms^{-1} ($v_\perp = v \sin\theta$), compared with the corresponding OTB results without the inclusion of local surface fields (dashed lines). Instead of a step function, the profiles with the inclusion of local surface fields appear much broader (resembling a cumulative normal distribution) and the mean field positions are shifted to lower fields (larger ionisation distances).

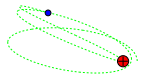

Figure 5.11 shows that the calculated profile with the inclusion of surface fields for the shallower 10° normal incidence trajectories is not simply a shift of the 15° curve. Two effects are at play. Firstly, the ionisation distances sampled by the trajectories are strongly dependent on the grazing angle of the Rydberg states: shallower incidence angles are much more likely to sample the peaks of the 'ionisation surface', leading to a much larger average ionisation distance compared with steeper trajectories. Secondly, although the overall extraction probability increases for shallower incidence angles as the kinetic energy in the direction normal to the surface decreases (see Eq. 1.14), there is also a greater broadening of the minimum detectable distance, since the ion has a higher probability of moving across local field regions that favour detection and regions that are more attractive towards the ion (hindering detection). Therefore, it can be seen that by carrying out trajectory simulations, it is possible to gain insight into some of the more subtle effects of local surface fields on the ionisation distance and the detection probability.

It is important to note that the trajectory calculations carried out above based on the classical OTB approach, by no means give a complete picture of the ionisation dynamics, and should be taken as a guide for elucidating some of the effects of local surface fields. The deficiencies of the OTB approach have been discussed in Section 2.4, and a direct comparison of the OTB approach with wavepacket calculations is presented in Section 5.1. Specifically in this case, the classical model above only takes into account the effect of the local fields on the height of the saddle point, and thus the classical ionisation distance. There are additional effects of the local surface fields that have not been considered, but can strongly affect the charge transfer process. For example, the introduction of an inhomogeneous electric field will cause mixing between Rydberg states of differing m_l values [98], which can result in the mixing of Rydberg polarisations as the surface is approached (*c.f.* the non-hydrogenic case in Chapter 4),

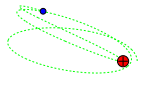

leading to a range of ionisation distances. The extent of this inhomogeneous field mixing can be estimated by carrying perturbative calculations such as those by Merkt and Zare [98]. Such perturbative calculations, and incorporation of stray surface fields into the wavepacket propagation approach, will be a focus of future investigations.

5.2.5 Modelling surface roughness

It has been observed experimentally, that the experimental ion detection profiles are broader and are shifted to lower extraction fields for a rough surface [44, 50]. These observations appear quite similar to the effects of the local surface fields that are studied in the previous section. Indeed, surface corrugations can lead to large local surface fields, particular at edges and steps [99]. But clearly, there are other intrinsic effects that could be at play, such as the introduction of a range of effective incident angles relative to the *local* surface plane. To investigate this, it is possible to apply similar trajectory simulations as the previous section to model the effect of surface roughness.

A rough surface plane can be crudely modelled by a set of smoothly varying periodic functions

$$z_{\text{rough}}(x, y) = h \sin(2\pi x/L) \sin(2\pi y/L) \tag{5.5}$$

where h is the amplitude of the corrugation about the average surface plane position $z = 0$, and L is the period of the corrugation along the x, y-dimensions. As a first approximation, the ionisation distance can be assumed to be unaffected, except by the effective height relative to the surface, and is simply given by

$$D_{\text{OTB}}^{\text{rough}}(x, y, F) = D_{\text{OTB}}(F) + z_{\text{rough}}(x, y), \tag{5.6}$$

where $D_{\text{OTB}}(F)$ is the over-the-barrier ionisation distance for a flat surface in the

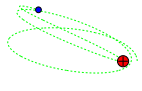

presence of an electric field F (Section 2.1). Note that unlike the local surface fields model presented in the previous section, the ionisation distances determined here does not include the possibility that the saddle point might not lie along the ion-core–surface normal axis, as a result of the full three dimensional potential for the corrugated surface. The ionisation distances given by Eq. 5.6 correspond to the 'ionisation surface' for the Rydberg trajectories at field F (which, in this case, directly maps the rough surface plane). The image-charge potential can also be assumed to be shifted by the surface corrugation in the same manner, such that the proton–image-proton interaction is given by

$$V_{pp}^{\text{rough}}(x, y, D) = -\frac{1}{4[D + z_{\text{rough}}(x, y)]}. \tag{5.7}$$

Thus, using the image-charge potential given by Eq. 5.7, ion trajectories can be carried out in the same way as the previous section.

It should be noted that although the rough surface calculation strongly resembles the local surface stray field calculation carried out in the previous section, the absolute magnitude of potential variation at the surface is replaced with the amplitude of the rough surface, and the size of the areas of positive and negative potentials are replaced with the periods of the surface modulation; they are subtly different. For the local surface fields calculations, the positive (negative) potential regions increase (decrease) both the ionisation distance and the ion extraction probability, and so even at an incidence angle of $\theta = 90°$ the ionisation profiles would be broadened (see Fig. 5.11). In contrast, for the rough surface model, the ionisation distance and the ion extraction probability above the *local* (x, y)-surface plane are the same as for a flat surface, and deviations of the ionisation profiles from a step function only occur as a result of the grazing trajectory ($\theta < 90°$).

Figure 5.12 shows the calculated ionisation profiles for the $k = -19, n = 20$ Stark state 15° incident at rough surface for various surface roughness parameters (L, h)

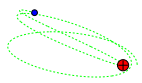

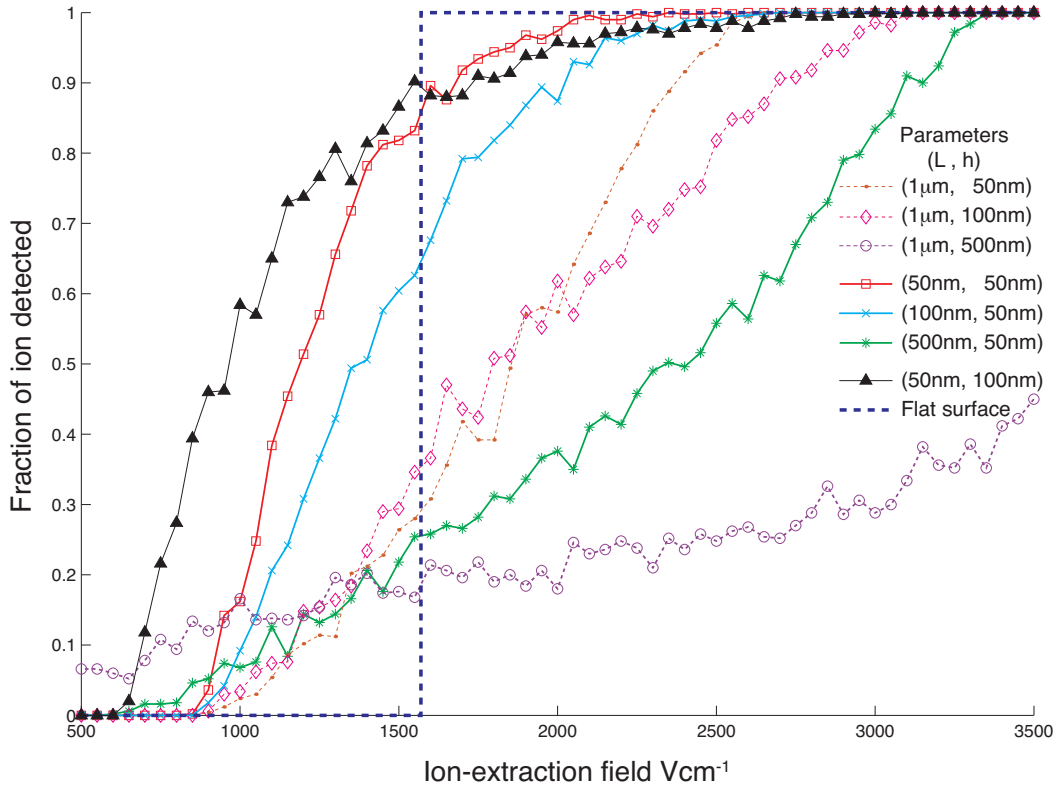

Figure 5.12: Fraction of ions detected as a function of extraction field, from trajectory simulations of the $k = -19, n = 20$ Stark state 15° incident at a rough surface modelled by various surface roughness parameters (L, h). The *total* velocity of the atoms is $v = 2535$ ms^{-1} ($v_\perp = v \sin\theta$). The blue dotted line is the expected step function for a flat surface.

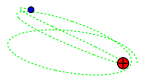

compared with a flat surface. It can be seen that indeed the surface ionisation profile is broadened, but the average ionisation distance is not always larger than a flat surface (with larger ion signal at lower fields, as observed experimentally), but is very sensitive to the period of the surface roughness L, and its ratio with surface roughness amplitude (h/L). In fact for periods $L = 1$ μm, the average ion-detection field is smaller than the flat surface. However, as L decreases and h increases, the ion detection signal shifts to lower fields (see Fig. 5.12), as observed experimentally. This can be explained by considering the geometry of the Rydberg trajectories. For Rydberg trajectories at grazing incidence angle θ, the largest fraction of ions collected corresponds to the case when the largest ionisation distances are sampled (the peaks of the rough surface); the grazing trajectory can then take the ion towards the troughs where the ion-detection probability is higher. And the highest probability of ionising at the peaks of the rough surface is when the amplitude of the surface modulation is high and the period is low. Thus, the model above (despite its crudeness), may give some indication of the relationship between the lateral and vertical variations of the experimental rough surface (although the experimental profile would have contributions from the local surface field effect as well). This is discussed in more detail in Section 7.6.

5.3 Conclusions

Ionisation distances as a function of ion-extraction field are calculated using the mean-field wavepacket propagation approach for the most extreme red- and blue-shifted Stark states of the $n = 2-10$ manifold. Comparing the results for the most red-shifted state with OTB predictions shows that although there is qualitative agreement with the wavepacket results, the OTB calculations overestimates the ionisation distances for high n values. Plotting the wavepacket results on scaled axes, such that the ionisation distance is scaled by n^2 and the electric field is scaled by n^{-4}, show that as the

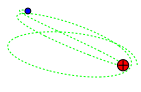

principal quantum number increases, the difference between the ionisation distances calculated for adjacent n value decreases, such that the scaled results obtained for $n = 10$ can be used as an approximate model for higher principal quantum numbers. The corresponding ionisation profiles (ion detection probability as a function of extraction field) obtained from the mean-field calculations are found to be broad (unlike the step function predicted from the OTB approach), as a result of the acceleration of the ion-core when approaching the metal surface.

For the most blue-shifted Stark state, surface ionisation occurs very close to the surface (typically $< 1.5n^2$ a_0). It is found that the corresponding field required to extract the ions is beyond the field ionisation threshold (the field ionisation lifetime of the Rydberg state is less than the typical time required to travel from the experimental excitation point to the surface). Consequently, the detection of ions from the surface ionisation of the most blue-shifted Stark state at the experimental range of principal quantum numbers is not expected to be possible.

Following the work of Dunning and co-workers [48], an over-the-barrier trajectory approach with the incorporation of local surface field effects is developed. The measured surface potential variations from Ref. [48] are used in the model. It is found that the surface fields both increase, and broaden the range of, the ionisation distances. The ion-detection probability is also strongly affected, such that at any given extraction field, there is range of detectable distances (rather than a single one, see Eq. 1.15). Consequently the corresponding plot of detected ion-signal versus extraction field (surface ionisation profile) resembles a cumulative normal distribution with width of the order of n^2 a_0 instead of a single step function (which is the OTB result without the effects of surface fields).

The trajectory calculations are modified to model the effects of surface roughness. It is found that the surface ionisation profiles are very sensitive to the vertical and lateral

variations of the model surface. Thus, comparison with the experimental profiles in Section 7.6 may provide information on the characteristics of the rough surface.

Chapter 6

Experimental details

In this chapter, details of the experimental study of the surface ionisation of Rydberg hydrogen atoms at metal surfaces are outlined. The experimental results are presented and discussed in the following chapter.

6.1 Experimental setup

The experimental work presented in this chapter has been performed in a new UHV apparatus; a schematic diagram of the experimental setup is shown in Fig. 6.1. Figure 6.2 presents a computer-aided design drawing of the experimental setup, and shows more explicitly the relative geometry of the gas beam, laser beams, metal surface and detection assembly.

6.1.1 Hydrogen atomic beam

The hydrogen atom source is based on the setup of Merkt and coworkers [100]. The H atoms are created by photodissociation of either pure ammonia, or seeded in a supersonic molecular beam of rare-gas (typically the rare-gas to ammonia ratio is $\sim (10-20):1$ respectively). The backing pressure is $\sim$ 800 mbar for pure NH_3,

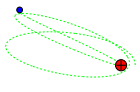

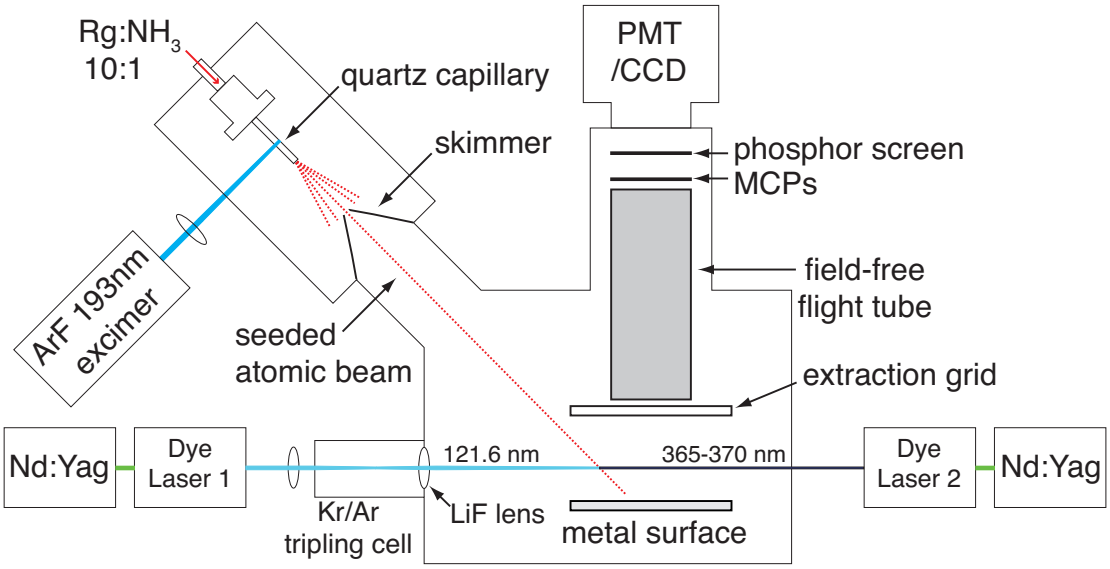

Figure 6.1: Schematic diagram of the experimental setup.

and is $\sim$ 2 bar for the rare-gas seeded beam. A faceplate with a 1 mm diameter aperture is mounted on a pulsed-solenoid valve (General Valve, Series 9) operating at 10 Hz, with pulse width of $\sim$ 100μs. On the faceplate, matching the position of the aperture, sits a 15 mm long, 1 mm inner diameter quartz capillary (Vitrocom CV1012S). The photodissociation of ammonia ($NH_3 \rightarrow NH_2 + H$) takes place within the quartz capillary, and is carried out by a weakly focused (by a fused silica spherical lens $f = 200$ mm) ArF excimer laser (GAM Ex5, 10Hz, $\sim$8 ns pulse width), operating at 193 nm and providing (4-5) mJ of energy per pulse. At a distance of $\sim$ 3 cm after the expansion at the end of the capillary, the atomic beam passes through a 1 mm diameter skimmer and travels a further 46 ± 0.8 cm to the interaction region of the UHV chamber.

In the interaction region, the H atoms are directed towards the target surface and are excited $\sim$2 mm from the surface to high Rydberg states with a two-laser excitation scheme (see next section). The surface is mounted on a xyz-vacuum manipulator and a rotation stage, and so the position of excitation relative to the surface and the

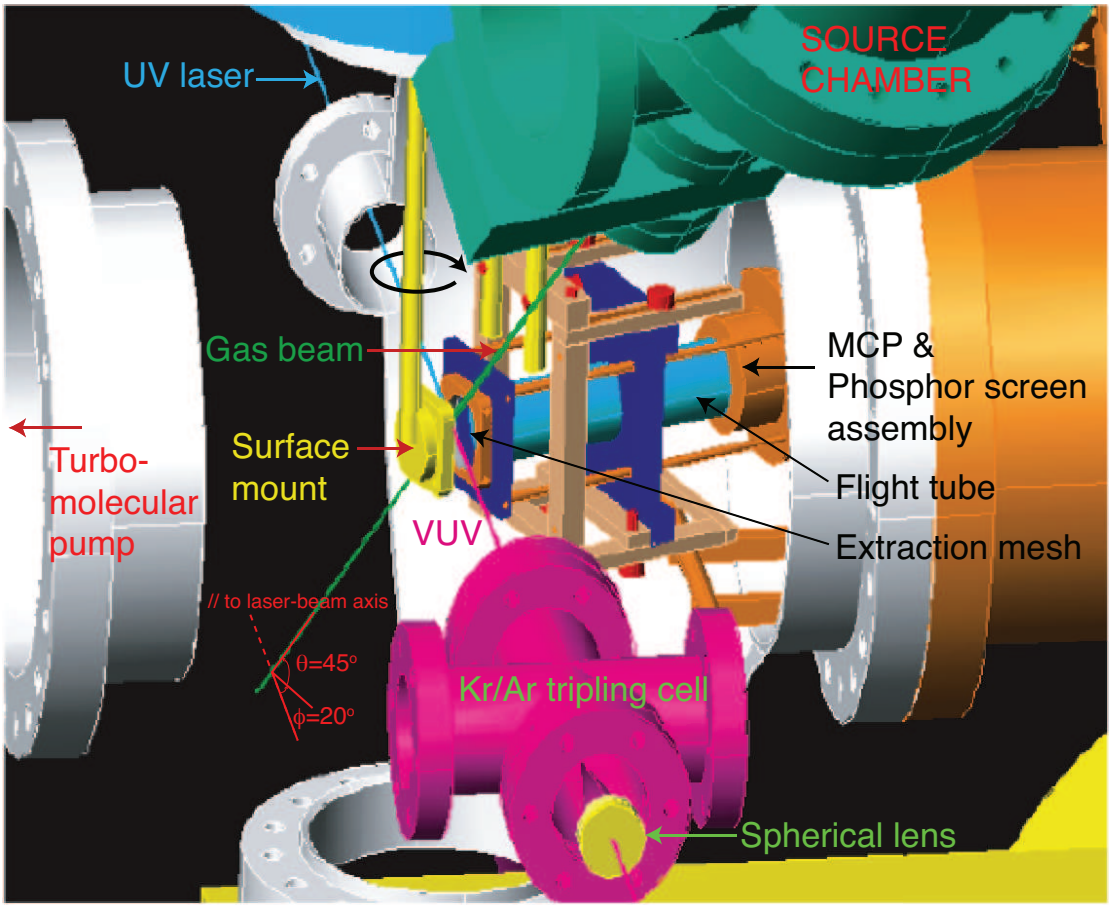

Figure 6.2: CAD drawing of the experimental setup. Note that the surface is mounted vertically, and the laser beams passes through the main chamber horizontally. The propagation axis of the gas beam is at a polar angle of $\theta = 45°$, and azimuthal angle of $\phi = 20°$ with respect to the laser beam axis. In the drawing, the surface and the detection assembly are rotated with respect to the laser beams to illustrate the rotation axis. In the experiments, the typical arrangement is with the surface plane parallel to the laser beam axis.

grazing incidence angle (and thus the velocity component perpendicular to the surface) can be varied. The collisional velocity of the atomic beam can also be modified by using different seeding gases and / or changing the time delay of the Rydberg laser excitation with respect to the photodissociation laser, such that the Rydberg trajectory over the surface (*i.e.*, the spread of incident positions and angles) is kept constant (see Section 6.1.4).

6.1.2 Charged particle detection

Typically ∼500 ns after the laser excitation (see Section 6.1.5), a variable pulsed potential (±4500 V, ramped up over a period of ∼100 ns [64]) is applied to the surface (1″ diameter), such that the Rydberg atoms can be detected as protons or electrons from field ionisation, or from surface ionisation if the field is sufficiently large to pull the protons or electrons away from the surface (but not large enough for field ionisation). Note that the surface interaction therefore occurs in the presence of the extraction field. To achieve a homogeneous field in the interaction region, a grounded extractor mesh (Precision Eforming nickel mesh 86.1% transmission), of the same size as the surface (1″ diameter), is mounted 1 cm away with its plane parallel to the metal surface. The extracted charged particles then pass through a second mesh at the entrance of the field-free flight-tube (∼0.3 cm away, see Fig. 6.1), which is held at the front micro-channel plate (MCP) voltage for ion-extraction, or is grounded for electron-extraction. The reason for a second stage of acceleration for ion-detection before passing through the field-free flight tube, is that, due to the large range of ion-extraction field that is studied (20-4500 $\mathrm{Vcm^{-1}}$), the protons can have very different arrival times at the MCP detector (lower extraction fields lead to later arrival time), making it difficult to set a single time-gate for each scan of field versus surface ionisation signal (see Section 6.2.1). Electrons are much lighter and do not suffer from this. By accelerating

through a second stage of homogeneous field before passing through the field-free flight tube, the extracted protons exhibit flight times that are roughly independent of the surface extraction field.

After ∼12 cm of field-free flight, the charged particles arrive at a set of micro-channel plates (Burle [MCP18/12/10/5 I 40:1 MS], 18 mm active diameter), and the resulting electrons hit a phosphor coated fibre-optic rod (P-47 coating). For ion-detection, the front MCP, back MCP and phosphor screen are typically held at potentials of -1200 V, 0 V and +3000 V respectively. For electron-detection, the front MCP, back MCP and phosphor screen are typically held at potentials of 0 V, +1300 V and +3800 V respectively. To detect the fluorescence from the phosphor screen, the back of the phosphor screen is optically coupled via flexible fibre optics (Beam Imaging Solutions, HRBIS-10000 series probe head, with a 9.1 mm × 6.6 mm viewable area) to a photomultiplier tube (PMT). The amplified output of the PMT is connected to a digital oscilloscope (Lecroy Wavesurfer 452), and the acquired data is transfered to a computer and recorded using custom-built LabVIEW^{TM} programs. The fluorescence can also be viewed directly with a charge-coupled device (CCD) camera, and the imaging is particularly useful for adjusting the field and surface ionisation signal (by moving the excitation lasers and the metal surface) to fit into the viewable area.

The detector and time-of-flight assembly is mounted on the same rotation stage as the target surface, such that the plane of the detector is always parallel to the surface when its angle is rotated with respect to the atomic beam (see Fig. 6.2), and the applied extraction electric field is always homogeneous.

6.1.3 Velocity distribution of the atomic beam

The distance between the photodissociation and Rydberg excitation point is known (46 ± 0.8 cm – the uncertainty arises mainly due to the possible paths between the

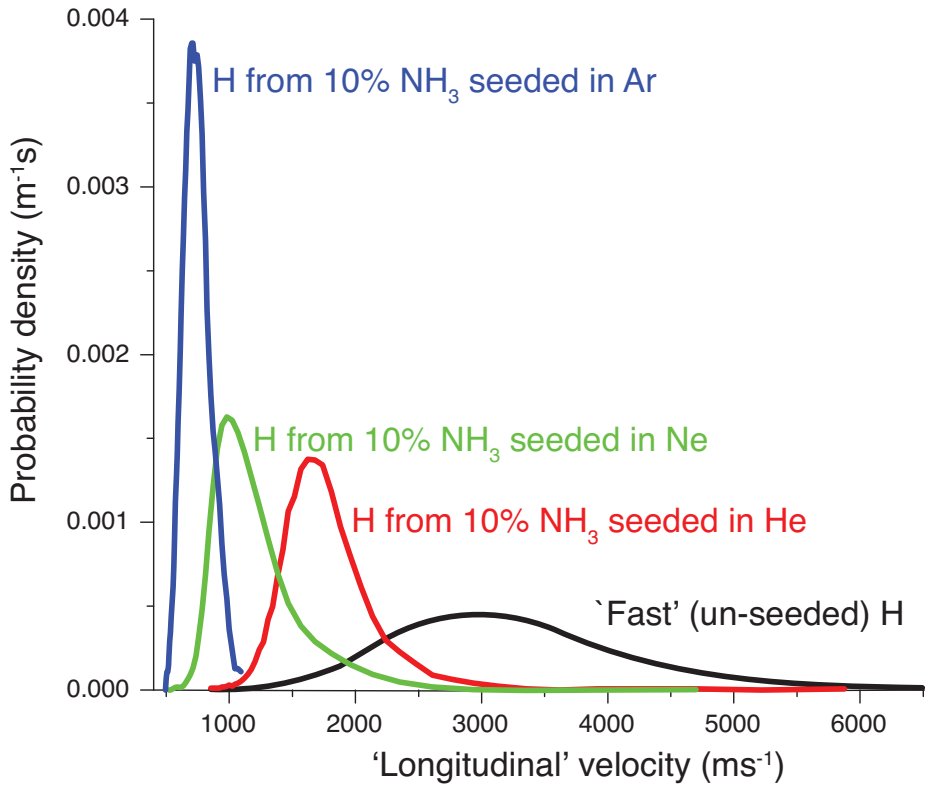

Figure 6.3: The measured velocity distribution of the hydrogen atoms for various rare-gas seeded and un-seeded ammonia gas beams. Note that this is not strictly the longitudinal velocity along the gas beam axis, as the laser beam axis is not perpendicular to the gas beam axis (see Fig. 6.2).

skimmer opening and the line of laser excitation (see below)), and so the velocity distribution of the hydrogen atom gas packet can be measured by monitoring the relative intensity of the Rydberg field ionisation signal as a function of Rydberg excitation time delay from the initial photodissociation laser. The results are shown in Fig. 6.3. Note that this is not strictly the longitudinal velocity along the gas beam axis, since the gas packet is intersected by the laser beams at a polar angle of $\theta = 45°$, and azimuthal angle of $\phi = 20°$ with respect to the laser axis (see Fig. 6.2). In Fig. 6.3, the 'fast' (unseeded) H atoms are produced by photodissociation in pure NH_3 – these atoms escape the carrier gas and travel at a mean velocity of ~ 2500 ms^{-1}. In the rare-gas seeded ammonia, the H atoms equilibrate with the velocity of the carrier

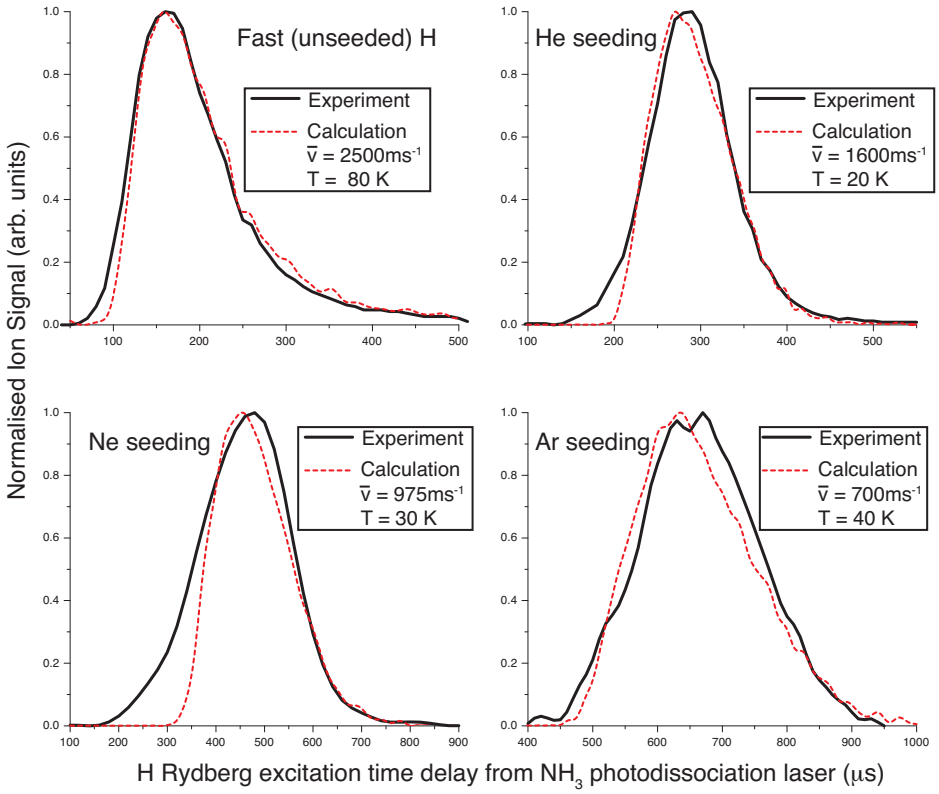

Figure 6.4: Black full lines: the experimentally detected ion signal from field ionisation as a function of time delay between the NH_3 photodissociation laser and the H Rydberg excitation lasers. Red dotted lines: calculated fits from Monte Carlo simulation by varying the temperature dependent velocity spreads $\sigma = \sqrt{kT/m}$ about the mean beam velocities.

beam within the quartz capillary and the mean velocity is approximately 1600 ms^{-1} in He, 975 ms^{-1} in Ne and 700 ms^{-1} in Ar. The velocity distributions can be fitted using Monte Carlo simulation to determine the translational temperature (with the initial velocity spread of $\sigma = \sqrt{kT/m}$ for each v_x, v_y, v_z component with respect to the gas beam axis). Figure 6.4 shows the fitting of the Monte Carlo simulations to the measured time profiles. For the 'fast' hydrogen atoms, the translational temperature is $\sim$ 80 K, which is unsurprising since the H atoms are allowed to escape the carrier gas. For the seeded beams, the temperature is in the range $(20 - 40)$ K; this is relatively high temperature for a supersonic beam, and may be attributed to the

poorer gas expansion from the end of the hand-cut quartz capillary compared to the conventionally used faceplate. One of the focus of future work should be on improving the supersonic expansion, possibly by varying the length of the capillary or tapering the capillary opening. However, the velocity distribution does not pose a problem for the experiments, since the use of nanosecond Rydberg excitation lasers allow a 'tight' velocity selection, with standard deviation of $\sim 1\%$ (*i.e.*, only a slice out of the velocity distribution is excited, see Section 6.1.4). Section 6.2.2 show that the collisional velocities can be confirmed by the measuring the time-of-flight of the surface ionisation signal with varying heights of Rydberg excitation.

Although Fig. 6.3 show that a range of rare-gas seeded mixtures can be chosen to produce a full range of collisional velocities, in practice, because the absolute signal intensity decreases with increasingly heavier seeding rare-gas, the work presented in this thesis only involve the use of pure NH_3 beam (producing 'fast' H atoms), and a 20% NH_3:He seeded beam.

The base vacuum pressure of the source chamber is $\sim 1\times10^{-8}$ mbar, with an operating pressure of $\sim 1 \times 10^{-6}$ mbar for the pure ammonia source, and $\sim 7 \times 10^{-5}$ mbar for the rare-gas seeded beam. While the base vacuum pressure of the interaction region is $\sim 4\times10^{-9}$ mbar, with an operating pressure of $\sim 7\times10^{-9}$ mbar for the pure ammonia source, and $\sim 1 \times 10^{-8}$ mbar for the rare-gas seeded beam.

6.1.4 Velocity distribution of the Rydberg atoms

The velocity distributions of the excited Rydberg H atoms impinging on the metal surface can be modelled from Monte Carlo simulation (with the fitted translational temperature in the previous section as input parameter). Figure 6.5(a) shows a histogram of the velocities (the total and the perpendicular component with respect to the surface) and the surface incidence angle of the atoms that are within the laser exci-

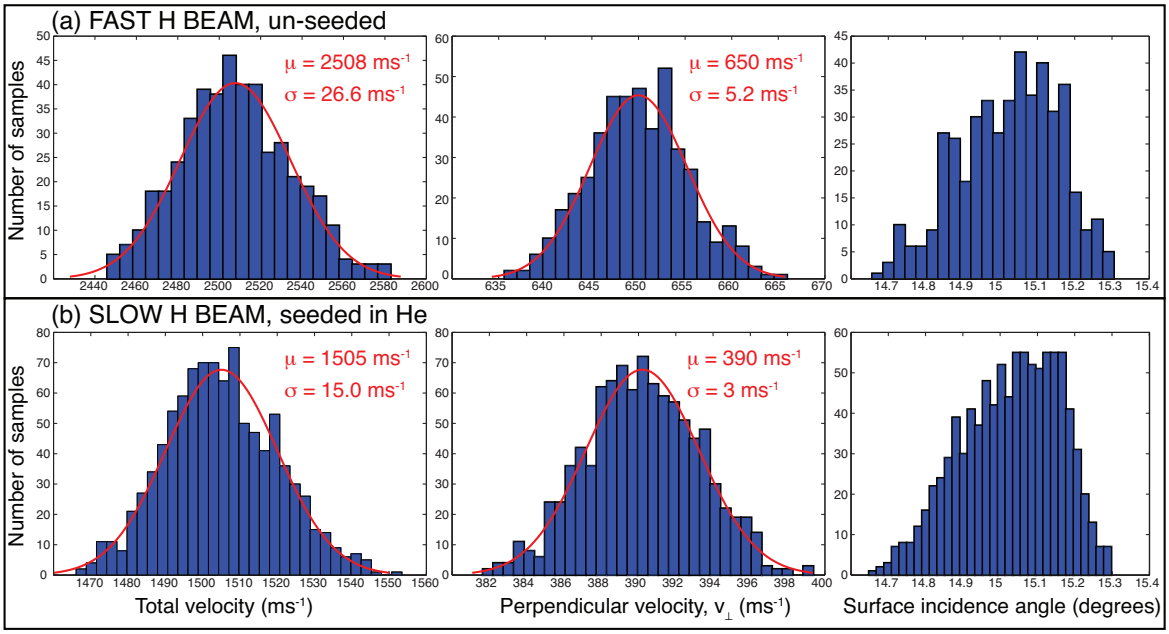

Figure 6.5: Velocities and incidence angle calculated from Monte Carlo simulation for the hydrogen atoms that are within the laser excitation volume during the Rydberg excitation laser pulse, *and* collide with the surface. (a) The results for the un-seeded beam of H atoms, with the excitation lasers pulsed at 180 μs delay from the NH_3 dissociation laser. (b) The results for the beam of H atoms seeded in helium, with the excitation lasers pulsed at 300 μs delay from the NH_3 dissociation laser. Red curves are the normal distribution fits of the velocities.

tation volume during the laser pulse, *and* collide with the surface, for a fast hydrogen atom beam (un-seeded) that is excited 180 μs after the NH_3 photodissociation laser. Figure 6.5(b) show the same, but for a slower beam that is seeded in helium, which is excited 300 μs after the photodissociation (since the slower atoms take longer to travel from the photodissociation point to the Rydberg excitation point). Effectively thin slices of the velocity distribution shown in Fig. 6.3 (with a given mean velocity) are taken by varying the delay times between the photodissociation and Rydberg excitation lasers. The sampled velocities are fitted to normal distributions, and are shown as red lines in Fig. 6.5. It can be seen that the standard deviations of both the total and the perpendicular component of velocity are ~ 1 %. The average incidence angle is $\sim 15^\circ$, and the distribution has a cut-off at angles $> 15.3^\circ$ due to geometry of the setup and the requirement that the atoms hit the surface.

The normal distribution fitting of perpendicular velocity distribution is used for the modelling of the experimental surface ionisation profiles with the over-the-barrier or the wavepacket approach (see Eq. 2.9 and Eq. 2.59). While the full array of velocities and incidence angles are stored and used as the initial starting conditions for the stray field trajectory calculations (see Section 5.2).

6.1.5 Laser excitation

The H atoms are excited to selected high-n levels ($n = 20 - 40$) with two counterpropagating laser beams using a two-colour resonant two-photon excitation scheme via the $2p$ level as an intermediate. The VUV beam at the Lyman-α wavelength (121.6 nm) is produced by frequency tripling of a frequency-doubled (364.8 nm, ~10mJ) Nd:YAG (Continuum Surelite III, 532 nm, ~430 mJ, ~9 ns pulse width, 10Hz) pumped dye laser (Sirah Cobra-Stretch, Pyridine 2 dye). The frequency tripling is carried out in a rare-gas cell containing a mixture of krypton and argon (with partial pressures of

200 mbar Kr and 580 mbar Ar). The 364.8 nm UV radiation is focused into the gas cell by a $f = 200$ mm fused silica spherical lens, and the resultant VUV radiation is refocused to the excitation region using a f =150 mm lithium fluoride (LiF) spherical lens. The different focal lengths of the UV and VUV radiation for the LiF lens ensure that only the VUV radiation is refocused at the excitation region. The second step of the excitation is driven by a second frequency-doubled Nd:YAG (Continuum Surelite III, 532 nm) pumped dye laser (Sirah Cobra-Stretch, Styryl 8 dye) operating in the range 365-370 nm ($\sim$5 mJ). The second laser is not focused, despite the smaller signal-to-noise ratio compared to a focused beam, as the Rydberg population was found to suffer from significant power broadening of the spectroscopic lines when a cylindrical lens ($f = 300$ mm) is used. This is illustrated in Fig. 6.6, which shows the field-ionisation signal of the $n = 24$ H Rydberg level excited in zero-field as a function of the second laser wavelength (the first laser wavelength is fixed).

Figure 6.7 presents the field (and surface) ionisation signal of the zero-field populated $17 < n < 40$ H atom Rydberg states as a function of the second laser wavelength at an ion-extraction field of 3000 Vcm^{-1} (for $n < 21$ this field is not sufficient for field ionisation, and so the integrated ion signal from the surface time gate (see Section 6.2.1) is shown instead). The variation in intensity of the lines of the Rydberg series is mainly due to the change in laser power over time, and the limited tuning range of the laser dye.

It can be seen from Fig. 6.6, that both spin-orbit components of the 2p level are populated by the VUV radiation. This is due to the linewidth of the VUV radiation: the $2P_{\frac{1}{2}}$–$2P_{\frac{3}{2}}$ spin-orbit splitting is ≈ 0.365 cm^{-1} [101] and the VUV linewidth is ≈ 0.3 cm^{-1} (the linewidth of the UV photon is ≈ 0.1 cm^{-1}). However, it is possible to tune the VUV wavelength to populate predominantly a single channel. For the experimental work presented below, the VUV wavelength is tuned to populate principally the

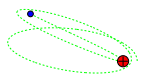

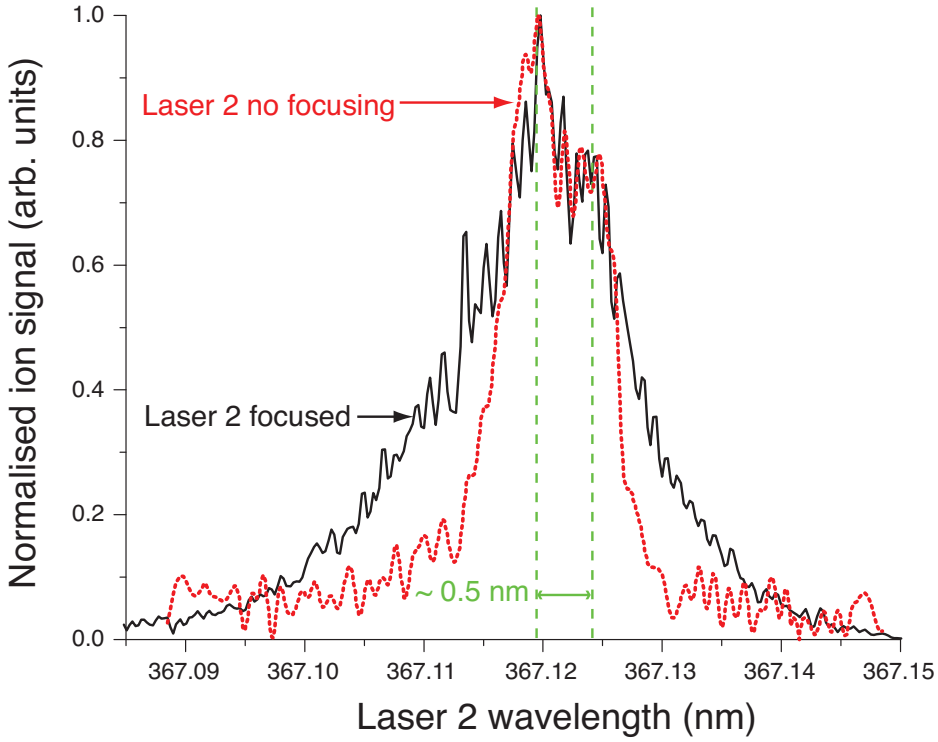

Figure 6.6: Field ionisation signal of the $n = 24$ H Rydberg level excited in zero-field as a function of the UV laser wavelength. Black full line: Spectrum taken when the UV laser is focused at the interaction region with a $f = 300$ mm cylindrical lens. Red dotted line: Spectrum taken when the UV laser is not focused. The spin-orbit splitting from the $2P_{\frac{1}{2}}$ and $2P_{\frac{3}{2}}$ level is shown by the green dashed lines.

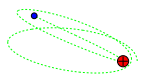

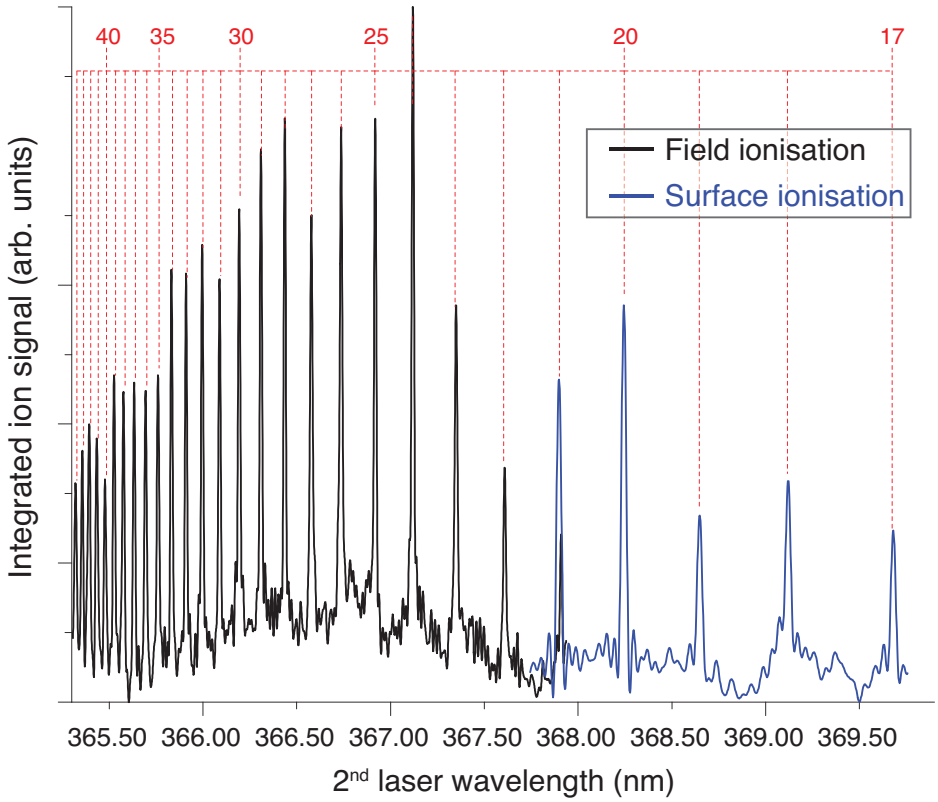

Figure 6.7: Integrated ion signal for the $17 < n < 40$ H Rydberg state excited in zero-field as a function of the UV laser wavelength with an ion-extraction field of 3000 Vcm^{-1}. Integrated ion signal from field and surface ionisation signal time gate (see Section 6.2.1) is shown as black and blue lines respectively. Red dotted lines are the calculated positions using the Rydberg formula (Eq. 1.1).

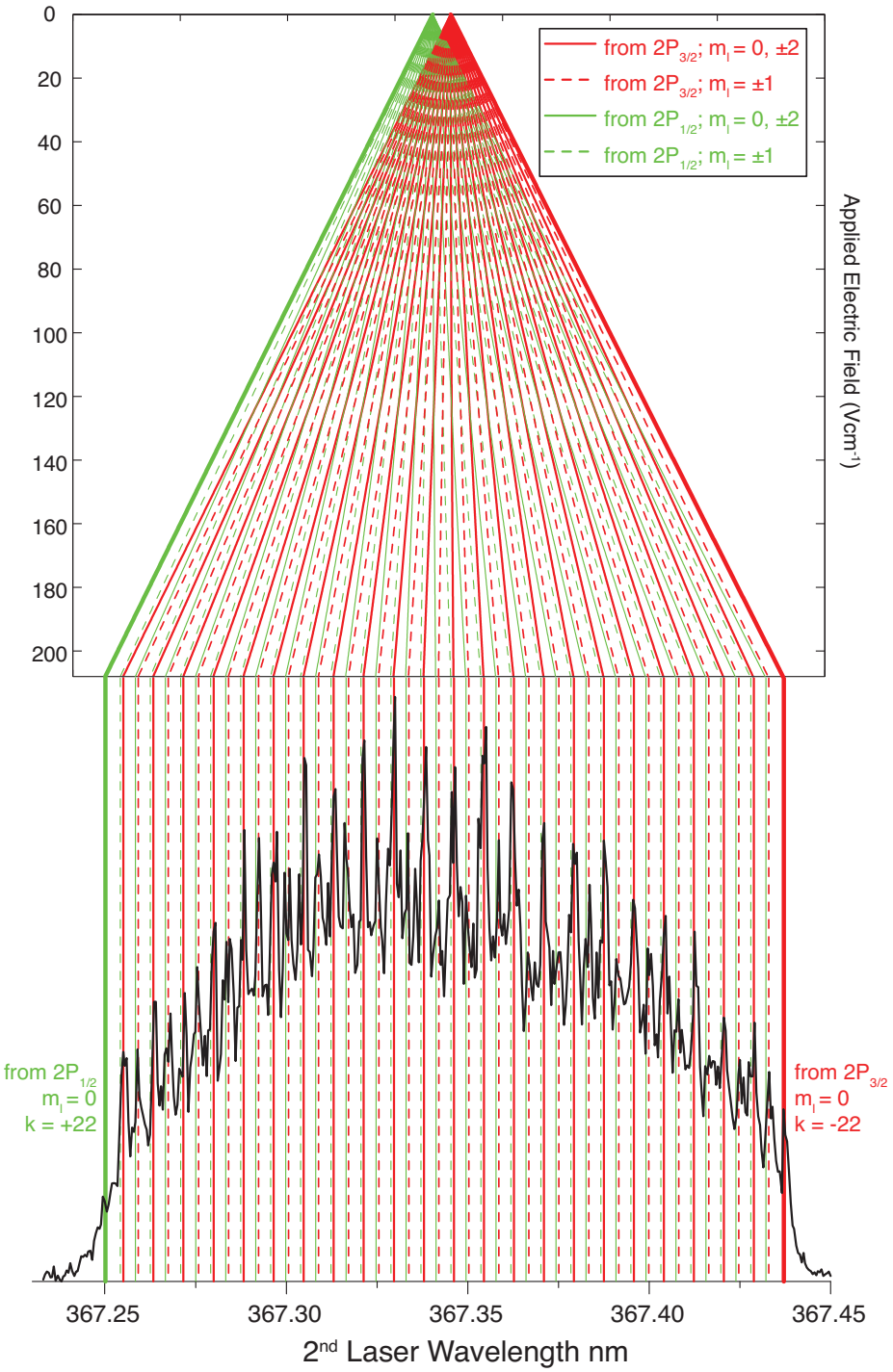

Figure 6.8: Top: Stark map of the $n = 23$ states; the plotted energies are relative to the respective $2P_{\frac{1}{2}}$ and $2P_{\frac{3}{2}}$ intermediates. Bottom: Direct field ionisation spectrum of the $n = 23$ Stark states excited in the presence of a homogenous field of 208 ± 1 Vcm^{-1}. The calculated positions of the Stark states excited from $2P_{\frac{1}{2}}$ and $2P_{\frac{3}{2}}$ intermediates are marked with green and red lines respectively. The VUV laser is tuned to populate mainly the $2P_{\frac{3}{2}}$ intermediate level. The full and dashed lines corresponds to $m_l = 0, \pm 2$ and $m_l = \pm 1$ states respectively.

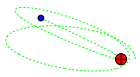

$2P_{\frac{3}{2}}$ state. This is illustrated in Fig. 6.8, which shows the $n = 23$ Stark spectrum (excited in a field of 208 ± 1 Vcm^{-1}), with the manifolds excited from the $2P_{\frac{1}{2}}$ and $2P_{\frac{3}{2}}$ intermediates marked by the green and red lines respectively.

The polarisation of the VUV and UV beams can be chosen to be perpendicular or parallel to the field direction. In principle this can lead to the population of either states with *principally* $m_l = 0$ (both parallel), $m_l = \pm 1$ (one parallel, one perpendicular) or $m_l = 0, \pm 2$ (both perpendicular). Note that due to spin-orbit coupling, the intermediate 2p levels populated are admixtures of $m_l = 0, \pm 1$ states [102]. It is found that the best resolution of Stark states populated in the presence of an electric field (see Fig. 6.8) can be achieved when both polarisations are set perpendicular to the field axis (*i.e.*, populating mainly $m_l = 0, \pm 2$). Although both $m_l = 0, \pm 2$ states are populated, the *most* extreme red and blue states of the manifold have pure $m = 0$ character.

6.2 Surface ionisation signal

In this section, the detection of the 'surface ionisation signal' from the Rydberg-surface charge transfer process is demonstrated. The way in which a typical 'surface ionisation profile' (a plot of ion signal from surface ionisation as a function of extraction field) is obtained, is also explained.

6.2.1 Spatial distribution and time-of-flight profile

The surface ionisation signal can be shown to be spatially and temporally separated from the 'gas phase' field ionisation signal. Figure 6.9(a) shows a CCD camera recorded image of the detected positive ion signal, and Fig. 6.9(b) shows the results of the Monte Carlo trajectory simulation superimposed on top of the image. The chosen extraction

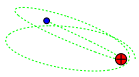

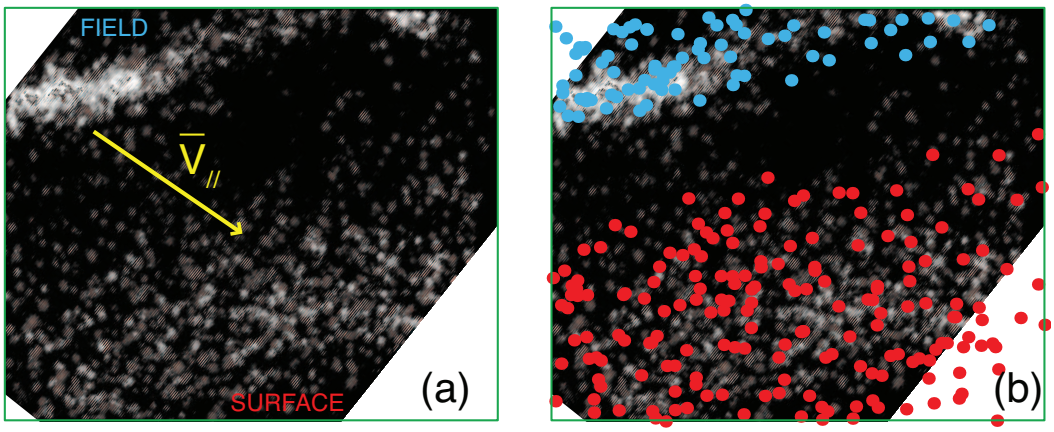

Figure 6.9: (a) CCD camera captured image of the field and surface ionisation signal. $v_{\parallel}$ represents the direction of the incoming Rydberg beam. (b) Image from (a), superimposed with Monte Carlo simulations of the atoms within the laser volume (blue dots) and the positions where they hit the surface (red dots). The atoms outside the 'viewing window' are not shown.

field is just at the cross-over limit between surface- and field-ionisation, to illustrate the different spatial distribution of two ionisation processes. The field ionisation signal appears as a line, determined by ions resulting from the two overlapping, counter-propagating laser beams. The width of the line mainly represents the width of the region of overlapping laser beams, which is approximately 1 mm. As expected, the ions produced from surface ionisation are more scattered along the beam propagation direction (as the signal is a projection of the spatial spread of Rydberg atoms in the direction perpendicular to the surface, *i.e.*, those formed further from the surface hits it later), and appears much further down along the gas beam path compared to the field ionisation signal (as the ionisation occurs later in time *at* the surface).

A typical experimental time-of-flight (TOF) trace for a 'fast' unseeded beam of Rydberg H atoms is shown in Fig. 6.10. Again, the extraction field is set at the cross-over limit between surface- and field-ionisation to illustrate the different TOFs of the protons from the two processes. Typically, the 'fast' unseeded and the He seeded H Rydberg atoms travel for ~ 4 μs and ~ 6.5 μs respectively before hitting the surface.

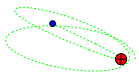

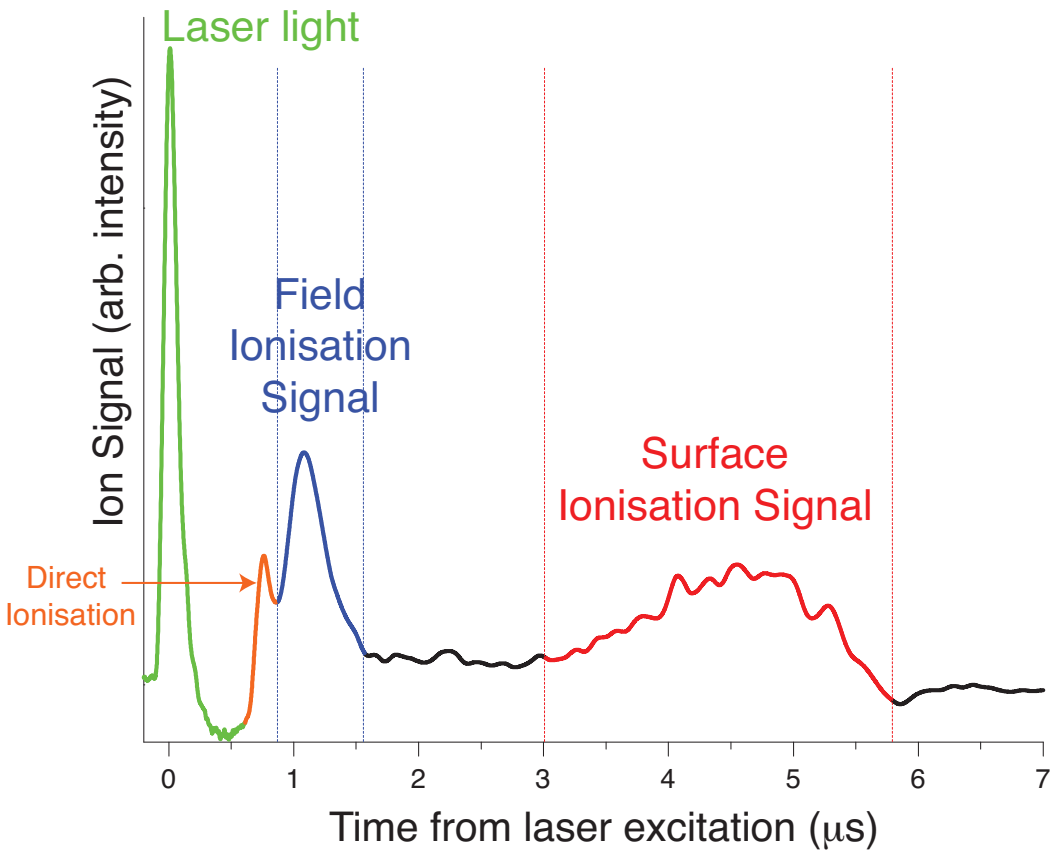

Figure 6.10: Experimental time-of-flight (TOF) trace of the detected ion-signal. The magnitude of the extraction field is chosen just at the onset of field ionisation, to illustrate both the temporal positions of the field and surface ionisation signal. Note that some of the UV radiation from the frequency tripling process leads to a small fraction of direct one-colour two-photon (VUV+UV) resonant ionisation.

It can be seen that the surface ionisation signal is broad, and at a much later time. The broad range of arrival times is mainly due to the finite size of the laser beams (∼1 mm diameter), forming Rydberg states at a range of initial separations from the surface, which then 'hit' the surface over a time range of $\sim 2-3$ μs. Integrating the surface ionisation signal within the 'surface time-gate' (see Fig. 6.10), and plotting as a function of extraction field for a given Rydberg state, results in a typical surface ionisation profile.

It can be seen from Fig. 6.9 that due to the limited viewable area of the fibre optic window (9.1 mm × 6.6 mm), it is not possible to detect all the Rydberg states that are excited and hit the surface. Consequently, it is not possible to determine an absolute surface ionisation signal. Previous studies involving Rydberg xenon atoms [45] have shown that the maximum integrated surface ionisation signal (just before the onset of field ionisation) is equal to the integrated field ionisation signal, *i.e.* a surface ionisation and ion-extraction efficiency of one. In principle, it is possible to model the signal 'lost' due to the spatial cutoff of the viewport by comparing the CCD camera image with trajectory simulations, such as those shown in Fig. 6.9. However, the spatial distribution of the detected ions, and consequently the detection efficiency ratio between the field- and surface-ionisation signal, is very sensitive to the laser and atomic beam alignment (and also the position of the surface), which changes frequently from the signal optimisations carried out throughout the day. Thus, following Ref. [49–51], as opposed to presenting the surface ionisation profiles as fractions of the total number of Rydberg atoms, unless stated otherwise, the profiles presented in this thesis are normalised with respect to the maximum integrated surface signal, which is typically at a field just before field ionisation, as observed by Dunning and co-workers [45]. In addition to the previous experimental observation [45], this normalisation can also be justified by the rapid increase of the surface ionisation distance near the field

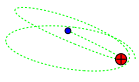

ionisation limit, which is predicted by theory (see Section 5.1). The problem of limited spatial detection area can be overcome in the future, either by introduction of focusing ion optics, or by increasing the overall detection area: larger MCPs, phosphor screen and fibre optic coupling.

The limited detection area can also lead to a change in the fraction of ions detected as a function of the extraction electric field, as the ions have non-zero parallel velocity with respect to the surface and the detector. However, it is shown in Appendix A that the change in the fraction of ions detected with extraction field and the consequent changes in the surface ionisation profiles is very small, and does not have a significant effect on the results presented in this work.

6.2.2 Height of excitation from the surface

Following the work of Lloyd *et al.* [50], one of the ways to demonstrate that the detected 'late' signal is indeed dependent on the surface, is by varying the height of the Rydberg excitation relative to the surface and observing a change in the arrival time of the surface ionisation signal, since it depends on the time taken for the Rydberg states to travel from the excitation point (∼2 mm from the surface) to the atom-surface separation at which surface ionisation takes place (∼60-400 nm). Figure 6.11 shows the change in the surface ionisation signal arrival time as a function of excitation height for a typical 'fast' (unseeded) H atom beam and a slower beam that is seeded with helium. As expected, the further the excitation point, the later the surface ionisation signal.

Figure 6.11(a) is obtained by changing the excitation height by moving the surface towards or away from the laser beams using the surface manipulator. The distance moved by the surface (or the change in the excitation height) can be confirmed by measuring the change in the Stark splitting of a given Rydberg manifold. Typically

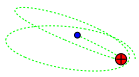

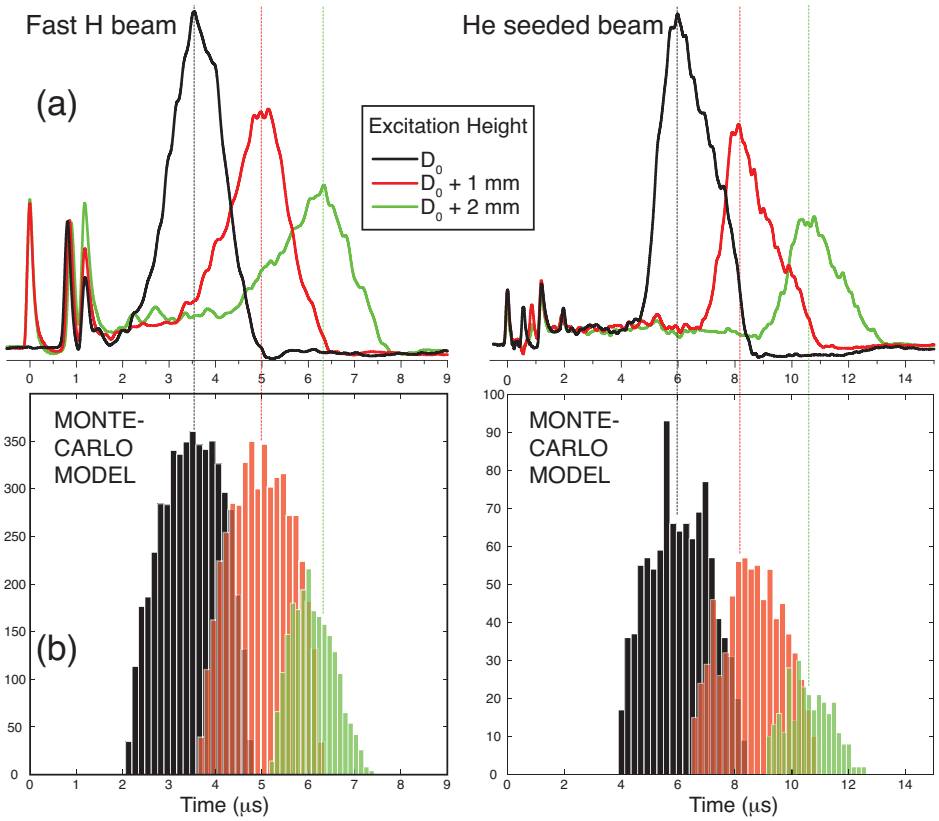

Figure 6.11: (a) The TOF spectra of the surface ionisation signal for various excitation heights from the metal surface. Left and right panels are the spectra from 'fast' H atoms excited at 180 μs after the NH_3 photodissociation laser (see Fig. 6.3), and from slower H atoms that are seeded in He and excited at 300 μs from the photodissociation, respectively. The initial excitation height D_0 is $\approx$ 2 mm. (b) The TOF spectra corresponding to (a), calculated from Monte-Carlo simulation.

the $n = 23$ Stark manifold (Fig. 6.8) is used for the calibration of the electric field and the extraction mesh to metal surface separation (since the potential difference is known). To ensure that the surface ionisation signals in Fig. 6.11 are shifting only due to the variation of the height of excitation, and not due to the different applied electric field as a result of the changing extraction mesh to surface separation, the mesh to metal surface separation is measured (from the Stark splitting) for each of traces shown in Fig. 6.11(a), and the applied potential is adjusted such that electric field is kept constant.

The perpendicular velocity of the Rydberg atoms (with respect to the surface) can be estimated by measuring the change in the time of arrival of the surface ionisation signal as a function of excitation height. From Figure 6.11, the inferred collisional velocity is $\sim 750 \pm 100$ ms^{-1} for the 'fast' hydrogen atoms excited at 180 μs after the excimer photodissociation laser (see Fig. 6.3), and $\sim 450 \pm 100$ ms^{-1} for the slower H atoms which are seeded in He and are excited at 300 μs after the photodissociation. These values are in accord with the velocities calculated from Monte Carlo simulation, which are 650 ± 5 ms^{-1} and 390 ± 3 ms^{-1} respectively. Figure 6.11(b) shows the corresponding TOFs predicted from Monte Carlo trajectory simulations, which are in good agreement with the experimental spectra (Fig. 6.11(a)).

6.2.3 Extraction delay

The surface ionisation signal can also be demonstrated by varying the time at which the extraction field is switched on [50]. Since surface ionisation occurs *at* the surface, and as the time at which the surface ionisation signal appears is only dependent on the velocity of the Rydberg atoms, the signal should be independent of when the electric field is switched on. Field ionisation on the other hand, occurs as soon as the extraction field is turned on (provided that it is sufficiently large to cause field

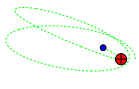

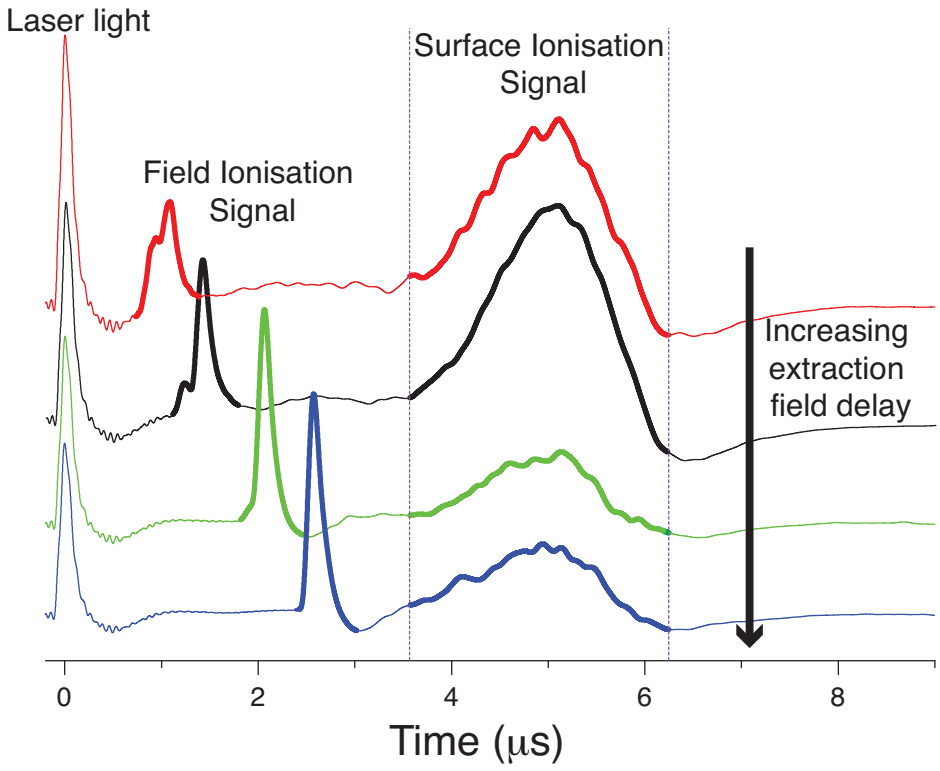

Figure 6.12: The TOF spectra for various time delays (1-3 μs) between the turning on of the electric field and the initial laser excitation of the H atoms. The magnitude of the extraction field is chosen just at the onset of field ionisation, such that both the field and surface ionisation signals are observed. The field ionisation signal shifts with extraction field delay, while the surface ionisation signal is independent of the time delay.

ionisation), and the arrival times of ions produced would depend on the time at which the field is present. This is illustrated by Fig. 6.12.

6.3 Surfaces

The surfaces studied in this work involve a gold surface, a rough aluminium surface and a single-crystal Cu(100) surface.

The gold surface has been prepared by an in-house surface facility, and is formed by metal-vapour deposition on a one-inch diameter polished Si(111) wafer (Compart Technology Ltd). To promote adhesion of the gold to the silicon surface, a 5 nm layer of chromium was first deposited onto the silicon wafer. The subsequent gold (99.99 %, Alfa) deposition is carried out at a controlled rate of approximately 1 nm s^{-1}, until a gold thickness of 200 nm is reached. The resulting evaporated gold surface is found to have surface roughness of less than 1 nm (as measured by AFM, reported in Ref. [50]).

The rough aluminium surface (30 mm x 30 mm) is machined from an aluminium block and polished on a lathe. The surface profile (along a line across the surface) has been measured using diamond needle profilometer, and is shown in Fig. 6.13. It can be seen that there are large vertical variations of ~ 2.5 μm over lateral periods of ~ 130 μm, while there are also smaller vertical variations of $\sim$0.1-0.5 μm in size with periods of $\sim 10 - 20$ μm.

The one inch diameter single-crystal Cu(100) (99.999%) surface is purchased from a commercial supplier (MaTeck GmbH). The single-crystal is grown using the Czochralski method, and is cut and chemo-mechanically polished to a roughness of less than 30 nm, and with surface orientation accuracy of better than 1 degree.

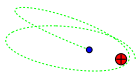

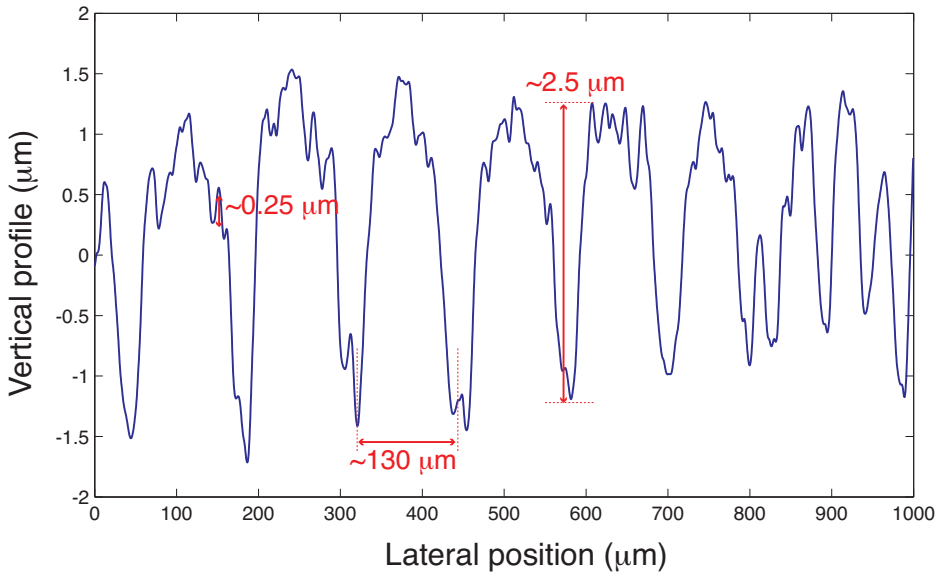

Figure 6.13: Vertical variations of the rough machined aluminium surface used in this work as a function of position across the surface. The vertical variations are measured at lateral intervals of 0.5 μm.

Chapter 7

Experimental study of Rydberg hydrogen atom-surface interaction

In this chapter, the first experimental study of the surface ionisation of Rydberg hydrogen atoms at metal surfaces is presented. The effects of Rydberg dimension and polarisation, collisional velocity and angle, direction and magnitude of the electric field, and the physical and electronic surface structure is investigated. The theoretical findings from the previous chapters will be used to explain some of the experimental observations. Unless stated otherwise, the results presented below are for the atomically flat evaporation-deposited gold surface.

7.1 Varying the Rydberg dimensions

Figure 7.1 shows the surface ionisation signal as a function of ion-extraction field for the most red-shifted state ($k = 1 - n$, $m_l = 0$) of the $n = 20 - 36$ manifolds. The profiles are normalised to the maximum signal, as discussed in Section 6.2.1. The error bars associated with the data points are also shown. As expected, the onset of surface ionisation signal is at progressively lower fields with increasing principal

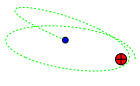

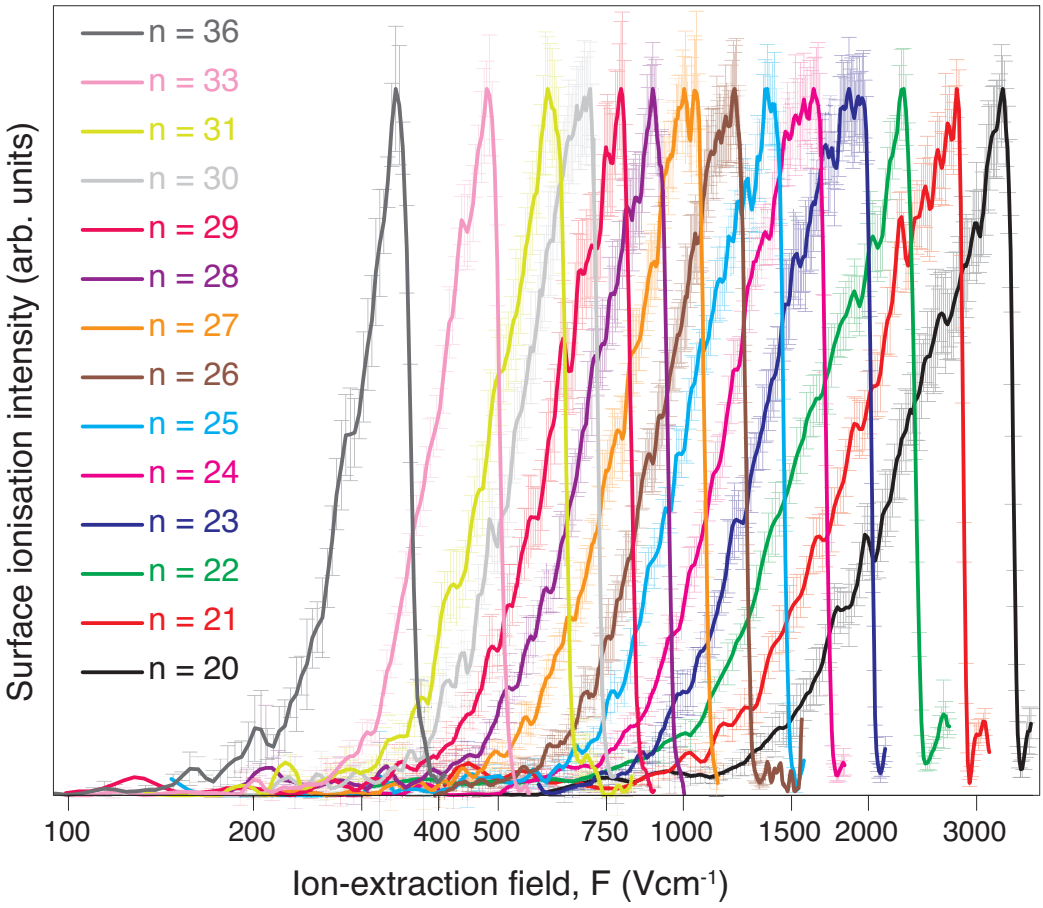

Figure 7.1: Surface ionisation signal as a function of ion-extraction field for the most red-shifted state ($k = 1 - n$, $m_l = 0$) of the $n = 20 - 36$ manifolds. The Rydberg H atoms with collisional velocities of $v_\perp \sim 650$ ms^{-1} are from an un-seeded beam (see Section 6.1.1) excited at 180 μs after the NH_3 photodissociation. The field axis is logarithmic to show the profiles more clearly.

quantum number, which reflects the increasing atom-surface separations at which the Rydberg to surface charge transfer occurs. As is typical for this type of measurement, the profiles gradually rise as the field increases, and exhibit a sharp cut off at a given field value, owing to field ionisation.

For a clearer picture of how the ion signal varies with principal quantum number, Figure 7.2 shows the ionisation profiles on a scaled field axis (by factor of n^{-4}). The results from the over-the-barrier and scaled wavepacket calculations including mean-

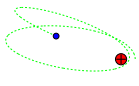

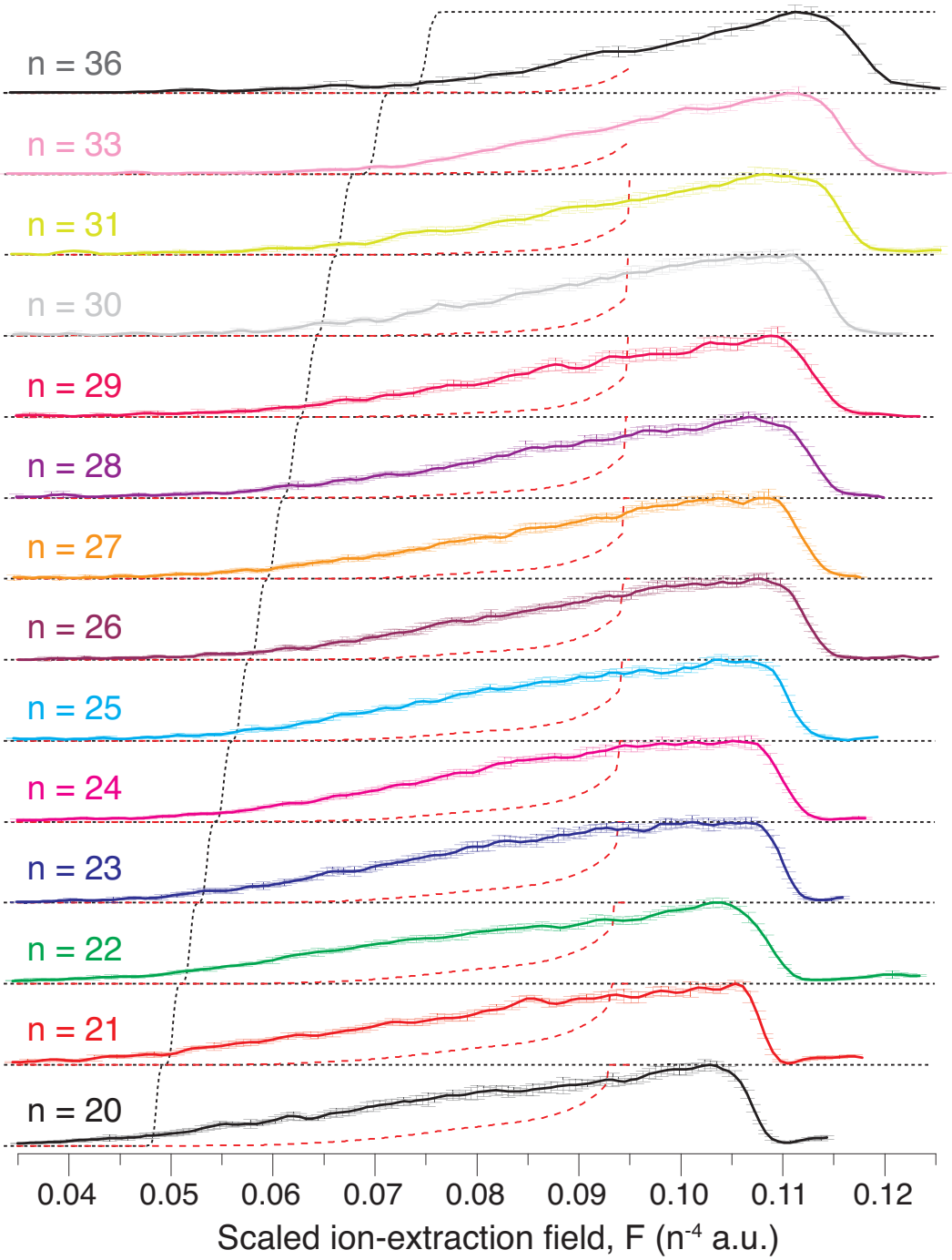

Figure 7.2: Surface ionisation signal as a function of *scaled* ion-extraction field for the most red-shifted state ($k = 1 - n$, $m_l = 0$) of the $n = 20 - 36$ manifolds. The Rydberg H atoms with collisional velocities of $v_\perp \sim 650$ ms^{-1} are from an un-seeded beam (see Section 6.1.1), excited at 180 μs after the NH_3 photodissociation. The field axis has been scaled by a factor of n^{-4}. The results of the OTB and scaled wavepacket calculations including mean-field acceleration (see Section 5.1) are shown as black dotted lines and red dashed lines respectively.

field acceleration (see Section 5.1) are also shown for comparison. It can be seen that the OTB approach provides a good estimation of the field required for the onset of surface ionisation, but does not account for the shallow rise in signal as ion-extraction field increases. The wavepacket approach on the other hand, does predict a shallow increase of ion-signal (until near the field ionisation limit, where the ion-detection probability increases rapidly), but the onset of ion signal is later than observed experimentally. Nonetheless, despite the fact that neither the OTB or the wavepacket approach provides a quantitative fit of the experimental result, it is encouraging that the experimental profiles appear to lie within the bounds of the two theoretical predictions.

It is possible that the larger fraction of ion signal detected at lower fields, which is not accounted for by the wavepacket calculations, is due to local surface fields as observed by Dunning and co-workers [48], who found that quantitative agreement of the surface ionisation profiles of Rydberg xenon atom can be achieved by carrying out over-the-barrier trajectory calculation with the inclusion of local surface fields (outlined in Section 5.2). The same calculations are carried out here for the hydrogen atom, but as discussed in Section 5.2, for the light hydrogen atom, the Rydberg trajectory can be strongly perturbed by the image-charge and local surface fields. Thus, to model the real system more closely, the acceleration of the Rydberg state under the image charge field is included by using Van der Waals energy shift given by Eq. 2.2, while the local surface field is assumed to be constant over the Rydberg dimension, such that the forces on the Rydberg atom can simply be estimated by the change in the Stark energy from the surface fields ($M\ddot{D} = -1.5nk\nabla F_{\mathrm{surf+field}}(D)$). Figure 7.3 shows the results of the calculation for several selected principal quantum numbers compared with the experimental profiles. The inclusion of the effect of local surface fields and image charge fields on the Rydberg trajectory leads to an acceleration towards the surface

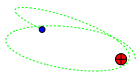

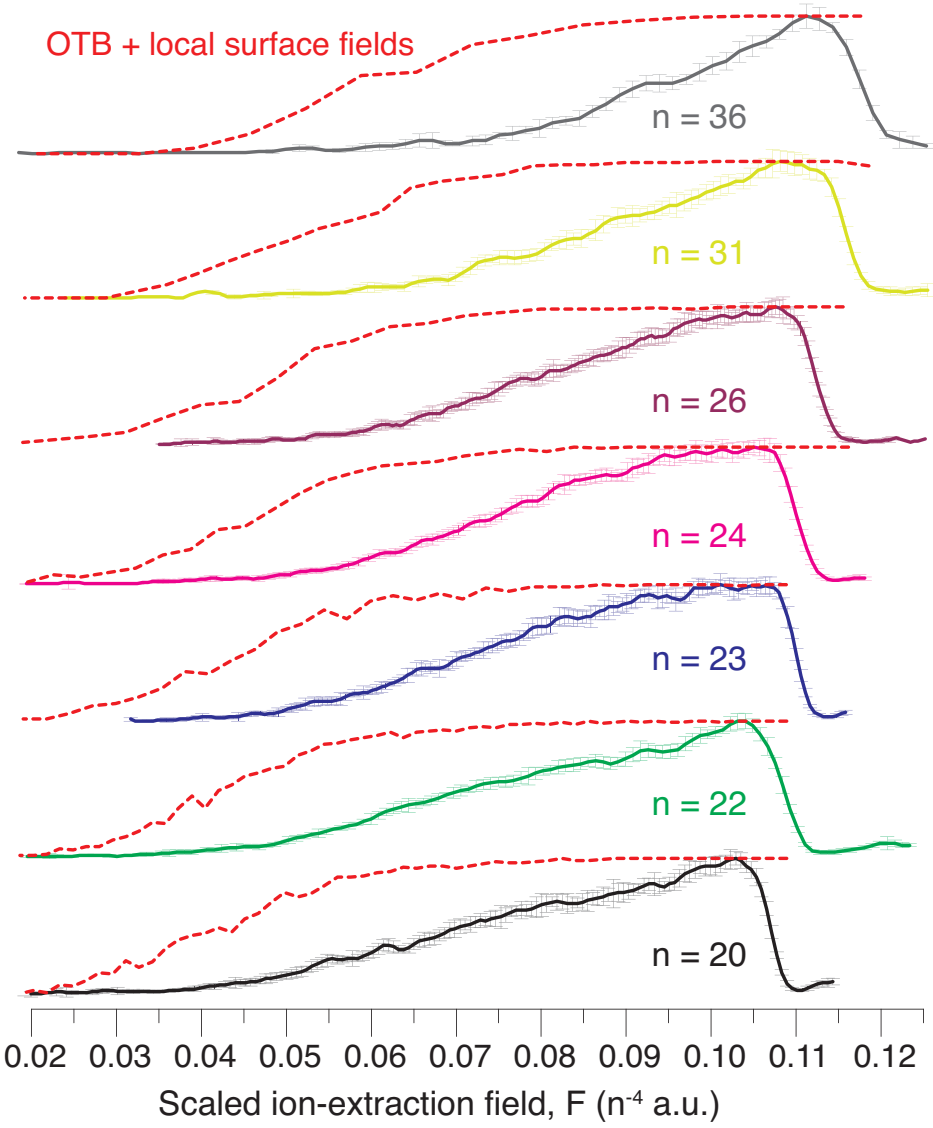

Figure 7.3: Surface ionisation signal as a function of *scaled* ion-extraction field for the most red-shifted state ($k = 1 - n$, $m_l = 0$) of the $n = 20 - 36$ manifolds. The red dashed lines show the results of the trajectory OTB calculations with the inclusion of local surface fields.

for the 'high-field seeking' (Stark energy decreasing with increasing field) red-shifted state (see Fig. 5.8), such that the mean extraction fields are shifted to higher values (Eq. 1.14). The range of ionisation distances and detection probabilities introduced by the local surface fields also leads to much broader ionisation profiles (see Section 5.2), with widths that are comparable with the experimental results. However, the onset of ion signal is still at much lower fields compared with the experimental profiles, and consequently the quantitative agreement with experiment is poor. This is unsurprising considering the quantitative differences between the results obtained from OTB and the wavepacket approach that has been observed in Section 5.1.

Surprisingly, the experimental results can be modelled very well using a semi-empirical approach. Surface ionisation is assumed to occur about some field dependent mean atom-surface separation $\mu(F)$, with standard deviation σ, such that the cumulative ionisation probability (*c.f.* Eq. 2.8) is given by

$$\Upsilon(D,F) = 1 - \frac{1}{2}\left[1 + \mathrm{erf}\left(\frac{\mathrm{D} - \mu(\mathrm{F})}{\sqrt{2\sigma^2}}\right)\right], \tag{7.1}$$

which is simply a normal cumulative distribution function. The ion detection probability is found in the same way as before using Eq. 2.9. Taking the mean ionisation distance $\mu(F)$ as a *shifted* over-the-barrier distance, such that $\mu(F) = D_{\mathrm{OTB}}(F) - n^2$, where $D_{\mathrm{OTB}}(F)$ is the OTB distance calculated as outlined in Section 2.1, and the standard deviation $\sigma = 2.5n^2$ $\mathrm{a_0}$, the corresponding ionisation profiles are in excellent agreement with the experimental results. This is shown in Figure 7.4. It is shown in Section 7.3, that this semi-empirical model also provides a good fit for experiments involving different collisional velocities.

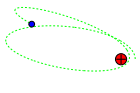

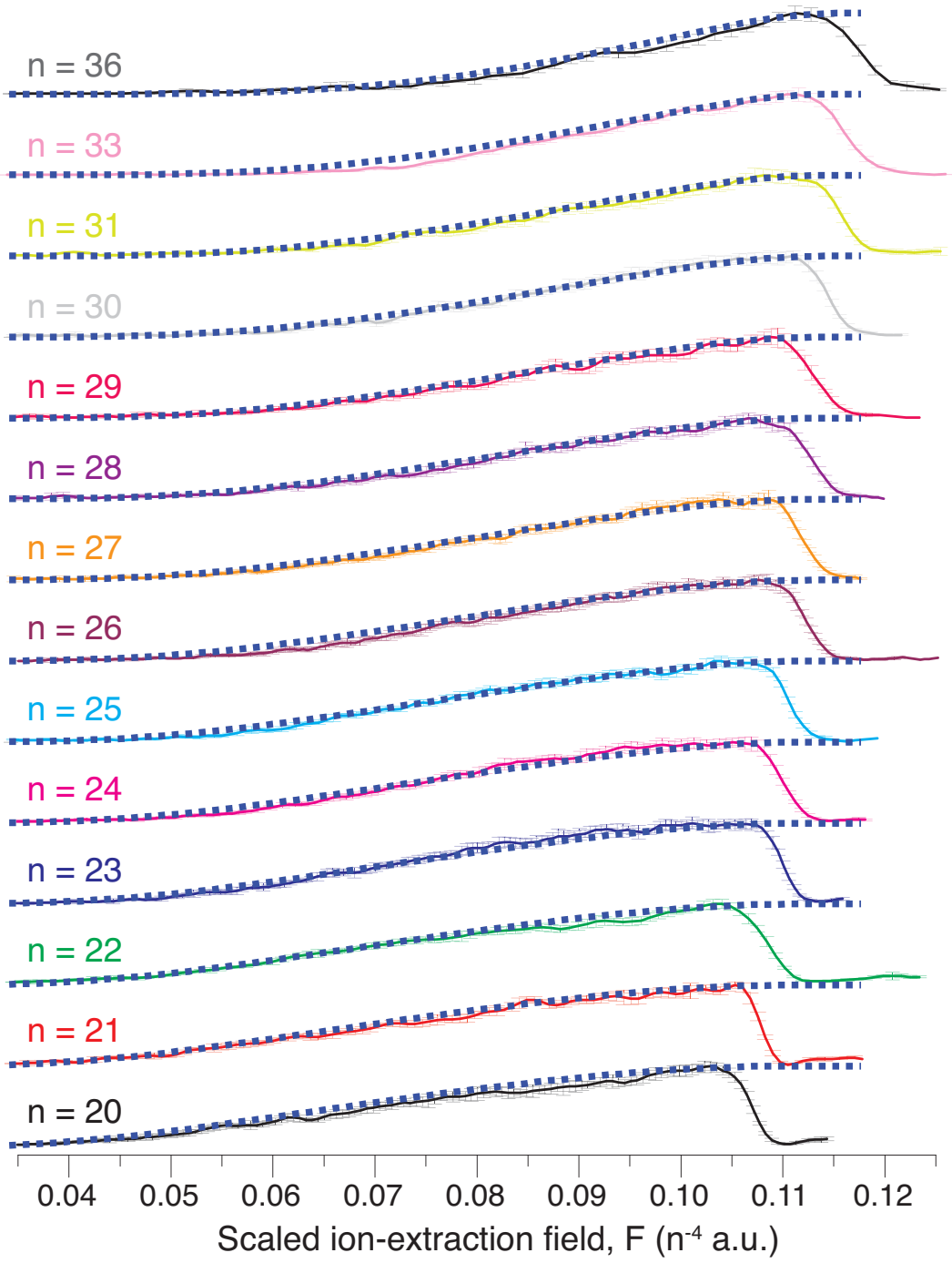

Figure 7.4: Surface ionisation signal as a function of *scaled* ion-extraction field for the most red-shifted state ($k = 1-n$, $m_l = 0$) of the $n = 20-36$ manifolds. The ionisation profiles calculated using a semi-empirical approach (see text) is shown as thick blue dotted lines.

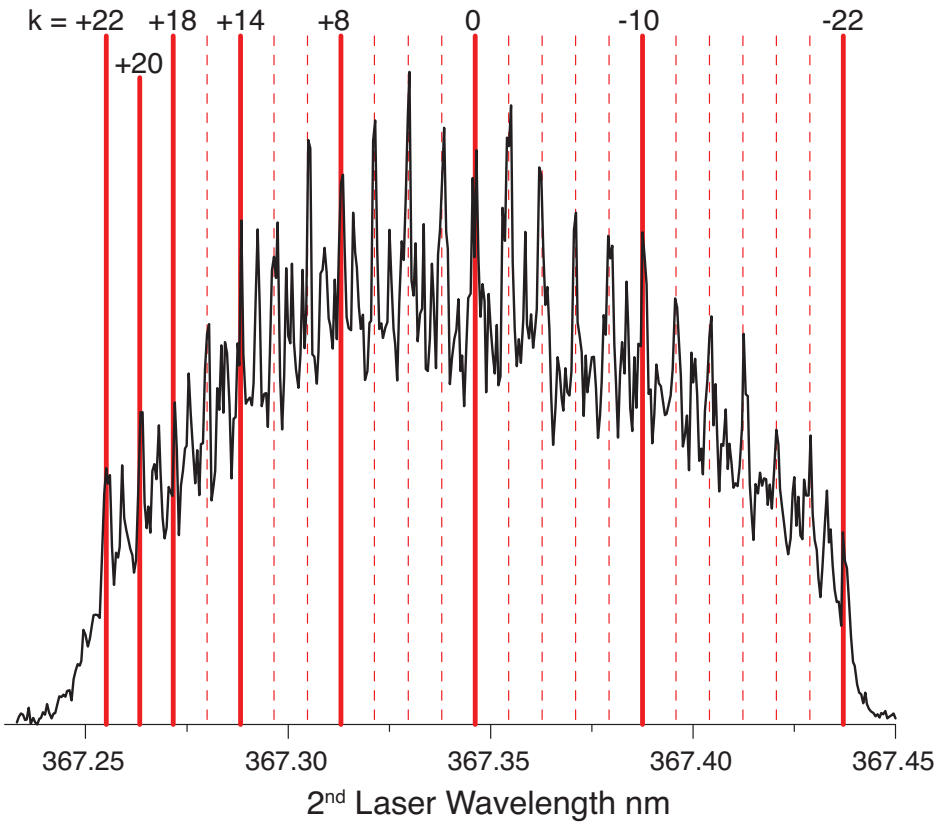

Figure 7.5: Direct field ionisation spectrum of the $n = 23$ Stark states excited in the presence of a homogenous field of 208 ± 1 Vcm^{-1}. Mainly the $m_l = 0, \pm 2$ states are populated. The Stark shifts calculated from Eq. 1.3 are shown as red vertical lines. The thick lines mark the $k = +22, +20, +18, +14, +8, 0, -10, -22$ states which is studied here.

7.2 Stark polarisation

In the previous section, it is shown that the atom-surface separation at which surface ionisation occurs can be varied by choosing Rydberg states of various principal quantum numbers. In this section, the variation of ionisation distances from Rydberg states belonging to the same n-manifold, but with different Stark polarisation (and thus k) is investigated.

Figure 7.5 shows the Stark spectrum of the $n = 23$ states excited in the presence

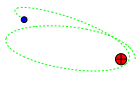

of a field of 208 ± 1 Vcm^{-1}; the Stark states studied here are marked with thick vertical lines. Figure 7.6 shows the surface ionisation profiles of the selected Stark states. Note that the surface ionisation intensities are normalised to the maximum signal of the most red-shifted state. The onset of ion signal is at progressively higher extraction fields on moving from red- to blue-shifted Stark states, reflecting the fact that the electron wavefunctions are progressively more polarised towards the vacuum (the $k = 0$ state is relatively un-polarised). This preservation of polarisation with respect to the surface, and the resulting differences in the ionisation distances, are in accord with the theory presented in Section 3.1. However, it is surprising that ions from the surface ionisation process can be detected for the most vacuum-oriented blue-shifted state, since the calculations in Section 5.1 predict that the range of fields required to pull the ions away from the surface is greater than the field ionisation threshold.

Figure 7.7 shows that surface ionisation profiles for the most extreme red- and blue-shifted states of the $m_l = 0$, $n = 24,\ 26$ manifolds. Similar to the $n = 23$ Stark states, the surface-oriented red-shifted states are detected at significantly lower fields compared with the vacuum-oriented blue-shifted state. Although it cannot be shown that the collisional velocity is constant throughout the Rydberg trajectory (and it is predicted not to be the case by the theory in Section 3.7), Eq. 1.15 can be used to give an estimate of the ionisation distances of the red- and blue-shifted states. Figure 7.8 shows the surface ionisation profiles of the most extreme red- and blue-shifted states of the $n = 23,\ 24,\ 26$ manifolds with the ion-extracted field axis converted to *approximate* ionisation distances. The most surface-oriented red-shifted states are ionised at $(2.5 - 4.3)n^2$ a$_0$, and the most vacuum-oriented blue-shifted states ionise at around $(1.6 - 2.1)n^2$ a$_0$, which are approximately in line with the theory given in Section 3.1.

Figure 7.6 shows that on moving from red- to blue-shifted states, the maximum surface

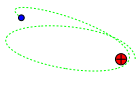

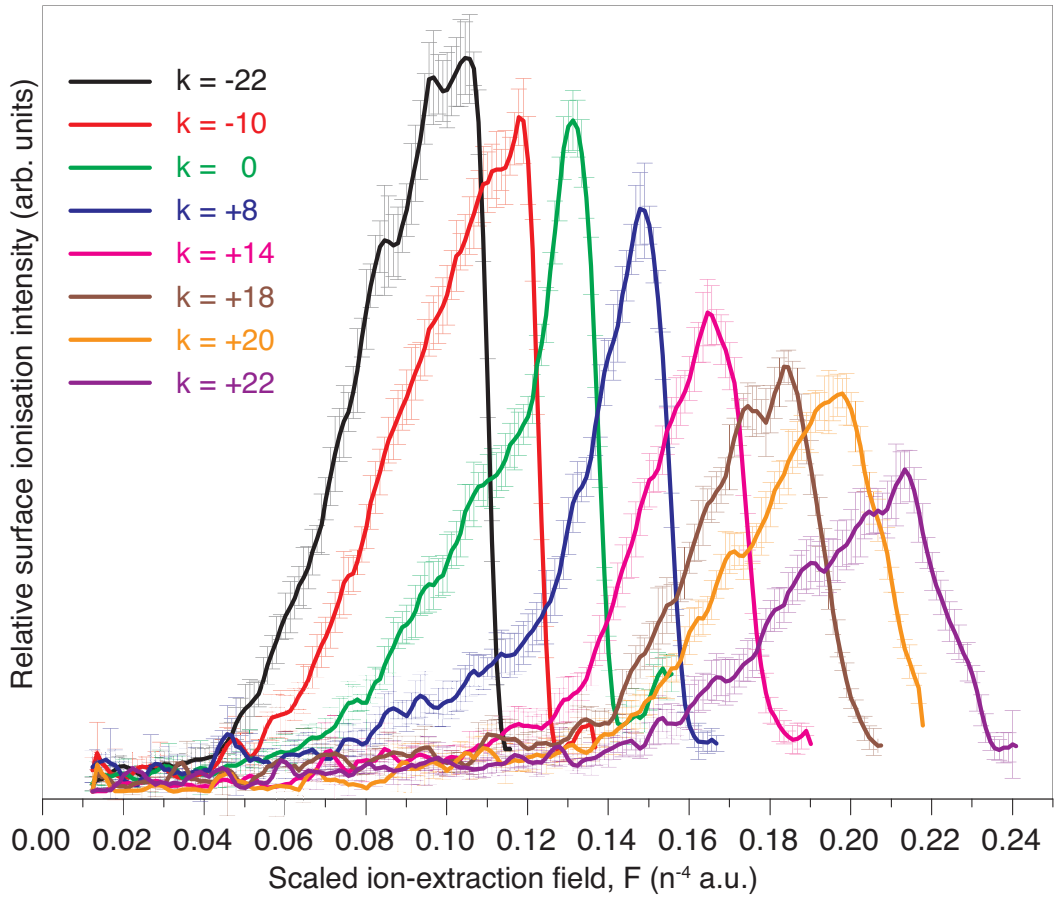

Figure 7.6: Relative surface ionisation signal of the $k = -22, -10, 0, +8, +14, +18, +20, +22$ Stark states of the $n = 23$ manifold as a function of scaled ion-extraction field. The Rydberg H atoms with collisional velocities of $v_\perp \sim 650$ ms^{-1} are from an un-seeded ammonia beam (see Section 6.1.1), excited at 180 μs after the NH_3 photodissociation.

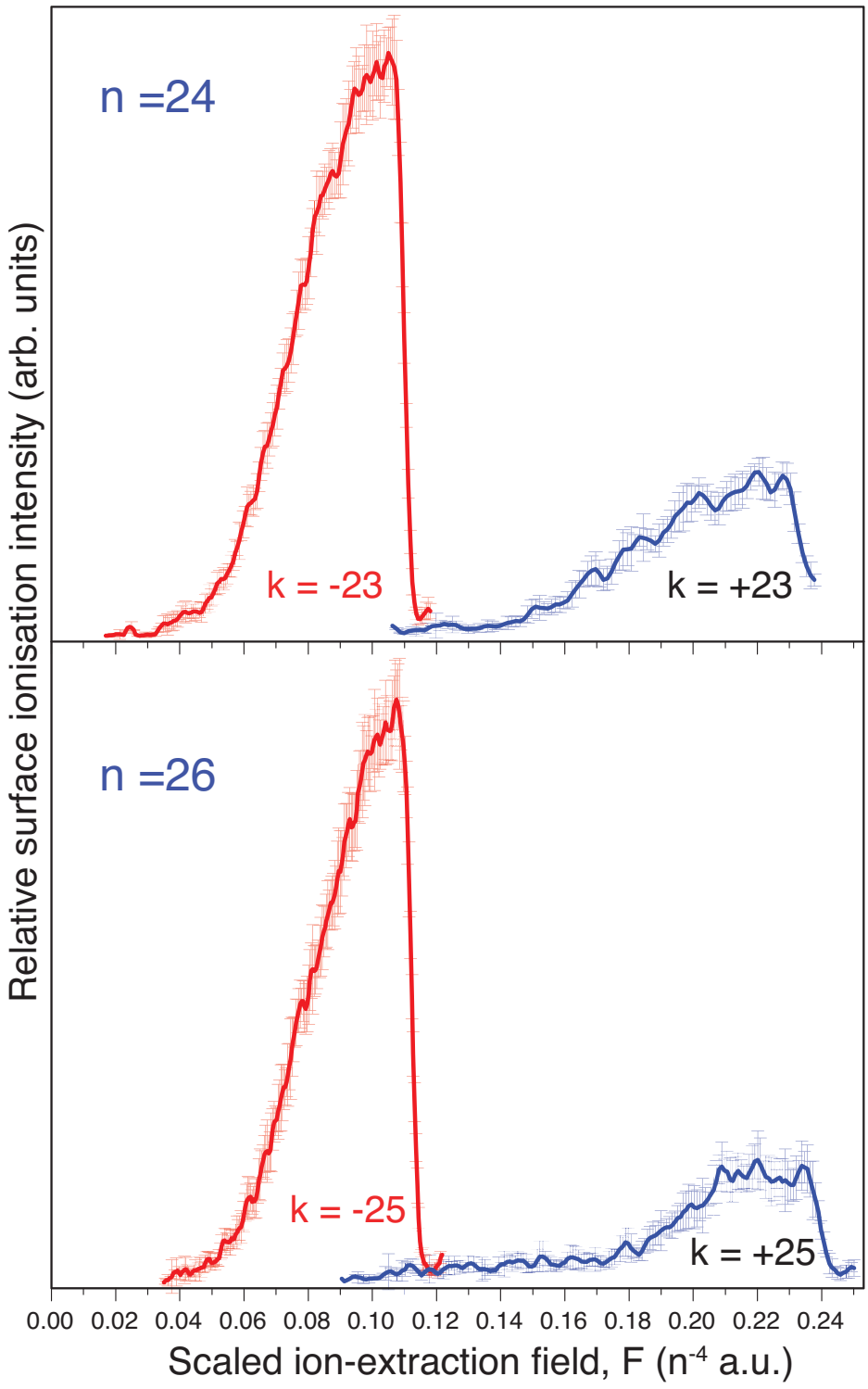

Figure 7.7: Relative surface ionisation signal of the most extreme red- and blue-shifted $m_l = 0$ Stark states of the $n = 24, 26$ manifolds as a function of scaled ion-extraction field.

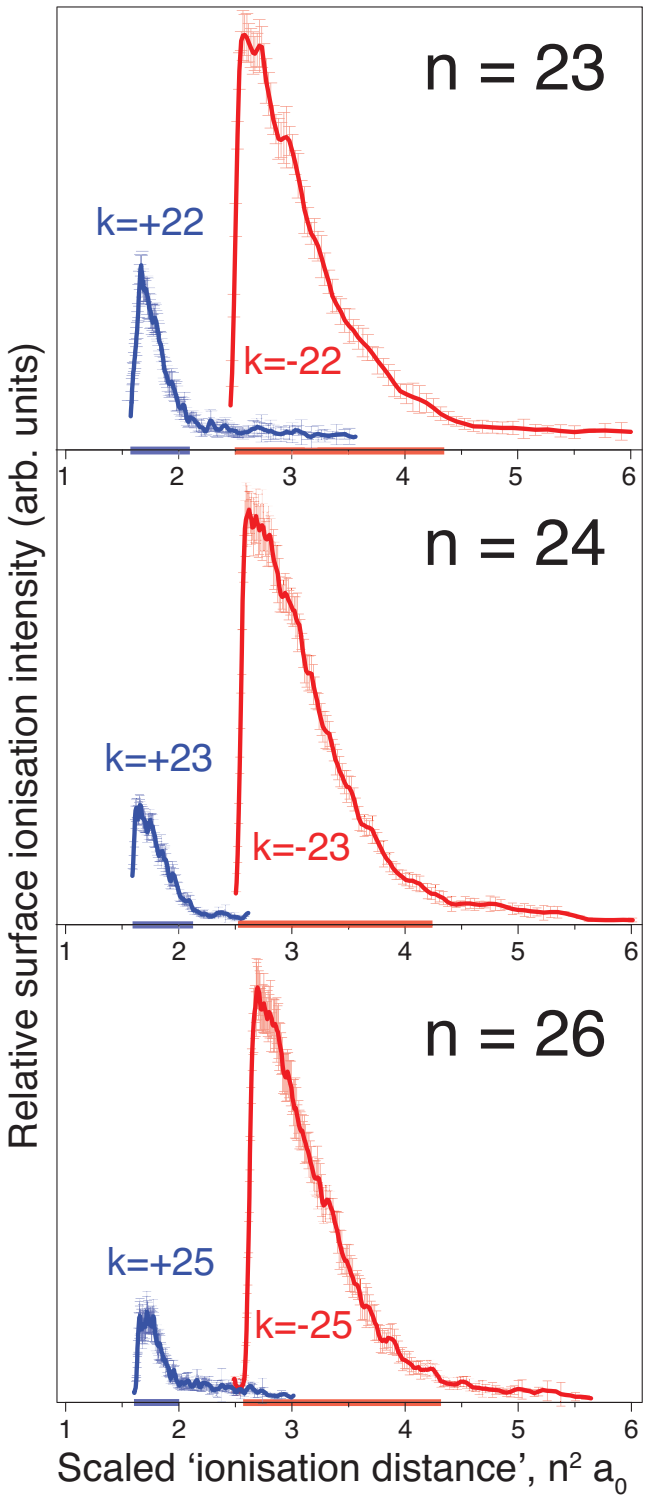

Figure 7.8: Relative surface ionisation signal of the most extreme red- and blue-shifted $m_l = 0$ Stark states of the $n = 23,\ 24,\ 26$ manifolds plotted as a function of scaled 'ionisation distance', calculated from Eq. 1.15, assuming that the Rydberg states approach the metal surface at a *constant* velocity of $v_\perp = 650$ ms^{-1}.

ionisation signal decreases. This implies that the onset of field ionisation is at a field value lower than that required to extract all the Rydberg states that undergo surface ionisation. It is also found that the surface ionisation signal for the most extreme blue-shifted Stark drops rapidly beyond $n = 26$; the signal at $n = 28$ (not shown here) is just above the signal to noise threshold, and no surface ionisation can be detected above $n = 28$. These observations partly support the theoretical predictions of Section 5.1 for the most blue-shifted state: that the onset of field ionisation is before the field required to extract the ions from the surface ionisation process. The small fractions of surface ionisation signal observed for principal quantum numbers $n < 28$ may be due to local surface fields as observed by Dunning and co-workers [48]. The local fields not only introduces a range of ionisation distances and detection probabilities, leading to a broadening of the ionisation profiles, but for the 'low-field seeking' blue-shifted Stark states, the Rydberg atoms can be decelerated when approaching a high-field region close to the surface (corresponding to the positive patch potentials which complements the ion-extraction field, see Fig. 5.8), allowing for subsequent ion-extraction at lower fields (Eq. 1.14). Trajectory simulation for the most blue-shifted state confirms this deceleration effect, and it is found that some of the trajectories are even deflected from the surface. The effect of the local surface field deceleration decreases with increasing principal quantum number (since ionisation takes place further from the surface), and could therefore accounts for the decreasing surface ionisation signal observed for increasing values of n in Fig. 7.8.

It is worth noting that this is the first demonstration of variation of the charge transfer distance by using different Stark-state polarisations. Previous experimental studies involving Rydberg xenon atoms and hydrogen molecules have shown that the ionisation profiles of red- and blue-shifted Stark states are very similar [45, 51] (see Fig. 1.11). This is due to the stronger level interactions of non-hydrogenic systems, allowing

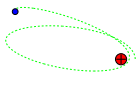

Rydberg states of different polarisations to mix as the surface is approached, and thus losing the character of the initial populated state. For the hydrogen atom, the intrinsic symmetry leads to more diabatic behaviour (see Section 3.3), allowing the initial Stark polarisation to be preserved as the atom approach the surface. However, as noted above, local surface fields may play an important role in the surface ionisation and ion detection, and in addition to the acceleration (or deceleration) of the incoming Rydberg atom, re-orientation of the Stark states with respect to the surface normal is possible if the direction of the resultant field vector (which may not necessarily be parallel to the surface normal) is followed adiabatically when approaching the surface. In theory, this should lead to a loss of control over the final orientation of the Stark states, in contrast to the experimental observation above. The apparent lack of re-orientation observed experimentally may be accounted for by considering that only the most blue-shifted states which ionise closest to the surface (experience the highest local surface fields) are likely to undergo re-orientation, and when the resultant field-axis has been re-oriented (or even reversed), the local surface region at which this occurs has a negative potential (opposing the direction of the extraction field), which attracts the resultant ions towards the surface and inhibits their detection. Thus, although re-orientation may take place for the most blue-shifted states, the resultant ions from the surface ionisation of the re-oriented Stark states are unlikely to be extracted and detected, thus the experimental ionisation profiles only show ionisation of the states which has (mostly) preserved its orientation with respect to the surface normal.

7.3 Collisional velocity

In this section, the effects of the collisional velocity of the incident H atoms are investigated. The mean collisional velocities studied are $\bar{v}_\perp = 650$ ms^{-1} and 390 ms^{-1}, and are achieved by using either an unseeded beam of ammonia or a gas beam that

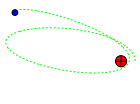

is seeded in helium, followed by a delay of 180 μs or 300 μs respectively between the photodissociation laser and the Rydberg excitation laser (the slower beam takes longer to reach the Rydberg excitation region); for more details see Section 6.1.1.

The change in collisional velocity mainly affects the minimum distances at which ions formed at the surface can be extracted (see Eq. 1.15), although the ionisation distances can also shift and the extent of non-adiabatic interactions can change (see Section 3.2). For the small range of velocities studied here, the variation in ionisation distances and non-adiabatic interactions are expected to be negligible. Figure 7.9 shows the surface ionisation profiles of the most extreme red-shifted $m_l = 0$ Stark states of the $n = 20{-}36$ manifolds at a mean collisional velocities of $\bar{v}_\perp = 650$ ms^{-1} (black lines) and 390 ms^{-1} (red lines). As expected, the ion-detection probability is higher at lower fields due to the decrease in the collisional velocity of the Rydberg atom.

Comparing the experimental profiles in Fig. 7.9 with the OTB and mean-field wavepacket calculations shows that, again, the OTB approach provides a good estimation of the onset of ion signal but does not account for the slow rise in signal with field, while the wavepacket approach predicts a broader profile, but the onset of ion signal is later than observed experimentally. Nonetheless, both theories shows the same qualitative behaviour as the experimental results. The semi-empirical model based on the calculated OTB ionisation distances given by Eq. 7.1 is shown in Fig. 7.9 as dashed lines. Again, this simple model provides an excellent quantitive fit of the experimental results.

7.4 Collisional angle and Rydberg trajectory

The effect of collisional velocity has been studied in the previous section by changing the overall kinetic energy of the atoms (both perpendicular and parallel components with respect to the surface), leaving the trajectory of the Rydberg atom over the

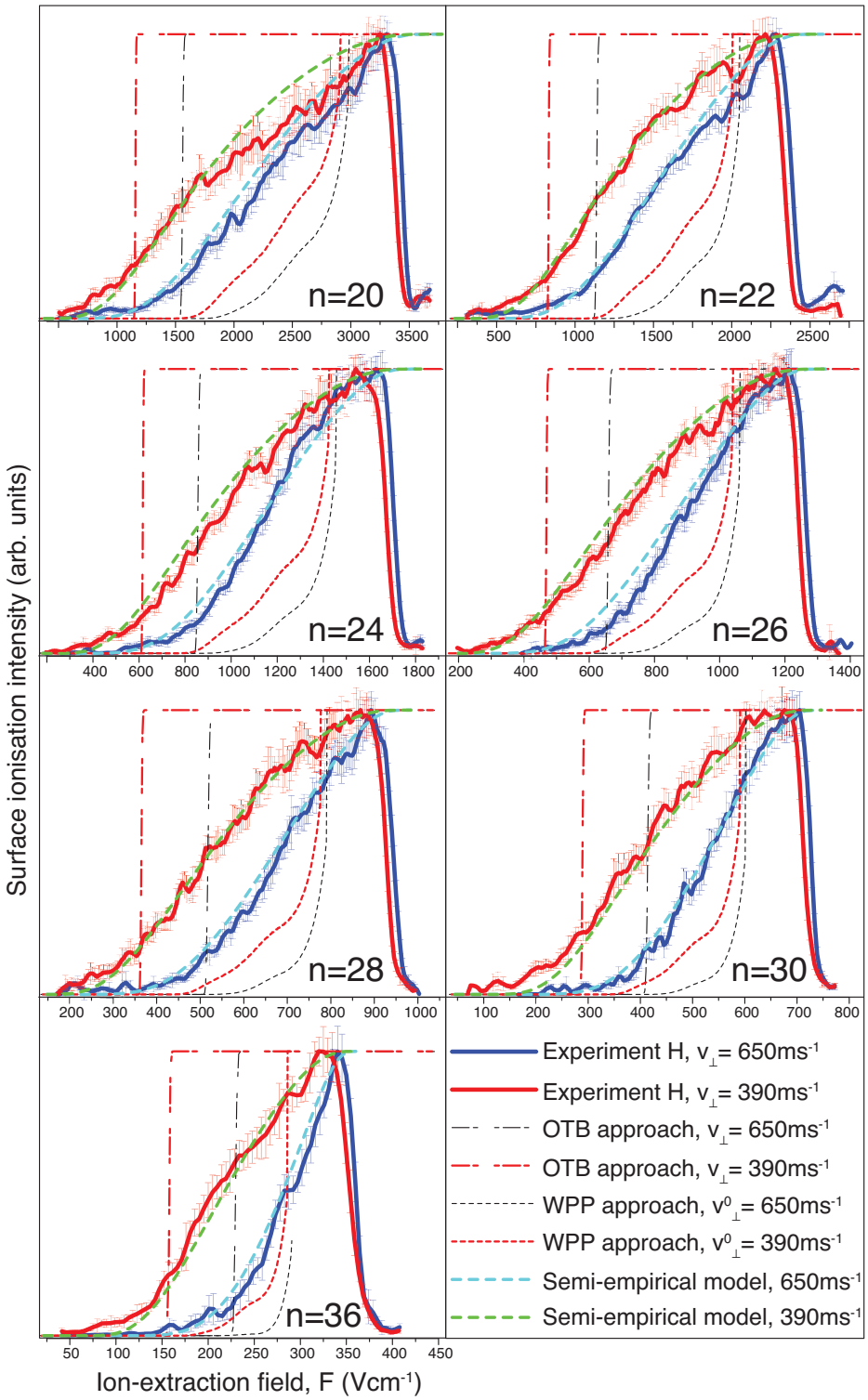

Figure 7.9: Surface ionisation signal of the most extreme red-shifted $m_l = 0$ Stark states of the $n = 20 - 36$ manifolds as a function of ion-extraction field. The results for H atoms with a mean collisional velocity of $\bar{v}_\perp = 650$ ms^{-1} and 390 ms^{-1} are shown in blue and red lines respectively. The results of the OTB, wavepacket propagation (WPP) and the semi-empirical model (Eq. 7.1) are also shown.

metal surface unchanged. The perpendicular and parallel velocity components can also be modified by changing the collisional incident angle of the Rydberg atoms, and in this case, the trajectory of the Rydberg atoms over the surface will be changed at the same time. If the surface is homogeneous, then the surface ionisation profiles from different collisional incidence angles should only vary due to effects of different collisional velocities (*i.e.*, the perpendicular velocity component). It has been shown in the previous section that such effects can be modelled very well using a modified semi-empirical OTB model (Eq. 7.1). Thus any deviations from the model can be attributed to change in the Rydberg trajectory parallel to the surface, and could provide some information on the possible surface inhomogeneities.

Figure 7.10 shows the surface ionisation signal of the most extreme red-shifted $m_l = 0$ Stark states of the $n = 20 - 36$ manifolds as a function of ion-extraction field, for H atoms at incident angles of $\sim 15°$ ($\bar{v}_\perp = 650$ ms^{-1}) and $\sim 10.2°$ ($\bar{v}_\perp = 443$ ms^{-1}) (the total velocity $\bar{v}_{\rm tot}^2 = \bar{v}_\parallel^2 + \bar{v}_\perp^2$ is constant). The angle of incidence is modified by rotating the surface and detector, which are both mounted on the same rotating flange, and the mean incidence angle of the Rydberg atoms is taken from the trajectory simulations outlined in Section 6.1.4. Decreasing the collisional angle decreases the kinetic energy component perpendicular to the surface, which makes ion extraction more facile for a given electric field (see Eq. 1.15). This is illustrated by the $n \geq 23$ experimental profiles in Fig. 7.10 and, as expected, the semi-empirical OTB model (Eq. 7.1) provides a good fit of the ionisation profiles at the shallower collisional angle of 10.2°. However, the experimental results for $n \leq 23$ appear qualitatively different from the behaviour at higher principal quantum numbers, and the model no longer fits. For $n = 23$ the ionisation profiles appear the same for both collisional angles, and for $n < 23$ (particularly the $n = 22$ profile) the ion-signal collected for the 10.2° incidence is even smaller than the 15° incidence. The lower ion signal at the shallower

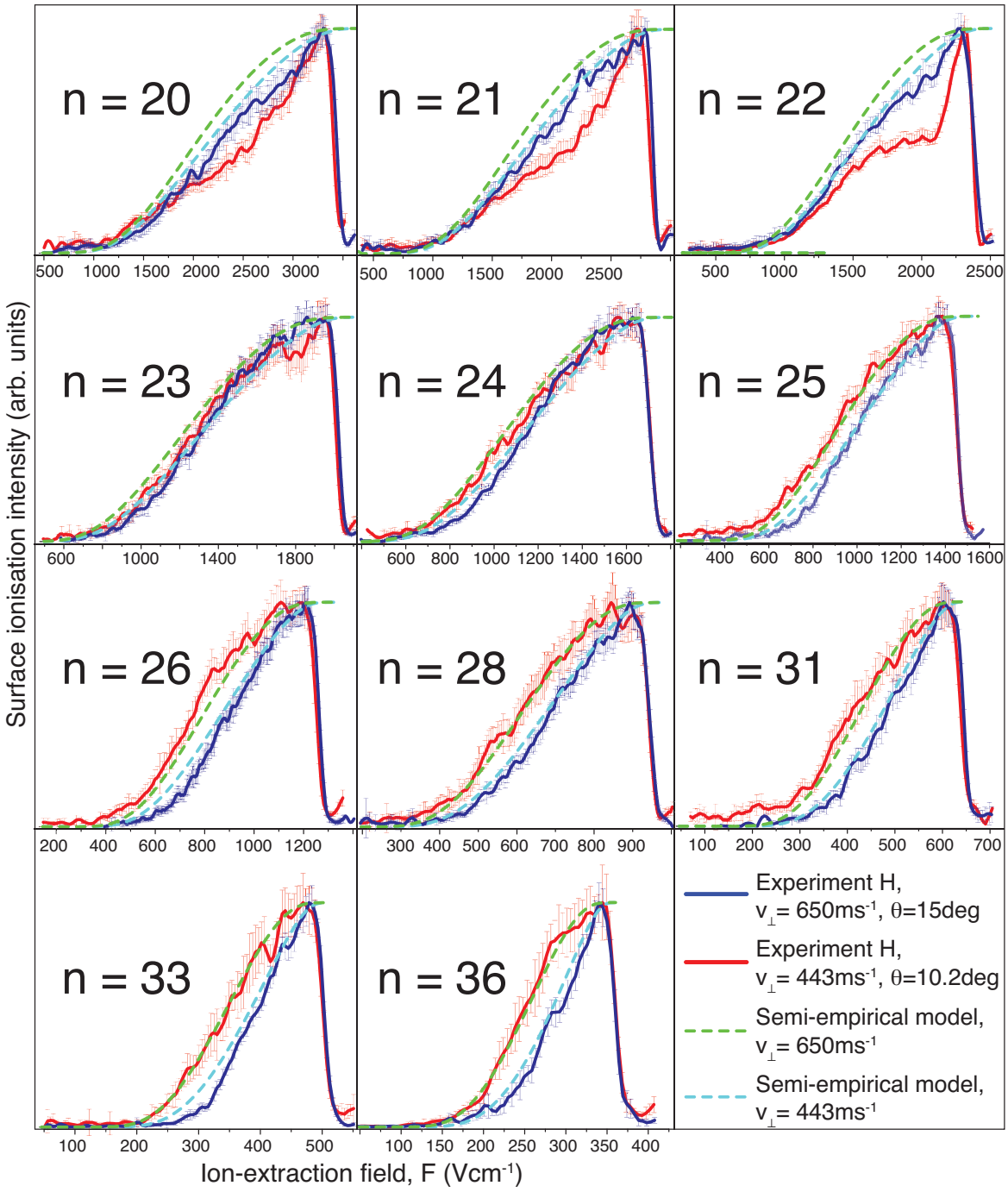

Figure 7.10: Surface ionisation signal of the most extreme red-shifted $m_l = 0$ Stark states of the $n = 20 - 36$ manifolds as a function of ion-extraction field. The results for H atoms with a mean *total* velocity of $\bar{v}_{\rm tot} = \sqrt{\bar{v}_{\parallel}^2 + \bar{v}_{\perp}^2} = 2500$ ms^{-1} at incident angles of $\sim 15°$ ($\bar{v}_{\perp} = 650$ ms^{-1}) and $\sim 10.2°$ ($\bar{v}_{\perp} = 443$ ms^{-1}) are shown in blue and red lines respectively. The results of the semi-empirical OTB model (Eq. 7.1) are shown as dashed lines.

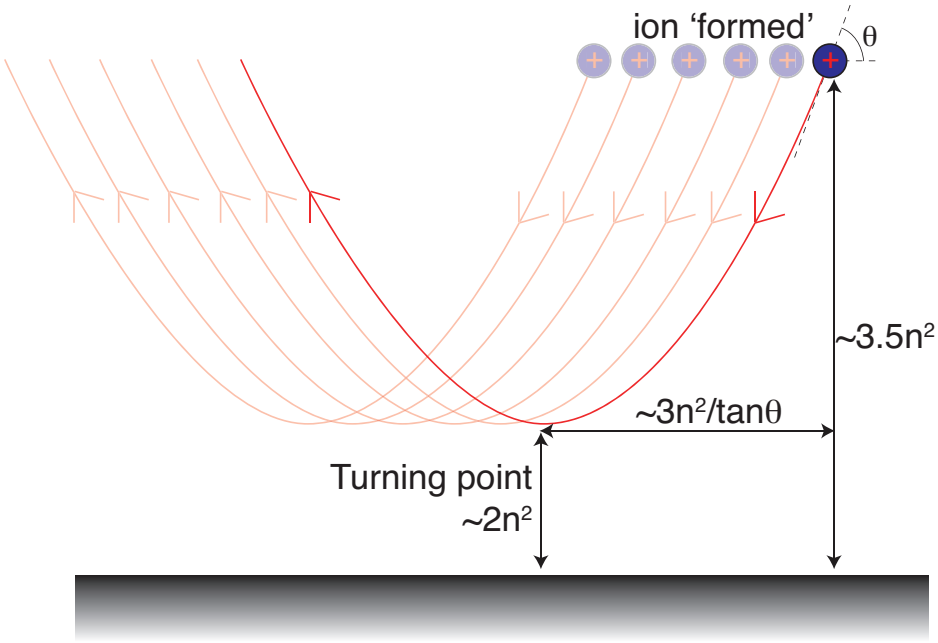

Figure 7.11: Illustration of the ion trajectory over the metal surface after ionisation, for an ion-extraction field just large enough to pull the ion away from the surface.

incidence angle is surprising, and cannot be reproduced from the local surface field model developed in Section 5.2.

As mentioned above, any deviations from the semi-empirical model should arise due to the change in the Rydberg trajectory parallel to the surface. As shown in Section 5.1, the ionisation profiles are more sensitive to the change in the ion-extraction probability (the minimum distance at which an ion can be extracted from) than to the change in the ionisation distance and so, as an approximation, the changes in the ionisation profiles are attributed to the changes in ion-extraction probability. A possible qualitative explanation for the decreased ion signal at smaller collisional angles is that the ion trajectory passes over larger area of the surface for more grazing collisions, and so the likelihood of traversing a local area for which the ion-extraction probability is lower, or for which the ion is more attracted (as a result of surface inhomogeneity), is also higher. Consequently, the total fraction of ions that can be extracted for a given

field is smaller for the more shallow incidence angle trajectories.

The dimensions of the surface inhomogeneities can be estimated from the experimental results. Typically surface ionisation occurs at approximately $3.5n^2$ a_0 from the surface (see Fig. 5.2) and, for this ionisation distance, the minimum ion-extraction field corresponds to a minimum ion-surface separation (where the ions are just turned around) of $\sim 2n^2$ a_0 (by considering only an image-charge potential). The corresponding horizontal distance (parallel to the surface) travelled by the ion before the turning point is $\approx 3n^2/\tan\theta$ a_0, where θ is the angle of incidence. Figure 7.11 illustrates the calculated ion trajectory. The observation that only Rydberg states with $n \leq 23$ deviate from the expected model behaviour when the collisional angle is changed suggests that the effects of the surface inhomogeneity causing the reduced ion signal extends as far as $\approx 2(23^2)$ $a_0 \simeq 50$ nm away from the surface, and the nature of the surface in the parallel direction 'probed' by the ion changes over a range of $\approx 3(23^2)(1/\tan 10 - 1/\tan 15) \simeq 3100$ $a_0 \simeq 150$ nm.

The dimensions given above are similar to the surface potential variations measured by Dunning and co-workers [48] (see Fig. 5.8). However the local surface field model in Section 5.2 always predicts a higher ion-signal for the lower collisional incident angle (see Fig. 5.11), and does not provide the desired outcome of a lower ion signal at the lower collisional angle. This is because in the model, the effect of increased ion-extraction probability from the lower kinetic energy perpendicular to the surface is dominant over the effects due to the change of Rydberg trajectory. Clearly, further theoretical work is required to explain the effects of different collisional angle on the surface ionisation ion signal, and this will be a focus for future investigations.

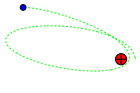

7.5 Electron detection

So far only the behaviour in ion-extraction fields has been considered. By reversing the direction of the applied field (see Section 6.1.2), electrons as opposed to protons can be detected in principle. The surface ionisation dynamics in the electron-extraction field has been studied theoretically in Section 3.4. It is found that Rydberg states are more likely to encounter avoided crossings with this field orientation rather than under ion-extraction fields, and for a sufficiently large electron-extraction field, vacuum-oriented states (red-shifted) can ionise by losing an electron in the direction of the vacuum as opposed to the metal surface, giving rise to a possible experimental electron signal. As in the previous experimental work involving Rydberg H_2 molecules [64], it is found that an electron signal from the surface ionisation process can also be detected for the Rydberg hydrogen atom system, and the results are discussed below.[1]

Figure 7.12 shows the surface ionisation signal (*electrons*) as a function of extraction field for selected most red-shifted ($k = 1 - n$, $m_l = 0$), vacuum-oriented states of the $n = 20 - 31$ manifolds (red lines). The profiles are very similar to those obtained for an ion-extraction field (see Fig. 7.4), with a slightly later onset of signal ($\sim 0.05n^{-4}$ a.u. as opposed to $\sim 0.04n^{-4}$ a.u.). The constant velocity wavepacket result for the fraction of backscattered electrons as a function of field for the $k = +9, m_l = 0, n = 10$ state is shown as green line in the bottom plot of Fig. 7.12. Although it does not fit quantitatively with the experimental profiles, it provides a plausible qualitative explanation for the detected electron signal: that the electrons come from a backscattered loss mechanism as the Rydberg state approaches the surface.

Surprisingly, a surface ionisation signal under electron-extraction fields can also be

[1]The electron signal can be shown to be surface dependent by changing the excitation height or the extraction field delay, as outlined in Section 6.2.2 and 6.2.3. As in Ref. [64], the electron signal at the 'surface signal time-gate' does not appear at electric fields beyond the field ionisation limit, therefore, the detected electrons are not from secondary processes due the neutralisation of the positive ion at the surface (see Fig. 1.10).

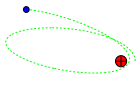

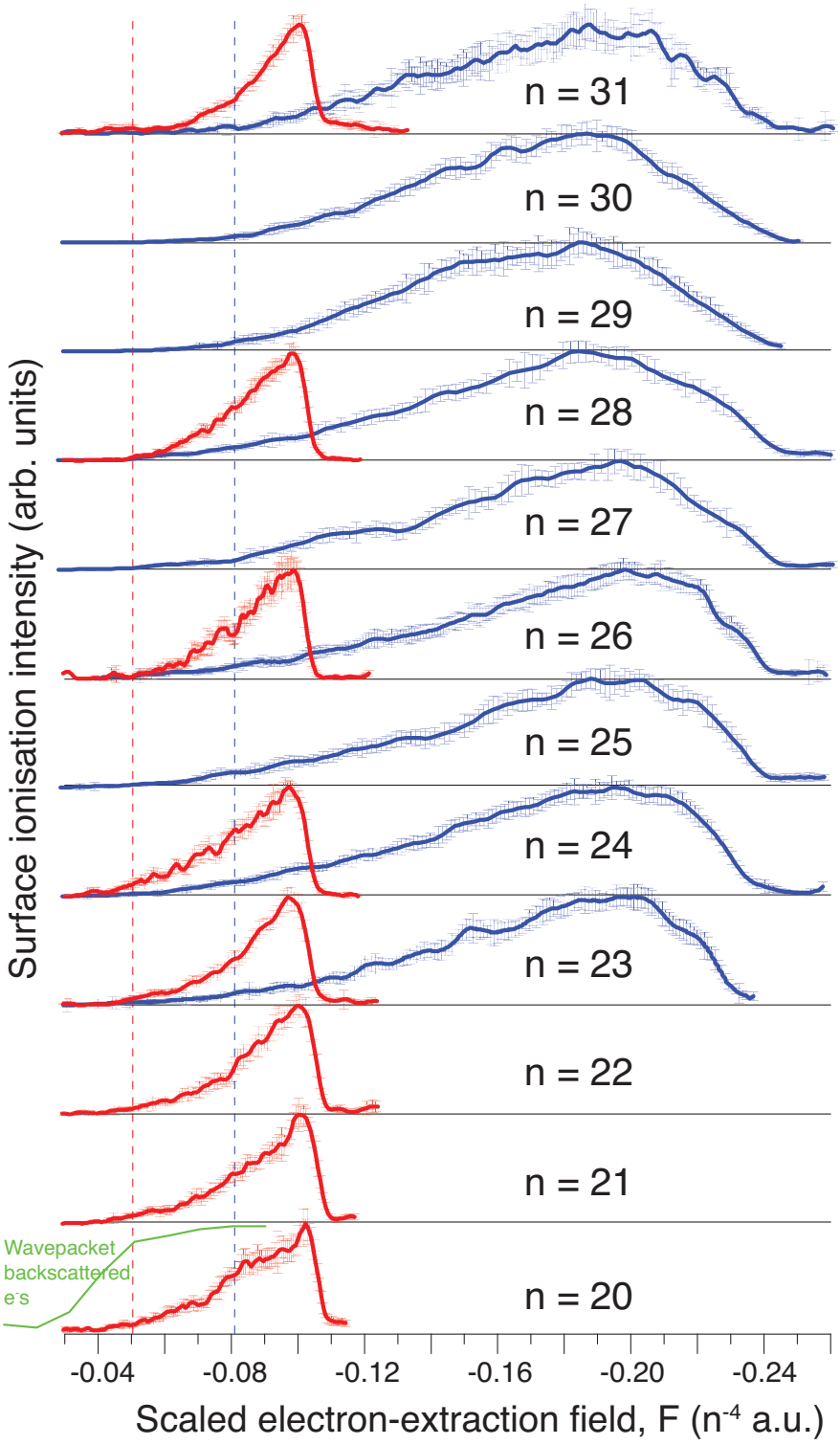

Figure 7.12: Surface ionisation signal (electrons) as a function of *scaled electron*-extraction field for selected most red- and blue-states of the $n = 20 - 31$ manifolds. The mean collisional velocity $\bar{v}_\perp = 650$ ms^{-1}. The profiles are normalised to the highest signal intensity. The dotted lines mark roughly the onset of the electron signals for the red and blue states. The constant velocity wavepacket result for the fraction of backscattered electrons as a function of field for the $k = +9, m_l = 0, n = 10$ state is shown as green line in the bottom plot.

detected for Stark states that are not red-shifted, *i.e.*, states which are not initially vacuum-oriented in the presence of an electron-extraction field. The blue lines in Fig. 7.12 show the *electron* surface ionisation signal of the most blue-shifted ($k = 1-n$, $m_l = 0$) states of the $n = 23 - 31$ manifolds. The signal is broad, and the signal intensity is much higher than for ion-extraction fields (note that the ionisation profiles in Fig. 7.12 have been normalised to the maximum intensities, as a direct relative measurement was not possible, but in general the maximum intensities of the signals for the red- and blue-shifted states are similar in electron-extraction fields). The onset of the electron signal for the most blue-shifted state is also at much lower fields ($\sim 0.08n^{-4}$) compared with the ion-extraction field case ($\sim 0.14n^{-4}$, see Fig. 7.7 and 7.6). To understand the origin of the electron signal for the surface-oriented states, Fig. 7.13 shows the surface ionisation signal of a range Stark states of the $n = 23$ manifold.

Figure 7.13 shows that unlike the ion-extraction case, where each Stark state has a distinct onset of surface ionisation signal (see Fig. 7.6), for electron-extraction fields, this is only the case for Stark states with $k \sim< +8$ (the blue curve), where the onset of ionisation signal is at progressively higher fields, while for $k \sim> +8$ the onsets of ionisation signal are very similar to states in the middle of the manifold ($k = 0$ state, the green curve). This suggest that the *initial* Stark polarisation of the surface-oriented blue-shifted states may not be preserved when approaching the surface, but instead acquires the ionisation characteristics of Stark states in the middle of the manifold and even red-shifted vacuum-oriented states, which consequently allows the electron to be lost towards the vacuum (instead of the metal). Indeed, Section 3.4 shows that under electron-extraction fields, Rydberg levels for a given manifold encounter significantly more avoided crossings than under ion-extraction fields (see Figure 3.8), and the blue-shifted states do exhibit some of the ionisation characteristics of Stark states in the

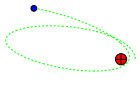

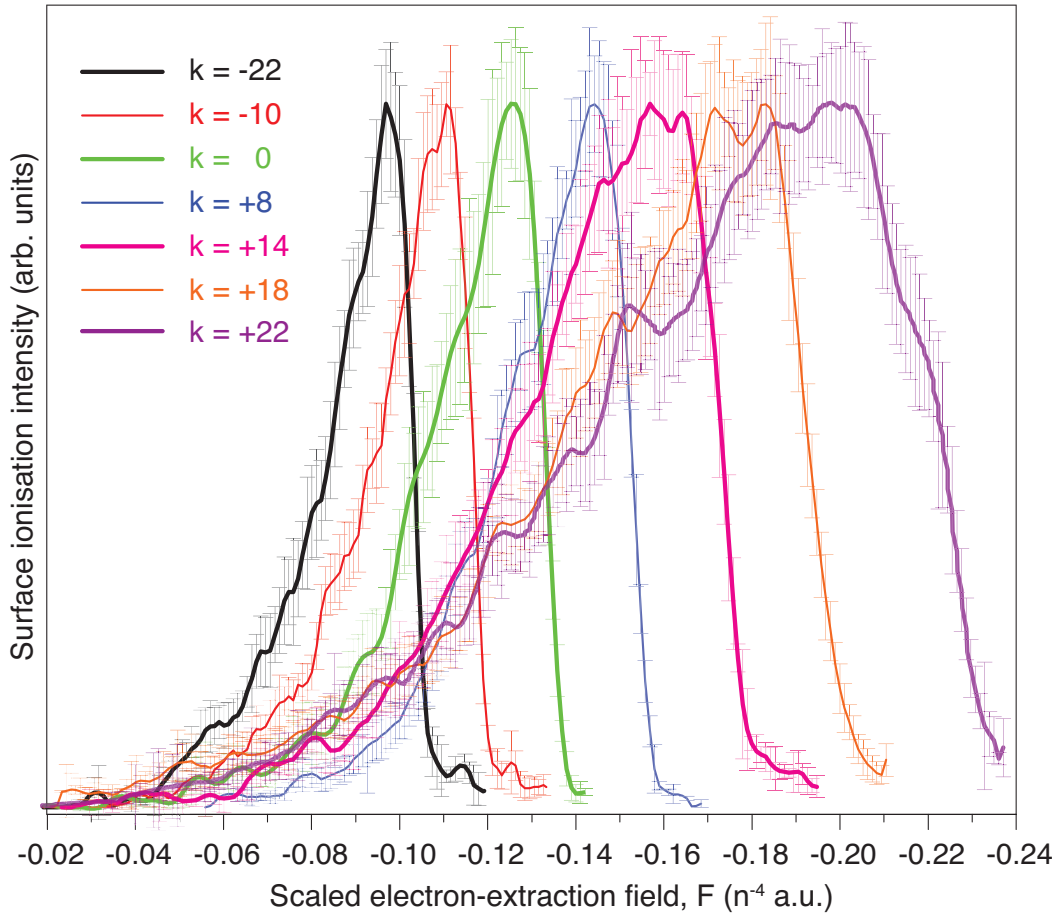

Figure 7.13: Surface ionisation signal (electrons) as a function of *scaled electron*-extraction field for selected Stark states of the $n = 23$ manifolds. The mean collisional velocity $\bar{v}_\perp = 650$ ms^{-1}. The profiles are normalised to the highest signal intensity.

centre of the manifold (see middle plot in Fig. 3.9). The extent of the mixing of Stark polarisation predicted for the $n = 10$ manifold is relatively small compared to what is apparently observed experimentally for $n \geq 20$. However, bearing in mind that the number of states within the n-manifold is much greater at the experimental range of n, and thus more possible avoided crossings and non-adiabatic transitions can occur, as well as the possibility of additional external perturbations, such as local surface fields [48], coupling the close-in-energy Rydberg states in the real system, it is plausible that the resulting extent of mixing of the states of different polarisation is sufficiently large to account for the experimental ionisation profiles. As noted in Section 7.2, the re-orientation of Stark states by the presence of local surface fields is possible, and may also play a role in the apparent loss of polarisation observed above. However, the contribution from the re-orientation effect is expected to be small because the re-orientation of the resultant field-axis occurs at small atom-surface separations over a local surface region with surface fields that opposes the direction of the extraction field, and thus inhibits the resultant detection of the charged particle of interest (in this case, electrons).

In some ways, this mixing of Stark polarisation when approaching the metal surface is similar to the observed surface ionisation behaviour of the Rydberg Xe most blue-shifted Stark states [53], where these vacuum-oriented states (under ion-extraction fields) exhibit a similar onset of ion signal compared to the most red-shifted, surface-oriented states, as a result of multiple level crossings as the surface is approached.

The collisional velocity of the Rydberg atom is predicted to strongly affect the extent of Stark mixing (see Chapter 3), and so in principle, the interpretation of the experimental results above can be tested by varying the velocity of the incident atomic beam. However, for the range of collisional velocity studied here ($\sim 390 - 780$ ms^{-1}), it is found that changing the collisional velocity of the Rydberg atom has a negligible

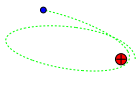

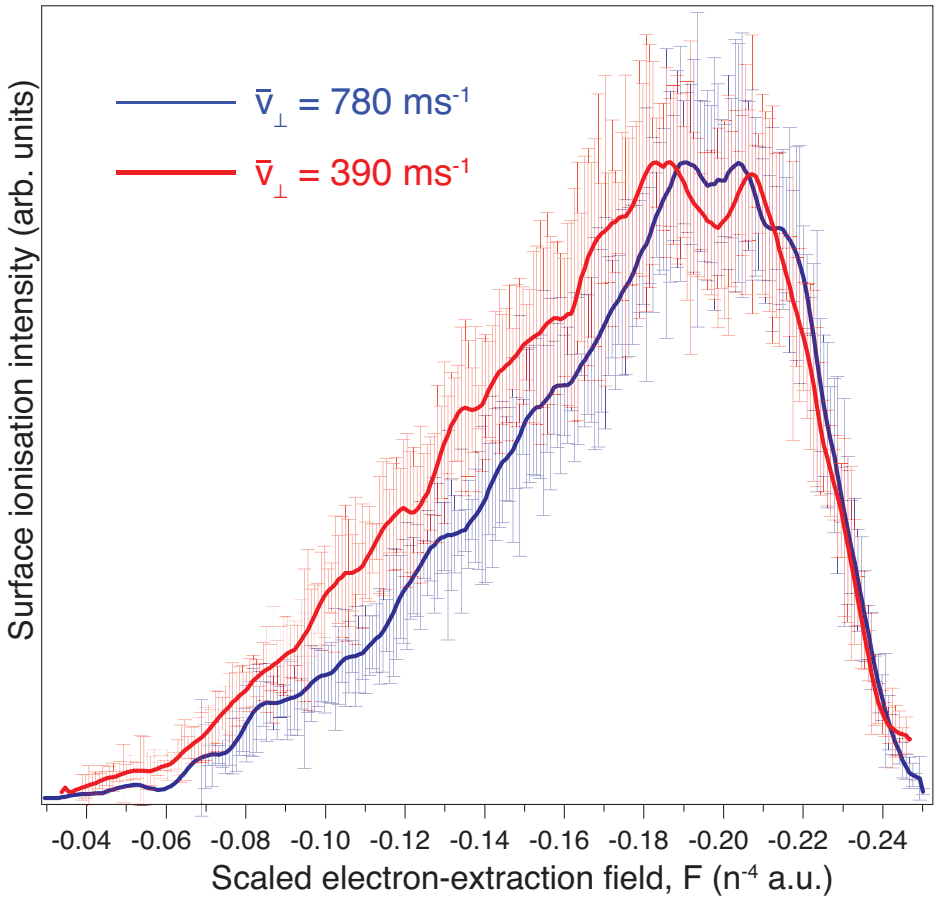

Figure 7.14: Surface ionisation signal (electrons) as a function of *scaled electron*-extraction field for the $k = +25, m_l = 0, n = 26$ state at collisional velocities of $\bar{v}_\perp = 780$ ms^{-1} and 390 ms^{-1}, selected by triggering the Rydberg excitation lasers 150 μs and 300 μs after the NH_3 photodissociation laser, and using an unseeded and a He seeded ammonia gas beam, respectively.

effect on the appearance of the ionisation profiles. As an example, Fig. 7.14 shows the surface ionisation profiles of the $k = +25, m_l = 0, n = 26$ state at collisional velocities of $\bar{v}_\perp = 780$ ms^{-1} and 390 ms^{-1}. Only a minor increase in electron signal is observed at the lower collisional velocity; the signal is relatively insensitive to velocity because of the high extraction probability of the electron which is very light.

It is shown in the following section that the study of the surface ionisation of Rydberg states at a rough machined aluminium surface can provide further insight into the ionisation dynamics of the most blue-shifted surface oriented Stark states under electron-extraction fields.

7.6 Surface roughness

Section 5.2 has shown that theoretically the detection probability of ions (or electrons) can be very different for a rough surface compared with a flat surface. In this section, the experimental results for the surface ionisation of Rydberg hydrogen atoms at a rough machined aluminium surface (described in Section 6.3) is discussed for both ion- and electron-detection fields.

7.6.1 Ion-extraction at a rough surface

Figure 7.15 shows the surface ionisation profiles for the most red-shifted, surface-oriented Stark states of the $n = 20 - 36$ manifolds for the rough surface compared with the atomically flat gold surface (Section 6.3). In accord with previous observations [44, 50], the ionisation profiles are broader and the onsets of ion-signal are at lower extraction fields for the rough surface. As explained in Ref. [50], this can be partly attributed to the larger range of effective collisional angles incident at the rough surface, resulting in a broad range of detection distances for a given electric field; but

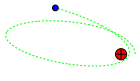

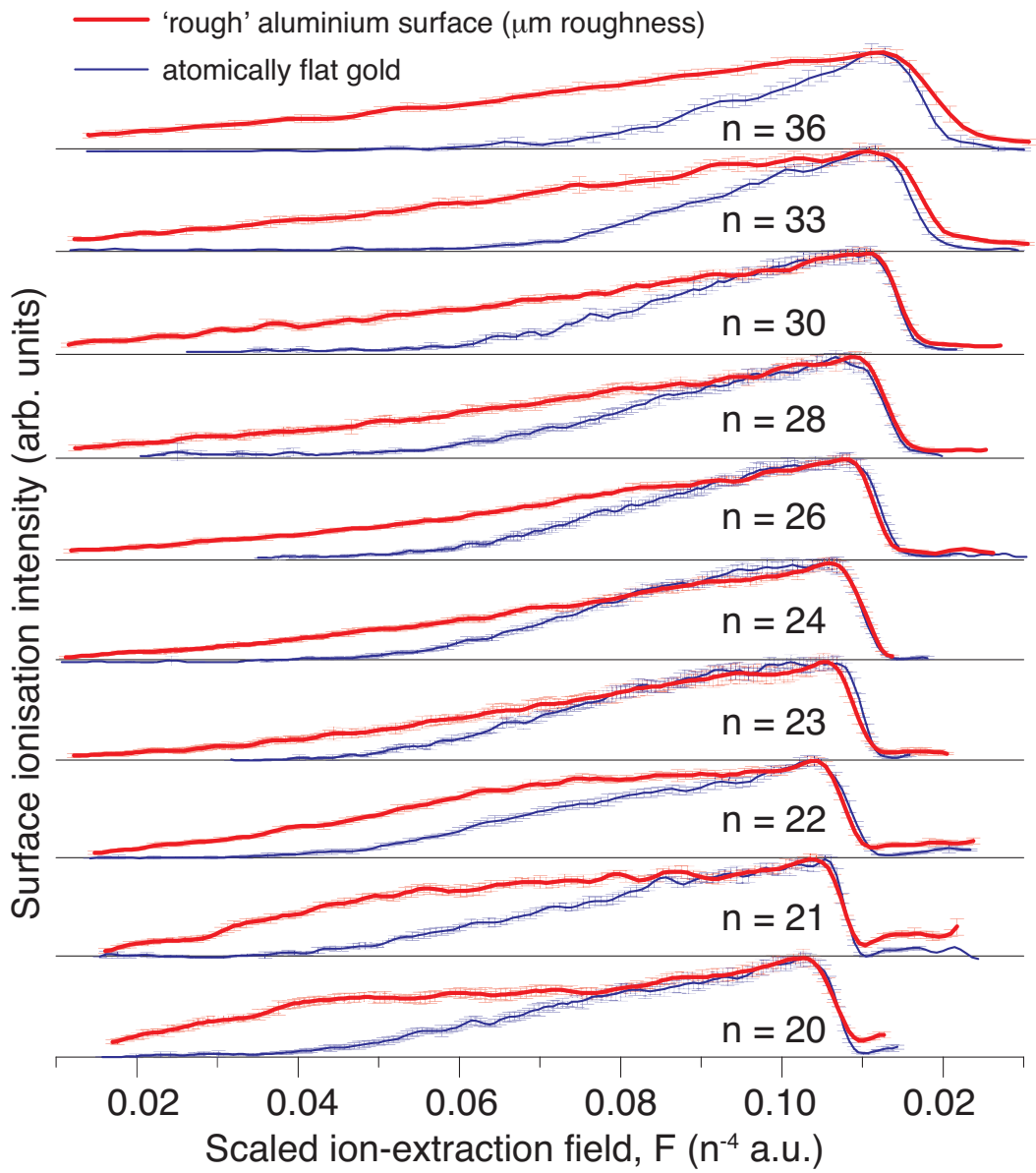

Figure 7.15: Surface ionisation signal as a function of scaled ion-extraction field for the most red-shifted, surface-oriented Stark states of the $n = 20 - 36$ manifolds incident at a rough aluminium surface with μm roughness (red lines) and at an atomically flat gold surface (blue lines). The collisional velocity of the hydrogen atoms is $\bar{v}_{\perp} = 650$ ms^{-1}.

the local surface fields are also likely to play a role in increasing the ionisation distance and enhancing the ion-extraction probability (see below).

Figure 7.15 shows that the form of the profiles appears different for $n \leq 22$ compared with those of higher ns. To show this more clearly, Fig. 7.16(a) shows ionisation profiles plotted on the same intensity axis. For $n > 22$ the ionisation profiles are nearly identical, exhibiting roughly a linear increase of ion signal with scaled extraction field. But for the $n = 20, 21, 22$ profiles, there appears to be three different gradients: a steep increase at lower extraction fields ($F < 0.05n^{-4}$ a.u.), followed by a shallow increase in a 'plateau' region, and finally a sharp rise again just before the field-ionisation limit.

Figure 7.16(b) presents the profiles on an unscaled field axis, and shows that the initial onsets of ion signal are nearly identical for the $n \leq 23$ profiles, and *independent* of n. These results can be interpreted in terms of a change in ionisation distance and / or a change in ion-extraction efficiency due to the rough surface variations and the associated local surface fields, but it is likely that both effects are strongly affected by the rough surface. Thus, beyond a certain 'critical' field, which would correspond to some range of distances from the rough surface (since Eq. 1.15 does not strictly apply for a rough surface), there is a sharp increase in ionisation probability *and (or)* ion-extraction efficiency, and a large fraction of the initially populated Rydberg states, which would otherwise ionise closer to the surface and would not be detected by the extraction field (if the surface was flat), are ionised and pulled away from the surface. For a given n state, the fraction of Rydberg states that are ionised and detected, depends partly on the difference between the 'critical' field (or the corresponding range of distances) and the field value for the onset of ion signal for the flat surface (or the 'flat-surface' ionisation distance); *e.g.*, the level of the 'plateau' for the $n = 20$ state is lower than that of the $n = 21$ state, which is lower than that of the $n = 22$ state.

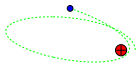

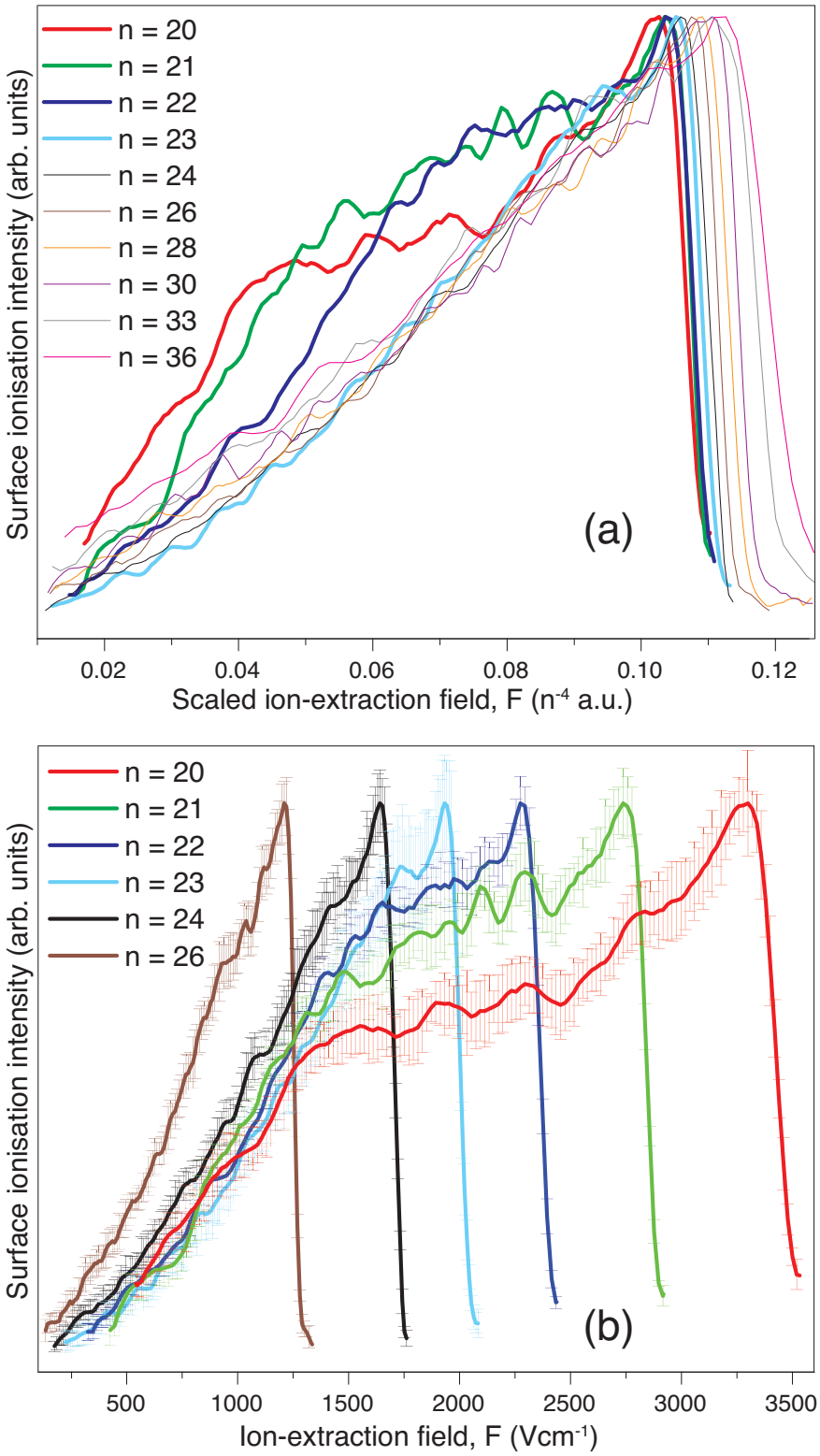

Figure 7.16: (a) Surface ionisation signal as a function of scaled ion-extraction field for the most red-shifted, surface-oriented Stark states of the $n = 20 - 36$ manifolds incident at a rough aluminium surface with μm roughness. The profiles for principal quantum numbers ≤ 23 are shown in bold. (b) Same as (a) but only for the $n = 20-26$ states, and on an un-scaled field axis.

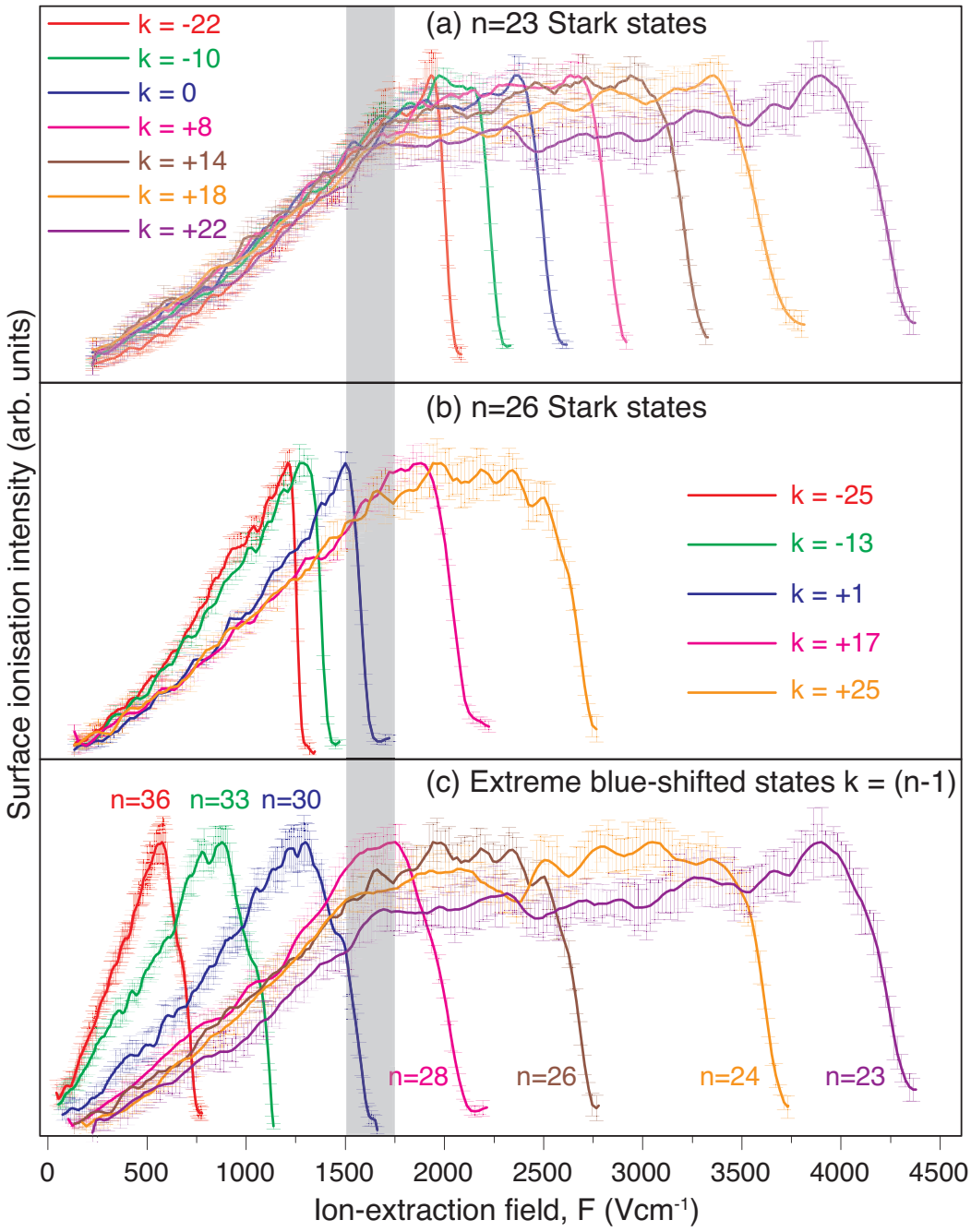

Figure 7.17: Surface ionisation profiles for Rydberg states incident at the rough machined aluminium surface with a collisional velocity of $\bar{v}_{\perp} = 650$ ms^{-1}. (a), (b) Results for the selected Stark states of the $n = 23$ and $n = 26$ manifolds respectively. (c) Results for the most extreme blue-shifted Stark state, $k = (n-1), m_l = 0$ of the $n = 23 - 36$ manifolds.

To further demonstrate that the 'critical' field introduced by the rough surface is a genuine effect, Fig. 7.17(a) and (b) shows the experimental surface ionisation profiles of the Stark states of the $n = 23$ and $n = 26$ manifolds respectively, and Fig. 7.17(c) shows the surface ionisation profiles of the most extreme blue-shifted states of the $n = 23-36$ manifolds. As noted in Section 7.2, for the case of the flat gold surface, the surface ionisation ion signal can only be detected for the most blue-shifted state of the $n \leq 28$ manifolds. For the rough surface, the surface ionisation signal can be detected for the full range of principal quantum numbers studied. It can be seen from Fig. 7.17 that all the ion signals are nearly at maximum intensity by a field of $\sim 1500-1750$ Vcm^{-1}, even for the most blue-shifted states of the $n = 23-26$ manifolds which would be extracted at much higher fields for a flat gold surface (see Fig. 7.6 and 7.7). As mentioned above, for a rough surface, there is no direct correspondence between the ion-extraction field and ionisation distance, since both the ionisation distance and the ion-extraction efficiency are likely to be strongly affected by the rough surface variations and the associated local surface fields. Nonetheless, to get a general idea of the distance range that the 'critical' field might corresponds to, using Eq. 1.15 (which is valid for a flat surface), the field range of $1500-1750$ Vcm^{-1} corresponds to a (flat surface) distance range of $\approx 70-80$ nm.

To examine how the experimentally observed rough surface 'critical' field (and the corresponding approximate distance range) might be related to the physical variations of the rough surface, Figure 7.18 shows the results of the rough surface trajectory calculations outlined in Section 5.2 for the most red-shifted state of the $n = 20-26$ manifold, but in one-dimension and with the rough surface described by repeating units of the experimentally measured profile shown in Fig. 6.13. The OTB critical fields are also shown for comparison. The ionisation profiles appear broadened from the OTB critical field, but do not exhibit the multiple gradients or the principal quan-

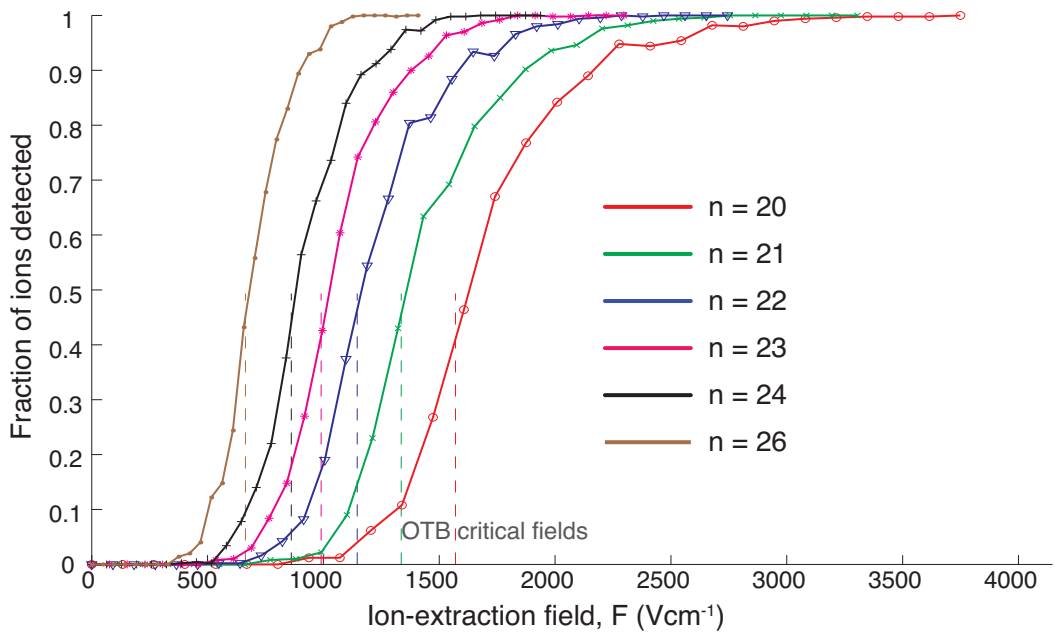

Figure 7.18: Calculated surface ionisation profiles for the most extreme red-shifted Stark state of the $n = 20 - 26$ manifold using the rough surface model outlined in Section 5.2. The measured profile shown in Fig. 6.13 is used to describe the rough surface in the 1D calculations. Vertical dashed lines mark the OTB critical fields, *i.e.* ionisation probability would be a step function at the critical fields for a 'flat' surface.

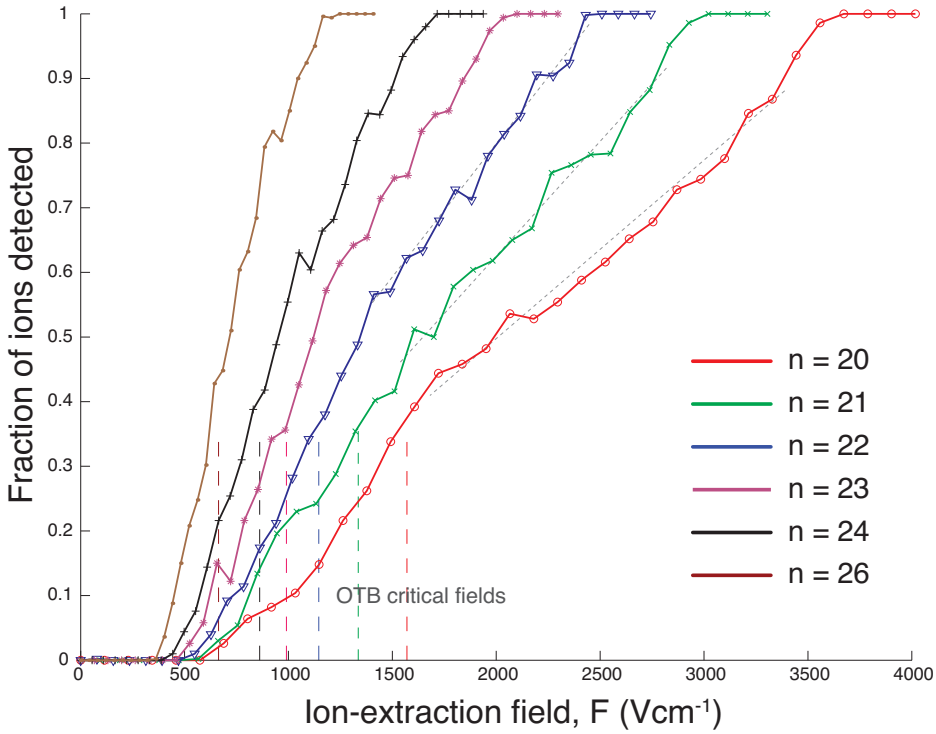

Figure 7.19: Calculated surface ionisation profiles for the most extreme red-shifted Stark state of the $n = 20 - 26$ manifold using the rough surface model outlined in Section 5.2. The surface parameters of $L = 500$ nm (lateral period of the surface variation), and $h = 100$ nm (maximum vertical variation) are used in the calculations. Vertical dashed lines mark the OTB critical fields. The grey dotted lines show the change of gradient of the ionisation profiles at a field of ~ 1500 Vcm^{-1}.

tum number independent onset of ion signal for $n \leq 23$ that are seen experimentally (Fig. 7.16(b)). The apparent small effect of the rough surface variations on the ionisation profiles is likely to be due to the limited resolution (500 nm) of the rough surface profile measurements: the Rydberg dimensions studied here and the lateral distance covered by the ion trajectories (shown by Fig. 7.11) are of the order of 100 nm, thus the *local* area sampled by the Rydberg state and resultant ion would appear nearly 'flat' in the current model.

In an attempt to reproduce the experimental behaviour shown by Fig. 7.16(b), a full range of corrugated surface parameters (the height of surface variations and lateral

period of the variations) are applied to the 2D rough surface model given in Section 5.2. Using parameters of $h = 100$ nm for the vertical variations and a period of $L = 500$ nm, ionisation profiles with some qualitative similarities to the experimental profiles (Fig. 7.16) can be obtained, and are shown in Fig. 7.19. The onsets of ion signal are similar (but *not* n-independent), and the ionisation profiles also exhibit multiple gradients similar to the experimental observation (there are changes of gradient at a field of $\sim 1500\,\mathrm{Vcm}^{-1}$, shown by grey dotted lines). In the model, the vertical variation h mainly affects the field value for the onset of the ion signal, while the lateral period L mainly affects the broadening of the ionisation profile from the initial onset of ion signal, and determines the 'form' of the profile (*i.e.* the multiple gradients). However, besides providing profiles with qualitative similarities with the experiment, there are no justifications for the empirical rough surface parameters used, and since the model applied here involves such a crude description of a rough surface (Section 5.2), it is difficult to argue whether these parameters might correspond the 'real' rough surface variations. Furthermore, it is shown in Fig. 7.19 that the striking n-independent rise of ion signal observed experimentally cannot be reproduced by the present theoretical model (compare Fig. 7.19 with Fig. 7.16(b)). Clearly, there are numerous factors that have not been included in the simple model given in Section 5.2, such as the local surface fields due to the surface corrugation (particularly at steps and edges [99]), and the effect of the full three dimensional environment of the rough surface on the ionisation distances (rather than only depending on the local height from the surface). The appropriate description and inclusion of these factors are likely to be critical for reproducing the experimental profiles and in particular, accounting for the apparent 'critical' field (or distance range). The development of such theoretical model is a challenging task that will be a focus of future work.

7.6.2 Collisional angle and Rydberg trajectory

Figure 7.20 shows the surface ionisation profiles of the most extreme red-shifted $m_l = 0$ Stark states of the $n = 20 - 36$ manifolds incident at the rough surface, for H atoms at collisional angles of $\sim 15°$ ($\bar{v}_\perp = 650$ ms^{-1}) and $\sim 10.2°$ ($\bar{v}_\perp = 443$ ms^{-1}) (the total velocity $\bar{v}^2_{\rm tot} = \bar{v}^2_\parallel + \bar{v}^2_\perp$ is constant). Unlike the gold surface results presented in Section 7.4, where for $n > 23$ a larger ion signal is observed at lower extraction fields for the smaller incident angle (due to the decrease in kinetic energy perpendicular to the surface and thus higher ion-extraction efficiency for a given field), the results for the rough surface for $n > 23$ are very similar for both collisional angles. The similar profiles for $n > 23$ can be understood in terms of the large range of *local* incident angles sampled by the Rydberg atoms at the inhomogeneous rough surface. And it appears to be the case here, that this range of angles is greater than the difference of $\sim 5°$ studied here (which is unsurprising for the rough surface), and consequently the change in collisional angle has negligible effect.

Figure 7.20 shows that as the principal quantum number decreases, the ionisation profiles for the more grazing collisional angle appears progressively smaller than that of the steeper incidence.[1] A plausible explanation is that the ion trajectories at a more grazing angle are more likely collide with a surface inhomogeneity (either physical or in terms of local fields), and consequently they are lost from the detection, and the resultant ion signal is smaller than that of the steeper incidence angle trajectories.

7.6.3 Electron detection at a rough surface

It is shown in Section 7.5 that electrons can be detected from the surface ionisation process for both red- and blue-shifted Stark states. The electron signal is attributed

[1]Note that smaller ion signals at more grazing angle are also observed for the atomically flat gold surface in Section 7.4 for $n < 23$.

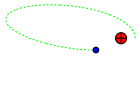

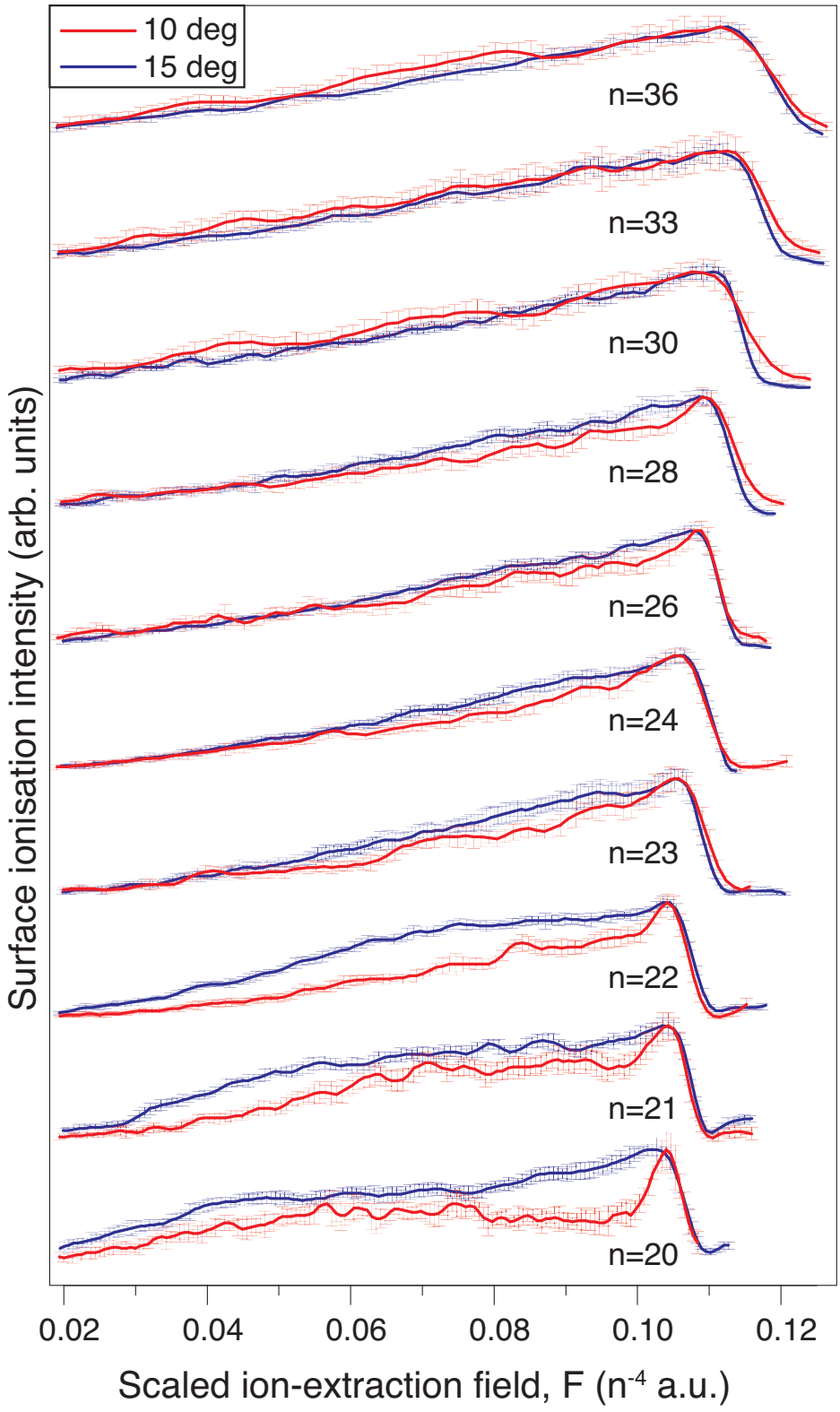

Figure 7.20: Surface ionisation signal of the most extreme red-shifted $m_l = 0$ Stark states of the $n = 20 - 36$ manifolds incident at the rough surface as a function of ion-extraction field. The results for H atoms with a mean *total* velocity of $\bar{v}_{\rm tot} = \sqrt{\bar{v}_{\parallel}^2 + \bar{v}_{\perp}^2} = 2500$ ms^{-1} at incident angles of $\sim 15^{\circ}$ ($\bar{v}_{\perp} = 650$ ms^{-1}) and $\sim 10.2^{\circ}$ ($\bar{v}_{\perp} = 443$ ms^{-1}) are shown in blue and red lines respectively.

to a backscattered electron loss mechanism that has been predicted by wavepacket calculations (Section 3.5). For red-shifted states which are vacuum-oriented under electron-extraction fields, backscattered ionisation can occur directly, while for blue-shifted states which are initially surface-oriented, backscattered electron loss is assumed to occur via mixing with other Stark states which exhibit vacuum-oriented characteristics (the Rydberg levels within the n-manifold converges in energy when approaching the surface under electron-extraction fields, see Section 3.4). Since the nature of the ionisation process is very different for electron-extraction fields, it will be of interest to see if similar strong differences can be observed for the ionisation profiles of the rough surface compared with those of the atomically flat gold surface.

Figure 7.21 shows the electron surface ionisation signal for the most red-shifted, surface-oriented Stark states of the $n = 20 - 28$ manifolds incident at the rough aluminium surface compared with the gold surface. Unlike the case of the ion-extraction fields, there are no 'critical' fields at which the surface ionisation signal rises sharply, but instead each Rydberg state has a different field value for the onset of electron signal. For $n > 24$ the ionisation profiles for the rough surface are similar to the gold surface, while for $n \leq 24$ the electron signal at lower extraction fields are slightly larger than for the flat gold surface, but the field values for the onset of the electron signal are still very similar for both surfaces. This relatively surface independent behaviour can be explained by the nature of the red-shifted Stark states *and* the mechanism of back-scattered electron loss. As explained in Section 3.5, the loss of electrons towards the vacuum is due to the lowering of the potential barrier on the vacuum side of the ion-core as a result of the electron-extraction field, and the long range repulsive surface potential essentially drives the electron over this barrier. Since the saddle point on the vacuum side of the ion-core is far from the surface, and the height of the barrier is dominated by the electric field, it is expected that the backscattered electron loss

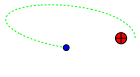

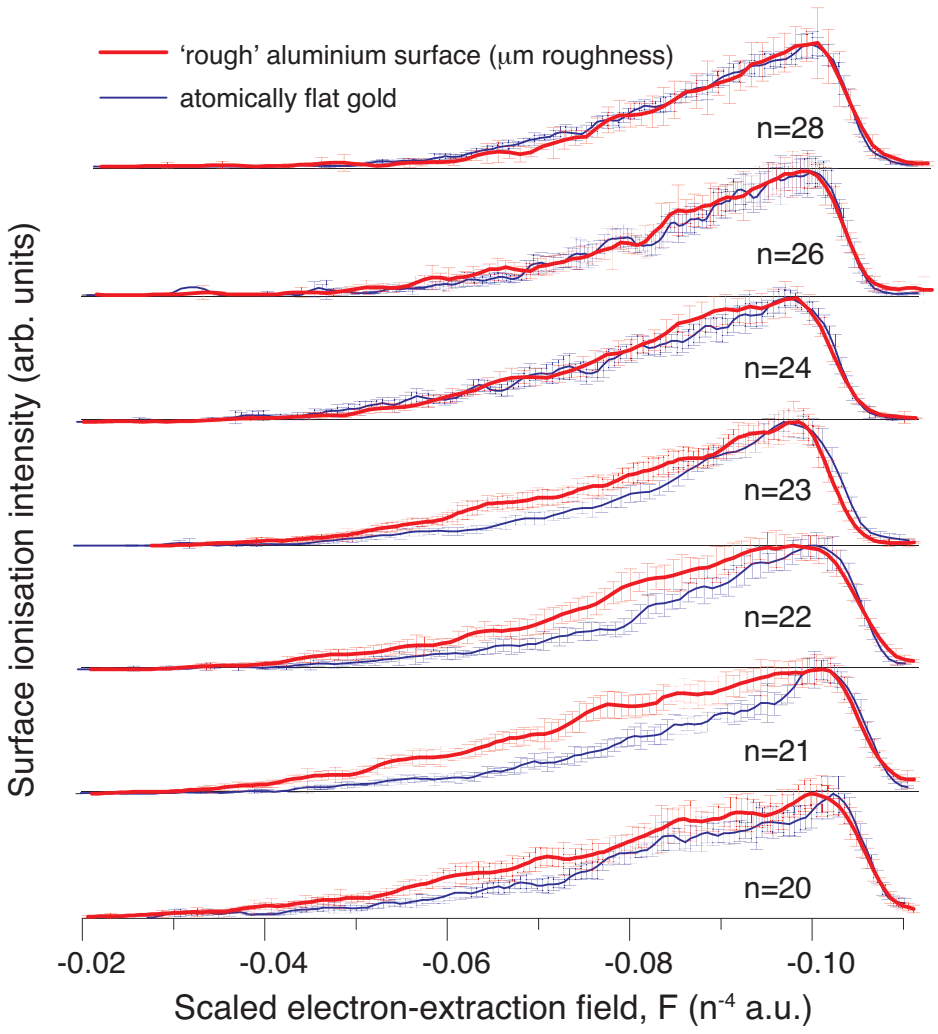

Figure 7.21: Surface ionisation signal as a function of scaled *electron*-extraction field for the most red-shifted, surface-oriented Stark states of the $n = 20 - 28$ manifolds incident at the rough aluminium surface (red lines) and at the atomically flat gold surface (blue lines). The collisional velocity of the hydrogen atoms is $\bar{v}_{\perp} = 650$ ms^{-1}.

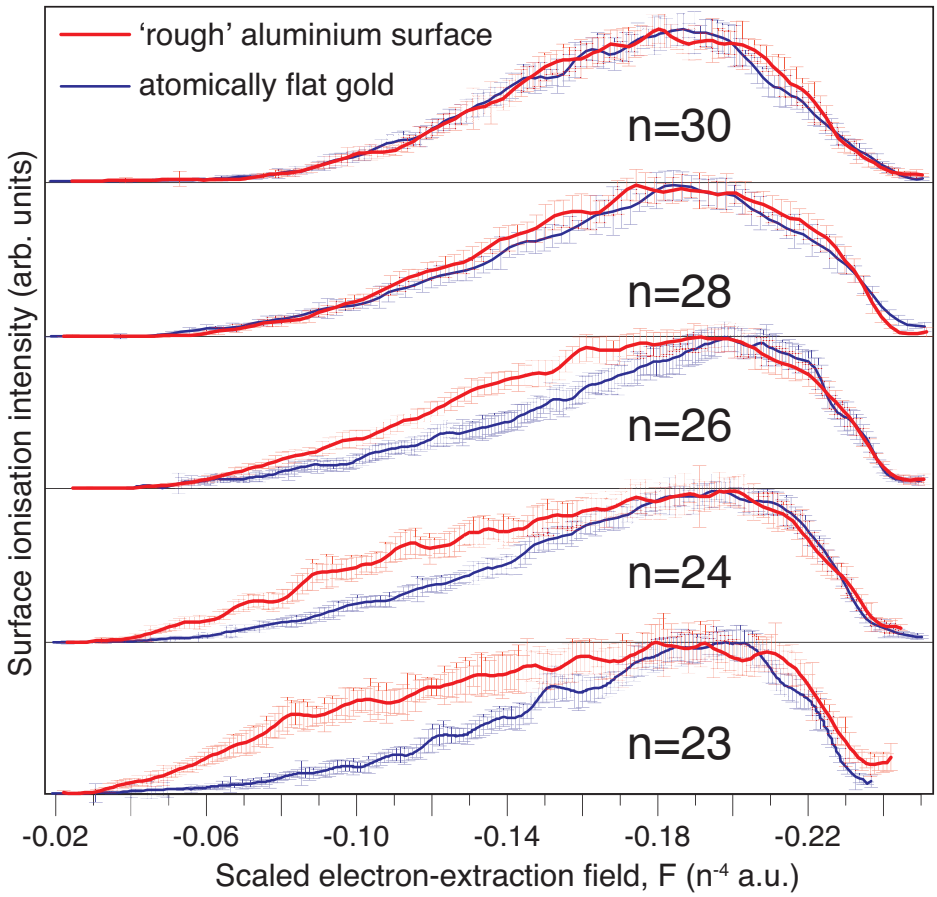

Figure 7.22: Surface ionisation signal as a function of scaled *electron*-extraction field for the most blue-shifted, vacuum-oriented Stark states of the $n = 23 - 30$ manifolds incident at the rough aluminium surface (red lines) and at the atomically flat gold surface (blue lines). The collisional velocity of the hydrogen atoms is $\bar{v}_\perp = 650$ ms^{-1}.

is relatively insensitive to the nature of the surface, but is instead dependent on the magnitude of the electric field. It is shown in Section 3.5 that for the most red-shifted Stark state, the field at which the back-scattered electron loss begins is $\sim 0.04n^{-4}$ a.u.; this is in accord with profiles shown in Fig. 7.21. Furthermore, the lack of sensitivity towards the nature of the surface is also helped by the fact that the red-shifted Stark states are vacuum-oriented under electron-extraction fields, and so do not probe the surface.

Figure 7.22 compares the surface ionisation profiles for the most blue-shifted Stark

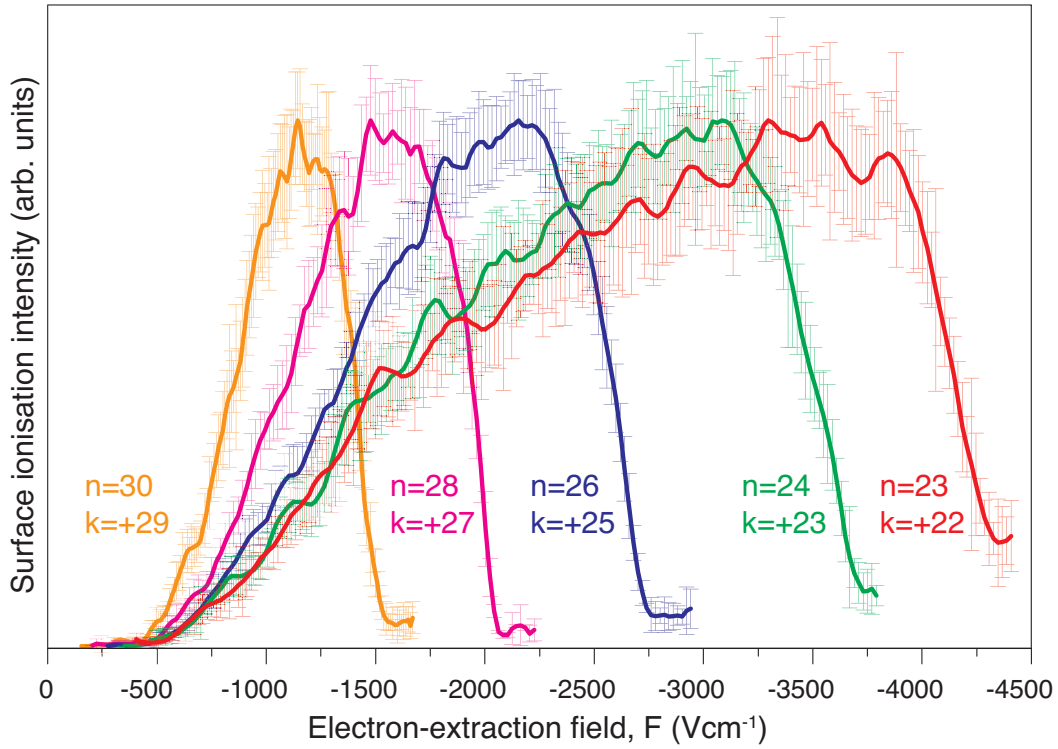

Figure 7.23: Surface ionisation signal as a function of *electron*-extraction field for the most blue-shifted, vacuum-oriented Stark states of the $n = 23 - 30$ manifolds incident at the rough aluminium surface. The collisional velocity of the hydrogen atoms is $\bar{v}_\perp = 650$ ms^{-1}.

states of the $n = 23 - 30$ manifolds incident at the rough surface and at the flat gold surface. While the electron signal is similar for $n \geq 28$, the signal at lower extraction fields is significantly larger for the rough surface. Figure 7.23 shows the same rough surface results, but on an *un-scaled* field axis. Similar to the results for ion-extraction fields where the onset of ion signal appear independent of principal quantum number (Fig. 7.17), the onset of surface ionisation signal for the most blue-shifted Stark state of the $n = 23$ and $n = 24$ manifolds occur at similar electric fields, and with similar initial gradient of increase. As explained above, for the blue-shifted, initially surface-oriented Stark states to undergo electron loss towards the vacuum, they must interact with other Stark states that exhibit vacuum-oriented characteristics. The extent of level interactions is much larger at a rough surface due to the local fields from the inhomogeneous surface boundary. Furthermore, the blue-shifted states are initially surface-oriented, and therefore are highly susceptible to the local perturbations at the surface interface. For high principal quantum numbers ($n \geq 28$) these level interactions occur occur relatively far from the surface ($>> 4{\cdot}28^2 = 3100$ a.u. ≈ 150 nm) and so are less affected by the nature of the surface, but for lower principal quantum numbers the rough surface perturbations have a strong effect on the Rydberg dynamics, resulting in the observed larger electron signals. The local surface fields from the rough surface inhomogeneities may also affect the ionisation dynamics in terms of re-orientation of the resultant field-axis (to which the Stark states are aligned), leading to the more pronounced loss of polarisation of the Stark states (particular for low n values) for the rough surface as observed above. But as explained in Section 7.5, the contribution from Stark states which have followed the re-orientated field-axis is expected to be small, since the local surface fields responsible for the 're-orientation' also inhibits the detection of the ionised electrons.

There is further evidence for the interpretation of population transfer from the initially

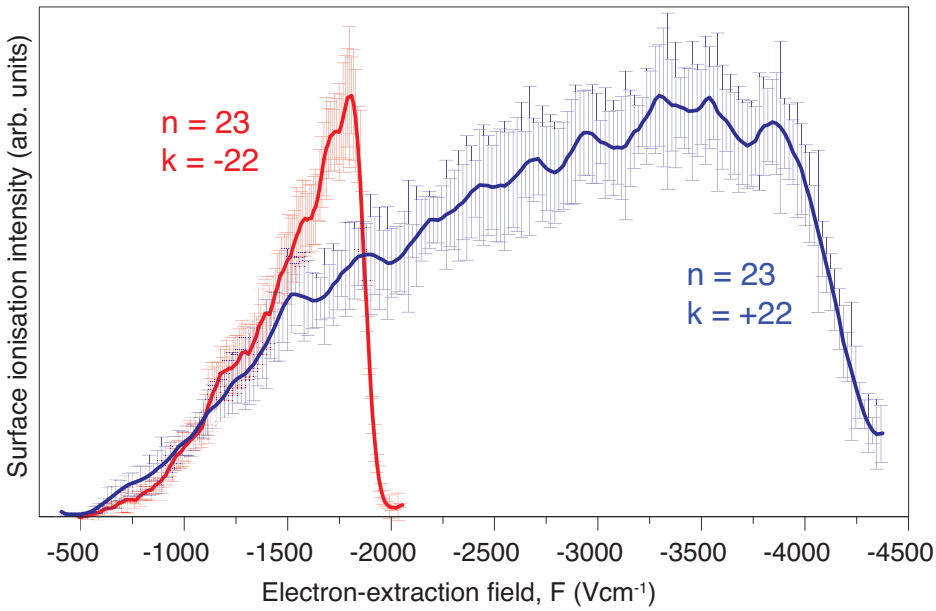

Figure 7.24: Surface ionisation signal as a function of *electron*-extraction field for the most red- ($k = -22$) and blue- ($k = +22$) shifted Stark states of the $n = 23$ manifold incident at the rough aluminium surface. The collisional velocity of the hydrogen atoms is $\bar{v}_{\perp} = 650$ ms^{-1}.

populated blue-shifted Stark state to red-shifted states as a route for surface ionisation under electron-extraction fields, when comparing the surface ionisation profiles of the most extreme red- and blue-shifted states of the $n = 23$ manifold, shown in Fig. 7.24. As a result of the enhanced level interactions between Rydberg states of the $n = 23$ manifold at the rough surface, the electron signal at low extraction fields is the same for both red- and blue-shifted Stark states (note that for the flat gold surface Fig. 7.13 shows that the onset of electron signal for the blue-shifted states is the same as for the centre of the manifold). This suggests that significant population is transferred through the Stark manifold from the most blue-shifted Stark state to the most red-shifted state. This is not implausible, since it is shown in Section 3.4 that under electron-extraction fields, the Rydberg levels within the n-manifold converge in energy when approaching the surface, and particularly with the addition of the larger perturbations from the surface inhomogeneities at the rough surface.

7.7 Electronically structured surface: Cu(100)

The wavepacket calculations in Section 3.6 predict that resonant tunnelling (with minimal parallel momentum) of the Rydberg electron to image states at the Cu(100) metal surface can allow surface ionisation to occur at larger atom-surface separations (by difference of $> 1n^2$ a_0) for certain Rydberg levels with $n \leq 8$. For the Cu(100) surface, the projected electronic band-gap extends beyond the vacuum level and exhibits a Rydberg series of image states embedded within the band-gap. Therefore in principle, the same resonant effect predicted by the theory for $n \leq 8$ should also be observable for the charge transfer of the higher principal quantum number ($n \geq 20$) Rydberg states of the hydrogen atom.

Figure 7.25 presents the surface ionisation profiles of the most extreme red-shifted $k = 1 - n, m_l = 0$ states of the $n = 20 - 31$ manifolds for the single-crystal Cu(100) surface compared with the deposited gold surface. Note that the ionisation profiles are normalised to the maximum intensity (see Section 6.2). For all states, the larger ion signal at lower extraction fields can be attributed to the greater surface roughness of the Cu(100) surface, which is specified as <30 nm, compared with the <1 nm roughness of the deposited gold surface (see Section 6.3). However, the extent of the ion-signal increase and the form of the ionisation profiles are different for some principal quantum numbers, most notably the ionisation profile for the $n = 24$ state, which clearly exhibits two gradients: a sharp rise to nearly the maximum intensity, and then a very shallow increase to the field ionisation limit. For a more quantitative examination of whether or not resonant effects are being observed, the surface ionisation profiles are integrated up to the field of maximum intensity (where the Cu(100) and gold profiles coincide) just before the sharp drop from the onset of field ionisation. The ratio of the integrated signals (Cu(100)/Au) for different principal quantum numbers are shown in Figure 7.26(a).

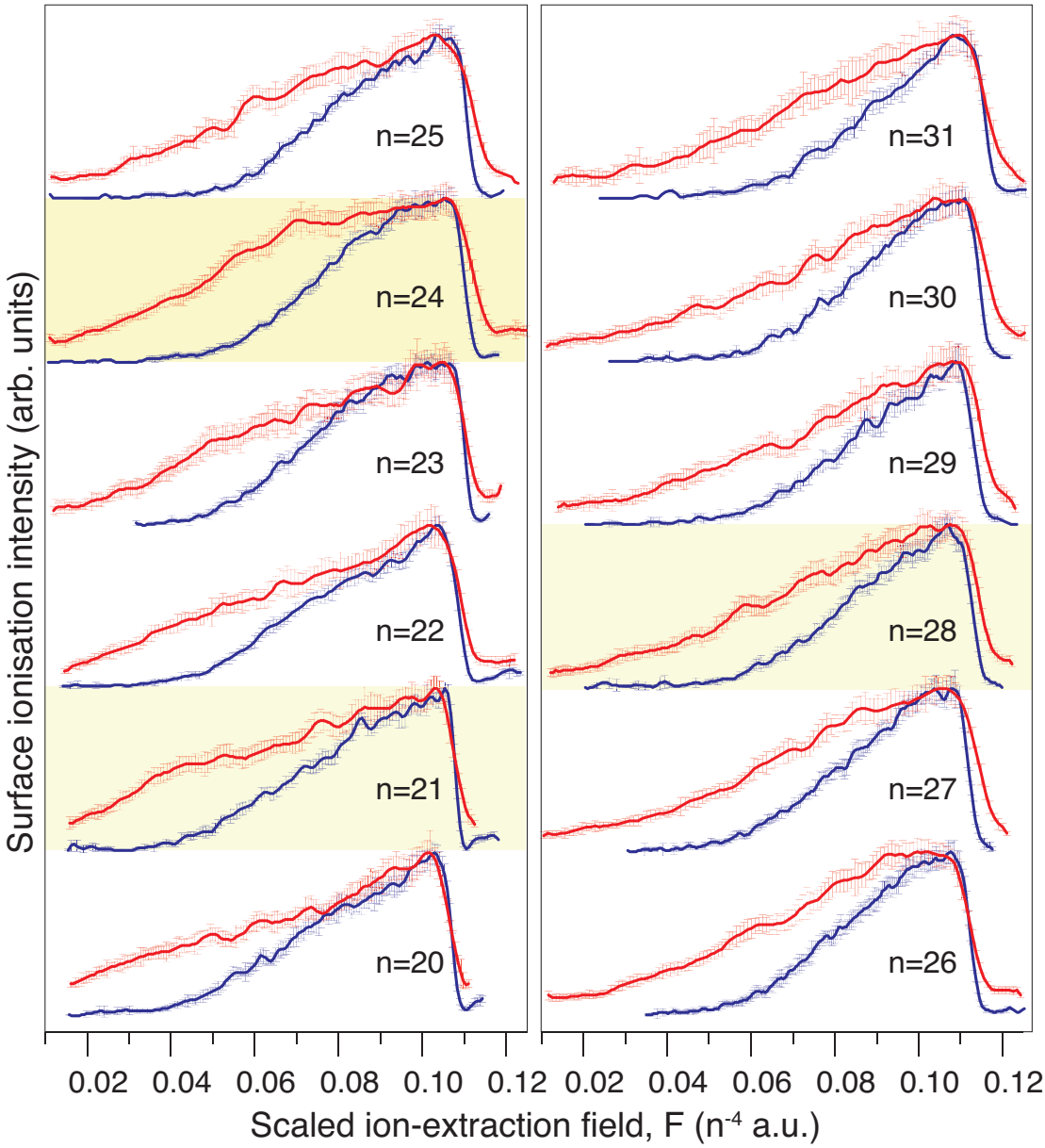

Figure 7.25: Surface ionisation signal as a function of scaled ion-extraction field for the most red-shifted ($k = 1 - n, m_l = 0$) Stark states of the $n = 20 - 31$ manifold incident at the Cu(100) surface (red lines) and at the gold surface (blue lines). The collisional velocity of the hydrogen atoms is $\bar{v}_\perp = 650$ ms^{-1}. Profiles corresponding to the 'peaks' of the ratio of the Cu(100)/Au integrated ion-signal shown in Fig. 7.26(a) are highlighted.

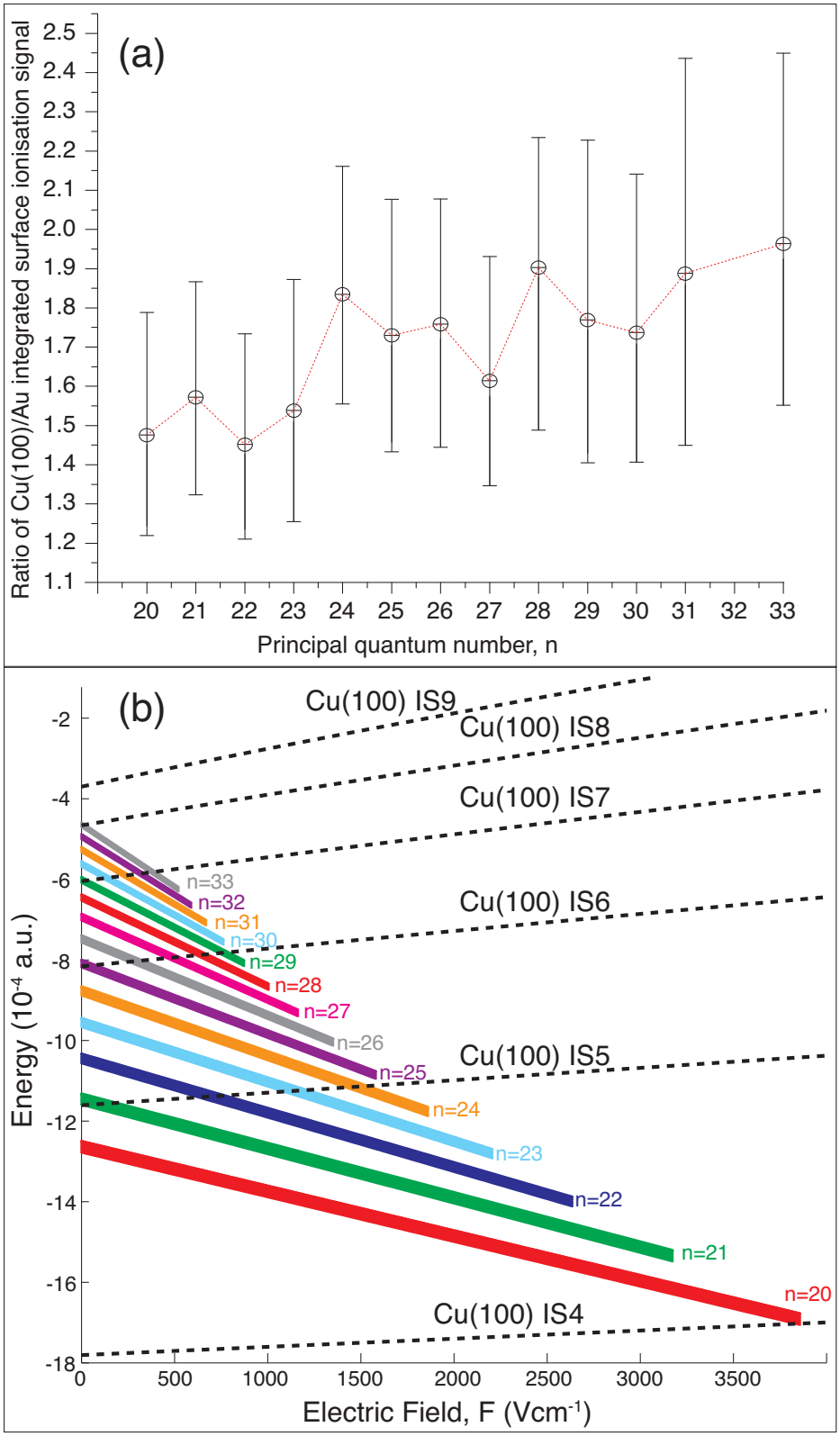

Figure 7.26: (a) Ratio of the integrated surface ion signal for the Cu(100) surface compared with the gold surface for the most red-shifted ($k = 1 - n, m_l = 0$) Stark states of the $n = 20 - 31$ manifold. (b) The energies of the H Stark states and the energies of the Cu(100) image states as a function of electric field. The broad width of the Rydberg levels shows the approximate shift in energy from $D = \infty$ to $D = 3n^2$ a_0 calculated using Eq. 2.2.

Figure 7.26(a) shows that the errors from determining the ratio of integrated signals are significant when compared with the variations with principal quantum number. The main source of error arises from the calculation of the integrated signal, where the lower and upper bounds are estimated by calculating area under the lower and upper error bars of the ionisation profiles shown in Fig. 7.25. Nonetheless, the results suggests that the integrated ion-signal for the $n = 21, 24, 28$ most red-shifted states is larger than for their adjacent principal quantum number states. The image state energies of the Cu(100) surface in zero-field can be calculated from Eq. 3.1 with the appropriate quantum defects [85], however, it is well known from STM experiments that the energies of image states can be strongly perturbed by external electric fields [103–106]. Following Ref. [104], the Stark shifted energies of the image states are calculated from the diagonalisation of Chulkov one-electron pseudo-potential given by Eq. 3.4, with the inclusion of a homogeneous electric field beyond the image plane. The energies of the most red shifted $n = 20 - 31$ Stark states of the hydrogen atom, and the $n_{\rm im} = 5 - 9$ image states of the Cu(100), as a function of the electric field are shown in Fig. 7.26(b). The broad width of the Rydberg energies shown in Fig. 7.26(b) represents the approximate shift in energy from $D = \infty$ to $D = 3n^2$ $\rm a_0$ calculated using first order perturbation theory (Eq. 2.2).

Figure 7.26(b) shows that due the Stark shift of the Rydberg states, most levels traverse at least one image-state resonance as the field increases. However, none of the profiles in Fig. 7.25 show a prominent peak at any particular field value. Although the energies of the $n = 21, 24, 28$ states are close to the $5^{\rm th}$, $6^{\rm th}$ and $7^{\rm th}$ image states respectively of the Cu(100) surface *at zero field*, from the energy level variations shown in Fig. 7.26(b), it is not clear why these state might exhibit larger integrated ion signals than their adjacent principal quantum numbers, given that the integration is performed over a range of fields.

As shown above, one of the problems in trying to observe resonant transfer of the Rydberg electron to the Cu(100) image states, is that the nature of the experiment requires a varying ion-extraction field, and consequently the energy of the Rydberg state of interest can vary significantly with the electric field. On one hand this might appear useful, as the energy of the Rydberg state can be 'tuned' into resonance with a particular image state, however, as the ion-extraction efficiency is strongly dependent on the magnitude of the electric field, any resonance effect could be dominated by changes in ion-extraction probability with the electric field (see Eq. 1.15), which is likely to be the case for the results above.

A much better choice of Rydberg states for trying to observe resonance effects would be states in the centre of the Stark manifold, since they exhibit negligible Stark shift. Stark states in the centre of the n-manifold can be populated straightforwardly experimentally without the need for scanning the whole Stark manifold, but simply by tuning the excitation wavelength to the zero-field value and then switching on the Stark field. Figure 7.27 shows the results for the $k \simeq 0$ Stark states of the $n = 20 - 38$ manifold incident at the Cu(100) surface compared with the gold surface. Again, the ion signal for the Cu(100) surface at lower extraction fields is generally larger than for the gold surface. Similar to the results shown for the most red-shifted states in Fig. 7.25, the $k \simeq 0$ ion signal for some principal quantum numbers is larger than others, and the form of the overall profile is different. This can be seen most clearly for the $n = 26$ state, which shows a similar, two-gradient, profile to the $k = -23, n = 24$ state in Fig. 7.25.

The ratio of the integrated surface ionisation signal for the Cu(100) surface compared to the gold surface is shown in Fig. 7.28(a). Much larger variations of integrated signal are seen compared with the results of the red-shifted states (Fig. 7.26), and the peaks of the signal ratio occur at $n = 22, 26, 31, 35$. Figure 7.28(b) shows the energies of

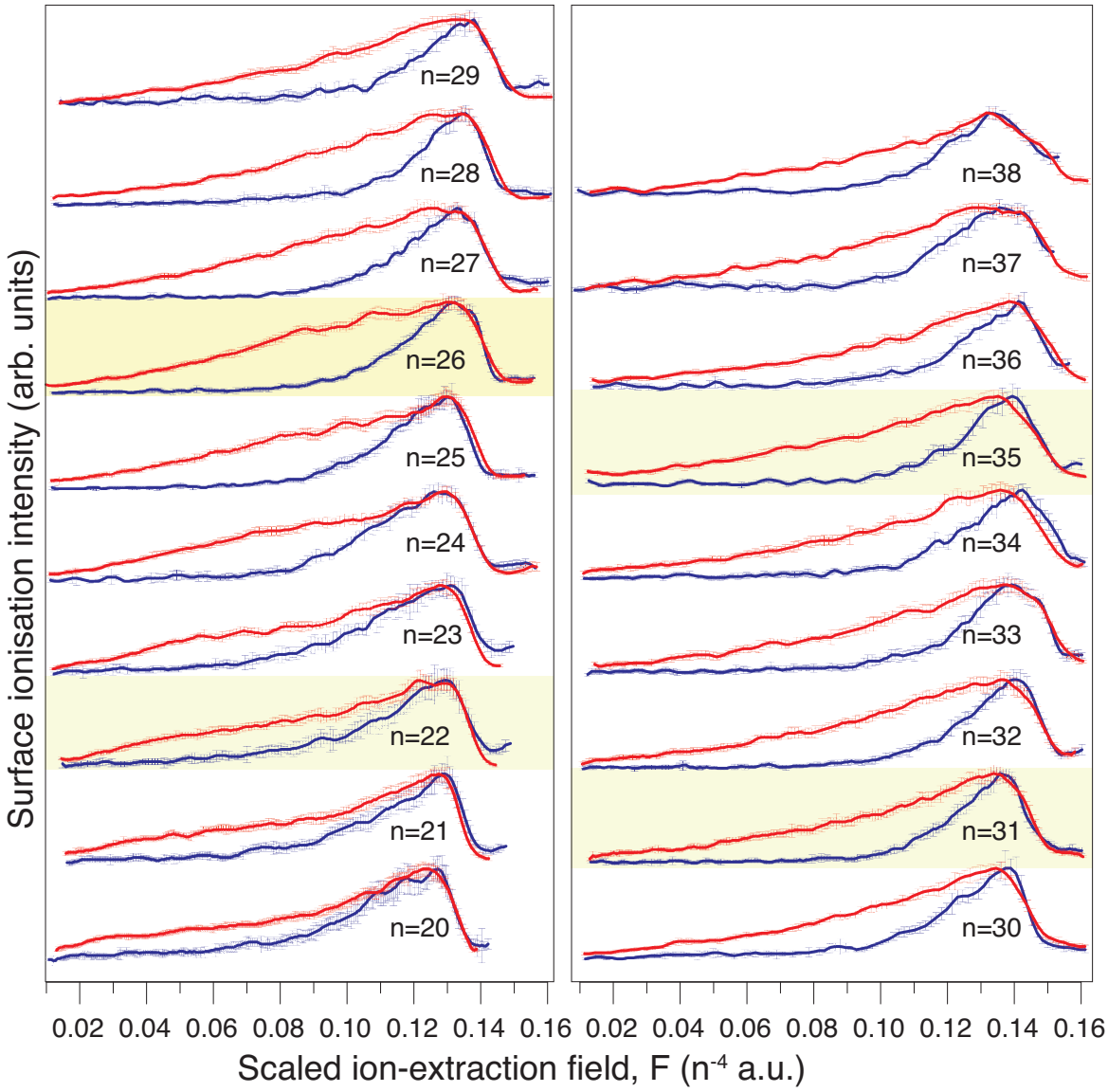

Figure 7.27: Surface ionisation signal as a function of scaled ion-extraction field for the $k \simeq 0$ Stark states of the $n = 20 - 38$ manifold incident at the Cu(100) surface (red lines) and at the gold surface (blue lines). The collisional velocity of the hydrogen atoms is $\bar{v}_\perp = 650$ ms^{-1}. Profiles corresponding to the 'peaks' of the ratio of the Cu(100)/Au integrated ion-signal shown in Fig. 7.28(a) are highlighted.

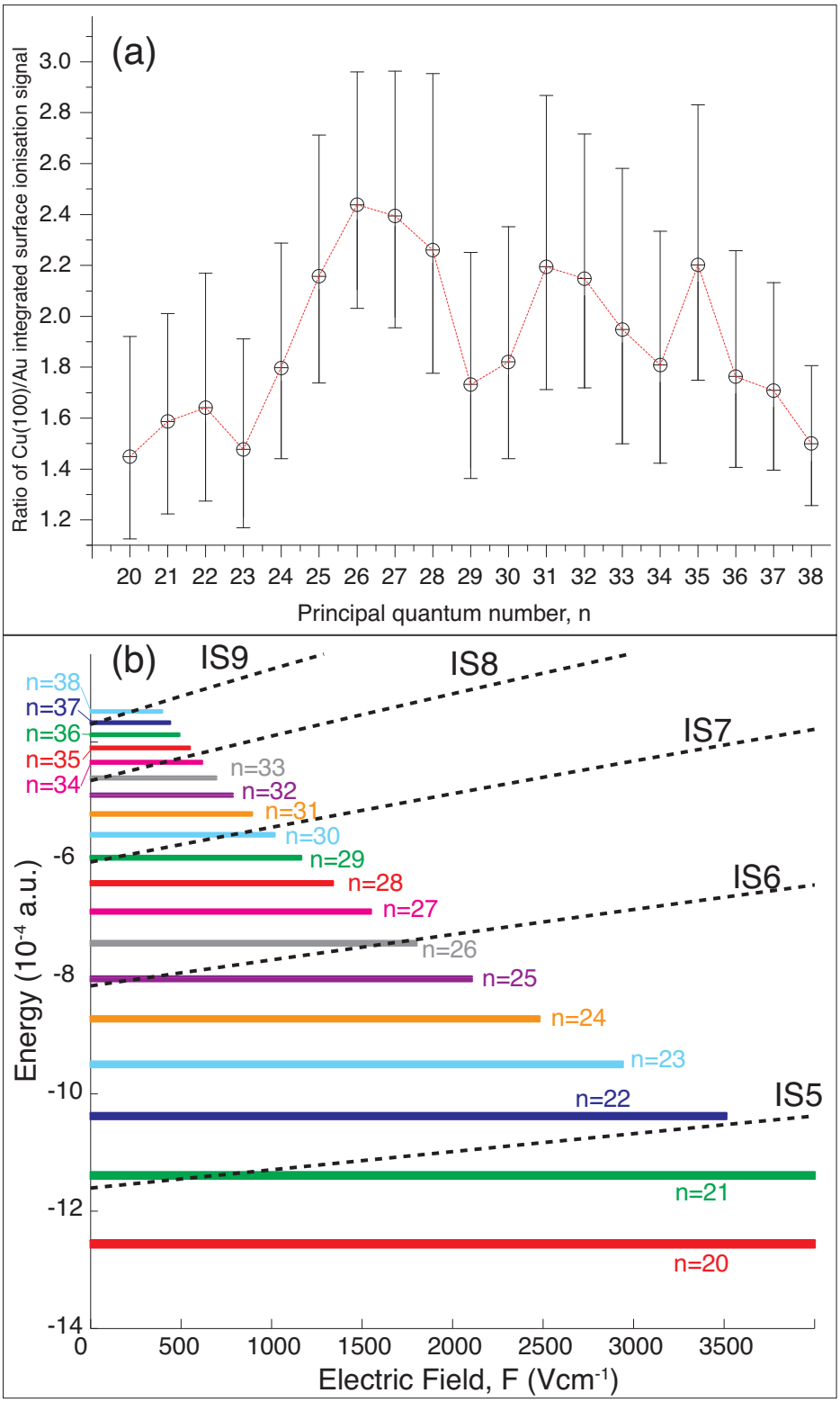

Figure 7.28: (a) Ratio of the integrated surface ion signal for the Cu(100) surface compared with the gold surface for the $k \simeq 0$ Stark states of the $n = 20 - 38$ manifold. (b) The energies of the $k = 0$ H Stark states and the energies of the Cu(100) image states as a function of electric field. The broad width of the Rydberg level shows the approximate shift in energy from $D = \infty$ to $D = 3n^2$ a_0 calculated using Eq. 2.2.

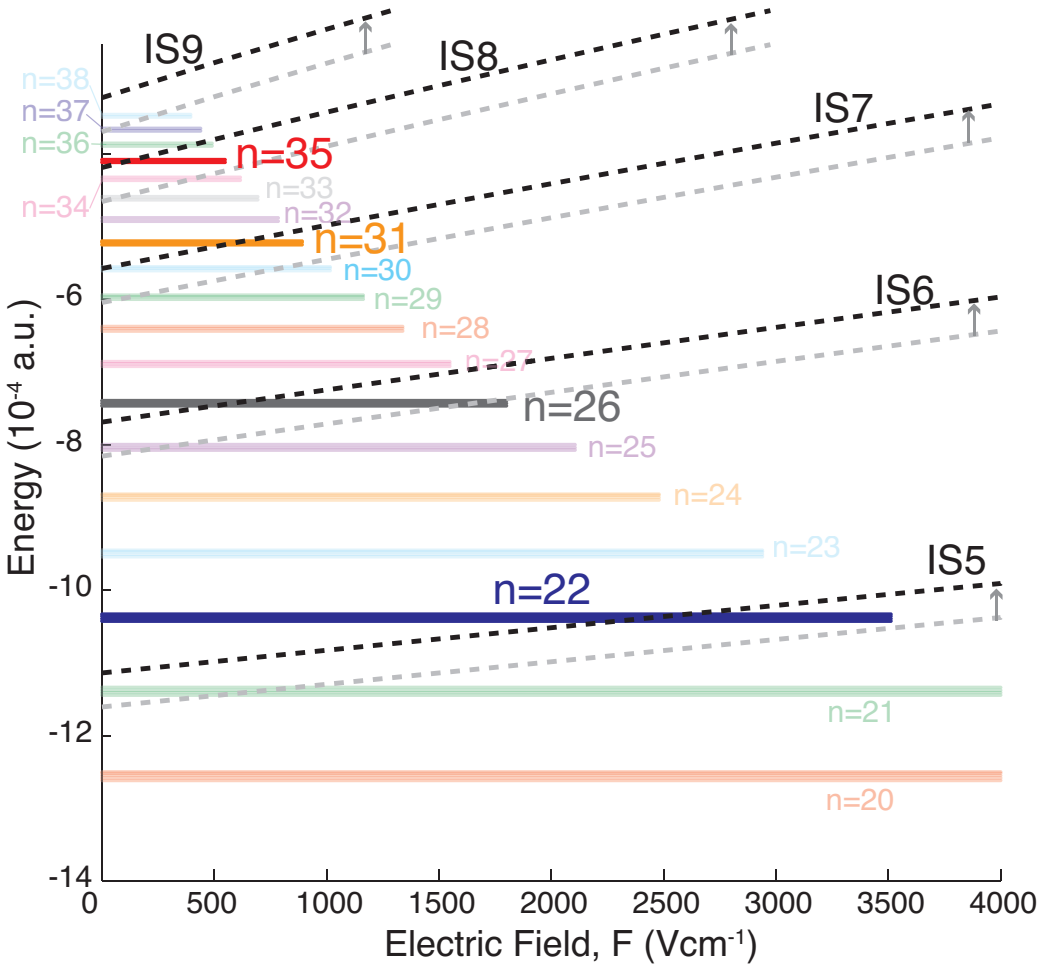

Figure 7.29: Same as Fig. 7.28(b), but with the image state energies shifted by 5×10^{-5} a.u. or 1.36 meV (from the grey to the black dashed lines).

the Rydberg states and the energies of the Cu(100) image states. The energies of the $n = 22, 26, 31, 35$ states appear just above the $5^{\text{th}}, 6^{\text{th}}, 7^{\text{th}}, 8^{\text{th}}$ image state energies respectively. An even better agreement between the Rydberg energies and the image states' can be obtained by shifting the image state energies up by 5×10^{-5} a.u. or 1.36 meV, and is shown in Fig. 7.29. This magnitude of energy shift is quite plausible considering that the perturbation from the presence of the Rydberg electron and ion-core on the image states has not been included, and the Rydberg energies are also likely to differ from the first order perturbation estimate.

Considering the errors in the integrated ionisation signal ratios shown in Fig. 7.28(a), the results above are by no means a definitive proof that a resonant effect from the image states of the Cu(100) surface is playing a role in the charge transfer process, especially as the same correlation between enhanced ionisation signal for particular principal quantum numbers and the image states' energies is not so clearly observed for the most red-shifted Stark states (although as explained above, the results for the most red-shifted states are further complicated by the Stark shift of the Rydberg energy as the field is increased). Furthermore, instead of the gradual increase of the resonance effect to specific principal quantum numbers as shown in Fig. 7.28(a), the theoretical results in Section 3.6 suggests a sharp rise in ion signal *at* the resonance energy and a gradual decay when the Rydberg energy is shifted further away (see Fig. 3.16). Nonetheless, the *periodicity* of the variation of the integrated ion signal with principal quantum number shown in Fig. 7.28(a), appears to match that of the relative energy spacings of the Cu(100) image states and the Rydberg states (Fig. 7.28(b)). And so the experimental results above provide some potential evidence of Rydberg-surface charge transfer via resonances with $n_{\text{im}} \geq 5$ image states, or seen differently, there is tentative evidence that Rydberg states can be used as probes of high image-states (in an energetic sense). To date, there has been no direct probe of the $n_{\text{im}} \geq 4$

image states of Cu(100); in femtosecond two-photon photoemission experiments (where energies of $n_{\rm im} < 3$ have been measured), the bandwidth of the laser excites a coherent superposition of high image states ($n_{\rm im} \geq 4$) to form wavepackets rather than exciting individual levels [107]. Thus the results shown above could lead to some exciting prospects for using Rydberg states as energy specific probes of electronic states at surfaces, given some improvements of the current experiments.

As future work, the experiment above can be improved in several ways. Firstly, to ensure that the surface is clean from adsorbates, the Cu(100) surface can be prepared by sputtering and annealing cycles in UHV, although it is likely that in the present experiments NH_3 from the H source will adsorb at the surface unless it is removed from the atomic beam (which has been demonstrated recently by deflection of decelerated Rydberg H Stark states by electric fields [56]). Secondly, a much larger number of repeat measurements for both the gold and copper surface will help to reduce the errors associated with the integrated ion signal[1], and more confidence can be placed on the positions of the image state resonances. Thirdly, as mentioned in Section 6.2, introduction of ion optics, or increasing the detection area, can increase the overall ion signal relative to noise, as well as allow absolute surface ionisation signals to be measured (so far it has been assumed that the ion-extraction probability reaches unity just before the onset of field ionisation, which was justified by theory and by previous experimental work, see Section 6.2). This will in turn provide a more genuine comparison of ion signals from the different surfaces.

[1]For the results presented above, each data point (the ion-intensity at a given field) is averaged over a minimum of 80 laser shots.

7.8 Conclusions

The experimental study of the surface interactions and charge transfer of Rydberg hydrogen atoms at metal surfaces is presented in this chapter. Surface ionisation at an evaporation-deposited gold surface, which is representative of a typical free-electron metal, is studied. By varying the principal quantum of the most red-shifted, surface-oriented state of a given Stark manifold under ion-extraction fields, it is shown that the atom-surface separation at which surface ionisation occurs scales approximately with the Rydberg dimensions (n^2 a_0) as predicted by the theory in Chapter 2 and 3. Quantitative comparison of the experimental and the calculated ion signal as a function of electric field (surface ionisation profiles) shows that the classical over-the-barrier provides a good estimate for the onset of ion-signal, but does not account for the broad range of fields over which signal is observed before the maximum intensity is reached; while the wavepacket calculations predict a similar broad range of fields, but the onset of ionisation is shifted to much higher fields. The stray field model of Dunning and co-workers [48], also predicts a broad rise of ion signal that is comparable with the experimental profiles, but the onset of ion-signal is now at much lower fields compared with the experiments. Using a semi-empirical over-the-barrier model, in which the calculated OTB is shifted by a constant ($-n^2$ a_0) and a range of ionisation distance is introduced ($\sigma = 2.5n^2$ a_0), such that the results of the semi-empirical model lies in between that of the OTB and the wavepacket calculations, an excellent agreement with the experimental profiles can be achieved.

The surface ionisation of various Stark states with different polarisation with respect to the surface is studied experimentally under ion-extraction fields. As predicted by the theory in Chapter 3, under ion-extraction fields, the polarisation of the initially populated Stark state is preserved throughout the Rydberg trajectory towards the surface. Consequently on moving from red- (surface-facing) to blue-shifted (vacuum-

facing) states, the onset of ion signal is at progressively higher fields, corresponding to progressively smaller ionisation distances. This behaviour is significantly different from that shown by the Rydberg Xe an H_2 system [45, 51], where the polarisation of the initially populated Stark states are not preserved, resulting in very similar the onsets of ion signal for the red- and blue-shifted states. However, theory in Section 5.1 suggests that for the hydrogen atom the minimum field required to extract the ions from the surface ionisation of the most blue-shifted states is beyond the field ionisation limit, and so the experimental detection of the surface ionisation signal was unexpected. The experimental surface ionisation signal for the most blue-shifted state of the $n < 28$ manifold may be accounted for by considering the deceleration of the low-field seeking blue-shifted states by possible strong local fields close to the surface (as measured recently by Dunning and co-workers for a deposited gold surface [48]), allowing for ion-detection at lower extraction fields.

The effect of changing the collisional velocity of the incident H atoms (without changing the trajectory over the surface) has been investigated. The main effect of decreasing the collisional velocity is the increase of the ion-extraction probability for a given electric field, such that ions formed much closer to the metal surface can be pulled away. The same semi-empirical OTB model provided excellent agreement with the experimental ionisation profiles at the different collisional velocities.

Changing the collisional angle of the H atoms, changes both the collisional velocity and the parallel components of the trajectories of the atoms and ions over the metal surface. For $n > 23$, there is good agreement between the experimental ionisation profiles at different incidence angles and the results from the semi-empirical OTB model. As expected, the more grazing collisions which correspond to a smaller kinetic energy component perpendicular to the surface, have higher ion signal at lower extraction fields, due to the increase in the ion-extraction probability. For $n \leq 23$, however,

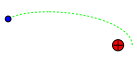

the behaviour is very different, and the ion signal is even smaller at the more grazing collisional angle, and the argument based on the change in collisional velocity does not apply. The deviation from the higher principal quantum numbers and the model calculation is attributed to the change in the ion-trajectory and surface inhomogeneities (either in form physical roughness or more likely, local surface fields) probed by the $n \leq 23$ Rydberg states and the resultant ions. A possible qualitative explanation may be that there is an increased probability for the ion to move to an local area of lower extraction probability (where the positive ions are more attracted towards the surface) as a result of the more grazing trajectory, leading to smaller ion signals. The approximate dimensions of these potential inhomogeneities are approximated to extend as far as ∼50 nm away from the surface, and vary laterally over ∼150 nm. Although these dimensions are in line with the surface potential variations measured recently by Dunning and co-workers for a deposited gold surface [48], in the OTB trajectory calculations, the increase in the ion-extraction probability for more grazing angles dominates over the effects of the change in the trajectory paths over the surface. Thus at this moment, there are no adequate theoretical models to reproduce the experimental observations, and further theoretical work is required in the future.

Electrons, rather than protons, can be extracted from the surface ionisation process. Theory attributes the electron signal to a backscattered loss of electrons towards the vacuum, due to the lowering of the potential barrier on the vacuum-side of the ion-core by the electron-extraction fields. For the most red-shifted, vacuum-oriented Stark state under electron-extraction fields, the onset of the ionisation signal is at a field of $\sim 0.05n^{-4}$ a.u., in accord with the theoretical predictions. Surprisingly, electron signals can also be detected for Stark states that are polarised towards the surface, where the electron density is far away from saddle point on the vacuum side of the ion-core. For the most blue-shifted Stark states, the surface ionisation profiles are broad, and

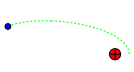

the onset of electron signal is at relatively low fields of $\sim 0.08n^{-4}$ a.u.. Studying the various Stark states of the $n = 23$ manifold shows that the onset of ionisation for the blue-shifted states is similar to the $k = 0$ states in the centre of the manifold. This suggests that as the blue-shifted Rydberg state approaches the metal surface it undergoes level crossings with states in the centre of the manifold (and even red-shifted states), and consequently the Rydberg state gains some vacuum-oriented characteristic and the electron can be lost towards the vacuum. Indeed, the theory from Section 3.4 shows that level interactions are stronger under electron-extraction fields, and the Stark manifold converges in energy when approaching the surface. This apparent loss of the initial polarisation may also have contributions from the local surface field re-orientation of the resultant field-axis which may be followed adiabatically by, and therefore defines the orientation of the Stark states with respect to the metal surface. However, the contribution of the re-oriented Stark states to the surface ionisation signal is expected to be small, since the local surface fields responsible for the re-orientation of the field-axis also inhibits the detection of the resultant charged particles after ionisation.

Surface ionisation of Rydberg H atoms at a rough machined aluminium surface is studied for both ion- and electron-extraction fields. Under ion-extraction fields, the ionisation profiles are much broader, and the ion-signal at lower fields is larger than those from the atomically flat gold surface. This is attributed to the larger range of collisional angles incident at the rough surface, resulting in a broad range of detection distances for a given electric field, as well as local surface fields which can increase the ionisation distance and enhance the ion-extraction probability. For both red-shifted and blue-shifted states that ionise at atom-surface separations $\approx<$ 80 nm for the flat gold surface, the corresponding onset of ion-signal at the rough surface is found to be independent of principal quantum number or polarisation, and for all states the ion

signal nearly reaches maximum intensity by a field of 1700 Vcm^{-1} (corresponding to ∼80 nm ionisation distance at a flat gold surface). This apparent 'critical' field or distance is attributed to a sharp rise in ionisation probability and (or) ion-extraction probability as a result of the strong local perturbations near the rough surface interface.

Study of a range of collisional angles at the rough surface, shows that for $n > 23$ the ion signal is relatively independent of the incidence angle, which is expected considering the large range of local angles presented to the Rydberg atom and resultant ion by the rough surface. However, similar to the case of the flat gold surface, when compared with the profiles of the steeper incidence, the ion signal at the more grazing angle is progressively smaller as n decreases. Qualitatively, this can be explained by the increased probability for the ions to collide with a surface inhomogeneity (either physical or in terms of local fields) as a result of the more grazing trajectory, and consequently they are lost from the detection.

For the rough surface, the electron-extracted surface ionisation profiles for the most red-shifted Stark state are very similar to those obtained for a gold surface. Although the profiles from the rough surface are slightly larger for $n < 23$, the differences are relatively minor compared with those observed for the ion-extraction fields. This is because the back-scattered electron process is strongly dependent on the magnitude of the electric field which determines the height of the potential barrier on the vacuum-side of the ion-core, rather the surface. However, this is not the case for the initially surface-oriented blue-shifted states, which depend on level crossings with vacuum-oriented states in order to lose electrons towards the vacuum. As expected, the extent of level interactions are much larger in the presence of a rough surface, particularly for lower n states ($n \leq 26$), and consequently the electron signal at lower extraction fields is larger, and the onset of the ionisation signal is also at a lower field. For the $n = 23$ manifold, the onset of ionisation for the most blue-shifted Stark state is nearly

the same as the most red-shifted state.

Finally, experiments involving a single-crystal Cu(100) surface are carried out, to investigate whether the resonance enhanced charge transfer to image states (that was studied theoretically in Section 3.6) can be observed experimentally for $n \geq 20$. The roughness of the copper surface is < 30 nm, while the evaporation-deposited gold surface is nearly atomically flat (< 1 nm), and so the overall ion signal for all the Rydberg states studied is larger for Cu(100) surface (for the same reasons as the rough aluminium surface). Detailed comparison of the ionisation profiles of the most red-shifted Stark state from the Cu(100) surface and the gold surface, shows that the form of the ionisation profiles and the relative increase in ion signal is different for particular principal quantum number states. Direct comparison of the energy levels of the red-shifted Stark states with the energies of the image states of the Cu(100) surface as a function of electric field, shows that as a result of the Stark energy shift, most of the Rydberg levels should encounter at least one image-state resonance for the full range of extraction fields studied, but no clear resonance peak can be observed in the profiles at specific field values. It is likely that the large change in ion-extraction probability with field masks the field-specific resonance effects.

To remove the problem of different Stark energy shifts at varying electric fields, the surface ionisation of the Rydberg states in the centre of the Stark manifold (which exhibit negligible Stark shift) is studied. Similar to the red-shifted states, the ion signal for particular principal quantum numbers is enhanced more than others. Taking the peak positions of the integrated ion signal ratio for the Cu(100) and gold surface (*i.e.*, the principal quantum numbers of the states that appear to exhibit significantly more ion signal), and comparing the energies of those Rydberg states with the image-state energies of the Cu(100) surface, shows that, the Rydberg energy levels appear to sit just above that of an image state (*i.e.*, when resonant charge transfer is expected to

be most efficient). Although the error bars associated with calculating the integrated ion signals are large, the results are also supported by the agreement between the periodicity of the variation of the integrated ion signal with principal quantum number and the relative energy spacings of the Cu(100) image states and the Rydberg states. Thus, the Cu(100) experimental results provide potential evidence that image-states at electronically structured surfaces play an important role in the surface ionisation dynamics of Rydberg states.

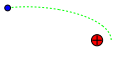

Chapter 8

Conclusions and future work

The interaction of Rydberg hydrogen atoms with metal surfaces and the associated charge-transfer process has been studied both theoretically and experimentally in this work. This first experimental study involving ionisation of Rydberg hydrogen atoms at an atomically flat deposited-gold surface, which is representative of a typical free-electron metal surface, has provided the opportunity for a genuine comparison of the experiments with the wide-range of existing theories. Due to computational demands, full time-dependent quantum calculations at the experimental range of principal quantum numbers ($20 \leq n \leq 40$) are not possible, and approximate scaling relationships have been employed. Comparison of the quantum theory with the experiments, shows a good qualitative agreement, but the experimental results cannot be fitted quantitively (although a semi-empirical model appears to work well). Future theoretical work focusing on extending the quantum calculations closer to the experimental range of principal quantum numbers should be carried out. It is also possible to extend the calculations to include the full three-dimensional surface potentials (and the associated surface fields) for a more realistic description of a deposited gold surface [48], rather than the 1D Jellium pseudo-potential employed here.

One of the main foci of this investigation has been on how the properties of the incident

Rydberg state, the target surface and the externally applied fields affect the atom-surface separation at which the charge-transfer occurs, and the detection probability of the charged particle from the surface ionisation. The incident Rydberg atoms can be manipulated in terms of the electronic wavefunction – the principal quantum number (and thus the size) and the polarisation with respect to the metal surface – and in terms of properties of the atomic beam; the collisional velocity and the collisional angle. The target surface can be physically structured, in terms of surface roughness or periodically structured, or electronically structured, in terms of an electronic band gap or discrete electronic states. The externally applied electric field can be varied in terms of its direction and magnitude.

From the study of the ionisation dynamics at the gold surface, it is demonstrated that the metal surface can provide a probe of the Rydberg properties and their evolution when approaching the surface. It is found that the surface ionisation distance changes intuitively with the dimensions of the Rydberg state. As the principal quantum number and size of the orbital increases, the ionisation distance also increases. For applied electric fields in which protons are repelled away from the surface, the surface ionisation of Stark states with different polarisation of electronic wavefunction with respect to the surface also occurs in the intuitive order: surface-oriented (red-shifted) states are ionised furthest from the surface, and vacuum-oriented (blue-shifted) states are ionised closest to the surface. This preservation of Stark polarisation when approaching the surface under ion-extraction fields has not been possible for the non-hydrogenic Xe and H_2 systems previously studied.

The ionisation behaviour under applied electric fields, in which electrons are repelled away from the surface, is more complicated but illustrates how dynamical information can be obtained from studying surface charge transfer. For the vacuum-oriented red-shifted Stark states, electrons can be lost towards the vacuum beyond a field of $\sim$

$-0.04n^{-4}$ a.u., when the potential barrier between the ion-core and the vacuum has been sufficiently lowered by the electric field. For the surface-oriented blue-shifted Stark states, they undergo level crossings with other states within the Stark manifold and gain some vacuum-oriented characteristic as the manifold converges in energy when approaching the surface. The electron is consequently lost towards the vacuum via the same backscattered mechanism as for the red-shifted states. In this case the threshold ionisation distances may be very similar for red- and blue-shifted states.

The Rydberg states of various principal quantum numbers and Stark polarisations with respect to the surface, can alternatively be viewed as a collection of 'surface probes' of various dimensions which are sensitive to perturbations above a certain height from the surface. In this way, the ionisation dynamics at a rough machined aluminium surface is studied and compared with the flat gold surface. For the rough surface, it is found that the ionisation distances and ion-extraction probabilities are significantly different to the flat surface, particularly for the lower principal quantum number states ($n \leq 23$) which ionise (and therefore probe) closer to the surface. It is found that for the $n \leq 23$ Rydberg states (which ionise at distances of < 80 nm for a flat surface), the onset of ion signal is independent of n, such that all states are ionised and detected beyond a 'critical' field of ~ 1700 Vcm^{-1}.

The 'probe depth' of the Rydberg atoms and resultant ions can also be altered by changing the collisional velocity of the incident atoms. The change of collisional velocity mainly affects the extraction probability of the protons from the surface for a given electric field; lower collisional velocity allows ions formed closer to the surface to be extracted (*i.e.* a closer probe of the surface). Theory also shows that when the velocity is changed by greater than an order of magnitude, the ionisation dynamics can also be significantly affected, in terms of the position of the average ionisation distance (since it is governed by a rate equation) and the extent of the non-adiabatic

interactions taking place.

For a homogeneous surface which is the same in all directions parallel to the surface normal, the change in collisional angle has the same effect as altering the velocity. But for an inhomogeneous surface, if the variations of the surface are smaller than the change in the trajectory paths of the Rydberg atoms and ions over the surface (associated with the change in incident angle), then the surface ionisation dynamics and ion-extraction probability will not be the same. Note that the lateral surface variations need not only be physical, in terms of an adsorbate or the surface roughness, but can also be a change in the surface potential due to patch charge effects leading to local surface fields. The effects of varying collisional angles have been studied experimentally for the deposited gold surface and a rough machined aluminium surface. In both cases, the change in ion signal cannot be simply accounted for by the change in collisional velocity, especially for the lower principal quantum number states ($n \leq 23$) which ionise closer to the surface and are more sensitive to local variations. The results can be explained qualitatively, in terms of the increased probability of encountering local surface inhomogenieties which prohibits the detection of ions for the more grazing trajectories over the surface. However, the results cannot be fully reproduced by the theories and modelling presented in this work. Thus, although the studies at different collisional angles have the potential to be a useful characterisation tool for lateral surface variations, appropriate accompanying theoretical models are required. As future work, studies involving surfaces with well-characterised periodic variations, such as nano-patterned [108], or vicinal [99] surfaces, may provide a useful reference for bringing together the theory and the experiment.

The incident Rydberg state can also be considered as an energy resolved probe of the electronic states at the metal surface. It is shown by theory, that for metal surfaces which exhibit surface and image states embedded in a projected band-gap along the

surface normal (specifically Cu(100) and Cu(111) surfaces), the surface ionisation process is particularly efficient (and occurs at larger distances) when the energy of the Rydberg state is nearly degenerate with the surface- or image-state energy associated with the surface normal (*i.e.*, the charge transfer occurs with a minimum component of momentum parallel to the surface). This enhancement is also partly due to possible overlap between the Rydberg states' wavefunction and the image states which extend far into the vacuum. The experimental study of the surface ionisation of $n = 20 - 38$ states at an electronically structured Cu(100) surface suggests the possible observation of this resonance transfer to the high image states ($n_{\mathrm{im}} \geq 5$) of the copper surface. Future experimental work involving the in-situ cleaning of the surface (by sputtering and annealing cycles) could produced clearer resonances, and the development of focusing ion-optics in the detection assembly can improve the signal-to-noise ratio and reduce the errors of the ionisation profiles.

Discrete electronic states as a result of quantum confinement are well known to exist in systems such as thin metallic films [79], rare-gas adlayers [109], vicinal surfaces [110, 111], nano-particles and nano-clusters [112], and quantum wires and quantum dots [113]. For the type of experiments outlined in this work, care needs to be taken when choosing the substrate, such that the relative energy spacing of the discrete levels are comparable to (or greater than) the Rydberg energy spacings that are experimentally accessible ($n \geq 20$). Nonetheless, the experimental technique presented in this thesis has the potential for providing many exciting future prospects for the probing of discrete electronic states at surfaces.

From the point of view chemical dynamics, future work involving metal surfaces covered with an adsorbate layer (hydrocarbons [114], or self-assembled monolayers of alkane-thiols [108, 115]) can provide opportunities to study a full range of possible processes at the surface. The charge transfer of the Rydberg electron from the in-

cident atom can induce electronic excitations at the metal surface, and in principle, electron stimulated desorption (ESD) of adsorbates from the surface (and associated processes such as bond dissociation for molecular adsorbates) can occur [116] (the energy available for excitation at the surface depends on the difference between the Rydberg state energy and the bottom of conduction band of the metal of interest, typically is $\sim$ 15 eV for free electron metals). For cases where surface ionisation is inhibited (for example by the presence of a dielectric or insulating interface), the available energy associated with the electronic de-excitation of the Rydberg state ($\sim$ 13 eV), is also sufficient for the cleavage of adsorbate bonds at the surface (*e.g.*, $C-H$ bonds of cyclohexane [114]). Furthermore, after the surface ionisation of the Rydberg state, the remaining positive ion can also allow for low-energy ion-adsorbate collisions, particularly for the case of electron-extraction fields where the ions are pulled towards the surface. Thus, the work presented in this thesis can help to provide an understanding of how to control these collisional processes at the surface. The challenge for the future will be the design of sensitive probes of these chemical processes.

In summary, the first experimental study of the surface ionisation of Rydberg hydrogen atoms at metal surfaces has been carried out. It has provided the opportunity for a genuine comparison of the experiment with theory, and is likely to promote further theoretical interest in the near future. The work presented in this thesis have demonstrated that studying the charge transfer of Rydberg states at metal surfaces can allow information on both the Rydberg state and the metal surface to be gained (including dynamical information). By manipulating the properties of the Rydberg state, the metal surface and the externally applied field, it is possible to gain some control over the surface interactions and the ionisation dynamics, which are important for the future prospective applications in surface characterisation and surface chemistry.

Appendix A

Detection probability as a function of ion-extraction field

It is noted in Section 6.2.1 that, due to the limited viewing area of the flexible optical fibre (9.1 mm $\times$ 6.6 mm), which couples the back of the phosphor screen to the photomultiplier tube, not all the ions formed from field- or surface-ionisation can be detected. Consequently, as the ions have non-zero parallel velocity with respect to the surface and the detector, there is an extraction field dependence for the fraction of ions that can be detected. It is explained in Section 6.1.2, that a second mesh at the entrance of the flight tube provides a second stage of acceleration for the positive ions in order to shorten the time they spend within the flight tube and to achieve an arrival time at the detector that is (nearly) extraction-field independent. The resulting *overall* flight times (from the surface to the detector) are $\sim 0.4 - 0.15$ μs for extraction fields of 100-4000 Vcm^{-1} (which is the typical range of fields for which ions are detected). Over this timescale, the corresponding parallel motion (across the detector) is typically $\sim 0.3 - 0.8$ mm. Figure A.1 shows the results of the Monte Carlo simulations that estimate the change in the fraction of ions detected as a function of ion-extraction field (normalised to the fraction of ions collected at the highest field). It can be seen that the change in the detected ion fraction is less than 15% over the typical range of

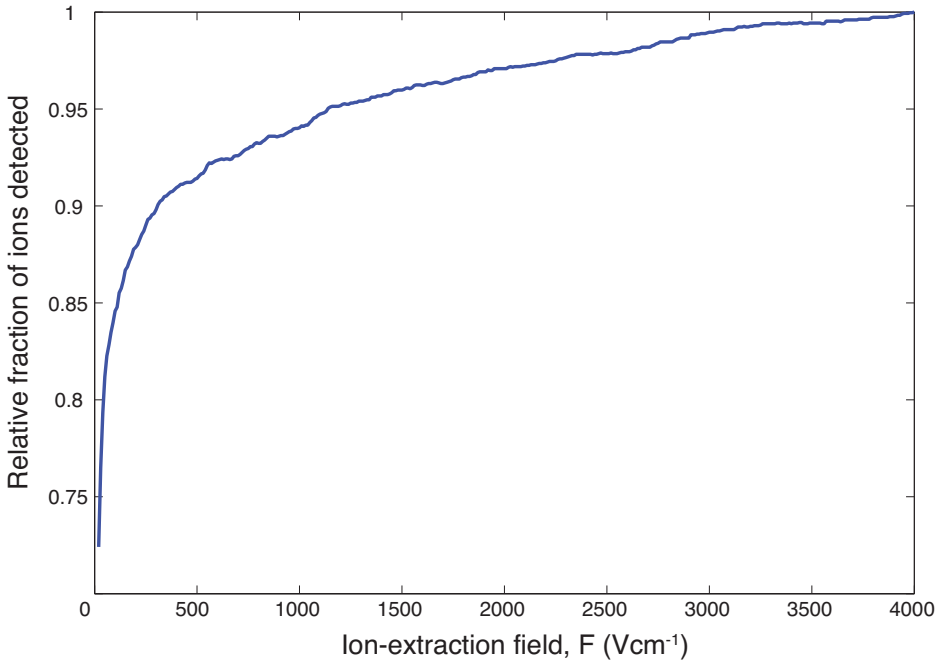

Figure A.1: The relative fraction of ions detected (relative to the highest field value) as a function of ion-extraction field, calculated from Monte Carlo simulations. The lower fractions at smaller extraction fields are due to ions with non-zero parallel velocity with respect to the detector moving out of the detection area.

detection fields.

To examine the effect of the field dependent detection probability on the surface ionisation profiles presented in this work, the Monte Carlo detection function shown in Fig. A.1 is fitted with a high-order polynomial, and applied to the surface ionisation profiles as an 'instrumental scaling function'. Since the change in the fraction of ions detected (due to their parallel motion with respect to the detector) is largest at low extraction fields (Fig. A.1), the surface ionisation profiles with the largest signal at low-extraction fields are likely to be affected the most. It is shown in Section 7.6 that the ion signal at lower extraction fields is much larger for the rough machined aluminium surface compared with the atomically flat evaporation-deposited gold surface. Figure A.2 shows the surface ionisation profiles for the most red-shifted state of the $n = 20 - 36$ manifold at a rough surface, before (blue lines) and after (red lines) the

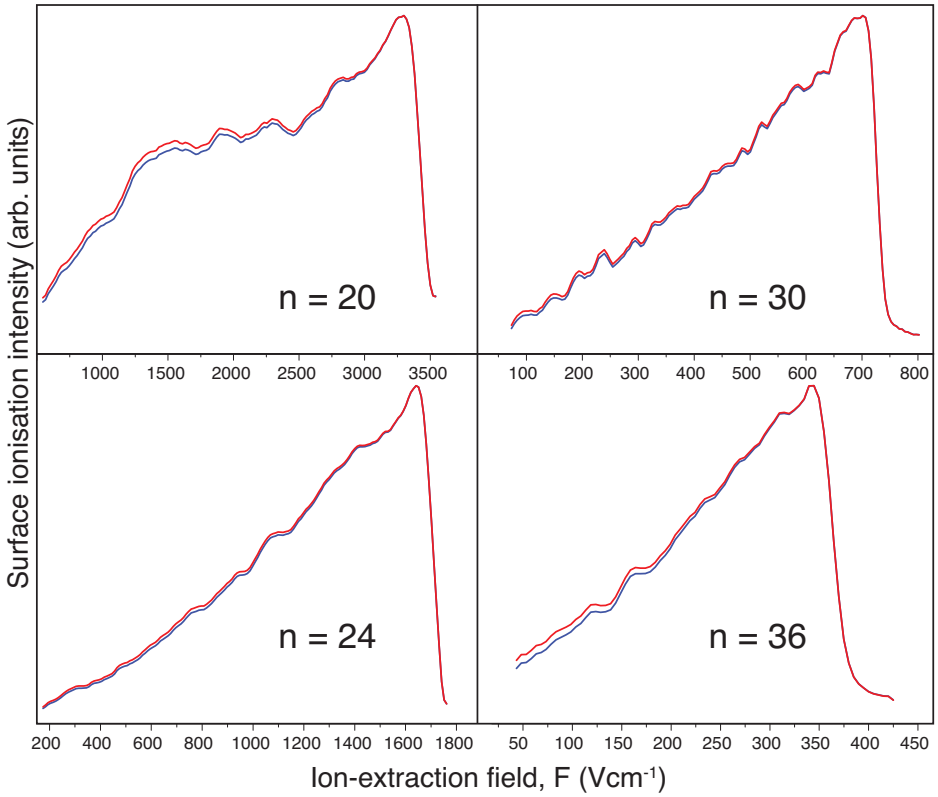

Figure A.2: The surface ionisation profiles for the red-shifted state ($k = 1 - n, m = 0$) of the $n = 20 - 36$ manifold at a rough surface. Blue lines are the un-scaled results, and the red lines are signal intensities that have been scaled with the 'instrumental function' given by Fig. A.1. The ionisation profiles are normalised to the maximum intensities.

application of the function described above. It can be seen that the change of the fraction of ions detected at each field has a very small effect on the surface ionisation profiles and is generally less than the noise level. It is therefore assumed that the change in ion-detection probability with ion-extraction field due to the parallel motion of the ions with respect to the detector does not have a significant effect on the results presented in this work.

References

[1] T. Sakurai and M. Toda, *Thin Solid Films*, **374**(2), 157–161 (2000).

[2] R. S. Mason, P. D. Miller, I. Mortimer, D. J. Mitchell, and N. A. Dash, *Phys. Rev. E*, **68**(1), 016408 (2003).

[3] N. Stolterfoht, D. Niemann, M. Grether, A. Spieler, and A. Arnau, *Scanning Microscopy*, **12**(3), 437–448 (1998).

[4] J. X. Wang and L. Holmlid, *Chem Phys*, **261**(3), 481–488 (2000).

[5] S. Badiei and L. Holmlid, *J. Phys. B: At. Mol. Opt. Phys.*, **39**(20), 4191–4212 (2006).

[6] N. A. Nguyen, B. K. Dey, M. Shapiro, and P. Brumer, *J Phys Chem A*, **108**(39), 7878–7888 (2004).

[7] T. Breeden and H. Metcalf, *Phys. Rev. Lett.*, **47**(24), 1726–1729 (1981).

[8] E. Vliegen and F. Merkt, *Phys. Rev. Lett.*, **97**(3), 033002 (2006).

[9] M. Saffman, T. G. Walker, and K. Mølmer, *Reviews of Modern Physics*, **82**(3), 2313–2363 (2010).

[10] J. Mozley, P. Hyafil, G. Nogues, M. Brune, J. M. Raimond, and S. Haroche, *The European Physical Journal D*, **35**(1), 43–57 (2005).

[11] A. Tauschinsky, R. M. T. Thijssen, S. Whitlock, H. B. van Linden van den Heuvell, and R. J. C. Spreeuw, *Phys. Rev. A*, **81**(6), 063411 (2010).

[12] H. Kuebler, J. P. Shaffer, T. Baluktsian, R. Loew, and T. Pfau, *Nat Photonics*, **4**(2), 112–116 (2010).

[13] E. Urban, T. A. Johnson, T. Henage, L. Isenhower, D. D. Yavuz, T. G. Walker, and M. Saffman, *Nat Phys*, **5**(2), 110 (2009).

[14] A. Gaëtan, Y. Miroshnychenko, T. Wilk, A. Chotia, M. Viteau, D. Comparat, P. Pillet, A. Browaeys, and P. Grangier, *Nat Phys*, **5**(2), 115 (2009).

[15] J. Burgdörfer, P. Lerner, and F. Meyer, *Phys. Rev. A*, **44**(9), 5674–5685 (1991).

[16] N. S. Simonovic, *J Phys B-At Mol Opt*, **30**, L613–L618 (1997).

[17] M. Iñarrea, V. Lanchares, J. Palacián, A. Pascual, J. Salas, and P. Yanguas, *Phys. Rev. A*, **76**(5), 052903 (2007).

[18] N. S. Simonovic and J. P. Salas, *Phys Lett A*, **279**(5-6), 379–384 (2001).

[19] D. Wang, K. Huang, and S. Lin, *Eur Phys J D*, **54**(3), 699–706 (2009).

[20] D. Wang, M. L. Du, and S. Lin, *J. Phys. B: At. Mol. Opt. Phys.*, **39**(17), 3529–3539 (2006).

[21] J. W. Gadsuk, *Surf Sci*, **6**(2), 133–158 (1967).

[22] M. Remy, *J Chem Phys*, **53**(6), 2487 (1970).

[23] K. Ganesan and K. T. Taylor, *J Phys B-At Mol Opt*, **29**(7), 1293–1306 (1996).

[24] A. Borisov, D. Teillet-Billy, and J. Gauyacq, *Nuclear Instruments and Methods B*, **78**(1-4), 49–55 (1993).

[25] P. Nordlander and J. Tully, *Physical Review B*, **42**(9), 5564–5578 (1990).

[26] P. Nordlander, *Physical Review B*, **53**(7), 4125–4132 (1996).

[27] J. Hanssen, C. F. Martin, and P. Nordlander, *Surf Sci*, **423**(2-3), L271–L276 (1999).

[28] N. Nedeljković and Lj. D. Nedeljković, *Phys. Rev. A*, **72**(3), 032901 (2005).

[29] N. N. Nedeljković, *Phys. Rev. A*, **81**(3), 032902 (2010).

[30] P. Kurpick, U. Thumm, and U. Wille, *Phys. Rev. A*, **56**(1), 543–554 (1997).

[31] A. Borisov, A. Kazansky, and J. Gauyacq, *Phys. Rev. B*, **59**(16), 10935–10949 (1999).

[32] J. Sjakste, A. G. Borisov, and J. P. Gauyacq, *Phys Rev A*, **73**(4), 042903 (2006).

[33] H. Chakraborty, T. Niederhausen, and U. Thumm, *Phys Rev A*, **70**(5), 052903 (2004).

[34] E So, M. T Bell, and T. P Softley, *Phys. Rev. A*, **79**(1), 012901 (2009).

[35] H. Bethe and E. Salpeter, *Quantum mechanics of one- and two-electron atoms*, Plenum Publishing Corporation, New York, 1977.

[36] H. Goldstein, *Am J Phys*, **44**(11), 1123–1124 (1976).

[37] A. Anderson, S. Haroche, E. Hinds, W. Jhe, and D. Meschede, *Phys. Rev. A*, **37**(9), 3594–3597 (1988).

[38] V. Sandoghdar, C. Sukenik, E. Hinds, and S. Haroche, *Phys. Rev. Lett.*, **68**(23), 3432–3435 (1992).

[39] V Sandoghdar, CI Sukenik, S Haroche, and EA Hinds, *Phys. Rev. A*, **53**(3), 1919–1922 (1996).

[40] C. Fabre, M. Gross, J. M. Raimond, and S. Haroche, *J Phys B-At Mol Opt*, **16**(21), L671–L677 (1983).

[41] C. A. Kocher and C. R. Taylor, *Phys Lett A*, **124**(1-2), 68–72 (1987).

[42] G. E. Mccown, C. R. Taylor, and C. A. Kocher, *Phys. Rev. A*, **38**(8), 3918–3936 (1988).

[43] D. F. Gray, Z. Zheng, K. A. Smith, and F. B. Dunning, *Phys. Rev. A*, **38**(3), 1601–1603 (1988).

[44] S. B. Hill, C. B. Haich, Z. Zhou, P. Nordlander, and F. B. Dunning, *Phys. Rev. Lett.*, **85**(25), 5444–5447 (2000).

[45] F. B. Dunning, S. Wethekam, H. R. Dunham, and J. C. Lancaster, *Nucl Instrum Meth B*, **258**(1), 61–67 (2007).

[46] D. D. Neufeld, H. R. Dunham, S. Wethekam, J. C. Lancaster, and F. B. Dunning, *Surf Sci*, **602**(7), 1306–1312 (2008).

[47] D. D. Neufeld, H. R. Dunham, S. Wethekam, J. C. Lancaster, and F. B. Dunning, *Phys. Rev. B*, **78**(11), 115423 (2008).

[48] Y. Pu, D. D. Neufeld, and F. B. Dunning, *Phys. Rev. A*, **81**(4), 042904 (2010).

[49] G. R. Lloyd, S. R. Procter, and T. P. Softley, *Phys. Rev. Lett.*, **95**(13), 1–4 (2005).

[50] G. R. Lloyd, S. R. Procter, E. A. McCormack, and T. P. Softley, *J Chem Phys*, **126**(18), 184702 (2007).

[51] E. A. McCormack, M. S. Ford, and T. P. Softley, *The Journal of Physical Chemistry A*, **114**, 11175—11188 (2010).

[52] C. Oubre, P. Nordlander, and F. B. Dunning, *J Phys Chem B*, **106**(33), 8338–8341 (2002).

[53] F. B. Dunning, H. R. Dunham, C. Oubre, and P. Nordlander, *Nucl Instrum Meth B*, **203**, 69–75 (2003).

[54] T. P. Softley, *Int Rev Phys Chem*, **23**(1), 1–78 (2004).

[55] J. D. Bekenstein and J. B. Krieger, *Phys Rev*, **188**(1), 130–& (1969).

[56] Ch. Seiler, S. Hogan, H. Schmutz, J. Agner, and F. Merkt, *Phys. Rev. Lett.*, **106**(7), 073003 (2011).

[57] R. J. Damburg and V. V. Kolosov, *J Phys B-At Mol Opt*, **12**(16), 2637–2643 (1979).

[58] R. O. Jones, P. J. Jennings, and O. Jepsen, *Phys. Rev. B*, **29**(12), 6474–6480 (1984).

[59] J. B. Camp, T. W. Darling, and R. E. Brown, *Journal of Applied Physics*, **69**(10), 7126 (1991).

[60] J. D. Carter and J. D. D. Martin, *Physical Review A*, **83**(3), 032902 (2011).

[61] C. Speake and C. Trenkel, *Phys. Rev. Lett.*, **90**(16), 160403 (2003).

[62] J. M. Obrecht, R. J. Wild, and E. A. Cornell, *Phys. Rev. A*, **75**(6), 62903 (2007).

[63] M. A. Cazalilla, N. Lorente, R. D. Muino, J. P. Gauyacq, D. Teillet-Billy, and P. M. Echenique, *Phys. Rev. B*, **58**(20), 13991–14006 (1998).

[64] E. A. Mccormack, Dphil thesis, University of Oxford, 2010.

[65] A. Borisov, R. Zimny, D. Teillet-Billy, and J. Gauyacq, *Phys. Rev. A*, **53**(4), 2457–2465 (1996).

[66] W. H. Press, S. A. Teukolsky, B. P. Flannery, and W. T. Vetterling, *Numerical Recipes in FORTRAN: The Art of Scientific Computing*, Cambridge University Press, New York, NY, USA, 1992.

[67] W. P. Reinhardt, *Annu Rev Phys Chem*, **33**, 223–255 (1982).

[68] D. Baye, M. Hesse, and M. Vincke, *Phys Rev E*, **65**(2), 026701 (2002).

[69] J. V. Lill, G. A. Parker, and J. C. Light, *Chem Phys Lett*, **89**(6), 483–489 (1982).

[70] A. M. Cohen, *Linear Algebra Appl*, **240**, 183–198 (1996).

[71] H. Suno, L. Andric, T. P. Grozdanov, and R. McCarroll, *Eur Phys J D*, **13**(2), 213–220 (2001).

[72] M. Vincke, L. Malegat, and D. Baye, *Journal of Physics B: Atomic, Molecular and Optical Physics*, **26**, 811 (1993).

[73] J. Rubbmark, M. Kash, M. Littman, and D. Kleppner, *Phys. Rev. A*, **23**(6), 3107–3117 (1981).

[74] K. M. Dunseath, J-M. Launay, M. Terao-Dunseath, and L. Mouret, *Journal of Physics B: Atomic, Molecular and Optical Physics*, **35**, 3539 (2002).

[75] M. Abramowitz and I. A. Stegun, *Handbook of Mathematical Functions with Formulas, Graphs, and Mathematical Tables*, Dover, New York, ninth ed., 1964.

[76] A. R. Barnett, *Computer Physics Communucations*, **27**, 147 (1982).

[77] T. Gonzalez-Lezana, E. J. Rackham, and D. E. Manolopoulos, *J Chem Phys*, **120**(5), 2247–2254 (2004).

[78] J. A. Fleck, J. R. Morris, and M. D. Feit, *Appl Phys*, **10**(2), 129–160 (1976).

[79] E. Y. Usman, I. F. Urazgil'din, A. G. Borisov, and J. P. Gauyacq, *Phys. Rev. B*, **64**(20), 205405 (2001).

[80] J. Gibbard, Private Communication.

[81] I. E. Tamm, *Z. Physik*, **76**(11-12), 849–850 (1932).

[82] W. Shockley, *Phys. Rev.*, **56**(4), 317–323 (1939).

[83] P. M. Echenique and J. B. Pendry, *J. Phys. C Solid State*, **11**(10), 2065–2075 (1978).

[84] E. V. Chulkov, V. M. Silkin, and P. M. Echenique, *Surf Sci*, **437**(3), 330–352 (1999).

[85] T. Klamroth, P. Saalfrank, and U. Höfer, *Phys. Rev. B*, **64**(3), 35420 (2001).

[86] A. G. Borisov, J. P. Gauyacq, and A. K. Kazansky, *Surf Sci*, **505**(1-3), 260–270 (2002).

[87] E. V. Chulkov, A. G. Borisov, J. P. Gauyacq, D. Sanchez-Portal, V. M. Silkin, V. P. Zhukov, and P. M. Echenique, *Chem Rev*, **106**(10), 4160–4206 (2006).

[88] A. G. Borisov, J. P. Gauyacq, A. K. Kazansky, E. V. Chulkov, V. M. Silkin, and P. M. Echenique, *Phys. Rev. Lett.*, **86**(3), 488–491 (2001).

[89] J. C. Tully, *Faraday Discuss.*, **110**, 407–419 (1998).

[90] D. M. Greenberger, *Phys. Rev. Lett.*, **87**(10), art. no.–100405 (2001).

[91] J. N. Bardsley, *Case Stud. At. Phys.*, **4**, 299 (1974).

[92] C. E. Moore, *Atomic energy levels*, Vol. III, Nat. Bur. Stand. (U.S.), U.S. GPO, Washington, D.C., 1958.

[93] L. Wang and R. D. Knight, *Phys. Rev. A*, **34**(5), 3902 (1986).

[94] N. Gaillard, M. Gros-Jean, D. Mariolle, F. Bertin, and A. Bsiesy, *Applied Physics Letters*, **89**(15), 154101 (2006).

[95] Y. Yamakita, S. R. Procter, A. L. Goodgame, T. P. Softley, and F. Merkt, *J Chem Phys*, **121**(3), 1419–1431 (2004).

[96] D. Townsend, A. Goodgame, S. Procter, S. Mackenzie, and T. P.Softley, *Journal of Physics B: Atomic, Molecular and Optical Physics*, **34**, 439 (2001).

[97] E. Vliegen and F. Merkt, *Phys. Rev. Lett.*, **97**(3), 1–4 (2006).

[98] F. Merkt and R. N. Zare, *J Chem Phys*, **101**(5), 3495–3505 (1994).

[99] B. Obreshkov and U. Thumm, *Phys. Rev. A*, **74**(1), 012901 (2006).

[100] S. Willitsch, J. M. Dyke, and F. Merkt, *Helv Chim Acta*, **86**(4), 1152–1166 (2003).

[101] P. W. Atkins, *Molecular Quantum Mechanics, Third Edition*, Oxford University Press, 1997.

[102] C. Delsart, L. Cabaret, C. Blondel, and R. J. Champeau, *J Phys B-At Mol Opt*, **20**(18), 4699–4713 (1987).

[103] G. Binning, K. H. Frank, H. Fuchs, N. Garcia, B. Reihl, H. Rohrer, F. Salvan, and A. R. Williams, *Phys. Rev. Lett.*, **55**(9), 991–994 (1985).

[104] P. Wahl, M. A. Schneider, L. Diekhoner, R. Vogelgesang, and K. Kern, *Phys. Rev. Lett.*, **91**(10), 106802 (2003).

[105] S. Crampin, *Phys. Rev. Lett.*, **95**(4), 046801 (2005).

[106] D. B. Dougherty, P. Maksymovych, J. Lee, M. Feng, H. Petek, and J. T. Yates, *Phys Rev B*, **76**(12), 125428 (2007).

[107] U. Hofer, I. L. Shumay, C. Reuß, U. Thomann, W. Wallauer, and T. Fauster, *Science*, **277**(5331), 1480 (1997).

[108] D. Wouters and U. S. Schubert, *Angew Chem Int Edit*, **43**(19), 2480–2495 (2004).

[109] J Gudde and U Hofer, *Prog Surf Sci*, **80**(3-4), 49–91 (2005).

[110] F. Schiller, M. Ruiz-Osés, J. Cordón, and J. Ortega, *Phys. Rev. Lett.*, **95**(6), 066805 (2005).

[111] A. Mugarza, A. Mascaraque, V. Perez-Dieste, V. Repain, S. Rousset, F. J. G. de. Abajo, and J. E. Ortega, *Phys. Rev. Lett.*, **87**(10), art. no.–107601 (2001).

[112] P. Rinke, K. Delaney, P. García-González, and R. W. Godby, *Phys. Rev. A*, **70**(6), 63201 (2004).

[113] M. Califano and P. Harrison, *Journal of Applied Physics*, **86**, 5054 (1999).

[114] D. Yamaguchi, T. Matsumoto, K. Watanabe, N. Takagi, and Y. Matsumoto, *Phys. Chem. Chem. Phys.*, **8**(1), 179–185 (2005).

[115] C. Urban, D. Ecija, Y. Wang, M. Trelka, I. Preda, A. Vollmer, N. Lorente, A. Arnau, M. Alcami, L. Soriano, N. Martin, F. Martin, R. Otero, J. M. Gallego, and R. Miranda, *J Phys Chem C*, **114**(14), 6503–6510 (2010).

[116] T. C. Shen and P. Avouris, *Surf Sci*, **390**(1-3), 35–44 (1997).